UNIVERSITY OF
BIRMINGHAM

Mixed Anion Amides for Hydrogen Storage

by

David R. Hewett

Supervisor: Dr Paul A. Anderson

A thesis submitted to The University of Birmingham for
the degree of Doctor of Philosophy

The School of Chemistry
College of Engineering and Physical Sciences
The University of Birmingham

August 2012

To Chloë

Abstract

Metal hydride materials have attracted much interest for their potential use as hydrogen storage materials. Complex hydrides are amongst the most promising due to their high gravimetric storage capacities and favourable de/rehydrogenation conditions. Here, mixed anion complex hydrides are investigated both through halide doping of $LiNH_2$ and Li_2NH, and though a mixed $LiNH_2$-$LiBH_4$ system.

The reaction of $LiNH_2$ and Li_2NH with lithium or magnesium chloride, bromide and iodide has been shown to form a series of amide- and imide-halide phases. The structures of these phases were investigated through powder diffraction methods as well as Raman spectroscopy. The hydrogen releasing properties of these materials were investigated through reaction with LiH and MgH_2; while the equivalent hydrogenation reactions were also tested. In both cases these materials performed more favourably than the pure $LiNH_2$-LiH system. The lithium ion conductivity of these materials was also investigated; it was shown that the most conducting materials were also the quickest to release and uptake hydrogen.

The $LiNH_2$-$LiBH_4$ system was studied, with particular focus on the decomposition product, Li_3BN_2. All three known polymorphs of this compound were shown to be able to form by the reaction of $2LiNH_2 + LiBH_4$ by carefully changing the reaction conditions. Further stages of this system were investigated through reaction of Li_2NH and Li_3N with $LiBH_4$. Here the products from these reactions were studied along with the thermal desorption properties of the systems.

Acknowledgements

Well here it is, at some points I didn't think I would make it, but I have now completed my thesis. There are many people who have helped and supported me during this work, and I owe them all a great deal of thanks. Firstly I would like to thank my supervisor Paul Anderson for all his help and guidance over the last few years. I would like to thank the other members of Paul's group, Big Matt, Alex, Alvaro, Ivan and Trang; with a special mention to Phil Chater for continuous help with this work. I would also like to thank the rest of Floor 5 for making it an enjoyable place to work. In Met & Mat I would like to thank David Book, Allan Walton and especially Dan Reed for the use of equipment.

Many friends have given a welcome relief from work over the years and for that I am grateful. My thanks to Laird, Luke, Matt, Hank, Jack, Gemma, Yan, Carey, Becky, Tom, Tim; as well as members of Bournville Village FC and BRAT athletics club. Hopefully I will be able to see much more of you all now that this is done.

I would like to thank my family for their continued support; thanks to Mum, Dad, Ruth, Nathan, Chris, Trish, Richard, Sam, Olivia, Bethany and Josh.

Finally I would to thank my wife Chloë, for telling me to do some work when I was being lazy, and for telling me to take a break when I needed one. Thank you for always believing in me.

Thank you all.

Contents

Chapter 1

Introduction

Currently the majority of the world's energy needs are met by the use of fossil fuels: coal, oil and natural gas. The use of fossil fuel as our main energy supply is not sustainable for two main reasons: first there is only a finite supply of these fossil fuels, a supply which is rapidly depleting; secondly the carbon released by the combustion of these fossil fuels has been linked to global climate change. For these reasons there is need to find a replacement for fossil fuels with ever increasing urgency.

Before the invention of the steam engine, man's energy requirements were met solely by the use of plants for fuel. This provided a carbon neutral cycle as the carbon released from this fuel was offset by that absorbed by plants *via* photosynthesis. After the invention of the steam engine, fossil fuels could be used to increase the amount of work man was able to do, and this led to the basis of an industrialised society, with ever increasing energy demands. Since the industrial revolution, the world's energy demands have increased dramatically, with around 80% of these needs being met by fossil fuels [1]. The use of these fossil fuels releases CO_2 into the atmosphere which was stored in the ground. Already the concentration of CO_2 in the atmosphere is over 30% above the level from before the industrial revolution and if the current rate of growth continues, the yearly rate of CO_2 emissions into the atmosphere will have doubled by 2050 [2, 3].

Hydrogen is an energy carrier, much like electricity, and as such it has the potential to help solve the world's energy needs. It can also be seen in equation 1.1 that there is a trend in the form of energy carriers away from carbon, towards a more hydrogen rich fuel, as well as from a solid fuel to a gaseous one. While by no means an argument by itself, this suggests that hydrogen could be an ideal energy carrier to help reduce CO_2 emissions.

$$C_{(s)} \text{ (coal)} \rightarrow \text{-}CH_2\text{-}_{(l)} \text{ (oil)} \rightarrow CH_{4(g)} \text{ (natural gas)} \rightarrow H_{2(g)} \tag{1.1}$$

1.1 Hydrogen Production

Hydrogen is comfortably the most abundant element in the universe, however, on earth less than 1% of this is found in its molecular form, H_2 gas. The vast majority found on earth is in the oxidation product of water, H_2O, while some is found in liquid or gaseous hydrocarbons [4]. It is the molecular, gaseous form of hydrogen which can be used a fuel, as such the first step towards to use of hydrogen as a fuel is the synthesis of the molecular form, H_2 [5]. The move to a hydrogen economy would therefore involve the move to a synthetic fuel rather than 'free energy' as with fossil fuels, where the energy has been naturally stored for millions of years and the cost is associated with the mining rather than synthesis. If the worlds demand for fossil fuels were to be met by hydrogen then roughly 100 times the present production rate would be required [1], more than 3 x 10^{12} kg. This move would require significant investment and the world economy would need to be convinced of the benefits.

1.1.1 Current Production

In recent years more than 90% of the world's hydrogen has been produced by the steam reforming process [6]. Steam reforming is a fuel processing technology where hydrocarbons are converted into a hydrogen rich steam. The process

involves the use of high temperature steam, above 500 °C, and occurs *via* the endothermic reaction shown in equation 1.2. Due to the formation of carbon monoxide, a water-gas shift reaction (equation 1.3) is used to turn this carbon monoxide into carbon dioxide and produce more H_2 in the process.

$$\text{-}(CH_2)\text{-}_{(n)} + H_2O \rightarrow CO + (n+1)H_2 \tag{1.2}$$

$$CO + H_2O \rightarrow CO_2 + H_2 \tag{1.3}$$

Two other primary fuel processing technologies of partial oxidation and autothermal reforming also convert hydrocarbons in hydrogen, however, steam reforming is by the far the most commonly used [7]. All of these techniques, however, use fossil fuels as the source of the hydrogen and therefore have an overall release of CO_2 from the process. While it is likely that hydrogen will continue to be produced *via* this method for the short-term, it is not sustainable in the long-term due to its reliance on fossil fuels and failure to reduce CO_2 emissions [8].

1.1.2 Hydrogen from Water

Splitting water to make hydrogen and oxygen is potentially the cleanest way to produce hydrogen and there has been a great deal of research into this; in fact, its commercial use dates back to the 1890's [7]. Despite the hydrogen not being produced from fossil fuels, how clean and sustainable the process is, is dependent upon the energy source used in the process.

The most common form of water splitting to make hydrogen is *via* electrolysis, this is simply using an electric current run through two electrodes, made of an inert metal, to break water apart to make hydrogen and oxygen. Reduction occurs at the negatively charged cathode to produce hydrogen, while oxidation occurs

at the positively charged anode; these process are shown in equations 1.4 and 1.5, respectively. As this process is thermodynamically unfavourable, an electric potential is required to drive process. An electrolyte is added to the water to increase the rate of electrolysis.

$$2H^{+}{}_{(aq)} + 2e^{-} \rightarrow H_{2(g)} \tag{1.4}$$

$$2H_2O_{(l)} \rightarrow O_{2(g)} + 4H^{+}{}_{(aq)} + 4e^{-} \tag{1.5}$$

Efficiencies from electrolysis of this type are around 70% at ambient conditions [9], however, improvements to the process can push to efficiency up as high as 85 % [10]. Electrolysis powered by electricity from renewable energy sources like wind turbines or photo-voltaics would provide a long-term and clean method of hydrogen production for the long-term.

Hydrogen can also be produced from water *via* thermochemical water splitting (or thermolysis). This is the decomposition of water to hydrogen and oxygen purely by heating. Water will decompose at around 2500 °C, however, suitable heating sources are not readily available. Solar furnaces can be built which focus the suns light energy onto a small area and are capable of reaching the required temperatures [11]. This process has the advantage of using a renewable energy source in the form of sunlight. Product gases must be separated to avoid recombination and so that the hydrogen produced may be used.

1.1.3 Hydrogen from Biomass

Producing hydrogen from biomass is seen by many as the most likely renewable substitute to petroleum in the short-term and in the United States it is second only to hydropower as a primary renewable energy source [7, 12]. Biomass is available from a wide range of sources including animal waste, municipal wastes

and agricultural wastes. Biomass can also be used to produce hydrogen; the main techniques for this are gasification and fermentation.

Gasification is a similar process to that of steam reformation. The biomass is heated and broken down to produce a mixture of H_2, CH_4, CO and CO_2 amongst other gases. Steam is then added to this mixture (eq. 1.2) to produce CO and H_2 before a water-gas shift reaction (eq. 1.3) produces CO_2 and further H_2. The process of hydrogen production through gasification of biomass can be considered carbon neutral; while CO_2 is released in the process, it is CO_2 which has originally been absorbed by the plant life which forms the biomass.

Dark fermentation of biomass can produce hydrogen and carbon dioxide. These are produced alongside oxygen from the anaerobic growth of bacteria on carbohydrate rich substrates. As is the case with gasification, this process can be considered as CO_2 neutral, however, this process has further advantages of being able to use low quality biomass which requires minimal pre-treatment; furthermore the system may be integrated to use the remaining substrate to produce further products such as CH_4 [13].

1.2 Hydrogen as a Fuel

Chemical potential energy is the energy relating to the valence electrons in atoms or molecules and their potential to form more stable arrangements through reaction. Hydrogen has the best ratio of valence electrons available to a reaction per unit mass as it is made up of only one electron and one proton. This makes hydrogen a very attractive source of chemical potential energy.

Hydrogen as a fuel is the cleanest burning; when burnt in oxygen the only exhaust gas is water. This gives hydrogen a large advantage over petroleum by cutting CO_2 emissions into the atmosphere. As hydrogen is a synthetic fuel it also overs energy independence and security, free from the need to import fuels.

Once produced, hydrogen also offers energy rich fuel; it has a lower heating

values of 120.1 MJ kg^{-1}, compared to that of petroleum (42.5 MJ kg^{-1}) [14]. This energy can either be harnessed in the same way as petroleum, through an internal combustion engine (ICE), producing mechanical power, or it can be harnessed through electrochemical means using a fuel cell.

1.2.1 Internal Combustion Engine

The internal combustion engine is a well established and extremely widely used technology and in fact the first ICE was designed and built to run on a mixture of hydrogen and oxygen. This was built by François Isaac de Rivaz in 1807 [15]. Hydrogen as a gas can be used directly in a modern day petroleum combustion engine, with limited modifications required. The hydrogen fuel is burnt in the same way as petroleum; some of the need for modification to the engine comes from the fact that the hydrogen burns hotter. Other modifications include the need for a lubricant which is resistant to reduction and an exhaust system which is capable of withstanding the water vapour [16].

The technology of ICEs is well established and has good background of reliability. While the efficiency of ICEs has been fine tuned and many improvements have been made, the energy efficiency of ICEs is partially limited by Carnot cycle. This thermodynamic limitation gives a theoretical efficiency of roughly 40 %, this has been shown by some diesel engines and has been achieved by hydrogen ICEs [17]. However, the real limitation on the efficiency of an ICE comes from not being able to operate at the maximum combustion temperature. This limitation is therefore imposed by materials constraints, not thermodynamics [18].

Due to the well established ICE technologies and the potential to use the current manufacturing infrastructure, it is possible that the use of hydrogen ICEs could be a good starting point for the development of a hydrogen infrastructure and economy. ICE technology is currently cheaper than that of fuel cells and when run with hydrogen as fuel offers huge reductions in CO_2 emissions. There is also much current research into using a hydrogen-petroleum bifuel ICE which

could further act as a stepping stone to a hydrogen economy while still offering some reduction on CO_2 emissions on a petroleum ICE [19]. Despite the possible advantages, only BMW, Ford and Mazda had active hydrogen ICE research programmes of the major automotive companies.

1.2.2 Fuel Cells

If ICEs are to be replaced then fuel cells are seen by many as the best alternative technology. Fuel cells were invented by William Grove in 1839 and are electrochemical energy conversion devices in which electrical energy is obtained directly from the chemical energy of a reaction. There is a large variety of fuel cells, characterised by the type of electrolyte used; some of the most common electrolytes are alkaline, solid oxide, phosphoric acid and polymer membrane. When used with hydrogen, produced from a sustainable source, as a fuel, fuel cells are seen as the best way to a clean energy future [20].

Polymer electrolyte membrane (or proton exchange membrane) fuel cells, PEMFC, are the primary candidate for next generation power sources for transportation applications due to a number a key advantages. The first of these advantages is that, when hydrogen is used as the fuel, the only exhaust gas is water, using oxygen from the air as the oxidant. Other advantages include the ability to work with high efficiencies at low temperatures of around 70 °C giving quick start up times; they have a high power density and can easily be scaled up *via* the use of a fuel stack to further increase the power density [21]. A disadvantage of PEMFCs is that the performance of the fuel cell is negatively affected by the presence of low levels of contaminants in the fuel supply such as ammonia, carbon monoxide and organic compounds [22]. One other problem with the large-scale use of PEMFCs is the high cost, relative to ICEs; including the high cost of materials such as platinum for electrode catalysts. However, as the technologies have improved the cost has reduced by around 30% in the last 5 years and is expected to continue to fall.

In a PEMFC, hydrogen gas is supplied to the anode, where a catalyst (usually platinum) splits the hydrogen into protons and electrons (equation 1.6). The polymer membrane itself acts as the electrolyte and allows the protons to permeate through but does not conduct electrons, therefore forcing these through an external circuit, producing electric power. At the cathode, oxygen, from air, combines with the protons and electrons to produce water (equation 1.7). A schematic of a PEMFC is shown in figure 1.1. Several automotive companies have produced cars using PEMFCs for the power supply including Toyota, Honda, General Motors, Hyundai, Kia and Daimler [21].

$$2H_2 \rightarrow 4H^+ + 4e^- \tag{1.6}$$

$$O_2 + 4H^+ \rightarrow H_2O \tag{1.7}$$

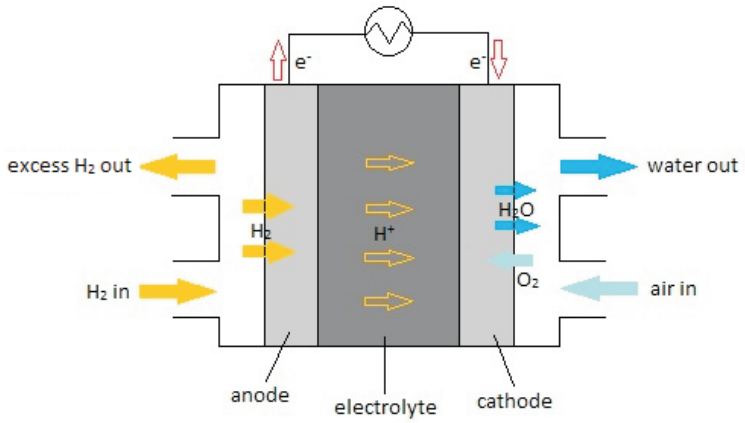

Figure 1.1: Schematic representation of a PEMFC, adapted from ref. [23].

1.3 Alternatives to Hydrogen

There are many different technologies available and currently being researched to replace fossil fuels and/or lower greenhouse gas emissions. For mobile applications

these include liquified petroleum gas (LPG) and biofuels. While made from fossil fuels, LPG has significantly lower CO_2 emissions than petrol and can be used in petrol ICEs with minor modifications. Biofuels can be made from different sources including food crops. The oil from these can either be used directly (biodiesel) or they can be treated to produce ethanol; both routes have lower emissions than petrol or diesel. However, the main alternative to hydrogen as a replacement for fossil fuels is the direct use of electricity, stored in batteries.

As mentioned previously, hydrogen needs to be synthesised, potentially *via* the process of electrolysis. The hydrogen is then converted back to electrical energy in a fuel cell as discussed in the previous section. This conversion of energy into hydrogen and back again has an effect on the efficiency of the hydrogen-fuel cell system compared to using electricity directly. Typically a hydrogen fuel efficiency is roughly two thirds that of a battery in the same system [24, 25].

This energy efficiency is a big advantage of the use of batteries in mobile applications. A further, and even bigger, advantage of batteries is that the infrastructure required for the use of this technology is already in place. Conversely the move to the use of hydrogen would need a huge amount of investment. One significant disadvantage to the use of batteries for mobile applications is that in contrast to a fuel cell which, if provided with fuel, can run continuously, a battery needs recharging which can take several hours; and the ranges between charges are currently low. It is likely that the majority of fuel cell vehicles will use a hybrid system, combining a battery and a fuel cell, to meet the energy demands for mobile applications [26].

1.4 Hydrogen Storage

The storage of hydrogen for use in mobile applications involves a balance and compromise between two properties of the storage system; the volumetric and gravimetric capacities.

Hydrogen has a density of 0.0899 kg m^{-3} at ambient temperatures and pressures. To travel around 400 km in a car, 4 kg of hydrogen would be required when used with a fuel cell; this compares favourably to 8 kg of hydrogen for use with an ICE or 24 kg of petrol in an ICE. However, due to its extremely low volumetric density, this 4 kg of hydrogen would take up an extremely impractical volume of 44 m^3 [4]. It is therefore clear that the challenge of volumetric storage capacity is to reduce this large volume of hydrogen. However, this increase in volumetric capacity will always have an effect on the gravimetric capacity of the system. For consideration of the gravimetric capacity of the system we need to consider not only the hydrogen itself but also any other material used in the system, for example, the vessel in which the hydrogen is contained. As such, a compromise between the volumetric and gravimetric storage capacities of the overall system must be made.

There are two broad categories of hydrogen storage which cover a range of different methods; these are storage of molecular hydrogen *via* the compression or liquefaction of hydrogen gas, or by adsorption onto a surface, or the storage of atomic/ionic hydrogen *via* reaction to form metal hydrides/complex hydrides.

1.4.1 Molecular Hydrogen

Compressed Gas

The storage of hydrogen at high pressures as a compressed gas is the most commonly used today. As this is also the most common storage technique for many other gases, the infrastructure is in place and any safety issues for handling high pressure gases are well understood. Traditionally hydrogen is stored at pressure of 200 bar in reasonably cheap steel vessels. This improves the volumetric capacity, although the volume required for 4 kg of hydrogen is still 225 litres [4]; however, the gravimetric cost of storing hydrogen at this pressure comes mainly from the mass of the steel required. This makes the overall system have a gravimetric

capacity of roughly 1 wt % hydrogen [5]. Higher pressures can be achieved, however, with the use of steel for the vessel, this only lowers the gravimetric capacity further.

While the majority of cylinders being made at the moment are stainless steel, copper or aluminium alloys, research has been carried out into the use of carbon fibre gas cylinders. These cylinders are lightweight and have a high density; they are capable of having a gravimetric hydrogen capacity of 10 wt % by storing the hydrogen at pressures of up to 1000 bar [5]. There are obvious advantages in the storage capacities of these extremely high pressure cylinders. However, there are also significant disadvantages, first there are problems relating to the safety of having such high pressure gas in mobile systems. There are also issues with the complexity of the system required to step the pressure down to a usable pressure. Finally there is the issue of the cost, financially and also in terms of energy, of compressing the gas to such great pressures, energy which can not be reclaimed upon using the gas [27].

Liquefaction

Hydrogen is a liquid at temperatures below $-252\,^{\circ}\mathrm{C}$; in this state the hydrogen has a gravimetric density of 70.8 kg m^{-3}. This is the highest density of hydrogen in any state and is a significant improvement on compressed gas storage which has gravimetric densities of <40 kg m^{-3} at realistic pressures (<800 bar) [1].

Liquefaction of hydrogen is unfortunately a very inefficient way of storing hydrogen. First there is the energy cost of cooling the hydrogen to the required temperature. This is extremely energy intensive, using roughly 30 % of the chemical energy of the liquefied hydrogen in the process [5]. There is then the problem of maintaining these low temperatures to prevent boil off. Even with the best available thermal insulation, hydrogen boil off cannot be reduced below around 1% a day in tanks large enough to be suitable for mobile applications. There are also the issues concerned with cooling all the components required

for the delivery and storage of the liquid hydrogen; this adds further cost both financially and energetically. These issues will limit the use of liquified hydrogen and make it unlikely to be used on a wide scale.

Physisorption

The two conventional methods of hydrogen storage discussed so far seem unlikely to solve the problem of hydrogen storage. The most likely alternative is the use of solid state storage. Here I discuss the use of physisorption, a way of storing molecular hydrogen in the solid state. In the following section I discuss solid state storage methods for atomic/ionic hydrogen (chapter 1.4.2).

Physisorption is the binding of hydrogen to or inside a host through weak interactions, generally van der Waals forces. As these interactions are weak, typically 2 - 20 kJ mol^{-1} H_2 [1], therefore the thermal energy at room temperature is enough to desorb the hydrogen. This restricts significant hydrogen adsorption to low temperatures (typically with liquid nitrogen as a coolant) or high pressures. Hydrogen will bind most strongly to the surface of the host solid, with subsequent layers binding more weakly. Therefore materials used for physisorption of hydrogen must have high surface areas. Typical materials include zeolites, metal organic frameworks (MOFs), covalent organic frameworks (COFs) or polymers of intrinsic microporosity (PIMs).

Zeolites are aluminosilicate based materials and were the first inorganic porous materials to be investigated for gas storage; hydrogen storage capacities of around 1.8 wt % have been seen [28, 29]. MOFs are made up of inorganic clusters connected *via* organic linkers and like zeolites, they can use binding to metal centres to increase hydrogen uptake [30]. Through this, gravimetric capacities of over 6 wt % have been obtained at 77 K [31]. COFs are similar to MOFs but rather than the organic units being held together by metals ions, they are held together by strong covalent bonds between light elements (C, O, B, Si, N) [32]. Due to having low densities and permanent, high porosity they are thought

to be promising for us for storing hydrogen [33]. PIMs are polymers with rigid structures which are unable to pack efficiently, this gives them large free volume and inner surface [34]. They have a range of potential applications including hydrogen storage where they have been shown to have gravimetric capacities at 77 K of around 2.7 wt % [35].

These materials for hydrogen storage tend to be relatively cheap and simple in design. However, the low temperatures required for hydrogen storage along with relatively poor gravimetric and volumetric storage capacities.

1.4.2 Atomic/Ionic Hydrogen

Atomic/ionic hydrogen can be chemically bound in a metal-based compound. The hydrogen adsorption process first involves a chemisorption step where the hydrogen molecule is dissociated at the surface before diffusing into the bulk material and forming the chemical bond. There is therefore a relatively strong chemical bond to the hydrogen and the transition back to the original material requires an increase in temperature or reduction in pressure.

In the following two sections I will discuss first the use of metal hydrides as hydrogen storage before moving onto the use of complex hydrides.

1.4.3 Metal Hydrides

Stoichiometric ionic hydrides are formed from the alkali and alkaline earth metals (e.g. MgH_2), whereas transition metal hydrides are seen to form non-stoichiometric interstitial hydrides (e.g $PdH_{0.6}$). Figure 1.2 shows a typical pressure-composition isotherm [1]. This can be used to understand the formation of interstitial hydrides. At low pressure hydrogen is dissolved into the lattice of the host metal, forming a solid solution (α phase). At higher pressures more hydrogen is absorbed, forming an ordered hydride phase (β phase). The area of interest of this graph is the plateau region where both the α and β phases co-exist. In this region the amount of hydrogen in the metal may be easily changed by changes in pres-

sure or temperature. Above a certain temperature, T_c this plateau behaviour is lost and a continuous transition between the two phases is seen.

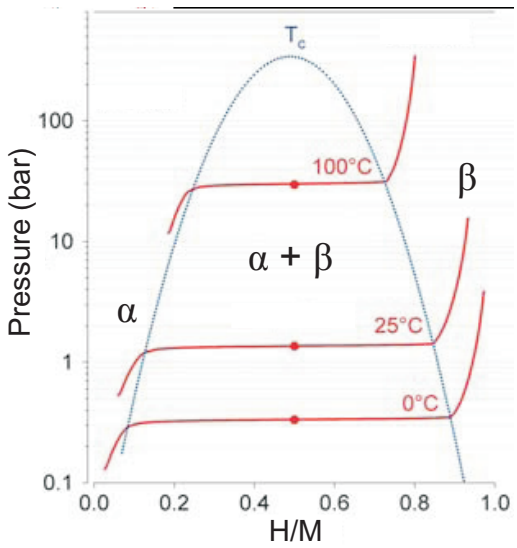

Figure 1.2: A pressure-composition-temperature plot for a metal hydride [1]

Metal hydrides have high volumetric hydrogen capacities, more than six times higher than that of hydrogen stored as a compressed gas at 200 bar [36]. However, metallic hydrides can be split broadly into two groups with opposing advantages and disadvantages for hydrogen storage applications.

The first of these groups is the intermetallic metal hydrides, for example $LaNi_5H_6$. This material has an extremely high volumetric hydrogen capacity with a density of 115 kg H_2 m^{-3} (compared to 70.8 kg H_2 m^{-3} for liquid hydrogen) and will release all of the hydrogen at pressures below 2 bar H_2 [1]. While $LaNi_5H_6$ is an excellent hydrogen storage material, for mobile applications the mass of the elements is too high, giving a gravimetric storage capacity of only 1.5 wt % H_2. This is the main issue with all intermetallic hydrides, with gravimetric capacities being limited to <4 wt % H_2 making them impractical for mobile applications [5].

The next group of materials is the light metal hydrides, through the use of light, alkali and alkaline earth metals, large increases in the gravimetric storage

capacities of metal hydrides can be achieved. Magnesium hydride, MgH_2, has the highest gravimetric storage capacity of the metal hydrides with proven reversibility with a gravimetric capacity of 7.7 wt % H_2. However, the problematic issue with MgH_2, along with other light metal hydrides, is the slow rates of hydrogen release and uptake [37]. The kinetics of the de/rehydrogenation reactions have been improved *via* the use of mechanical milling, with and without precious metals, and the inclusion of $LiBH_4$ [38]. However, temperatures greater than 275 °C are still required for reasonable rates of hydrogen release and uptake.

1.4.4 Complex Hydrides

Many different metal-hydrogen complexes can be formed from the simple metal hydrides discussed previously. In these materials, hydrogen is covalently bonded to a central atom to form a complex anion. This then forms an ionic bond to a metal cation [39]. The complex anions which will be discussed here are aluminium hydrides, AlH_4^-, amides, NH_2^- and borohydrides, BH_4^-. Along with heavier, transitions metals, complex hydrides form with most alkali and alkaline earth metals. When they are formed with light metals such as lithium, magnesium, sodium and aluminium they have high gravimetric storage capacities and are considered to be among the best candidates for hydrogen storage in mobile applications.

Aluminium Hydrides

Lithium and sodium aluminium hydrides (or alanates) can be synthesised directly from the elements or through reaction of aluminium halides with the appropriate metal hydride in solution [40]. While magnesium aluminium hydride can be easily prepared from $NaAlH_4$ and MgH_2 *via* a salt metathesis reaction [41].

$LiAlH_4$ and $NaAlH_4$ have high gravimetric storage capacties of 10.5 wt % H_2 and 7.4 wt % H_2 respectively. These two aluminiun hydrides release hydrogen *via* the two step reaction shown in equation 1.8, The first step of decompos-

tion of $LiAlH_4$ beginning at around 190°C, with the second step at 230 °C [42]. In the case of $NaAlH_4$ the two stages begin at around 210 °C and 250 °C [43]. Decomposition of the relevant metal hydride will occur at considerably higher temperatures.

$$3MAlH_4 \rightarrow M_3AlH_6 + 2Al + 3H_2 \rightarrow 3MH + 3Al + 9/2H_2 \tag{1.8}$$

$Mg(AlH_4)_2$ also has a high gravimetric storage capacity of 9.4 wt % H_2 and releases hydrogen at the lower temperature of 163 °C [41]. However, this decomposition is a one step reaction without the formation of an $(AlH_6)^{3-}$ complex anion as shown in equation 1.9.

$$Mg(AlH_4)_2 \rightarrow MgH_2 + 2Al + 3H_2 \tag{1.9}$$

Only the rehydrogenation of $NaAlH_4$ is thermodynamically favourable under moderate conditions of the considered aluminium hydrides, and further kinetic issues mean that full rehydrogenation of this system requires temperatures greater than 250 °C and pressures of 150 bar H_2 [39]. The kinetics of hydrogenation were greatly improved *via* Ti doping, this gave a decomposition temperature of 150 °C and full hydrogenation at 170 °C and 152 bar H_2 [44]. While the potential gravimetric hydrogen capacity of this system is 7.5 wt % H_2, cycling studies of the $NaAlH_4$ doped with titanium gave a reversible capacity of 3 - 4 wt % H_2 [45].

Amides

The complex amide anion (NH_2^-), along with the partially dehydrogenated imide anion (NH^{2-}), have high gravimetric hydrogen storage capacities when in compounds with light metals. $LiNH_2$ was synthesised as early as 1894 and it was later shown that $LiNH_2$ can readily be formed from reaction of the molten metal or the metal hydride with ammonia, or from a metal-ammonia solution [46, 47].

Other amides such as sodium and potassium can also be synthesised this way. The synthesis of $Mg(NH_2)_2$ was also reported by reaction of Mg_3N_2 or magnesium metal with ammonia, however, the reaction would take days to go to completion [47]. More recently the reaction of MgH_2 with ammonia has been used to form $Mg(NH_2)_2$ more readily [48].

Pure $LiNH_2$ decomposes to lithium imide, Li_2NH, and ammonia. However, the breakthrough in the use of the system for hydrogen storage came from beginning at the fully dehydrogenated product, lithium nitride, Li_3N. It was seen that Li_3N could absorb 9.3 wt % H_2 in a two step process shown in equation 1.10 [49]. This reaction was shown to be fully reversible with a theoretical gravimetric capacity of 10.4 wt % H_2.

$$Li_3N + H_2 \leftrightarrow Li_2NH + LiH + H_2 \leftrightarrow LiNH_2 + 2LiH \tag{1.10}$$

The first step of this reaction was not found to be readily reversible, requiring temperatures in excess of 400 °C for hydrogen release and having very slow hydrogen uptake. The second step of this reaction, however, is reversible under realistic conditions for hydrogen storage applications, with a good gravimetric storage capacity of 6.5 wt % H_2. Due to its obvious promise this reaction has been subject to extensive research, although the mechanism is still not completely understood. It was first thought that it was direct reaction of $LiNH_2$ with LiH to give Li_2NH with H_2 [49]. However, the mechanism was investigated further and it was concluded that it was in fact a two stage reaction where $LiNH_2$ first decomposed to Li_2NH and NH_3 (equation 1.11) before the NH_3 then reacts rapidly with LiH (equation 1.12) [50]. It was also concluded that the mechanism of hydrogen release involved the combination of protic (δ^+) hydrogen bonded to nitrogen atoms and hydridic (δ^-) hydrogen bonded to the lithium [51]. Lithium ion mobility has also been highlighted as a key factor in both stages of equation 1.10. There is a structural relationship between $LiNH_2$ and Li_2NH which main-

tains a face centred cubic nitrogen lattice, with a topotactic de/rehydrogenation equating to the diffusion of Li^+ and H^+ into and out of the bulk. This is thought to occur *via* a solid solution of the form $Li_{(1+x)}NH_{(2-x)}$ [52].

$$2LiNH_2 \rightarrow Li_2NH + NH_3 \tag{1.11}$$

$$NH_3 + LiH \rightarrow LiNH_2 + H_2 \tag{1.12}$$

As is the case with $LiNH_2$, $Mg(NH_2)_2$ decomposes to magnesium imide, MgNH, with the release of ammonia, however, the rate of the reaction is extremely slow. The decomposition of $Mg(NH_2)_2$ with MgH_2 was investigated and it was initially found that only the desorption from $Mg(NH_2)_2$ was seen [48]; however, it was later found that hydrogen desorption was seen after energetic ball milling of the mixture [53]. Despite occurring at a lower temperature than the $LiNH_2$ reaction, it took 72 hours to complete the hydrogen desorption, showing that the kinetics of this system are too slow for practical use.

To try and tune the thermodynamics and kinetics of amide system, mixed lithium and magnesium combination systems have received much research interest [54, 55]. As LiH is known to react extremely quickly with NH_3 [50], a system of $Mg(NH_2)_2$-2LiH was investigated and it was found to form a mixed lithium-magnesium imide as show in equation 1.13. This system was found to reversibly store around 5.5 wt % H_2 at 200 °C and 35 bar [56]. A system of $2LiNH_2$-MgH_2 has also been investigated, however the products from the decomposition, rehydrogenated back to $Mg(NH_2)_2$-2LiH as this is the thermodynamically favourable product [54].

$$Mg(NH_2)_2 + 2LiH \leftrightarrow Li_2Mg(NH)_2 + 2H_2 \tag{1.13}$$

Further research has been carried out into the optimisation of these amide systems for hydrogen storage applications including the use of ball milling to reduce particle size [57] and the use of catalysts which have been shown to increase the rate of hydrogen release, however, it should be noted that the particle size of the catalyst is also important [58].

Borohydrides

Borohydrides have been known for many years, having first been synthesised as early as 1940 *via* the reaction of ethyllithium and diborane [59], and later synthesised from the relevant metal hydride [60]. Borohydrides are strong reducing agents and are widely used in organic chemistry, however, in recent years there has been much research into their potential use for hydrogen storage applications.

Lithium borohydride, $LiBH_4$, is one of the most promising materials for hydrogen storage applications with a gravimetric hydrogen capacity of 18.5 wt % and a volumetric density of 121 kg H_2 m^{-3}. The decomposition gives only LiH as a crystalline product, through the reaction shown in equation 1.14. This hydrogen release from the decomposition does not begin until over 280 °C, with the main release of hydrogen occurring at over 380 °C, although this temperature can be significantly lowered by the addition of SiO_2 [61]. This process does not release all of the hydrogen and therefore has a gravimetric storage capacity of 13.9 wt % H_2.

$$2LiBH_4 \rightarrow 2LiH + 2B + 3H_2 \tag{1.14}$$

The exact mechanism of the decomposition of $LiBH_4$ is still not fully understood, however, it is known that equation 1.14 is not the complete story. The decomposition is thought to go *via* an intermediate, with computational studies giving the phase $Li_2B_{12}H_{12}$ as the most likely [62]. The presence of this intermediate phase was later confirmed by Raman and NMR spectroscopy [63, 64].

The desorption from $LiBH_4$ is a reversible process, however, rehydrogenation requires harsh conditions of 600 °C and 350 bar. Even under these conditions the absorption is not completed after 12 hours [65].

As these conditions are considered too severe for mobile applications, several techniques have been tried to improve the reversibility of $LiBH_4$. These include the destabilisation of $LiBH_4$ by the addition of another material, the use of catalysts or by nano-structuring.

A much researched form of destabilisation is the use of a $2LiBH_4$-MgH_2 system which gives a different decomposition pathway (equation 1.15) to that of pure $LiBH_4$. This system still has high gravimetric storage capacity of 11.6 wt % H_2 and has been shown to have improved thermodynamics, releasing hydrogen from above 250 °C and absorbing greater than 10 wt % H_2 at 400 °C and 24 bar [66].

$$2LiBH_4 + MgH_2 \rightarrow 2LiH + MgB_2 + 4H_2 \tag{1.15}$$

The addition of catalysts has a significant affect on reducing the dehydriding temperature of $LiBH_4$, as previously mentioned with the use of SiO_2 [61]. The lowest hydrogen desorption temperature was achieved with a mixture of $LiBH_4$-$0.2MgCl_2$-$0.1TiCl_3$, where hydrogen release began at 60 °C. This mixture desorbed 5 wt % H_2 at 400 °C and absorbed 4.5 wt % H_2 at 600 °C and 70 bar [67].

One method of nanoengineering which has been researched is the incorporation of $LiBH_4$ into an activated carbon (AC) scaffold. This $LiBH_4$/AC composite material had a hydrogen desorption temperature over 150 °C lower than that of bulk $LiBH_4$ (around 220 °C); the dehydrogenation conditions were also significantly lowered and the rate increased by over an order of magnitude [68].

Two other metal borohydrides which have received interest as hydrogen storage materials are that of sodium and magnesium borohydride. $NaBH_4$ releases around 10 wt % H_2; this desorption begins at temperatures around of 150 °C

but significant release is not seen until closer to 550 °C. The difference to the decomposition of $LiBH_4$ is that NaH decomposes at a much lower temperature than LiH and therefore the decomposition of $NaBH_4$ goes through to sodium metal [69]. $Mg(BH_4)_2$ has an extremely high gravimetric storage capacity, decomposing at temperatures greater than 300 °C to form MgB_2, while releasing 14.8 wt % H_2. Rehydrogenation of over 11 wt % H_2 has been seen, although high pressures (>600 bar) are required [70]. Recent work has reported a porous form of $Mg(BH_4)_2$. This nanostructuring has been shown to improve the kinetics of both hydrogen desorption and uptake [71].

1.4.5 Mixed Complex Hydride Anions

In an attempt to tune the thermodynamics of complex hydride systems while maintaining a high gravimetric capacity, research has been done into light-metal mixed-anion complex hydrides, combining two different complex hyrdide anion groups.

Reaction of $LiNH_2$ and $LiBH_4$ gave rise to new crystalline compounds at molar ratios of both 1:1 and 3:1. These materials are considered as $Li_2BH_4NH_2$ and $Li_4BH_4(NH_2)_3$ as structural work confirmed that the NH_2^- and BH_4^- groups remain within the new structures [72, 73]. These new compounds formed at a 1:1 and 3:1 ratio have high hydrogen storage capacities of 13.5 and 11 wt % H_2, respectively, and release this hydrogen at temperatures of around 250 °C. It is thought that combining the protic hydrogen from the amide group and the hydridic hydrogens from the borohydride group in one compound may be beneficial to the hydrogen desorption process. However, the decomposition product from these materials is Li_3BN_2 which has so far only shown limited reversibility [74]. An analogous sodium amide-borohydride can also be synthesised of the form $Na_2BH_4NH_2$. This system releases around 7.8 wt % H_2 from roughly 290 °C, accompanied by a small amount of ammonia [75]. More recent work has focussed on a mixed aluminium hydride-borohydride material using both $LiBH_4$-$NaAlH_4$

and $LiBH_4$-$LiAlH_4$-$CaCl_2$ [76]. While not forming new, distinct, mixed phases, the work suggested altered thermodynamics to the pure systems.

1.4.6 Halides in Hydrogen Storage

Halide containing materials have been used with metal hydrides and complex hydrides for hydrogen storage applications for many years. For the most part, these have been used as catalysts to tune the kinetics and thermodynamics of the de/rehydriding process. Examples of this have been discussed in the previous sections where $TiCl_3$ was used to dope $NaAlH_4$, giving a significant reduction in the conditions required for hydrogen release and uptake [44]. Similarly a mixture of $MgCl_2$ and $TiCl_3$ was used to improve the de/rehydriding conditions of $LiBH_4$ [67].

Further extensive research has been carried out into using transition metal halides to catalyse similar reactions, $TiCl_3$, $TiCl_4$, $AlCl_3$ and VCl_3 have all been used with $LiAlH_4$ and have been shown change the decomposition pathway and reduce the decomposition temperature by over 50 °C [77]. The effect of various transition metal halides, namely $TiCl_3$, VCl_3, $ScCl_3$ and $NiCl_2$, have been tested on the de/rehydriding kinetics of the Li-Mg-N-H complex hydride system. It was found that a significant decrease in the hydrogen desorption temperature was achieved, however, after cycling, no significant kinetic effect remained from the catalytic doping [78]. The effects of halide based additives were also investigated in the decomposition of MgH_2. It was found that transition metal halides such as ZrF_4, VCl_3 and $TiCl_3$ had a significant effect on reducing the decomposition temperature of MgH_2 [79].

While this work has focussed on the use of transition metal halides as catalysts, more recent research has looked into the incorporation of halides anions into the structures of complex hydrides. Research has been carried out into iodide substitution in $LiBH_4$. It was found that no new distinct phase was formed but a solid solution of the form $Li(BH_4)_{1-x}I_x$ was seen [80]. While much of this

research focussed on the high lithium ion conduction of this material as compared to pure $LiBH_4$, particularly at low temperatures [81], it has also been seen that this material rehydrides much more readily than pure $LiBH_4$ [80]. Similar research has been carried out into fluoride and chloride doping of $Ca(BH_4)_2$. While it was found that this doping could change the decomposition pathway from that of pure $Ca(BH_4)_2$, it was calculated that the thermodynamics of the system would only have a limited change (<10 °C on the decomposition temperature) [82]. There has also been limited research done on halide doped lithium amide. A bromide-doped amide of the form, Li_2NH_2Br was synthesised in 1994 and more recently an imide doped material of the form $Li_3(NH_2)_2I$ [83, 84]. Again these materials were predominantly researched as fast lithium ion conductors and not for hydrogen storage properties.

1.5 Thermodynamics of Hydrogen Storage

The thermodynamic properties of a hydride material can be used to predict and/or explain the hydrogen storage properties of the material; the relationship between the two properties has been discussed in great detail [85].

If you consider the decomposition of a metal hydride as shown in equation 1.16, this can be related to the thermodynamic parameters shown in equation 1.17. In this equation ΔH°_{dec} is equal to the negative of the standard enthalpy of formation of the hydride, ΔH°_f.

$$MH_n \rightarrow M + n/2\ H_{2(g)} \tag{1.16}$$

$$\Delta G^\circ_{dec} = \Delta H^\circ_{dec} - T\Delta S^\circ_{dec} \tag{1.17}$$

In the majority of cases the entropy term in equation 1.17 will be dominated by the change from an ordered solid in the metal hydride to disordered gaseous

hydrogen. Therefore it can be said that $\Delta S^{\circ}_{dec} \approx S(H^{\circ}_2) = 130.7$ J mol^{-1} K^{-1}. For a stable hydride thermodynamically to decompose, ΔG°_{dec} must fall below zero. This occurs when at the decomposition temperature, T_{dec}, is reached and the entropy factor overcomes the enthalpy contribution. At this point where ΔG°_{dec} falls below zero and thermal decompostion can proceed, it can be said that:

$$0 = \Delta H^{\circ}_{dec} - (n/2)T_{dec}S(H_2)^{\circ} \tag{1.18}$$

and from this the thermal decomposition temperature can be calcluated from equation 1.19.

$$T_{dec} = (\Delta H^{\circ}_{dec}/n)(2/S(H_2)^{\circ}) \tag{1.19}$$

In this equation the term, $(\Delta H^{\circ}_{dec}/n)$ is equal to the negative of the enthalpy of formation of the hydride per atom of hydrogen atom stored. From equation 1.19 it can be shown that to reach an equilibrium pressure of 1 bar at 300 K, the standard enthalpy of formation of the hydride for each hydrogen atom stored should be +19.6 kJ mol$_H{}^{-1}$. Therefore the ideal decomposition reaction from a metal hydride should be endothermic, so that the rehydriding reaction may be thermodynamically favourable.

This method is a relatively easy and extremely useful tool for predicting the reversible hydrogen storage properties of metal hydrides, however, materials which do not match the criteria from this method should not be ruled out immediately. It is generally considered that when used with a fuel cell, the supply of hydrogen will be required to be at a pressure greater than 1 bar; equally, for rehydrogenation to proceed at high enough rates, pressures of considerably higher than 1 bar will be required. It is therefore likely that some reactions which are irreversible at 1 bar and 300 K will be reversible at increased pressures. A different consideration altogether is the kinetics of a reaction, this is not easily predicted and will have a major effect on the reversibility of a material.

1.6 Hydrogen Storage Targets

With the main problems of hydrogen storage for use as a fuel being related to the gravimetric and volumetric capacities of the storage system, the most demanding challenge is to use in mobile applications, where both the size and weight of the storage system are critical. The U. S. Department of Energy has set out criteria for the practical use of hydrogen storage in mobile applications [86]. As further knowledge of the working of hydrogen vehicles was gained, these targets were considered to be extremely optimistic and have since been revised. A selection of the current targets are shown in table 1.1; along with the criteria set out here the system must be of a low enough cost to be commercially viable as well as meeting all safety regulations.

Storage Parameter	Current	2017	Ultimate
Gravimetric capacity	4.5 wt %	5.5 wt %	7.5 wt %
Volumetric capacity	0.028 kg H_2 L^{-1}	0.040 kg H_2 L^{-1}	0.070 kg H_2 L^{-1}
Delivery temperature	−40 / 85 °C	−40 / 85 °C	−40 / 85 °C
Delivery pressure	5 bar	5 bar	3 bar
Cycle life	1000	1500	1500
System fill time (5 kg)	4.2 mins	3.3 mins	2.5 mins

Table 1.1: Selected targets for onboard hydrogen storage systems for light-duty vehicles [86].

It should also be taken into account that these criteria are for the whole system, not just, in the case of solid state storage, the storage material itself. This has to therefore include the storage vessel itself, as well as any other components such as heat exchangers or pressure regulators that may be required for use of the hydrogen storage system with a fuel cell or ICE. The general term for this is the 'balance of plant' and it needs to be taken into consideration that the hydrogen storage material itself will need significantly higher capacities (particularly the gravimetric capacity) than the figures quoted in table 1.1 to compensate for this.

These criteria put serious constraints on the hydrogen storage technology that can be used and as of yet no single system has met all of these criteria.

Serious reduction from the quoted hydrogen storage capacities of certain systems can be incurred when the a full hydrogen storage system is considered with these criteria. For example, storage through physisorption in framework materials such as zeolites or MOFs can give high gravimetric storage capacities as previously discussed. However, to meet these criteria the hydrogen must be delivered at pressures of 3 - 5 bar for use with a fuel cell (35 bar for ICE). This severely limits the amount of hydrogen that can be desorbed from these systems. Similarly, complex hydrides may offer high gravimetric hydrogen capacities, however, only a small proportion of this hydrogen may be released at the desired operating temperatures ($<100\,^{\circ}\mathrm{C}$) and considerably higher temperatures may be required to release all of the hydrogen.

These are just a couple of examples in which it is demonstrated that the meeting of the criteria will be extremely challenging. Further research is required to find a system to store hydrogen reversibly at temperatures between -40 and $85\,^{\circ}\mathrm{C}$ at moderate pressures, with a high volumetric and gravimetric capacity, whilst also being safe and low cost.

1.7 Aims

Complex hydrides are identified as the most likely hydrogen storage materials to fulfil the criteria for a high gravimetric storage capacity combined with favourable de/rehydrogenation conditions. Two of the most promising complex hydride hydrogen storage systems to date are that of $LiNH_2$-LiH system and the mixed amide-borohydride, $Li_4BH_2(NH_2)_3$.

The aims of this project were to investigate new mixed anion complex hydrides *via* halide doping of $LiNH_2$ in the hope of improving the thermodynamics and kinetics of the system. Also to investigate fully the amide-borohydride system, in particular looking at the decomposition product, Li_3BN_2, and investigate other areas of the system, namely the interaction of $LiBH_4$ with the partially and fully dehydrogenated products, Li_2NH and Li_3N.

Chapter 2

Experimental

2.1 Solid State Synthesis under Inert Gas

All manipulations in this work were performed under inert conditions due to the materials being used having a high reactivity towards moisture and oxygen. The samples were weighed out on an analytical balance (up to an accuracy of 0.1 mg) in an argon filled glove box (MBraun, UniLab, <1ppm O_2, <0.1ppm H_2O) and ground together by hand using a pestle and mortar.

After being prepared in the glove box, samples were transferred into a quartz reaction tube (0.5" O/D), sealed with a Young's tap T-piece with an Ultra-torr® fitting before being removed from the glove box. The quartz reaction tube was then clamped in place so that the sample was in the centre of the hot zone of the vertical tube furnace (Lenton Furnaces, LTF 12/25/250 fitted with a Eurotherm 3216P1 controller). Argon gas was then connected to the T-piece so that it flowed over the reaction, first purging the gas line of air before opening the Young's tap. In general, a ramp rate of $2\,^{\circ}\mathrm{C\ min^{-1}}$ was used so that the furnace would accurately control the temperature, with the reaction being held at temperature for 12 hours before being allowed to cool at around $1 - 2\,^{\circ}\mathrm{C\ min^{-1}}$.

2.2 Hydrogenation

Hydrogen absorption reactions were performed under pressures of up to 100 bar H_2; these were carried out in a stainless steel reactor connected to a gas manifold (figure 2.1). Reactions were performed at temperatures up to 400 °C for times between 1 and 60 hours.

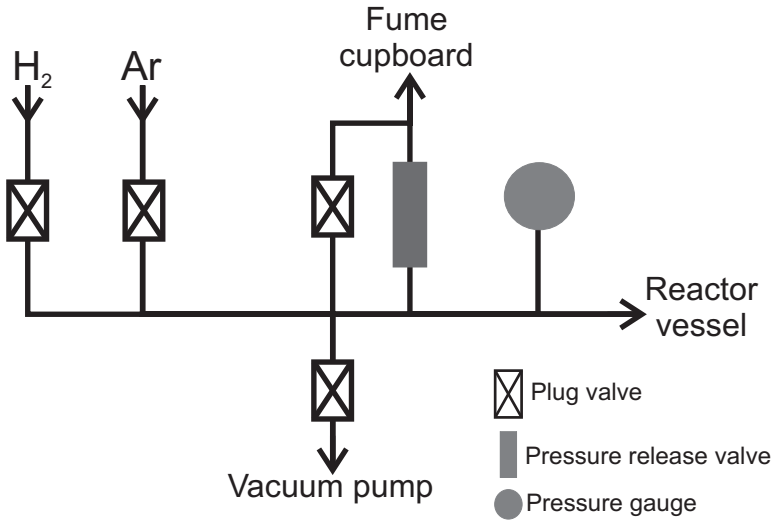

Figure 2.1: Schematic diagram of the gas manifold.

Initial sample manipulations were carried out in an argon filled glove box due to the air sensitive nature of these materials. Samples were loaded into quartz tubes and then placed into the stainless steel reactor. The reactor was then sealed using a torque wrench set to 90 Nm^2, before being removed from the glove box. The reactor was connected to an argon filled manifold system, the whole system was then evacuated and purged with a low pressure of hydrogen. The manifold system is fitted with a pressure gauge and pressure release valve.

The pressure of hydrogen was then set to a pressure below 100 bar to allow for the increase in pressure with temperature ($\approx$ 80 bar). A furnace was then fitted around the reactor vessel and the temperature set. At all stages of this process hydrogen detectors were used to check for leaks in the system. Once the furnace program has been completed the hydrogen gas was allowed to vent before

the system was evacuated and purged with argon. The reactor vessel was then disconnected from the manifold before being opened with an argon filled glove box.

2.3 Crystallography [87, 88, 89]

When in the solid state [87], all crystalline materials adopt a regular arrangement of atoms in three dimensions. The unit cell of a structure is defined as the simplest portion of the structure which, through translational symmetry, can give the full structure. The lattice parameters of a unit cell are the three lengths of the unit cell and the angles between them, the lengths denoted a, b and c, and the angles α, β and γ. Different combinations and relationships between these lengths and angles give rise to seven different crystal systems with varying levels of symmetry; these are shown in table 2.1.

In these materials, an array of equivalent points (or atoms) in three dimensions is defined as a lattice. The environment of an atom placed at one of these points would be identical to that of an atom on any other equivalent point. Lattices do not give information on the atomic positions within space, but show the translational symmetry of a structure *via* the locations of equivalent positions. In three dimensions there are four potential lattice types in crystals. The simplest of these is a primitive cell (P), which contains only a single lattice point at the corners of the cell. The addition of a lattice point at the centre of the unit cell gives a body centred cell (I), while the addition of further lattice points in the centre of all the cell walls gives a face centred cell (F). It is also possible to have lattice points at the centre of just one unit cell wall; by convention these are denoted as C lattices where the lattice point is located at the centre of the ab plane. The combination of these four lattice types with the seven crystal types gives fourteen possible combinations, these are known as Bravais lattices and are shown in table 2.1.

As discussed, crystal structures are described by their lattice parameters, but they are also described by atomic positions within the unit cell as well as the internal symmetry of the cell. Atomic positions are described as fractional coordinates along each unit cell direction from one corner. Atoms within a unit cell result in further symmetry elements being required to describe the Bravais lattice. The combination of all the symmetry elements gives rise to 230 possible space groups which then completely describe the symmetry within a unit cell.

Crystal system	Unit cell dimensions	Essential symmetry	Allowed lattices
Cubic	$a = b = c$ $\alpha = \beta = \gamma = 90°$	Four threefold axes	P, I, F
Tetragonal	$a = b \neq c$ $\alpha = \beta = \gamma = 90°$	One fourfold axis	P, I
Orthorhombic	$a \neq b \neq c$ $\alpha = \beta = \gamma = 90°$	Three twofold axes	P, I, F, C
Hexagonal	$a = b \neq c$ $\alpha = \beta = 90° \ \gamma = 120°$	One sixfold axis	P
Rhombohedral	$a = b = c$ $\alpha = \beta = \gamma \neq 90°$	One threefold axis	R (P)
Monoclinic	$a \neq b \neq c$ $\alpha = \gamma = 90° \ \beta \neq 90°$	One twofold axis	P, C
Triclinic	$a \neq b \neq c$ $\alpha \neq \beta \neq \gamma \neq 90°$	none	P

Table 2.1: The 7 possible crystal systems and 14 Bravais lattices

Lattice points which form a repeatable array in three dimensions can be connected together to form lattice planes. These planes are part of a repeatable, equally spaced set and each lattice point lies on one of these lattice planes. The planes are defined by Miller indices, which are determined by the points at which the lattice planes intersect the unit cell. For each set of lattice planes three Miller indices are required and these are denoted as h, k and l and are given by the reciprocal of the fractional intercepts along the unit cell edges of the first plane from the origin. The distance between equivalent planes is known as the d-spacing (d_{hkl}) and can also be considered as the distance from the origin to the first plane, perpendicular to the plane itself. A relationship between d-spacing

and lattice parameters is dependent on the system, for cubic systems it can be calculated using equation 2.1.

$$d = \frac{a}{\sqrt{h^2 + k^2 + l^2}} \tag{2.1}$$

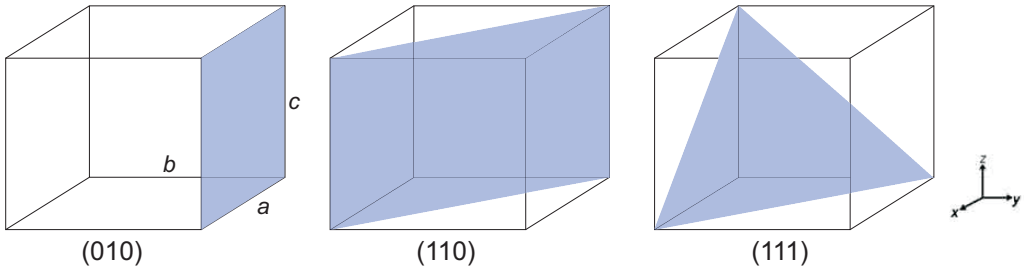

Figure 2.2: Examples of lattice planes and the corresponding Miller indices

2.4 Diffraction

2.4.1 X-ray Diffraction [88, 90]

X-rays are electromagnetic radiation with a wavelength of the order of the distances between atoms in a solid and as such are suitable for use with crystalline materials. X-rays interact with the electrons in crystalline materials and the d-spacing between the atoms gives a diffraction pattern unique to a particular material.

Not all scattering will give rise to peaks in an X-ray diffraction pattern. Only peaks which obey Bragg's Law give a significant amount of diffracted intensity and if we consider the diffraction of X-rays with atoms on a set of lattice planes, shown in figure 2.3, we may see why this is the case. If scattering of two X-ray photons occurs from atoms on two lattice planes at points A and D then the second wave travels a further distance than the first. Using the geometry shown in figure 2.3 the difference in path length can be shown as related to both the d-spacing and the angle of the X-ray beam.

$$\text{difference in path length} = \text{BD} + \text{DC} = 2.\text{d}_{hkl}.\sin\theta \tag{2.2}$$

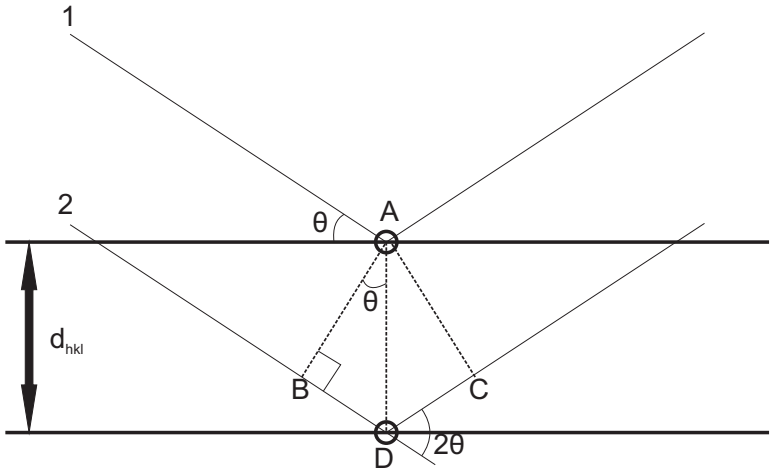

Figure 2.3: Geometry used for derivation of Bragg's Law.

Where the path difference is equal to an integer of the X-ray wavelength ($n\lambda$) constructive interference is seen and therefore it can be written that:

$$\text{n}\lambda = 2.\text{d}.\sin\theta \text{ where n} = 0, 1, 2... \tag{2.3}$$

This therefore shows that where Bragg's law is satisfied, constructive interference between waves occurs and a strong peak intensity is seen. Where Bragg's law is not met (at angles other than the Bragg angle) destructive interference occurs and no peak intensity is seen in the diffraction pattern. It should be noted that in reality X-ray scattering occurs through thousands of consecutive planes in the crystal system and that the X-ray scattering occurs from the electron cloud and not from the nucleus of the atom.

X-ray generation

X-ray radiation is produced when high energy electrons strike a metal plate, this causes an electron to be ejected from a core orbital of the metal. This hole is then

filled *via* electron decay, with the emission of radiation. X-rays are also produced by the slowing down of electrons as they enter the metal target, producing a more broad spectrum of wavelengths (figure 2.4). In standard laboratory diffractometers this metal is usually copper, here electron decay occurs *via* both 2p $\rightarrow$ 1s and 3p $\rightarrow$ 1s transitions (denoted K_α and K_β, respectively). Both of these lines are in fact doublets (figure 2.4) giving two separate wavelengths for each line; for the K_α line these are 1.5406 Å and 1.5444 Å respectively for $K_{\alpha 1}$ and $K_{\alpha 2}$. Synchrotron X-rays are high energy waves, produced in a synchrotron particle accelerator. Here charged particles are accelerated to relativistic speeds and controlled in a circular orbit by magnetic fields. When these charged particles change speed, synchrotron radiation is released over a wide range of wavelengths.

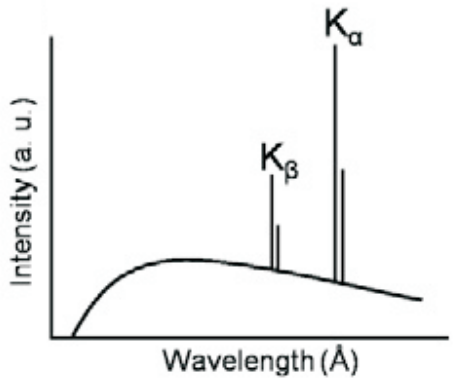

Figure 2.4: The X-ray spectrum from a copper target

Monochromation

As already discussed X-rays are produced with a wide range of wavelengths, however, for X-ray diffraction experiments, a single, intense wavelength is required, this is achieved through monochromation. In most laboratory based diffractometers a crystal monochromator is used. This is a single crystal orientated to a particular angle so that Bragg's law (equation 2.3) is satisfied. Through use of this set orientation, only one wavelength is diffracted from the crystal; for a cop-

per source the $K_{\alpha 1}$ wavelength is used as this is the most intense. Synchrotron X-ray sources generally use insertion devices to produce polarised radiation of high intensity. These devices include wigglers and undulators.

2.4.2 Powder Diffraction

In a powder sample (as opposed to a single crystal) there are many small crystallites, which are randomly orientated, covering essentially all possible orientations. As such, the lattice planes within the structure of the crystallite will also be randomly orientated and X-rays will therefore be diffracted in all directions. This means that each set of equivalent lattice planes give a cone of diffraction rather than a single point, this cone is made up of many dots, where each dot corresponds to diffraction from a single crystallite in the sample. The X-ray diffractometer detects the amount of X-rays at a given angle, 2θ, where the amount of X-rays reaching the detector is directly proportional to the signal intensity.

As all crystalline materials have a characteristic diffraction pattern then powder diffraction pattern can be used to identify which crystalline phases are present within the powder sample as well as giving structural information on these phases. The majority of information from a powder diffraction pattern is found in the peak position, peak shape and peak intensity.

The positions of the Bragg peaks in an X-ray diffraction pattern are determined by the unit cell size, shape and symmetry, as well as the wavelength of radiation used in the experiment. Through the Bragg law (equation 2.3) the peak positions correspond to the distances between lattice planes in the unit cell. Other factors such as an error in the height of the sample could cause a change in the observed peak positions.

The peak shapes are predominantly affected by the particle size and the crystallinity of the sample. There will also be instrumental factors which have some effect on the peak shape. The Bragg law (equation 2.3) is only truly satisfied for an infinite sized crystallite. For a finite crystal size the intensity of any Bragg

peak will be spread over an area; the peak width can therefore be used to calculate the crystallite size.

While the overall intensity of the diffraction pattern is determined by experimental and instrumental factors, the relative peak intensities between phases is affected by the amount of each phase present in the sample. The relative peak intensities within a phase give information on the type of atoms present in the unit cell as well as their positions. They are therefore essential for the solving of crystal structures. As it is electrons with which X-rays interact then it can be said simply that heavy atoms scatter X-rays more strongly than light atoms. However, to calculate the intensity of a given Bragg peak, many factors need to be taken into account. These factors include the number of equivalent (hkl) planes, an absorption correction to take into account X-rays which are absorbed by the sample rather than scattered, and the Lorentz factor, which is a correction for the amount of time lattice planes are in the correct position to satisfy Bragg's law. The greatest influence on the intensity of a Bragg peak is from the structure factor, which in itself has many contributing factors which are shown in equation 2.4.

$$F_{hkl} = \sum_{n} f_n N_n \exp[2\pi i(hx_n + ky_n + lz_n)] \exp[-B_n sin^2\theta/\lambda^2] \qquad (2.4)$$

Within the structure factor there are terms for the atomic scattering power (f_n) for the n^{th} atom within the a unit cell with the coordinates (x_n, y_n, z_n). It also includes the site occupancy (N_n). The final term ($\exp[-B_n[\sin^2\theta/\lambda^2]$) is the thermal factor; diffraction experiments take a snap shot of the atomic positions but in reality the atoms move about these positions, causing a drop off in scattering power. This term takes into account this drop off in scattering power.

2.4.3 Neutron Diffraction [91, 92]

Neutrons can also be used to probe the structures of crystalline materials. They are predominantly scattered by atomic nuclei rather than the electron clouds as is the case with X-rays. For this reason the neutron scattering factor of an atom is in many cases very different to that of X-rays, meaning that neutron diffraction is much more sensitive to certain light elements such as hydrogen.

Neutrons can be generated in two ways for use in diffraction experiments; either in a nuclear reactor or by the process of spallation. Spallation is when pulses of high energy protons are fired onto a heavy metal target causing it to release neutrons with a broad range of wavelengths. Neutrons scatter more weakly than X-rays, however they also penetrate further into samples than X-rays and therefore larger samples are required along with longer collection times.

In this work samples were prepared inside an argon filled glove box and sealed inside a vanadium can with an iridium wire. The samples were then run at the ISIS neutron source at the Rutherford Appleton Laboratory, Oxfordshire. At ISIS monochromation is not used; instead all wavelengths are used and the time to reach the target (time of flight) is measured. As such the wavelength is the variable, not the angle.

2.5 Rietveld Analysis [93, 94]

Rietveld analysis works on the principle that an accurate structural model of a crystal system can be built, so that a simulated diffraction pattern can then be produced which can be fitted to experimental data. This simulated diffraction pattern is made from the structural model, which describes the crystal structure with parameters such as the unit cell parameters, the atomic positions, their occupancies and thermal motions. This is then combined with parameters describing the experiment to give a diffraction pattern. The Rietveld analyis process is one of refinement, where the parameters within the model are adjusted and a

least-squares method is used to give the best fit to the entire observed diffraction pattern. This means that a good starting model is essential for the process. This least-squares refinement is the process of minimising the residual (S_y) *via* equation 2.5, which includes a weighting factor (w_i) based upon the estimated error in intensity and the observed and calculated intensities for i^{th} step ($y_i(obs)$ and $y_i(calc)$).

$$S_y = \sum w_i[y_i(obs) - y_i(calc)]^2 \tag{2.5}$$

It is important to inspect visually how the calculated diffraction pattern is matching the observed data. A difference line is displayed which, for a good fit, will be close to a straight line. While the visual fit of the calculated pattern is important, another aspect of the Rietveld refinement is that various statistics are produced during the process; these are known as 'R-values'. These numerical values show how good the fit is and gives an indication of how the fit is affected as parameters are changed within the model. The statistical value of 'R-weighted pattern' (R_{wp}) gives a measure of the complete calculated pattern to the complete observed pattern. The method for calculating R_{wp} is shown in equation 2.6 and it can be seen that it contains the residual from equation 2.5. As such it is the best measure for how the refinement is fitting. As this statistical value is based on how well the entire pattern is fitting it is important to note that artifically high values of R_{wp} will be obtained if not all of the observed peaks are fitted by the calculated pattern. As it is easier to get a good fit to a slowly varying background than it is to a set of Bragg peaks, R_{wp} can also give artificially low values if there is a high, well fitted background in the pattern. For this reason, background corrected versions of R_{wp} and other statistical measures are possible.

$$R_{wp} = 100\sqrt{\frac{\sum w_i[y_i(obs) - y_i(calc)]^2}{\sum w_i[y_i(obs)]^2}} \tag{2.6}$$

The statisically best possible fit that could be gained for a given data set is called 'R-expected' (R_{exp}). It should therefore be expected that the R_{wp} value should approach this R_{exp} value as the refinement progesses. The value of R_{wp} is determined largely by the quality of the data and is calculated from equation 2.7 where N is the number of observables, P is the number of refined parameters and C is the number of contraints used.

$$R_{exp} = 100\sqrt{\frac{N-P-C}{\sum w_i[y_i(obs)]^2}} \tag{2.7}$$

These two R-values allow us to define a further statistical measure χ^2 shown in equation 2.8. This is a useful value as it contains the number of refinable parameters used within the refinement. However, it should be noted that high data quality can produce artificially high values for χ^2, while a low data quality can mask errors in the model and produce artificially low χ^2 values.

$$\chi^2 = [R_{wp}/R_{exp}]^2 \tag{2.8}$$

2.6 Mass Spectrometry [95, 96]

Mass spectrometry is an analytical technique in which the mass to charge (m/z) ratio of charged gaseous particles is measured along with the abundances of each ratio. The mass spectrometer can either scan a range of m/z ratios and measure the relative abundances of each, or it may be set to measure a selected m/z ratio to determine the amount of this species released by the sample. Simply put, a mass spectrometer uses electromagnetic fields to control the flow of charged ions, however, the process can be split into three main areas: ionisation, separation and detection.

The ionisation process is the removal or addition of an electron or proton to make charged, ionic species. There are many forms of ionisation techniques

used in mass spectrometry, however, the technique used in this study, and also the most common technique, is that of electron impact (EI). EI uses an electron beam generated from a tungsten filament. This beam of electrons is accelerated and knocks an electron from the neutral sample material. The acceleration/energy of the electron beam is tuned so that a majority of singly charged ions are formed, with a limited amount of multiple ionisation. The formation of singly charged ions is preferable as it is the m/z ratio of the ions which is detected. Excess energy from the ionisation process can be sufficient to cause the ionic species to break up into smaller ionic fragments; this process is known as fragmentation. The smaller fragment will also be detected at a lower m/z ratio. This is a process which cannot be ignored and an understanding of the fragmentation of a molecule can be crucial for accurate determination of the analyte. This is particularly true for large organic molecules.

Following ionisation the ions are accelerated through a voltage before being focussed into the analyser where the next process of separation occurs. The ions are separated based upon their m/z ratio. Originally mass spectrometers used analysers which were curved, tunable, electromagnets. The mass spectrometer would then vary the strength of the magnetic field to scan through the whole range of m/z ratios, with lighter ions being deflected round the curve in a lower magnetic field than heavier ions. Therefore as the magnetic field is varied a certain m/z ratio will reach the detector while lighter and heavier ions will be neutralised *via* collisions. Currently the most common form of analyser used a quadrupole mass spectrum analyser. Here, rather than bending the ions round a curve, an electric field from parallel electrodes oscillating at radio frequencies is used to stabilise the path of ions of a certain m/z ratio which then reaches the detector, with other m/z ratios being neutralised through collisions. As the frequency is varied, the whole range of m/z ratios is measured.

Finally the ions that reach the detector generate an ion current for the value of the m/z ratio; this signal is then amplified before being output as a mass

spectrum. Where the majority of the ions in the sample will produce a large ion current a Faraday cup detector is used. This is a conductive cup where, as a charged particle hits the surface, an electron is emitted. The amount of electrons is directly proportional to the number of ions hitting the detector. Where smaller samples are used, or a greater sensitivity is needed, a secondary electron multiplier detector may be used. Here the electrons that are produced from the collision are amplified by a series of electrodes, each at an increased potential. This produces a cascade of electrons for each electrode, the amplication from this can result in an increase in sensitivity of the order of x 10^6.

2.7 Temperature Programmed Desorption

Temperature programmed desorption (TPD) is the term given to the controlled heating of a sample whilst the desorption products are monitored. The sample is heated at a controlled rate under a flowing atmosphere, and the gaseous desorption products are detected through mass spectrometry. In this work a homebuilt TPD apparatus was used.

In this study TPD experiments were performed under a flowing argon atmosphere, with the gases being monitored by mass spectrometry (TPD-MS). A schematic of this apparatus is shown in figure 2.5. The sample of mass $\approx$ 0.1 g was weighed out inside an argon filled glove box and placed into a quartz reaction tube (7 mm O/D, 4 mm I/D) before being sealed within the reaction chamber. The sealed reaction chamber was then transferred to the TPD apparatus, avoiding exposure to the atmosphere. A barrel heater was placed around the reaction chamber to heat the sample; this heating was controlled with a thermocouple which is in contact with the sample. This positioning of the thermocouple meant that endothermic and exothermic events from the sample were visible within the temperature trace. The flow of the argon is regulated using a mass flow controller (Hastings 200 series, Teledyne) at a constant flow of 100 ml min^{-1}. The gaseous

desorption products from the sample are measured with a quadrupole mass spectrometer (HPR-20, Hiden Analytical) with a secondary electron multiplier.

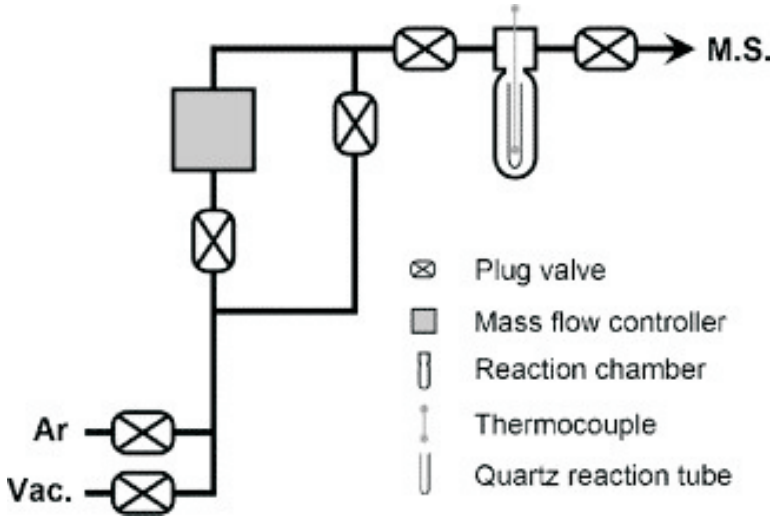

Figure 2.5: Schematic diagram of the TPD-MS apparatus [75].

Calibration

In this work, hydrogen and ammonia are the main desorption products of interest. To determine the true sensitivity of the mass spectrometer towards these gases a calibration gas was used (BOC Speciality Gases, 4736 ppm H_2, 4898 ppm NH_3, balance Ar). With respect to the determination of NH_3 with the mass spectrometer, there are problems as the main mass fragment, NH_3^+, has the same m/z ratio as the OH^+ fragment of water, which is generally present to some extent in vacuum systems. For this reason the NH_2^+ fragment was used to determine the true amount of NH_3 present. This fragment has approximately 80 % of the intensity of the NH_3^+ fragment.

The calibration gas was flowed through the TPD apparatus in the same way that the argon gas is used during experiments. The mass spectrometer was set to record the partial pressures (P_n) for m/z values of 2 (H_2^+), 16 (NH_2^+), 17 (NH_3^+/OH^+), 18 (H_2O^+), 28 (N_2^+), 32 (O_2^+) and 40 (Ar^+); these signals were

recorded until they appeared settled and consistent. The equivalent spectrum was collected for the argon carrier gas so that any background signal for $H_2{}^+$ and $NH_2{}^+$ could be accounted for. The total signal in the mass spectrum is dependent on the total amount of gas entering the mass spectrometer, therefore the partial pressures of $H_2{}^+$ and $NH_2{}^+$ (P_2 and P_{16}) were converted into a fraction of the argon signal (P_{40}):

$$x_2 = \frac{P_2}{P_{40}} \qquad x_{16} = \frac{P_{16}}{P_{40}} \tag{2.9}$$

The fractional signals of H_2 and NH_2 from the pure argon carrier gas (x_2^o and x_{16}^o) were then deducted from the from the equivalent fractional signals for the calibration gas (x_2 and x_{16}). These background subtracted signals were then divided by the true molar fraction of $H_2{}^+$ and $NH_2{}^+$ in the calibration gas, given by the calibration gas certificate. These values are 4.736 x 10^{-3} and 4.898 x 10^{-3}, respectively, and give relative sensitivity values for each species (equation 2.10). These relative sensitivity values were then used to correct the observed $H_2{}^+$ and $NH_2{}^+$ signals obtained from TPD-MS experiments to give true values for H_2 and NH_3.

$$R_{H_2} = \frac{x_2 - x_2^o}{4.736\text{x}10^{-3}} \qquad R_{NH_3} = \frac{x_{16} - x_{16}^o}{4.898\text{x}10^{-3}} \tag{2.10}$$

During a TPD-MS experiment, the same mass channels were collected during the data collection as for the calibration. Prior to the experiment start proper (where sample heating was begun), MS data was collected for a period of time until the signal appeared consistent. This allows for determination of background signals for m/z values of 2 and 16 (x_2^o and x_{16}^o). The MS data was converted again to a fraction of the argon signal as in equation 2.9. For the mass signals of m/z values of 2 and 16, the background signal which was determined before heating began was subtracted from the signals from the experiment proper. The corrected fractional values were then divided by the previously determined relative

sensitivity values (equation 2.10) to give corrected molar fractions of H_2 and NH_3 as shown in equation 2.11.

$$x^*_{H_2} = \frac{x_2 - x^o_2}{R_{H_2}} \qquad x^*_{NH_3} = \frac{x_{16} - x^o_{16}}{R_{NH_3}} \tag{2.11}$$

2.8 Vibrational Spectroscopy [97, 98]

Atoms in solid materials vibrate at frequencies of 10^{12} to 10^{13} Hz and vibrational modes can be excited into higher energy states by the absorption of radiation of the appropriate frequency. Infrared (IR) and Raman spectra are experimental techniques which plot the intensity of absorption or scattering as a function of frequency or wavenumber.

2.8.1 Infrared

The energy of IR radiation is of the order required for the vibration of chemical bonds. When the incoming photon has an energy which corresponds to the gap in energy between the vibrational ground state of a molecule and an excited state, the photon may be absorbed to excite the molecule. The IR spectrum is a result of these transitions between vibrational energy states. In an IR experiment the frequency of the incident radiation is varied and then the amount of radiation absorbed or transmitted by the sample is measured. Transitions from the vibrational ground state to the first excited state generally have energies corresponding to the middle of the IR region (400 cm^{-1} to 4000 cm^{-1}).

Not all vibrational modes are IR active; the vibration must result in a change in the dipole moment of the molecule. Therefore centrosymmetric vibrational modes, which cause no change in the dipole moment, are IR inactive while asymmetric stretches, which tend to result in larger changes in the dipole moment, are IR active resulting in more intense absorption bands in the IR spectra.

The amount of IR radiation absorbed at each wavelength is given by equation 2.12. The sample intensity (I) at each wavelength is measured and then compared to the intensity of a blank reading with no sample present (I_0). The absorbance (A) is then plotted as a function of the wavelength.

$$A_\lambda = -\log_{10}(I/I_0) \tag{2.12}$$

2.8.2 Raman

In Raman spectroscopy the sample is illuminated with monochromatic light, most commonly generated by a laser. The single wavelength of radiation, which is anywhere from infrared to ultraviolet, is scattered from the molecules and it is that which is shifted by one vibrational unit of energy that is detected. It is the difference in energy between this scattered radiation and the incident radiation which is of interest.

As with IR spectroscopy, not all vibrational modes are Raman active. For it to be active the vibrational mode must cause a change in the direction or size of the polarisability of the molecule. Also as with IR, the symmetry of the molecule determines which vibrations are Raman active. However, unlike IR, it is symmetrical stretches which, in general, give more intense bands in the Raman spectrum, whereas asymmetric vibrations give relatively weak bands. As such, IR and Raman spectroscopy can be used as complementary techniques to see more of the vibrational modes in a molecule.

In a Raman experiment, the incident light interacts with the molecule, polarising the electron cloud surrounding the nuclei in the molecule. This forms a short lived excited virtual state. This excited state is unstable and quickly relaxes with the release of a photon of different energy. The most common form of scattering is known as Rayleigh scattering (shown in figure 2.6); here only the electron cloud is involved in the scattering and therefore the energy difference between

the photons is small. This scattering can essentially be considered as elastic. It is, however, inelastic scattering which is considered to be 'Raman scattering'. In a small amount of scattering events nuclear motion may be induced within the molecule and here energy is transferred between the photon and the molecule. There are two types of Raman scattering, shown in figure 2.6. Stokes scattering occurs when the scattering event occurs from the vibration ground state ($\nu = 0$) and the molecule absorbs energy and forms a vibrational excited state ($\nu = 1$). The photon scattered from this event is therefore reduced in energy by the energy difference between the two vibrational states. Alternatively if the molecule is in an excited state ($\nu = 1$) and undergoes scattering, this vibrational energy can be transferred to the photon, increasing its energy by the difference in vibrational energies. This is known as anti-Stokes scattering. In this study Raman experiments were carried out at room temperature where most of the molecules will be in the vibrational ground state ($\nu = 0$), therefore Stokes scattering will be the most common type of Raman scattering.

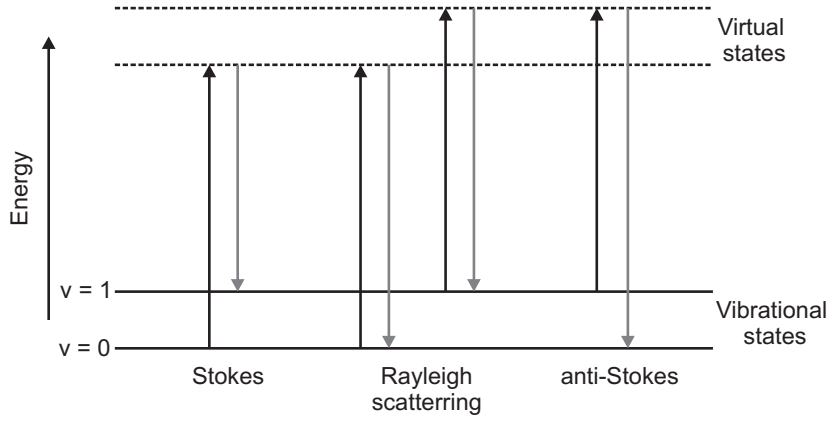

Figure 2.6: Diagram of the Raman and Rayleigh scattering processes.

In this work, Raman spectra were collected using a Renishaw InVia Raman microscope using an Ar ion laser with a wavelength of 488 nm. The samples were loaded into an Instec sample cell in an argon filled glove box. This sample cell was then transferred onto the Raman microscope and data was collected in

a sealed environment.

2.9 Intelligent Gravimetric Analysis

An Intelligent Gravimetric Analyser (IGA, Hiden Analytical) is a pressure controlled thermo-gravimetric balance with complete environmental control. The sample is loaded into a stainless steel holder which is then placed on a hang-down which is attached to a microbalance head. The mass of the sample can then be measured under different conditions. This allows sample weight changes to be followed through changing temperature and pressure. The microbalance head, its counterweight, as well as the sample itself are kept in the same environmental conditions, allowing for much more accurate masses to be obtained, reducing the affects of buoyancy. The sample temperature is controlled by an external furnace surrounding the reaction; this temperature is then monitored by a positive temperature coefficient sensor located next to the sample.

An important feature of the IGA is the ability to load samples in an inert way. This was done *via* the use of a portable glove box. First the mass of the empty stainless steel sample holder must be recorded, following this the sample was loaded in an argon filled glove box and sealed within the sample cartridge. The portable glove box was then attached around the reaction chamber which was lowered and the sample catridge inserted into the portable glove box. The portable glove box is unable to withstand high/low pressures and for this reason it was cycled around 200 times with argon between pressures of 1050 mbar and 1250 mbar. Folowing cycling the sample cartridge was opened and the sample transferred to the balance hang-down using a mechanical arm. The portable glove box can also be used after the experiment to unload samples inertly.

The IGA has two modes in which experiments may be run, pressure control mode, used in this work, and flowing gas mode in which decomposition gases may be monitored. In pressure control mode the desired pressure and ramp

rate are set, and the IGA then controls the pressure by continually admitting small amounts of gas through the inlet stepping motor until the desired pressure is reached. The pressure was then controlled through the IGA allowing small amounts of gas in to increase the pressure or by bleeding small amounts of gas to the vacuum pump to decrease the pressure. In this work hydrogen and argon were the only gas used with the IGA and pressure control mode was used to test the hydrogenation of samples through changes in the sample mass.

2.10 AC Impedance

AC impedance is a method of determining the conductivity of a sample. This is done by measuring the sample's ability to oppose a flow of current, or resistance. The powder samples were first made into pellets before electrodes were attached to either side of the pellet and an alternating voltage was applied. The current was measured from the sample and the plot from this data gives both the capacitance and resistance of the sample. From this data, along with the mass and size of the pellet, the conductivity of the sample can be calculated.

In this study AC impedance measurements were made using a Hewlett Packard 4192A LF impedance analyser. The samples were first sealed inside an argon filled glove box into an air tight 13 mm diameter die press before being removed from the glove box and being pressed into cylindrical pellets using an axial force of around 1 - 2 tonnes. The pellets were then put back into the glove box and were transferred to a homebuilt airtight cell. The faces of the pellets were coated with a gallium-indium alloy to which the electrical contacts were made. This cell was then taken to the impedance analyser and experiments were run between 298 K and 375 K.

2.11 Scanning Electron Microscopy [99, 100]

Scanning electron microscopy (SEM) is a technique used for studying the texture, morphology and the surface features of powder and solid samples. SEM has a very high depths of field and provides a 3D type quality to the images. In SEM an electron beam, from a cathode filament (usually tungsten) is shone across the samples surface after being focussed through lenses. Upon hitting the sample, the electrons slow down and lose energy. These backscattered electrons and electrons emitted from the atoms within the sample are detected and used to produce an image of the sample. From this image, SEM can be used to study the sample's structure on a μm scale as well as investigating the size and shape of particles within the sample. The experiment takes place under vacuum inside an evacuated chamber, the samples must be electrically conducting, therefore the samples are coated in a thin layer of gold so that charge will not accumulate at the surface.

Chapter 3

Synthesis and Crystal Structure Determination of Amide- and Imide-Halides

3.1 Introduction

Reaction 3.1 shows the Li-N-H system which has been shown to be promising for hydrogen storage applications [49]. While ammonia is thought to play a role in the mechanism, for both of the stages of this reaction it has been proposed that the mobility of the Li^+ ions is the key factor [52]. The de/rehydrogenation process can be seen to go *via* a solid solution of $Li_{(1+x)}NH_{(2-x)}$. The structural transformation between the closely related structures of $LiNH_2$ and Li_2NH (fig. 3.1) allows for a topotactic reaction which equates to the diffusion of Li^+ into and H^+ out of the FCC anion lattice.

$$LiNH_2 + 2LiH \leftrightharpoons Li_2NH + LiH + H_2\uparrow \leftrightharpoons Li_3N + 2H_2\uparrow \tag{3.1}$$

The fully hydrogenated product $LiNH_2$ has a relatively low room temperature ionic conductivity of below 10^{-8} S cm^{-1}, rising to 5 x 10^{-6} S cm^{-1} at 127 °C

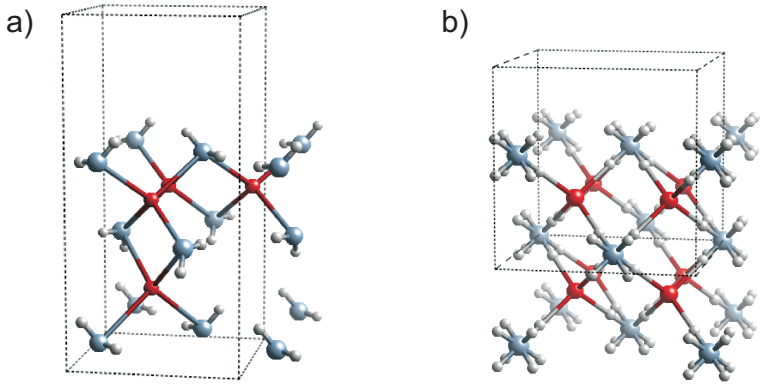

Figure 3.1: Schematic representation of portions of the crystal structures of a) $LiNH_2$[101] and Li_2NH[102]. Lithium is represented by red spheres, nitrogen by blue spheres and hydrogen by grey spheres. The unit cells are shown as dotted black lines.

[84]. The partially hydrogenated product Li_2NH has room temperature ionic conductivity of 3 x 10^{-4} S cm^{-1}, increasing to 2 x 10^{-2} S cm^{-1} at 100 °C [103]. It is therefore thought that the reduced ionic mobility in the hydrogen-rich compositions may slow hydrogen release from $LiNH_2$ as well as impeding full bulk rehydrogenation.

In this section I report the synthesis and crystal structure determination of a series of lithium amide-halides, with the aim of studying the effect of halides on the hydrogen release and uptake in lithium amide and lithium imide, respectively. Magnesium halides were also studied in addition to the lithium counterparts as magnesium has been shown to have a beneficial effect on the properties of the Li-N-H system [104, 105].

3.2 Experimental

Samples of ground mixtures of lithium amide (Sigma-Aldrich, 95% purity) and either LiX or MgX_2, where X = Cl, Br, I (Sigma-Aldrich, anhydrous, beads, -10mesh, 99.998%) were prepared in an argon filled glove box (<10 ppm O_2, <1 ppm H_2O). The samples were prepared in various stoichiometries and heated in

quartz tubes under flowing argon at temperatures up to 400 °C for up to 12 hours.

Powder X-ray diffraction data were collected using a Bruker D8 instrument in transmission geometry with a wavelength of 1.54059 Å (chapter 2.4.1) and powder synchrotron X-ray diffraction data were collected at Diamond Light Source on the I11 beamline with a wavelength of 0.825594 Å. Powder neutron diffraction data were collected at ISIS using the General Materials (GEM) instrument (chapter 2.4.3). Raman spectroscopy was also performed on the samples (chapter 2.8.2) and is discussed in this chapter. The hydrogen storage properties of these materials are discussed at a later point.

3.3 Amide-chlorides: $xLiNH_2$ + yLiCl or $(y/2)MgCl_2$

3.3.1 Synthesis

Lithium amide and lithium chloride were ground together at molar ratios between 1:1 and 6:1 and heated at temperatures between 200 and 400 °C. The reaction appeared to proceed extremely slowly below 300 °C but at 400 °C a new phase was seen to form.

This phase was seen to form as a single product from a reaction of $3LiNH_2$ + LiCl, heated at 2 °C min^{-1} to 400 °C for 1 hour. The new phase has been assigned the formula $Li_4(NH_2)_3Cl$ and has been indexed to a hexagonal unit cell, space group $R\bar{3}$, with lattice parameters $a = 9.6755(4)$ Å and $c = 8.8971(4)$ Å, and rhombohedral symmetry. A Pawley fit to the data based on this unit cell is shown (fig. 3.2).

After longer heating times of around 12 hours, a different pure phase was seen to be favoured from reaction at the same molar ratio of reactants at the same temperature. This phase was indexed to a body centred cubic cell, space group $I2_13$, with lattice parameter $a = 10.4303(4)$ Å (fig. 3.3).

In the case of reaction of lithium amide and magnesium chloride, molar ratios were chosen so as to maintain the NH_2^- to Cl^- ratios similar to the equivalent

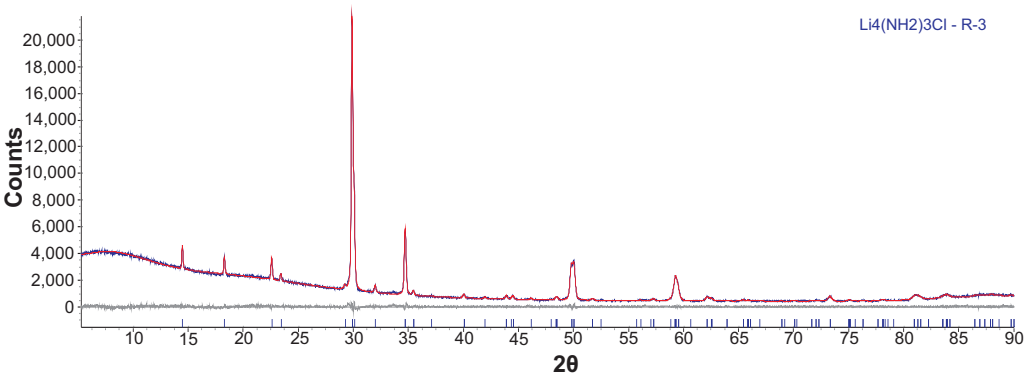

Figure 3.2: Powder X-ray diffraction pattern of hexagonal $Li_4(NH_2)_3Cl$ made by reaction of $3LiNH_2 + LiCl$ at 400 °C for one hour, showing observed (blue), calculated Pawley fit (red) and difference (grey) plots. Peak positions for $Li_4(NH_2)_3Cl$ are shown (blue).

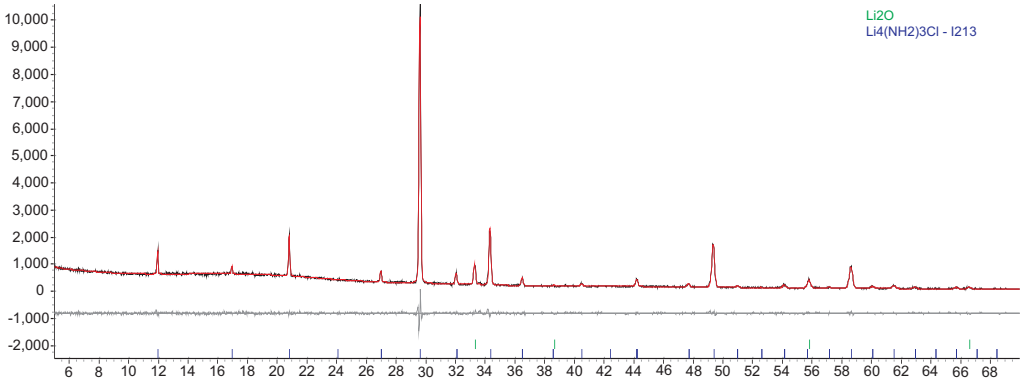

Figure 3.3: Powder X-ray diffraction pattern of cubic $Li_4(NH_2)_3Cl$ made by reaction of $3LiNH_2 + LiCl$ at 400 °C for twelve hours, showing observed (black), calculated Pawley fit (red) and difference (grey) plots. Peak positions for $Li_4(NH_2)_3Cl$ are shown (blue).

purely lithium reaction. The reaction of $3LiNH_2 + 1/2MgCl_2$ did not form a rhombohedral phase but did form a body centred cubic phase nearly identical to the lithium-only equivalent. This cubic phase had a lattice parameter of $a = 10.4561(8)$ Å, slightly larger than that of the lithium-only phase, and was formed at 350 °C (fig. 3.4). Investigations into the crystal structure of phases formed is discussed at a later point (chapters 3.3.3, 3.3.4 and 3.3.5).

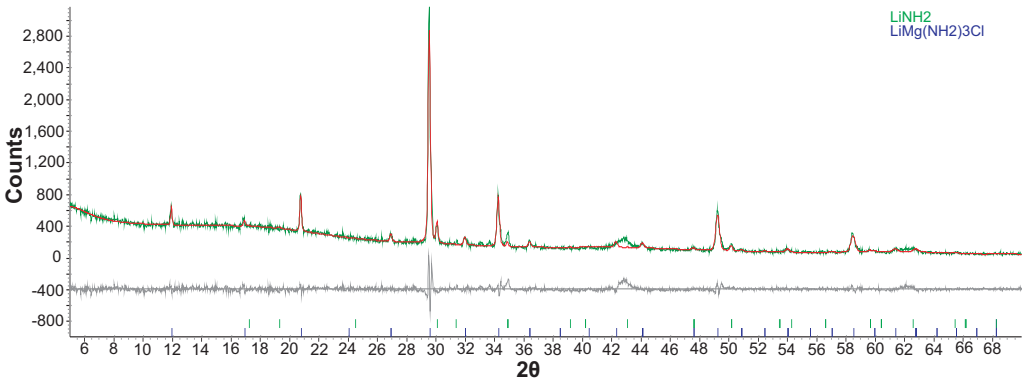

Figure 3.4: Powder X-ray diffraction pattern of cubic $Li_3Mg_{0.5}(NH_2)_3Cl$ made by reaction of $3LiNH_2$ + 1/2MgCl at 350 °C for twelve hour, showing observed (green), calculated Pawley fit (red) and difference (grey) plots. Peak positions for $Li_4(NH_2)_3Cl$ are shown (blue).

3.3.2 Raman Spectroscopy

400 °C is above the temperature at which $LiNH_2$ will begin slowly to decompose from the molten state with the release of ammonia according to equation 3.2,

$$2LiNH_2 \rightarrow Li_2NH + NH_3 \tag{3.2}$$

Hence Raman spectroscopy was performed in order to check that the new phases contained NH_2^- and were not imides or amide-imide mixtures. An ideal NH_2^- anion would be bent with the point group C_{2v} (as is the case for the water molecule). In the case of $LiNH_2$ the amide ion lies on a general position giving point symmetry of C_s, although this reduction in symmetry does not change the number of vibrational modes that can be observed.

The reducible representation (Γ_{red}) for this basis set can be reduced to an irreducible representation (Γ_{irr}), shown in table 3.1 and 3.2 respectively. The translational and rotational modes are then removed to give the normal vibrational modes (Γ_{3n-6}), where the Raman active modes are shown and assigned as fundamental modes.

For an ideal NH_2^- the fundamental modes of v_1 (A_1), v_2 (A_1) and v_3 (B_2)

Table 3.1: Point group table for C_{2v}.

	E	C_2 (z)	σ_v (xz)	σ_v (yz)	Linear, rotations	Quadratic
A_1	1	1	1	1	z	x^2, y^2, z^2
A_2	1	1	−1	−1	R_z	xy
B_1	1	−1	1	−1	x, R_y	xz
B_2	1	−1	−1	1	y, R_x	yz
Γ_{red}	9	−1	1	3		

Table 3.2: Deconvolution of Γ_{irr} for C_{2v} NH_2^-.

	Γ_{irr}	Γ_{trans}	Γ_{rot}	Γ_{vib}	Γ_{IR}	Γ_{Raman}	Fundamental mode
A_1	3	1	0	2	2	2	ν_1, ν_2
A_2	1	0	1	0	0	0	-
B_1	2	1	1	0	0	0	-
B_2	3	1	1	1	1	1	ν_3

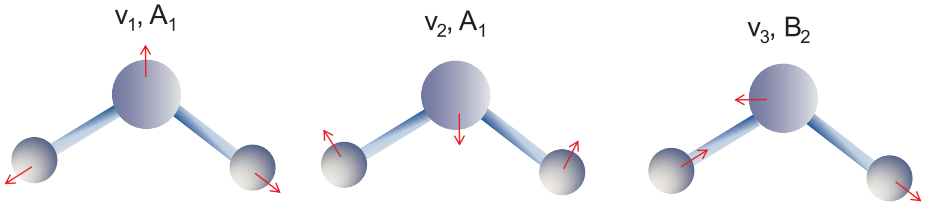

Figure 3.5: Vibrational modes of the NH_2^- anion.

correspond to the singly degenerate modes of the symmetric strectch, the bend and the asymmetric stretch, respectively (fig. 3.5).

The Raman spectra of the $LiNH_2$ starting material and the partially dehydrogenated product Li_2NH are are shown in figure 3.6. These spectra focus on the region where the predominant N-H peaks are found, although it is worth noting that small peaks at around 1500 cm^{-1} are also seen, corresponding to the v_2, bend vibration. The peak positions are highlighted with dotted lines so that they may be easily compared to those of the newly formed amide-halide phases. The observed peak positions match up well with those published in the literature (table 3.3), although all the bands were seen at a slightly higher wavenumber.

The spectra of the three new phases formed are shown in figure 3.7. The peak positions (as well as the sharpness of the peaks) confirm that the NH_2^- group remained intact and that the materials synthesised are amide-halides of the form

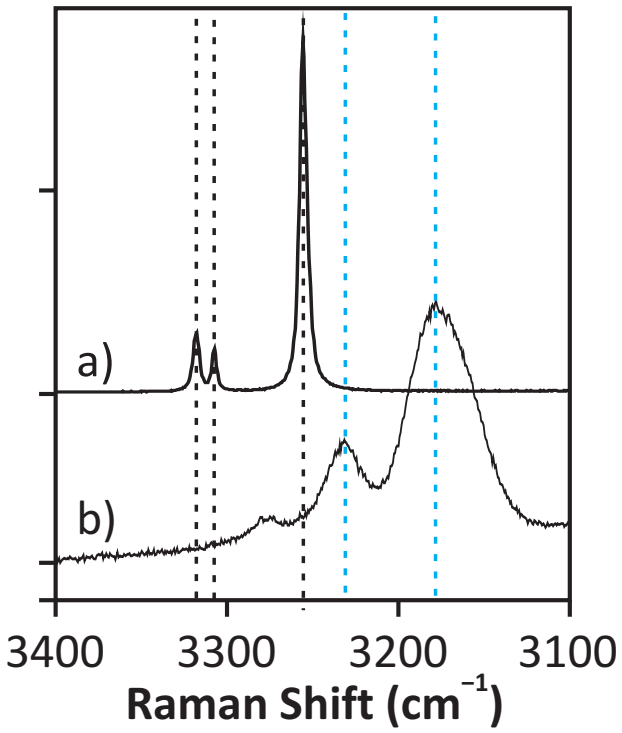

Figure 3.6: Raman spectra of (a) $LiNH_2$ and (b) Li_2NH. Peak positions highlighted by black ($LiNH_2$) and blue (Li_2NH) dotted lines.

Table 3.3: Literature (Lit.) and observed (Obs.) Raman stretching modes for $LiNH_2$ and Li_2NH.

$LiNH_2$			Li_2NH		
Lit. [106]	Obs.		Lit. [107]	Obs.	
v	v	Ass.	v	v	Ass.
3258	3262	v_1	3180	3179	v_1
3310	3314	v_3	3250	3235	v_3
3315	3324	-			

$Li_4(NH_2)_3Cl$ and $Li_3Mg_{0.5}(NH_2)_3Cl$.

The spectra for all the new materials show the N-H stretches occurring at a lower wavenumber than that of the starting material, while the spectrum of the hexagonal phase (fig. 3.7 a) shows two symmetric and asymmetric stretches.

This lowering in the wavenumber shows that the N-H bond is longer and therefore weaker in the new materials compared to $LiNH_2$. Since the release of hydrogen from these materials involves the breaking of the N-H bond, this might be expected to lower the temperature of hydrogen release; this will be discussed further in the following chapter (4.3.1). The appearance of more stretches in the hexagonal phase is indicative of two different NH_2^- environments; the crystal structure of this phase is discussed in the next section (3.3.3).

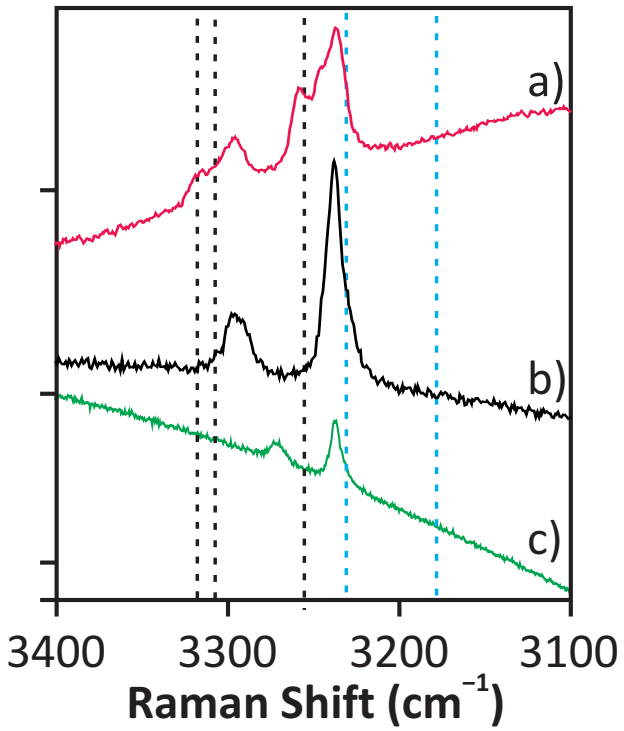

Figure 3.7: Raman spectra of (a) rhombohedral $Li_4(NH_2)_3Cl$, (b) cubic $Li_4(NH_2)_3Cl$ and (c) $Li_3Mg_{0.5}(NH_2)_3Cl$. Peak positions highlighted by black ($LiNH_2$) and blue (Li_2NH) dotted lines.

3.3.3 Crystal Structure Investigation - hexagonal $Li_4(NH_2)_3Cl$

The crystal structure of $Li_4(NH_2)_3Cl$ was investigated with powder synchrotron X-ray diffraction data (Diamond, I11) and powder neutron diffraction data (ISIS, GEM), using the computer program Topas [108].

The observed peak positions from the X-ray diffraction pattern of $Li_4(NH_2)_3Cl$ were run through the indexing routine of the computer program Topas [108]. This gave the most likely assignment of a rhombohedral unit cell with hexagonal symmetry, space group $R\bar{3}$ (number 148) with $a = 9.74$ Å and $c = 8.94$ Å. These lattice values were refined in Topas using a Pawley fit; this fit is shown in figure 3.8. The Pawley fit allowed for the more accurate lattice parameters of $a = 9.74487(8)$ Å and $c = 8.9365(3)$ Å to be obtained, giving a unit cell volume of 734.930(3) Å^3. To see how well our structure is fitting to the observed pattern at a later point it is worth noting the statistical values obtained from this Pawley fit for comparision. For the fit shown below (fig. 3.8) values of $R_{wp} = 6.287$, $R_{exp} = 3.112$ and $\chi^2 = 4.080$ were obtained. Due to the relatively low value of R_{exp} for this data (from two hour collection time), values of χ^2 tend to be high (the same fit to laboratory data gives $\chi^2 = 1.26$). I will therefore mostly use R_{wp} values to compare fits statistically throughout this work. At this point the Pawley fit was tested on the neutron diffraction data to make sure that an acceptable fit was achieved to this data as well (fig. 3.9).

The volume of the starting material $LiNH_2$ is 260.77 Å^3[101], with eight $LiNH_2$ formula units within each unit cell ($Z = 8$), giving each formula unit a volume of approximately 32.60 Å^3. In the case of the other starting material, LiCl, a similar but slightly larger formula unit volume of 32.77 Å^3 is found, from a smaller unit cell size of 131.09 Å^3 but with a value of $Z = 4$.

If we assume that formula unit volumes are approximately equal to those of the starting materials then one formula unit of the product (made from three $LiNH_2$ units and one LiCl unit) has a volume of approximately 130.57 Å^3. Given

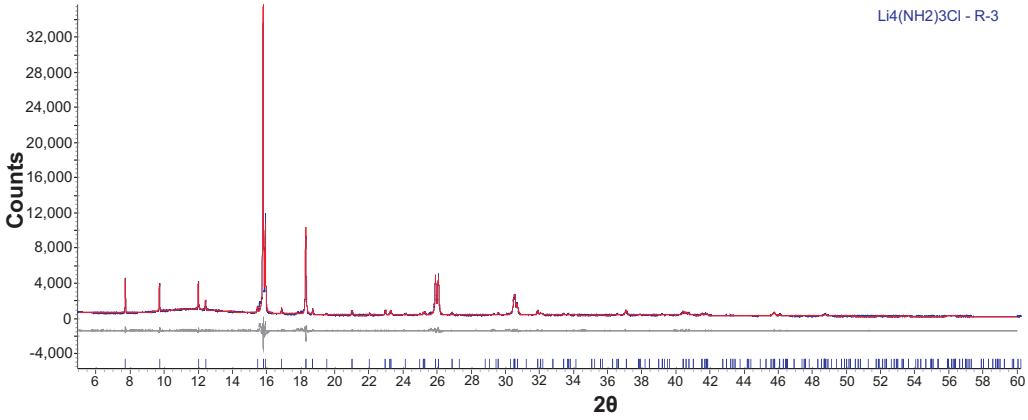

Figure 3.8: Powder synchrotron X-ray diffraction pattern showing a Pawley fit to the hexagonal $Li_4(NH_2)_3Cl$ phase, showing observed (blue), calculated Pawley fit (red) and difference (grey) plots. Peak positions for $Li_4(NH_2)_3Cl$ are shown (blue).

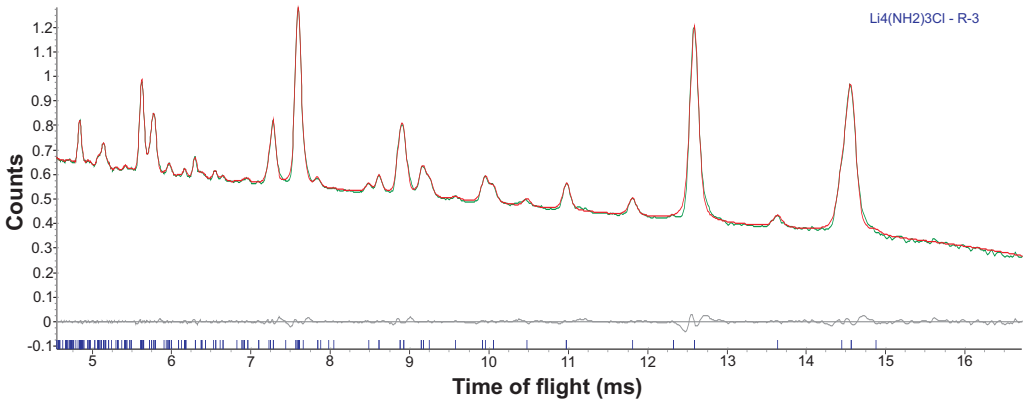

Figure 3.9: Powder neutron diffraction pattern (bank 4) showing a Pawley fit to the hexagonal $Li_4(NH_2)_3Cl$ phase, showing observed (green), calculated Pawley fit (red) and difference (grey) plots. Peak positions for $Li_4(NH_2)_3Cl$ are shown (blue).

the overall unit cell volume of 734.930 Å^3 obtained from the Pawley fit, this gives a value of $Z = 5.63$. By consideration of the allowed site multiplicities for the space group $R\bar{3}$ (table 3.4) of three, six or nine, it is likely that there are six $Li_4(NH_2)_3Cl$ formula units within the unit cell. This is further backed up by looking at the calculated crystallographic densities of the materials involved, for $LiNH_2$ and LiCl these are 1.17 and 2.15 g cm^{-3} respectively. Calculated values of $Li_4(NH_2)_3Cl$ with unit cell volume 734.930 Å^3 gives crystallographic densities of 0.75 g cm^{-3} for a value of $Z = 3$, 1.50 g cm $^{-3}$ for $Z = 6$ and 2.26 g cm $^{-3}$ for $Z = 9$. This again indicates a value of $Z = 6$ as the most likely as the density of the product is likely to fall between the density of the two starting materials.

Table 3.4: Special positions available for the space group $R\bar{3}$ (No. 148).

Multiplicity	Wyckoff letter	Site symmetry	Coordinates
18	f	1	(x,y,z)
9	e	-1	$(\frac{1}{2},0,\frac{1}{2})$
9	d	-1	$(\frac{1}{2},\frac{1}{2},\frac{1}{2})$
6	c	3	(0,0,z)
3	b	-3	$(0,0,\frac{1}{2})$
3	a	-3	(0,0,0)

To produce a model for this structure, a Rietveld refinement was performed against the X-ray diffraction data. To begin the heaviest X-ray scattering element was added to the model first, in this case, chlorine. Five possible special positions with multiplicity three, six and nine were considered, these are the 3a, 3b, 6c and 9d and 9e sites (table 3.4). Chlorine atoms were introduced to each of these sites in turn, refining the occupancy and, in the case of the 6c site $(0,0,x)$, the atomic position. It was seen that for the 3b, 9d and 9e sites the occupancy refined to zero; in the case of the 6c site $(0,0,x)$ the value for x refined towards zero and the occupancy refined to 0.5. This strongly suggests that the chlorine atom sits on the 3a (0,0,0) site, and when put on that site the occupancy did, as expected, refine to one; the occupancy was then fixed at one for further refinements.

This first chlorine site has a multiplicity of 3, therefore for a value of $Z =$

6, 3 further chlorine sites are required. Chlorine atoms were tested on each of the four remaining special positions available for this space group, with the occupancy both allowed to refine freely and fixed to give a total of three chlorine atoms on the site. On all of these sites the occupancies refined towards zero when allowed to and gave a poor fit when they were fixed. For this reason the chlorine atom was placed on the general 18f site (x,y,z) and allowed to refine. The chlorine atom quickly refined to a steady position, however it was seen that the occupancy of the site increased to above 1 ($\approx$ 1.1). Based on this, an 18f site was tested as a mixed site. Chlorine and the next heaviest scattering atom, nitrogen, were placed on the same site and the position allowed to refine. The occupancy was allowed to refine separately for each atom type, but constrained to give a total value of one on this site. This gave values of approximately 1/9 for chlorine and 8/9 for nitrogen. This gives a total of 5 chlorine atoms within the unit cell and 16 nitrogen atoms, close to the stoichiometric 1:3 ratio. At this point there was a good visual fit to the observed XRD pattern (fig. 3.10) and the statistics were reasonable with R_{wp} = 13.746. The crystal structure using only the refined chlorine and nitrogen positions is shown in figure 3.11. This structure shows a face centred cubic arrangement of the nitrogen atoms similar to that seen in $LiNH_2$ and Li_2NH (figure 3.1), as no phases were found at other stoichiometric ratios it is likely that the two chlorine atoms on the 18f site are ordered. However the positions could not be determined in this work.

The next stage of the model was to add in the lower scattering lithium atoms. To maintain the value of $Z \approx 5$ - 6 for the unit cell, this will require there to be between twenty-one and twenty-four lithium atoms in the unit cell, giving several possibilities for the sites that the lithium occupies. Firstly the lithium atoms were placed on two fully occupied sites, the 18f and 6c sites. This gave a reasonable fit, lowering R_{wp} to 12.021; when the occupancies were allowed to refine they remained close to one. Next the lithium atoms were placed on two 18f sites and the values for (x,y,z) allowed to refine as well as the occupancies. Both

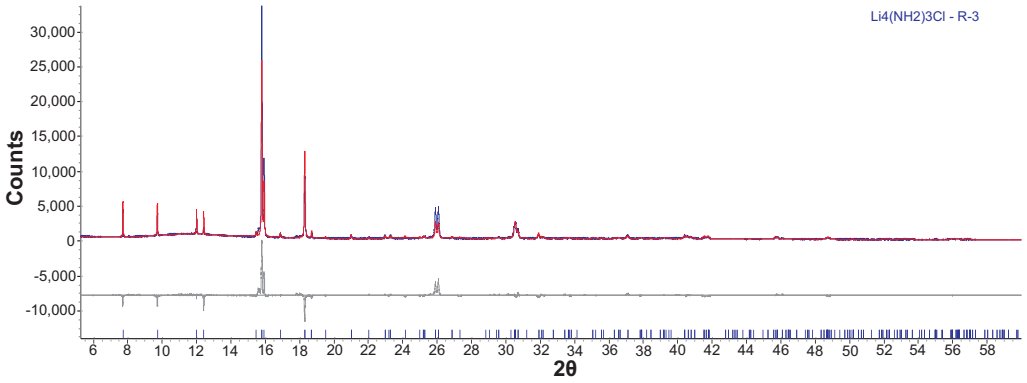

Figure 3.10: Powder synchrotron X-ray diffraction pattern showing a Rietveld refinement to the hexagonal $Li_4(NH_2)_3Cl$ phase with only Cl and N atoms, showing observed (blue), calculated Rietveld fit (blue) and difference (grey) plots. Peak positions for $Li_4(NH_2)_3Cl$ are shown (blue).

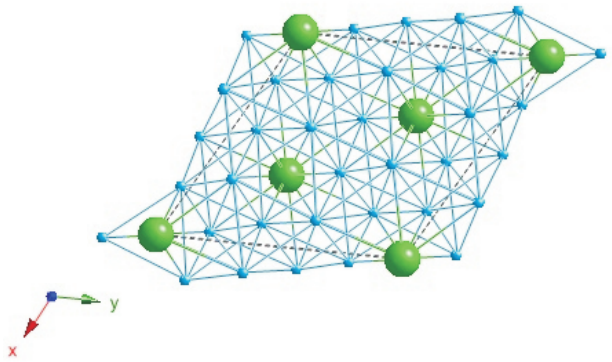

Figure 3.11: Crystal structure of hexagonal $Li_4(NH_2)_3Cl$ showing only the chlorine (green) and nitrogen (blue) atoms. The unit cell is shown as a black dotted line.

sites refined to stable atomic positions with occupancies of around 0.7; this was then fixed at 0.66 to give the correct number of lithium atoms in the unit cell. This gave a good fit both visually and statistically with $R_{wp} = 8.822$. Finally, three 18f sites were tried, in this case two of the sites refined to the same position with equal occupancies. From this is was taken that the lithium atoms sit on two 18f sites which are both two-thirds occupied.

The final atoms to be added to the structure were the hydrogen atoms. Due to the poor X-ray scattering of hydrogen atoms these were introduced as NH_2^- rigid bodies. These rigid bodies were placed on the refined nitrogen positions

and allowed to rotate freely. The N-H bond length was refined from a starting value of 1.0 Å while the H-N-H bond angle was initially fixed at 107°. Following this the nitrogen sites were allowed to refine along with the H-N-H bond angle. This refinement did not change the nitrogen positions, while giving an N-H bond length of 1.06 Å and an H-N-H bond angle of 109°. The neutron diffraction data was then used for a joint refinement; this used the model obtained from the X-ray data as a starting point, refining each atom in turn. Using the neutron data the hydrogen atoms were allowed to refine freely, outside of a rigid body.

Once a good structural model had been formed a full Rietveld refinement was performed in Topas by refining a zero point error, a pseudo-Voigt peak shape (6 parameters) and a Chebyshev background function (16 parameters). Atomic positions were refined as well as the thermal parameters (B_{iso}) for each site. The resultant crystal structure (fig. 3.12) and Rietveld plot to the X-ray (fig. 3.13) and neutron (fig. 3.14) data are shown below. The refined crystallographic data are shown in table 3.5.

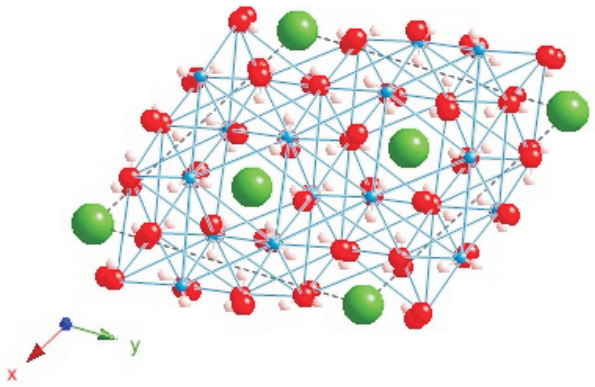

Figure 3.12: Crystal structure of hexagonal $Li_4(NH_2)_3Cl$ showing the chlorine (green), nitrogen (blue), lithium (red) and hydrogen (white) atoms. The unit cell is shown as a black dotted line.

To further understand the structure produced for this unit cell the geometries around different atoms were looked at more closely; these are shown in figure 3.15. It can be seen that lithiums on the Li1 site form a distorted tetrahedron with

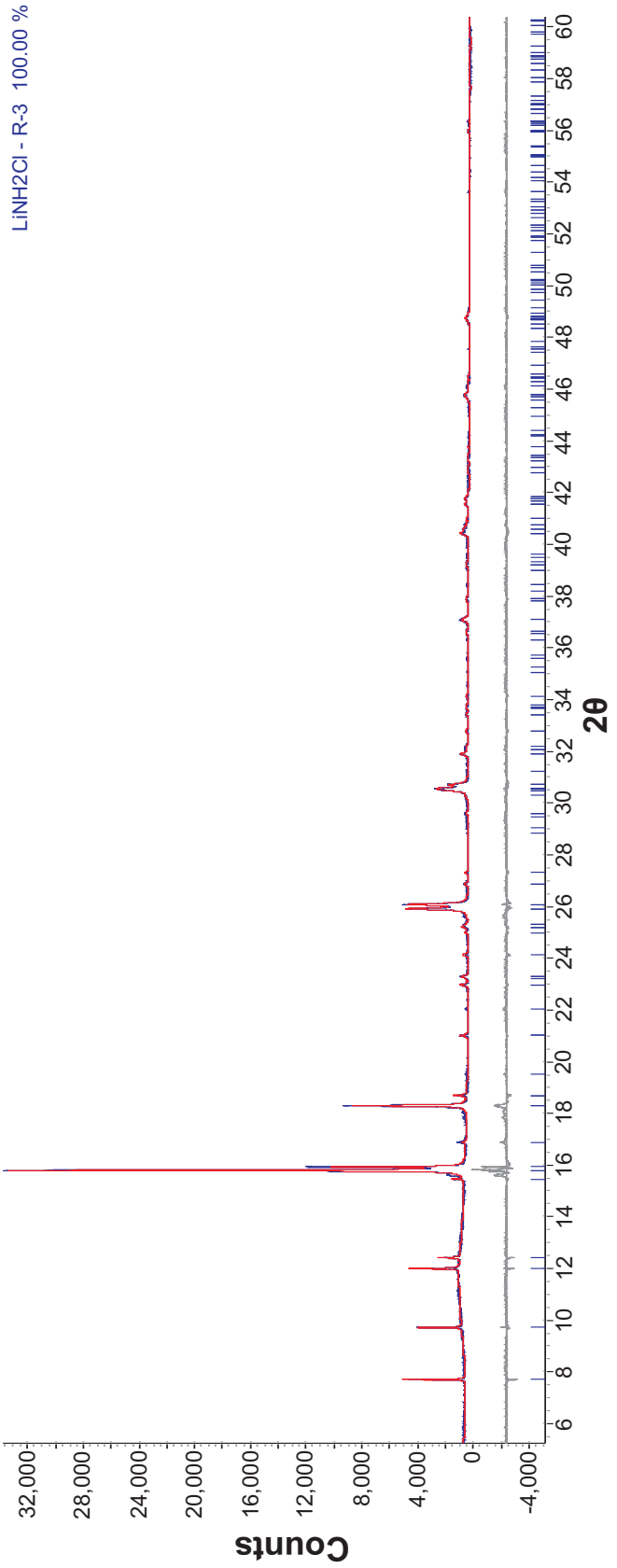

Figure 3.13: Powder synchrotron X-ray diffraction pattern showing the final Rietveld refinement for the hexagonal $Li_4(NH_2)_3Cl$ phase. Observed (blue), calculated Rietveld fit (red), difference (grey) plots, and peak positions for $Li_4(NH_2)_3Cl$ are shown (blue).

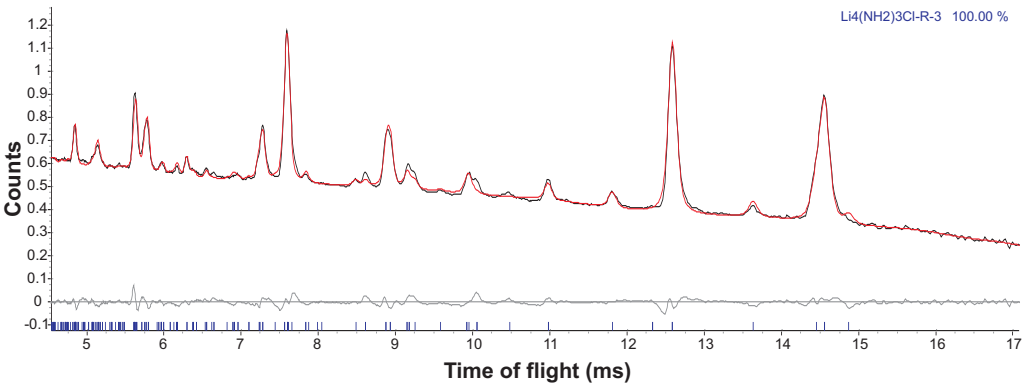

Figure 3.14: Powder neutron diffraction pattern showing the final Rietveld refinement to the hexagonal $Li_4(NH_2)_3Cl$ phase, showing observed (black), calculated Rietveld fit (red) and difference (grey) plots. Peak positions for $Li_4(NH_2)_3Cl$ are shown (blue).

Table 3.5: Refined crystallographic data for hexagonal $Li_4(NH_2)_3Cl$

Atom	Site	x	y	z	Occupancy	B_{iso}
Cl1	3a	0	0	0	1	2.79(9)
Cl2	18f	0.1962(5)	0.2345(8)	0.6524(5)	1/9	1.3(3)
N	18f	0.1962(5)	0.2345(8)	0.6524(5)	8/9	1.3(3)
H1	18f	0.217(6)	0.310(3)	0.678(4)	1	6.3(3)
H2	18f	0.136(3)	0.175(3)	0.696(3)	1	6.3(3)
Li1	18f	0.1907(6)	0.1948(4)	0.4095(4)	2/3	3.2(6)
Li2	18f	0.1427(4)	0.4423(8)	0.7792(4)	2/3	3.4(6)

Space group $R\bar{3}$ (no. 148), $a = 9.74487(8)$ Å, $c = 8.9365(3)$ Å
X-ray data: $R_{wp} = 8.368$, $R_{exp} = 3.152$, $\chi^2 = 7.049$
Neutron data: $R_{wp} = 1.718$, $R_{exp} = 0.654$, $\chi^2 = 6.896$

four nitrogen atoms (3.15a). The Li-N bond lengths are between 1.864(9) and 2.498(8) Å and the N-Li-N bond angles are between 94 and 123°. The distortion from a regular tetrahedron is likely due to the fact that some of the nitrogen atoms will be chlorine atoms as discussed previously. This compares to more ideal tetrahedron in $LiNH_2$ and Li_2NH, both with bond angles of 109 ° and Li-N bond lengths of 2.06 and 2.23 Å, respectively. The NH_2^- groups have a bond length of 0.7 Å with an H-N-H bond angle of 112°. The chlorine atoms on the Cl1 site sit octahedrally between six lithium atoms on Li2 sites (3.15b). The Li-Cl bond lengths are all equal at 2.276(9) Å, however the Li-Cl-Li bond angles vary

between 78 and 102°, it should be noted that both lithium sites in this structure are not fully occupied.

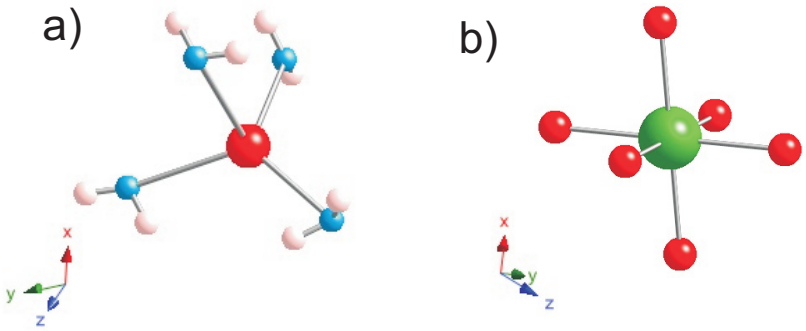

Figure 3.15: Diagram of the geometry around a) Li1 site and b) Cl1 site within hexagonal $Li_4(NH_2)_3Cl$ showing the chlorine (green), nitrogen (blue), lithium (red) and hydrogen (white) atoms.

By looking at these geometries within the structure as whole we can more clearly see how the atoms are arranged within the unit cell; figure 3.16 looks at the unit cell down the x direction. Figure 3.16a does not contain the Li2 site and the tetrahedrally coordinated Li1 site can be seen clearly between the planes of chlorine atoms. In figure 3.16b the Li1 site is not included and the octahedrally coordinated chlorine atoms can be seen within the cubic array of nitrogen atoms.

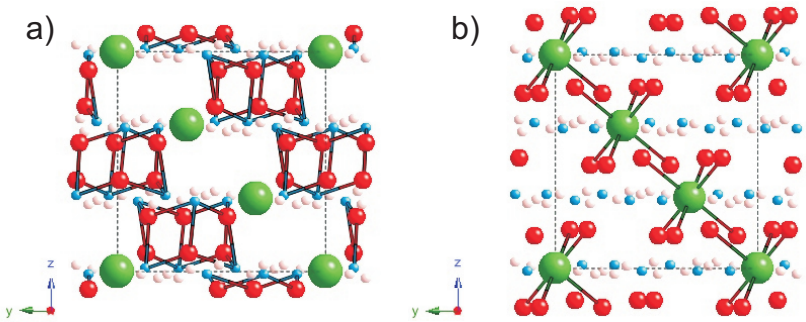

Figure 3.16: Crystal structure of hexagonal $Li_4(NH_2)_3Cl$ showing the chlorine (green), nitrogen (blue), lithium (red) and hydrogen (white) atoms. Only the a) Li1 sites and b) Li2 sites are present for the lithium atoms.

3.3.4 Crystal Structure Investigation - cubic $Li_4(NH_2)_3Cl$

The observed peak positions from the X-ray diffraction pattern for cubic $Li_4(NH_2)_3Cl$ were run through the indexing routine of the computer program Topas[108]. This gave the most likely assignment to a cubic unit cell, space group $I2_13$ (number 199) with $a = 10.44$ Å. A Pawley fit was run with these lattice parameters and this gave the more accurate lattice parameter of $a = 10.4452(3)$ Å, with a cell volume of 1139.5821(6) Å^3. This fit had $R_{wp} = 6.704$. A Pawley fit was also run on the neutron data, this is shown in figure 3.18.

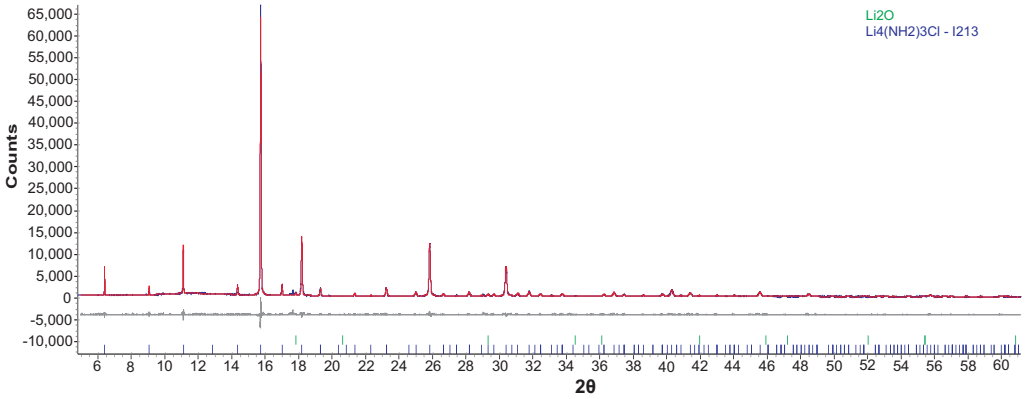

Figure 3.17: Powder synchrotron X-ray diffraction pattern showing a Pawley fit for the cubic $Li_4(NH_2)_3Cl$ phase. Observed (blue), calculated Pawley fit (red), difference (grey) plots, and peak positions for $Li_4(NH_2)_3Cl$ are shown (blue).

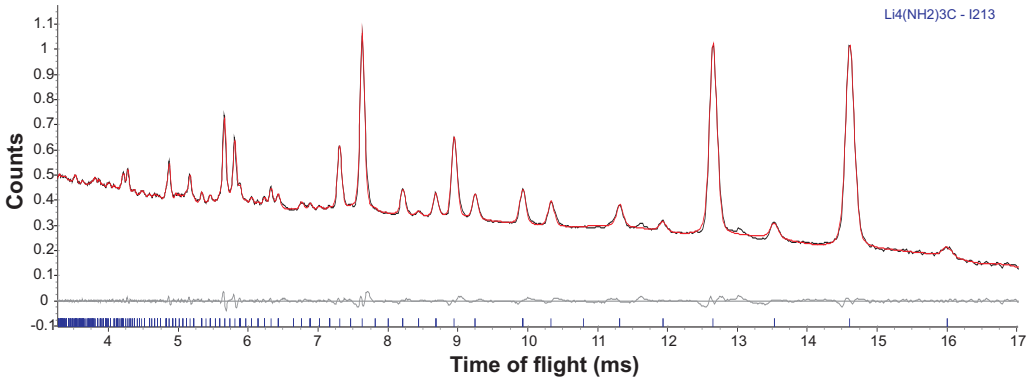

Figure 3.18: Powder neutron X-ray diffraction pattern showing a Pawley fit for the cubic $Li_4(NH_2)_3Cl$ phase. Observed (blue), calculated Pawley fit (red), difference (grey) plots, and peak positions for $Li_4(NH_2)_3Cl$ are shown (blue).

There is a striking similarity between the X-ray diffraction pattern of the body centred cubic form of $Li_4(NH_2)_3Cl$ and that of $Li_4BH_4(NH_2)_3$[73]; this similarity is shown in figure 3.19. As with the last section, one formula unit of $Li_4(NH_2)_3Cl$ has a volume of around 130.57 Å^3, with the total unit cell volume of 1139.59 Å^3 this gives a value of $Z = 8.72$ and a crystallographic density of 1.29 g cm^{-3}; a value of $Z = 8$ fits with the multiplicity of the available special positions in the $I2_13$ space group (table 3.6). The structure of $Li_4BH_4(NH_2)_3$ also has a value of $Z = 8$ with the slightly lower density of 0.99 g cm^{-3}. For this reason the published structure of $Li_4BH_4(NH_2)_3$ was used as a starting model for determining the structure of cubic $Li_4(NH_2)_3Cl$. To begin with a Rietveld refinement was run simply using the $Li_4BH_4(NH_2)_3$ structure, placing the chlorine atoms on the boron sites (and removing the corresponding hydrogen atoms). This gave a reasonable fit to the data (fig. 3.20) with a value of $R_{wp} = 24.527$.

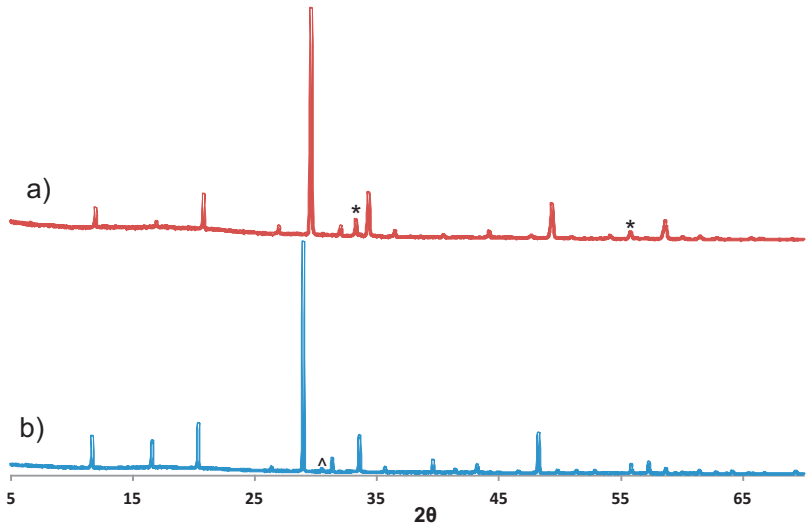

Figure 3.19: Powder X-ray diffraction patterns of a) $Li_4(NH_2)_3Cl$ and b) $Li_4BH_4(NH_2)_3$, peaks for Li_2O (*) and $LiNH_2$ (^) are highlighted.

The atomic positions were then allowed to refine in turn to improve the fit for this structure. Firstly the chlorine position was refined, this stayed on an 8a site with an occupancy of one, refining the position only slightly. The nitrogen

Table 3.6: Special positions available for the space group $I2_13$ (No. 199).

Multiplicity	Wyckoff letter	Site symmetry	Coordinates
24	c	1	(x,y,z)
12	b	2	(x,0,$\frac{1}{4}$)
8	a	3	(x,x,x)

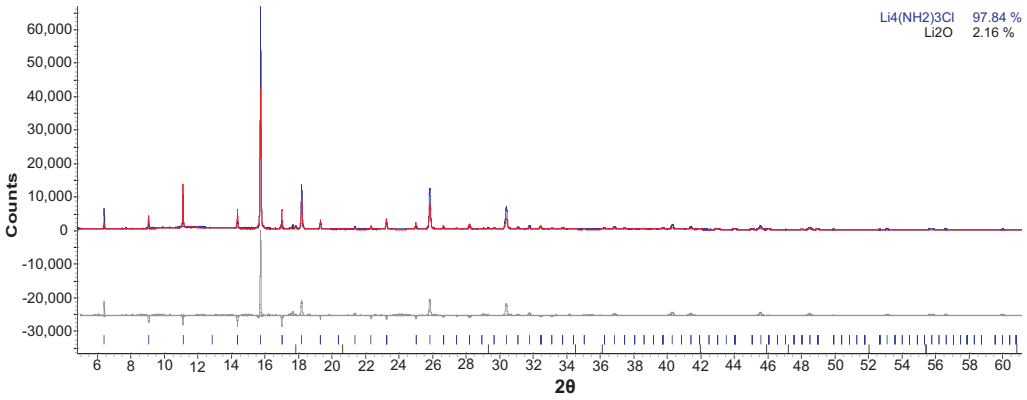

Figure 3.20: Powder synchrotron X-ray diffraction pattern of cubic $Li_4(NH_2)_3Cl$ with a Rietveld refinement using the structure of $Li_4BH_4(NH_2)_3$ with Cl placed on the B sites, showing observed (blue), calculated Rietveld fit (blue) and difference (grey) plots. Peak positions for $Li_4(NH_2)_3Cl$ are shown (blue).

atoms were refined next. As with the chlorine atom this remained on the same fully occupied site (24c) with a refined atomic position. Other sites with lower multiplicity were tried but the occupancies of the sites always refined towards zero. Various combinations of sites were tried with the lithium atoms but the only good fit was from having one 8a and two 12b sites fully occupied. The positions refined to within error (3 ESD's) of those of the $Li_4BH_4(NH_2)_3$ structure so were fixed to the published positions. Finally the hydrogen atoms were added as an NH_2^- rigid body, placed on the refined nitrogen position and allowed to rotate freely, refining the N-H bond length to 0.99 Å and the H-N-H bond angle to 104.1°. This model was then tested on the neutron diffraction data with no constraints on the hydrogen atoms.

After the $Li_4BH_4(NH_2)_3$ structural model had been refined for this compound a full Rietveld refinement was performed in Topas, refining a zero point error, a pseudo-Voigt peak shape (6 parameters) and a Chebyshev background function

(16 parameters); atomic positions were also refined. The refined crystallographic data are shown in table 3.7, with the final crystal structure (fig. 3.23) and Rietveld plot of the X-ray (fig. 3.21) and neutron (fig. 3.22) data shown below.

Table 3.7: Refined crystallographic data for cubic $Li_4(NH_2)_3Cl$.

Atom	Site	x	y	z	Occupancy	B_{iso}
Cl	8a	0.1263(1)	x	x	1	1.5
N	24c	0.1324(4)	0.3729(3)	0.3717(2)	1	1.5
H1	24c	0.178(3)	0.404(6)	0.409(3)	1	5.6
H2	24c	0.076(3)	0.376(3)	0.408(6)	1	5.6
Li1	12b	0.9572(6)	0	0.25	1	1.5
Li2	12b	0.7378(6)	0	0.25	1	1.5
Li3	8a	0.2722(5)	x	x	1	1.5

Space group $I2_13$ (no. 199), $a = 10.4452(3)$ Å
X-ray data: $R_{wp} = 9.451$, $R_{exp} = 3.632$, $\chi^2 = 6.770$
Neutron data: $R_{wp} = 1.800$, $R_{exp} = 0.696$, $\chi^2 = 6.687$

This structure shows a cubic arrangement of nitrogen atoms as seen in $LiNH_2$ and the hexagonal form of $Li_4(NH_2)_3Cl$ discussed in the previous section. There is also a cubic arrangement of the lithium atoms, although this arrangement is distorted by the presence of the large Cl^- atoms. Inspection of the geometry around some of the individual atoms within this structure shows tetrahedral environments (fig. 3.24). It can be seen that lithium atoms in site Li2 are tetrahedrally coordinated to four nitrogen atoms (fig. 3.24a), here there are two separate bond lengths (2.248(6) Å and 2.154(6) Å) and bond angles (approximately 105° and 111°). The chlorine atom is tetrahedrally bonded to three lithium atoms (three Li1 and one Li3 sites), the lithium on the Li3 site is then also bonded to three nitrogen atoms. The bond lengths are Cl-Li1 2.556(6) Å and Cl-Li3 2.638(7) Å with bond angles between 104° and 113°. This geometry around the chlorine atoms is seen to be a key difference between this cubic phase of $Li_4(NH_2)_3Cl$ and the hexagonal phase discussed previously.

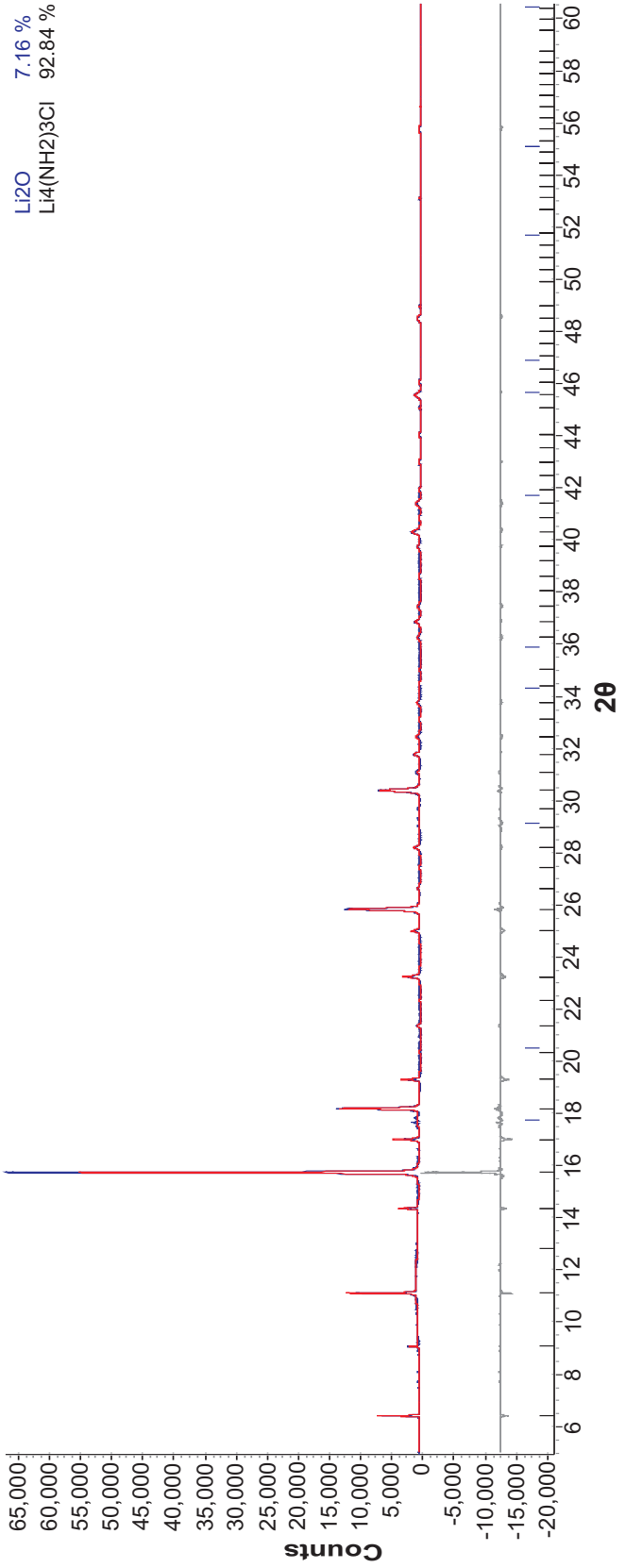

Figure 3.21: Powder synchrotron X-ray diffraction pattern showing the final Rietveld refinement to the cubic $Li_4(NH_2)_3Cl$ phase, showing observed (blue), calculated Rietveld fit (red) and difference (grey) plots. Peak positions for $Li_4(NH_2)_3Cl$ are shown (black).

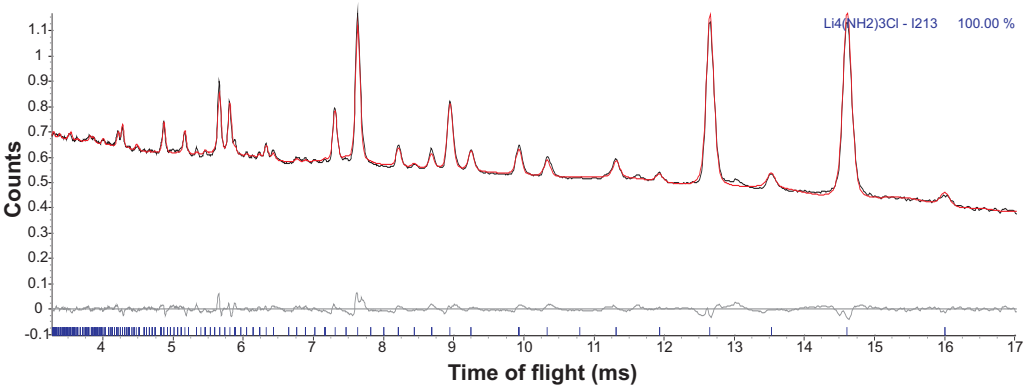

Figure 3.22: Powder neutron diffraction pattern showing the final Rietveld refinement to the cubic $Li_4(NH_2)_3Cl$ phase, showing observed (black), calculated Rietveld fit (red) and difference (grey) plots. Peak positions for $Li_4(NH_2)_3Cl$ are shown (black).

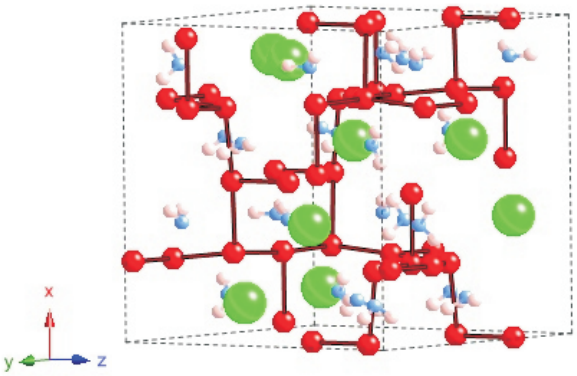

Figure 3.23: Crystal structure of cubic $Li_4(NH_2)_3Cl$ showing the chlorine (green), nitrogen (blue), lithium (red) and hydrogen (white) atoms. The unit cell is shown as a black dotted line.

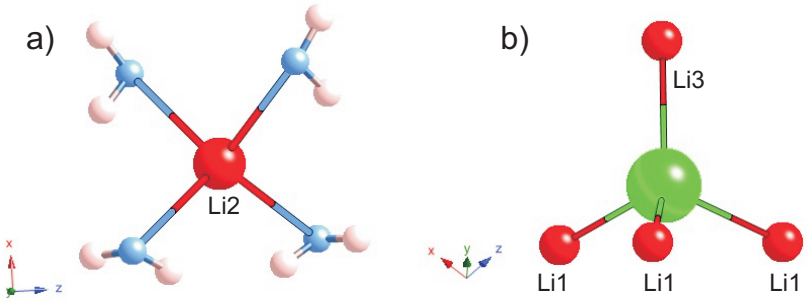

Figure 3.24: Diagram of the geometry around a) Li2 site and b) Cl site within cubic $Li_4(NH_2)_3Cl$ showing the chlorine (green), nitrogen (blue), lithium (red) and hydrogen (white) atoms.

3.3.5 Crystal Structure Investigation - $Li_3Mg_{0.5}(NH_2)_3Cl$

The mixed lithium-magnesium amide-chloride of the form $Li_3Mg_{0.5}(NH_2)_3Cl$, has a nearly identical diffraction pattern to that of the cubic lithium only amide-chloride, $Li_4(NH_2)_3Cl$. When the observed peak positions from the X-ray diffraction pattern were run through the the indexing routine of the computer program Topas[108], this similarity was confirmed. This gave a cubic unit cell of space group $I2_13$ (number 199) with lattice parameter $a = 10.46$ Å as the most likely assignment (around 0.75 % cell volume increase from the pure lithium form). A Pawley fit to this data was run with these lattice parameters and gave the accurate value of $a = 10.4561(8)$ Å, with a cell volume of 1143.05(3) Å^3 and having $R_{wp} = 10.221$ %.

Due to the similarity in the diffraction patterns between the pure lithium and the mixed lithium-magnesium amide-chloride, the pure lithium structure, cubic $Li_4(NH_2)_3Cl$, discussed previously (chapter 3.3.4) was used as a starting point for this Rietveld refinement. From the Pawley fit the background, lattice parameters and peak shape were fixed and a refinement was run using the $Li_4(NH_2)_3Cl$ structure from table 3.7. This gave a good fit to the data with $R_{wp} = 11.226$ %. The magnesium atoms were placed on lithium sites; the occupancies were allowed to refine from a starting position to give the appropriate amount of atoms for the unit cell (24 Li^+ and 4 Mg^{2+}). While all of the combinations of lithium and magnesium atoms gave reasonable fits to the data, no one arrangement was better than the others, or gave better statistics than the original lithium only structure. From this it was concluded that from the lithium only structure (table 3.7) there is a disordered replacement of a quarter of the Li^+ ions by half as many Mg^{2+} ions. The chlorine and nitrogen atoms were allowed to refine but did not move outside of error so were taken as the original values.

A full Rietveld refinement was performed in Topas; this was done using only lithium atoms as no fixed magnesium positions were found, refining the zero point

error, a pseudo-Voigt peak shape (6 parameters) and a Chebyshev background function (16 parameters); atomic positions were refined maintaining a fixed geometry within the NH_2^- rigid body. This Rietveld plot of the X-ray data is shown in figure 3.25, this fit gave statistical values of R_{wp} = 11.123 %, R_{exp} = 6.557 % and χ^2 = 2.876.

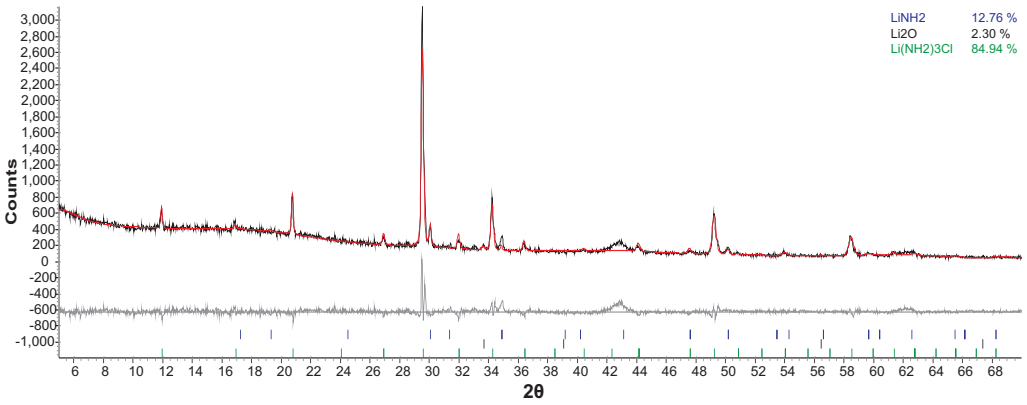

Figure 3.25: Powder X-ray diffraction pattern showing the final Rietveld refinement to the cubic $Li_3Mg_{0.5}(NH_2)_3Cl$ phase, showing observed (black), calculated Rietveld fit (red) and difference (grey) plots. Peak positions for $Li_4(NH_2)_3Cl$ are shown (green).

3.3.6 Investigations into a Solid Solution Range

Due to the relatively heavy nature of the chloride ions in these systems there is a decrease in the H_2 wt % storage of the systems, compared to the pure amide system. Because of this it was decided to investigate the lower limit of the new structures with regards to the chloride ion, forming phases of the form $Li_4(NH_2)_{3+x}Cl_{1-x}$. The hope was that the H_2 wt % could be maximised while maintaining the H_2 storage properties of the system, as discussed in the next chapter (4.3.1). Reactions of the stoichiometry $(3+x)LiNH_2$ + $(1-x)LiCl$ were performed with values of x = 0 - 0.5, these mixtures were heated at 400 °C for 1 hour, resulting in the formation of the hexagonal unit cell of amide-chloride.

Figure 3.26 shows the change in the cell volume of the hexagonal form of $Li_4(NH_2)_3Cl$ formed in this series of experiments, varying the value of x between

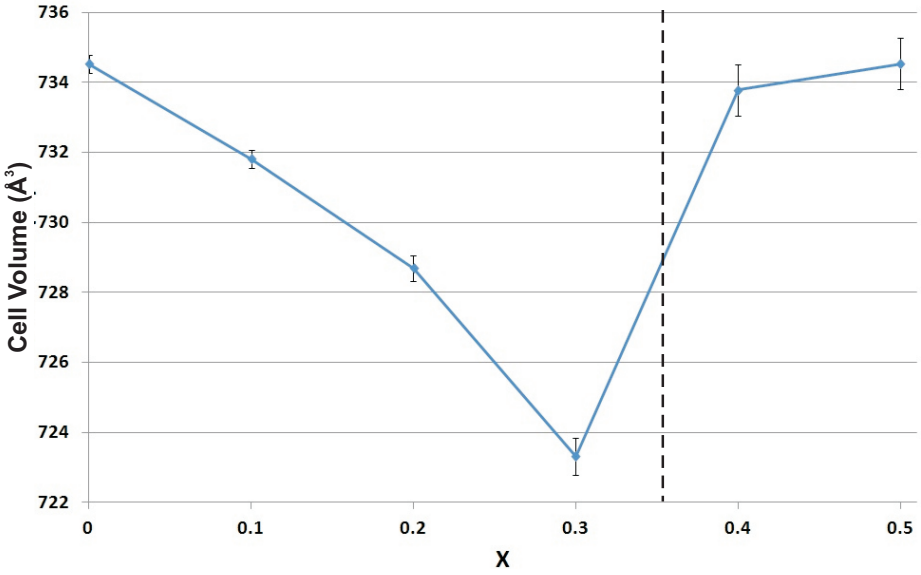

Figure 3.26: Graph showing the change in cell volume for materials of the form $Li_4(NH_2)_{3+x}Cl_{1-x}$. Products to the left of the dotted line formed a pure phase, those on the right contained $LiNH_2$ starting material. Error bars are shown as 3 ESD.

0 and 0.5 to give materials of the formula $Li_4(NH_2)_{3+x}Cl_{1-x}$. The values for this graph may be found in appendix table A.1.

It can be seen that for values of $x = 0$ to 0.3, there was a steady decrease in the cell volume. This equates to a total decrease of around 1.5 % from the stoichiometric unit cell. In this range of x values, a single pure phase was formed (fig. 3.27 shows the XRD pattern where $x = 0.3$) and the decrease in unit cell volume is expected due to the smaller size of the NH_2^- ion compared to the Cl^- ion (1.68 Å [109] and 1.81 Å [110] respectively). The change in stoichiometry from $Li_4(NH_2)_3Cl$ to $Li_4(NH_2)_{3.3}Cl_{0.7}$ equates to a decrease in weight of 5.23 % per formula unit and, when reacted with LiH, an increase in more than 0.5 wt % H_2 released from the samples; this will be discussed further in the following chapter (4.3.1).

For values of x of 0.4 and 0.5, the unit cell volume returned to a value similar to that of the stoichiometric phase of $x = 0$ (fig. 3.26). This result is explained by analysis of the X-ray diffraction patterns of the products of these reactions

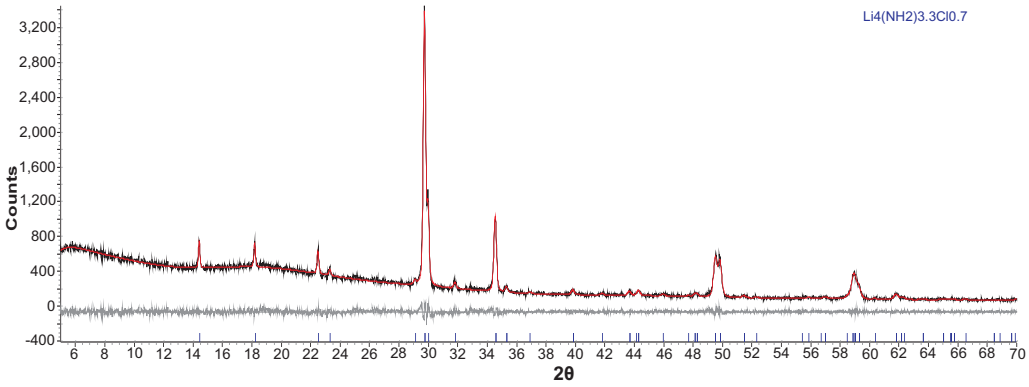

Figure 3.27: Powder X-ray diffraction pattern of the products of the reaction of $3.3LiNH_2$ + $0.7LiCl$ at 400 °C for one hour, showing observed (black), calculated Pawley fit (red) and difference (grey) plots. Peak positions for hexagonal $Li_4(NH_2)_3Cl$ are shown (blue).

(fig. 3.28, shows the XRD pattern where $x = 0.4$) which show remaining $LiNH_2$ along with the rhombohedral amide-chloride.

These results are further confirmed by analysis of the a and c lattice parameters of the hexagonal unit cell (fig. 3.29). These both show similar trends to that of the overall cell volume, showing a decrease in length of around 0.45 and 0.62% respectively, with the minimum at a value of $x = 0.3$. This shows that the effect is an overall contraction of the unit cell, as opposed to a contraction in one unit cell direction.

These results show that the material $Li_4(NH_2)_3Cl$ can accommodate a degree of non-stoichiometry, allowing the amount of hydrogen stored in the material to be maximised. While the lower limit of this non-stoichiometry, with respect to NH_2^-, has not been determined in this work as it would decrease the amount of hydrogen in the material, it is seen that above the higher limit the material forms the stoichiometric 3 amide : 1 chloride with remaining $LiNH_2$.

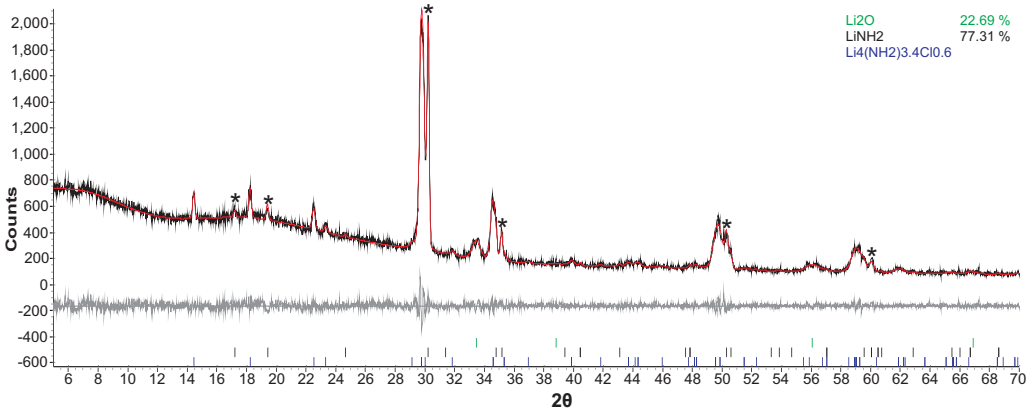

Figure 3.28: Powder X-ray diffraction pattern of the products of reaction of $3.4LiNH_2 + 0.6LiCl$ at 400 °C for one hour, showing observed (black), calculated Pawley fit (red) and difference (grey) plots. Peak positions for $Li_4(NH_2)_3Cl$ are shown (blue), those for $LiNH_2$ are highlighted (*).

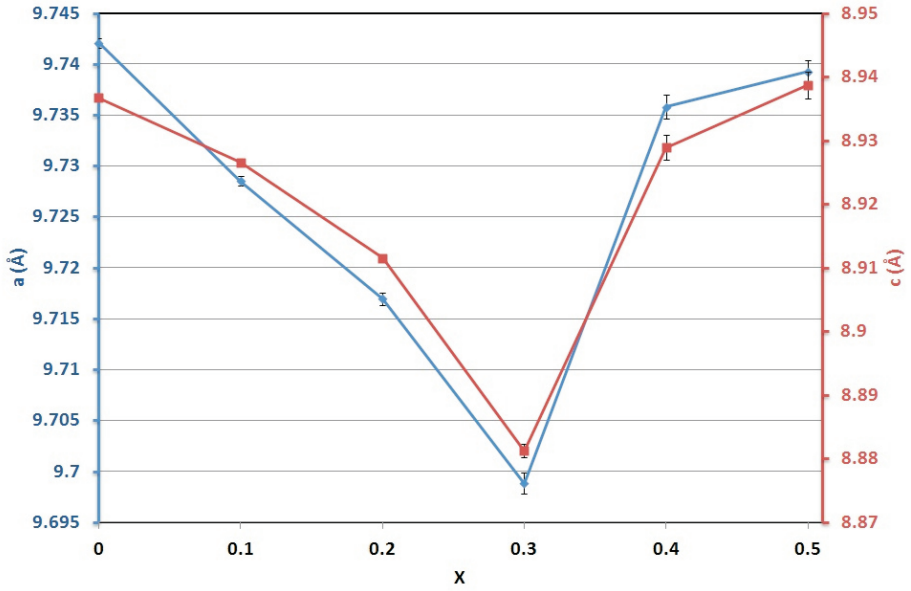

Figure 3.29: Graph showing the change in a (blue) and c (red) lattice parameter for materials of the form $Li_4(NH_2)_{3+x}Cl_{1-x}$.

3.4 Imide-chlorides: $xLi_2NH + yLiCl$ or $(y/2)MgCl_2$

3.4.1 Synthesis

In this section, Li_2NH was used to prepare both pure lithium and mixed lithium-magnesium imide-chlorides through reaction with lithium and magnesium chloride at 400 °C. The reaction stoichiometries were selected to match the nitrogen to halide ratio of the amide-halides prepared in section 3.3.1. As we shall see, the equivalent phases were also formed *via* the reaction of the amide-chlorides with LiH. The decomposition of these phases will be discussed at a later point (chapter 4.3.1) but the products will be looked at here for comparison with those formed directly from Li_2NH.

Reaction of Li_2NH with LiCl did not show the formation of a pure phase (fig. 3.30). Instead there seemed to be a face centred cubic solid solution range; the indexing routine of Topas suggested phases with space group $Fm\bar{3}m$ formed with a lattice parameter varying between that of the two starting materials (a = 5.13Å - 5.21Å). This solid solution range is indicated by the broad and uneven peaks and the poor fit to a single unit cell. This is shown in figure 3.31; the calculated pattern shown has a unit cell parameter of a = 5.15Å and can be seen to give a poor fit to the observed data.

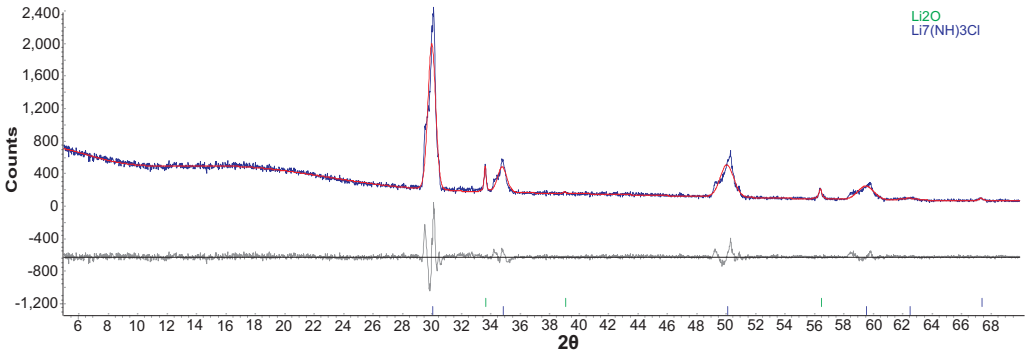

Figure 3.30: Powder X-ray diffraction pattern of the products of the reaction of $3Li_2NH$ + LiCl at 400 °C for 12 hours, showing observed (blue), calculated Pawley fit (red) and difference (grey) plots. Peaks positions for cubic $Fm\bar{3}m$ cell are shown in blue.

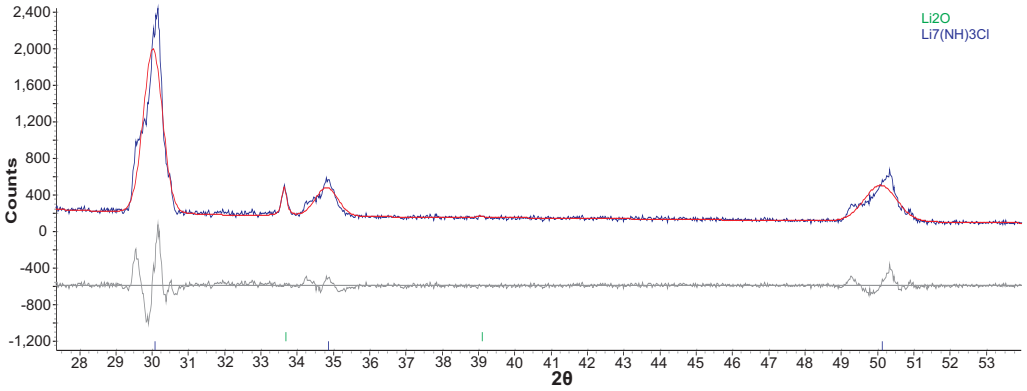

Figure 3.31: Powder X-ray diffraction pattern of the products of the reaction of $3Li_2NH + LiCl$ at 400 °C for 12 hours with a narrower 2θ range, showing observed (blue), calculated Pawley fit (red) and difference (grey) plots. Peaks positions for cubic $Fm\bar{3}m$ cell are shown in blue.

The product formed from the decomposition of $Li_4(NH_2)_3Cl$ with LiH (fig. 3.32) showed a close resemblance to the product formed directly from Li_2NH, showing a fit to the same unit cell, $Fm\bar{3}m$. In this case, however, it appears that a much purer phase was formed. The peaks appear much sharper and narrower with no shoulders or asymmetry; from these peaks a more accurate lattice parameter could be attained of a = 5.157(3) Å. A comparison of the powder diffraction patterns from each of the synthetic methods is shown in figure 3.33.

The lack of any starting materials in these diffraction patterns along with the similarity of the products formed from Li_2NH and from the decomposition of the amide-chloride leads to the tentative assignment of a pure lithium imide-chloride of the form, $Li_7(NH)_3Cl$. Investigations into the limits of the solid solution range of this system are discussed in the next section (chapter 3.4.2).

In the case of the mixed lithium and magnesium imide-chloride, reaction of Li_2NH with $MgCl_2$ at 400 °C showed the formation of a pure phase (fig. 3.34). The product had a cubic unit cell with a lattice parameter of a = 5.137(1) Å, similar in size to the pure lithium system, $Li_7(NH)_3Cl$. However, in this case the presence of the (211) Bragg reflection ruled out the possibility of a face

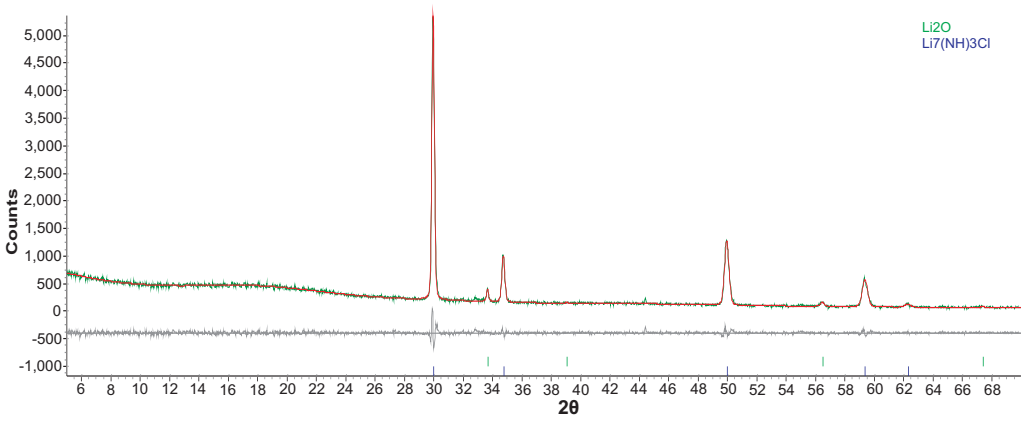

Figure 3.32: Powder X-ray diffraction pattern of the products from the decomposition of $Li_4(NH_2)_3Cl$ with LiH at 400 °C, showing observed (green), calculated Pawley fit (red) and difference (grey) plots. Peaks positions for cubic $Fm\bar{3}m$ cell are shown in blue.

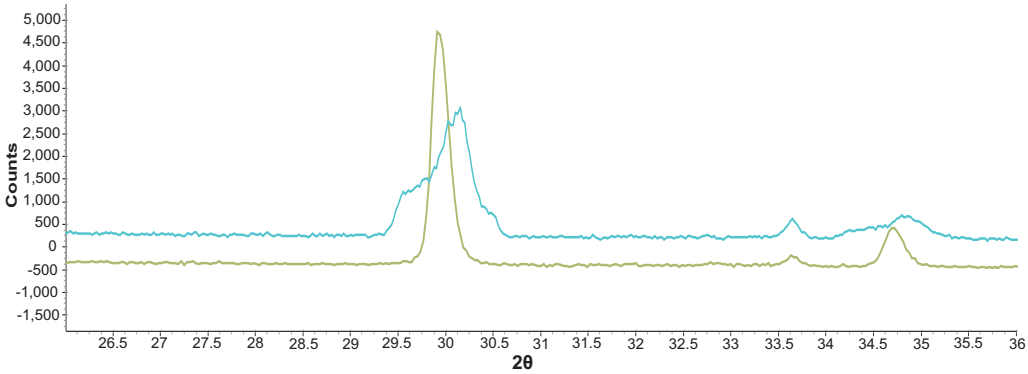

Figure 3.33: Comparison of a section of the powder X-ray diffraction patterns of lithium imide-chlorides formed from reaction of Li_2NH with LiCl (blue) and from the decomposition of $Li_4(NH_2)_3Cl$ with LiH (green).

centred cell, instead indicating a primitive cell. It is also worth pointing out that there are differences in the peak shape of the (211) peak, compared to the other reflections. This suggests that there may be two phases present with similar lattice parameters, one primitive and one face centred cubic.

The product formed from the decomposition of $Li_3Mg_{0.5}(NH_2)_3Cl$ with LiH closely resembles that formed from Li_2NH. However, in this case there was a larger lattice parameter of a = 5.169(3) Å, which gives in increase in unit cell size of around 1.8%, although the peaks are seen to be more broad than the product

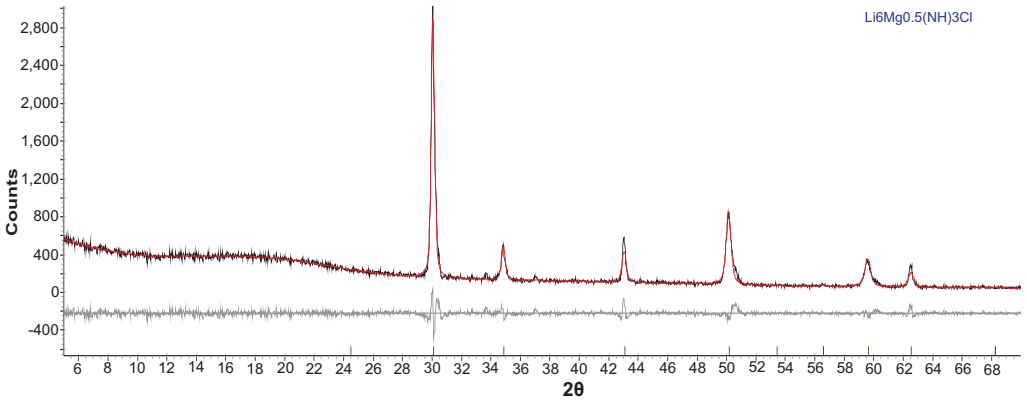

Figure 3.34: Powder X-ray diffraction pattern of the products of the reaction of $3Li_2NH + 1/2MgCl_2$ at 400 °C for 12 hours, showing observed (black), calculated Pawley fit (red) and difference (grey) plots. Peaks positions for cubic $Pn\bar{3}$ cell are shown in blue.

formed from Li_2NH. This is again a strong indicator for the ability of these materials to form solid solution ranges with varying amounts of halide present within the unit cell. This material was tentatively assigned as $Li_6Mg_{0.5}(NH)_3Cl$.

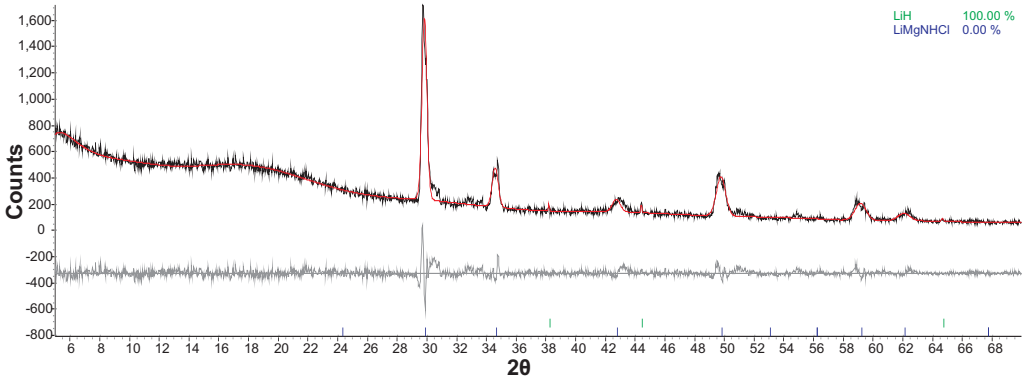

Figure 3.35: Powder X-ray diffraction pattern of the products from the decomposition of $Li_3Mg_{0.5}(NH_2)_3Cl$ with LiH at 400 °C, showing observed (black), calculated Pawley fit (red) and difference (grey) plots. Peaks positions for cubic $Pn\bar{3}$ cell are shown in blue.

It is worth mentioning at this point that the decompostion of the relevant amide-chlorides were also tested with MgH_2 as well as the LiH stated above. The products from these reactions were not found to be of imide-chloride form so will not be discussed here.

3.4.2 Investigations of a Solid Solution Range

As with $Li_4(NH_2)_3Cl$ discussed earlier in this chapter (3.3.6), the range of non-stoichiometry was investigated in the equivalent imide-chloride, $Li_7(NH)_3Cl$, in an attempt to maximise the hydrogen storage capacity. Due to the fact that no distinct phase was formed from reaction of Li_2NH with LiCl (fig. 3.33), these phases were investigated from the decomposition of the appropriate amide-chloride with LiH (equation 3.3). The hydrogen storage properties of these reactions will be discussed in the following chapter (chapter 4.3.1)).

$$Li_4(NH_2)_{3+x}Cl_{1-x} + (3+x)LiH \rightarrow Li_{7+x}(NH)_{3+x}Cl_{1-x} + (3+x)H_2 \uparrow \qquad (3.3)$$

It can be seen in figure 3.36 that there was a decrease in the lattice parameter in this cubic cell for values of x = 0 - 0.3 for the system $Li_{7+x}(NH)_{3+x}Cl_{1-x}$, before it increased again for values of x = 0.4. This equates to a decrease of around 0.62% in the a lattice parameter and around 1.87% in the cell volume. The values for this graph may be found in appendix table A.2. This contraction of the unit cell can also be seen clearly by examination of the position of the (111) peak in the X-ray diffraction patterns of these products. Figure 3.37 shows the shift of the (111) peak to a higher position as the value of x increased, consistent with the decrease in unit cell size.

3.5 Amide-bromides: $xLiNH_2$ + $yLiBr$ or $(y/2)MgBr_2$

3.5.1 Synthesis

Lithium amide and lithium bromide were ground together at molar ratios between 1:1 and 8:1 and heated at temperatures between 200 and 400 °C. No reaction was seen below 150 °C but at temperatures higher than this a new phase was formed.

This new phase was seen to form as a single product from the reaction of $6LiNH_2$ + LiBr, heated at 2 °C min^{-1} to 250 °C for 12 hours. The new phase

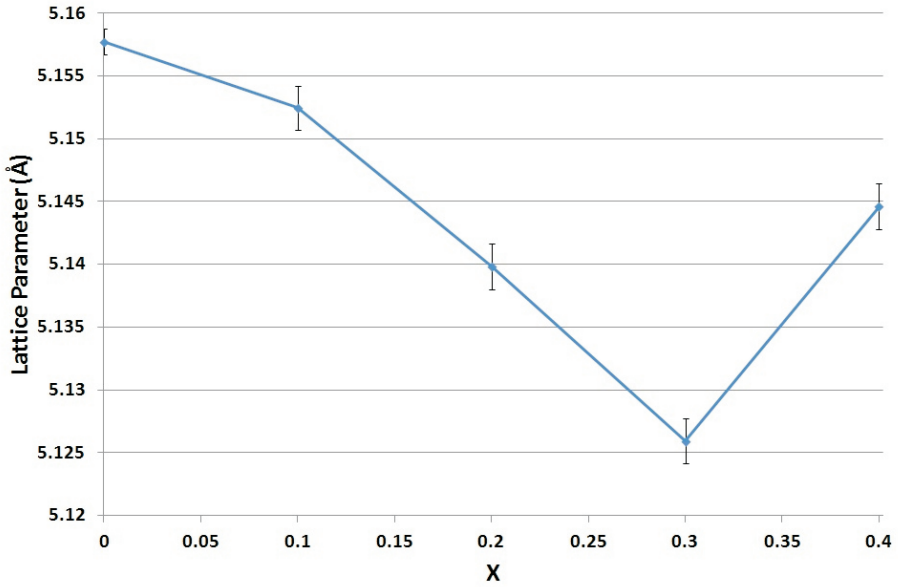

Figure 3.36: Lattice parameter for materials of the form $Li_7(NH)_{3+x}Cl_{1-x}$, formed from reaction of $Li_4(NH_2)_{3+x}Cl_{1-x}$ + (3+x) LiH at 400 °C.

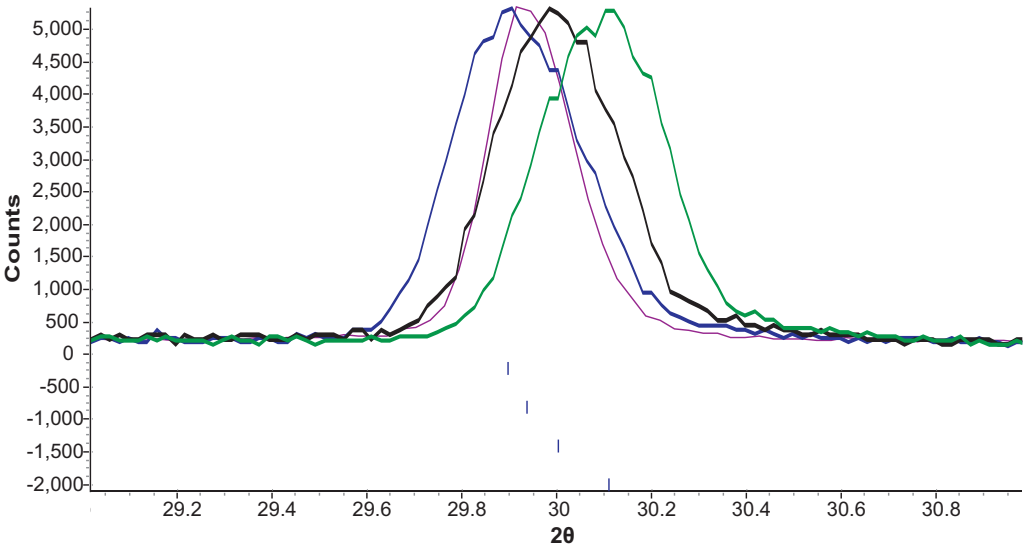

Figure 3.37: Section of XRD patterns for materials of the form $Li_7(NH)_{3+x}Cl_{1-x}$, where $x = 0$ (blue), 0.1 (purple), 0.2 (black) and 0.3 (green). Peak positions for the (111) peak are shown below.

has been assigned the formula $Li_7(NH_2)_6Br$ and has been indexed to a hexagonal unit cell, space group $R\bar{3}$, similar to that of $Li_4(NH_2)_3Cl$ discussed previously, with lattice parameters $a = 9.84893(9)$ Å and $c = 8.9845(3)$ Å. A Pawley fit to the data based on this unit cell is shown in figure 3.38.

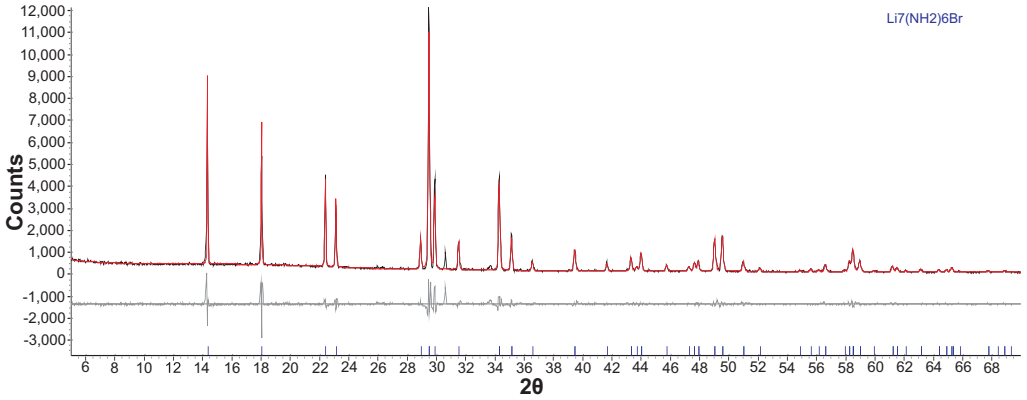

Figure 3.38: Powder X-ray diffraction pattern of hexagonal $Li_7(NH_2)_6Br$ made by reaction of $6LiNH_2$ + LiBr at 250 °C for twelve hours, showing observed (black), calculated Pawley fit (red) and difference (grey) plots. Peak positions for $Li_7(NH_2)_6Br$ are shown (blue).

In the case of reaction between lithium amide and magnesium bromide, molar ratios were again chosen so as to maintain the NH_2^- to Br^- ratios similar to the equivalent purely lithium reaction. The reaction of $6LiNH_2$ + $1/2MgBr_2$, heated at 2 °C min^{-1} 250 °C for 12 hours formed a similar unit cell to that of the purely lithium equivalent. This phase has the space group $R\bar{3}$ with lattice parameters $a = 9.8111(6)$ Å and $c = 8.9558(6)$, a Pawley fit to the data based on this unit cell is shown in figure 3.39.

A previously reported phase, Li_2NH_2Br, formed from a reaction of $LiNH_2$ + LiBr in a 1:1 ratio was also made. A further reported phase $LiMg_{0.5}NH_2Br$ was not formed[83]; instead we saw a metathesis reaction forming LiBr and $Mg(NH_2)_2$ (eq. 3.4). In this work I will focus on the new and more hydrogen rich 6:1 phases.

$$LiNH_2 + 1/2MgBr_2 \rightarrow LiBr + 1/2Mg(NH_2)_2 \quad (3.4)$$

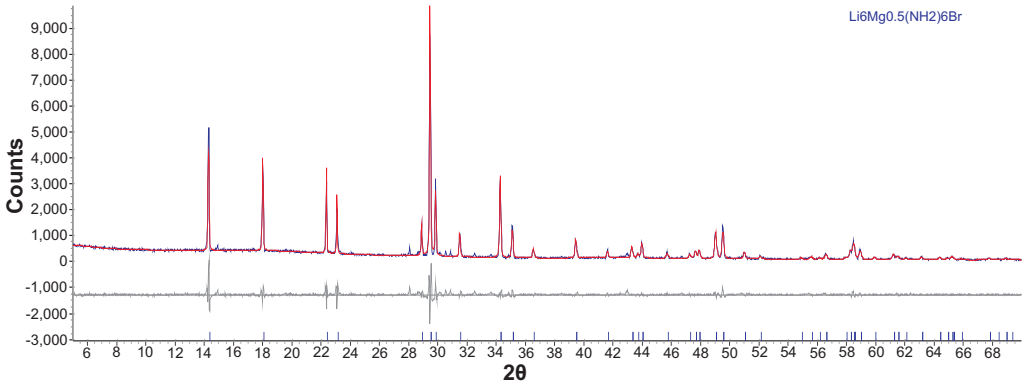

Figure 3.39: Powder X-ray diffraction pattern of hexagonal $Li_6Mg_{0.5}(NH_2)_6Br$ made by reaction of $6LiNH_2$ + $1/2MgBr_2$ at 250 °C for twelve hours, showing observed (blue), calculated Pawley fit (red) and difference (grey) plots. Peak positions for $Li_6Mg_{0.5}(NH_2)_6Br$ are shown (blue).

3.5.2 Raman Spectroscopy

As with the amide-chlorides discussed previously, Raman spectroscopy was performed on these samples to check that the new phases contained purely NH_2^- groups and not NH^{2-} imide groups. The geometry and symmetry of the NH_2^- group has been discussed previously (chapter 3.3.2) and the assignments will be used here.

The Raman spectra of the two new phases formed in this section are shown in figure 3.40, along with the peak positions of $LiNH_2$ and Li_2NH from figure 3.6. The positions and sharpness of the peaks of both of these phases clearly show that they are NH_2^- groups; as in the case of hexagonal $Li_4(NH_2)_3Cl$, the spectra display two symmetric (ν_s) and two asymmetric (ν_{as}) stretches; this is indicative of two different NH_2^- environments.

3.5.3 Crystal Structure Investigation - $Li_7(NH_2)_6Br$

The crystal structure of $Li_7(NH_2)_6Br$ was investigated with powder synchrotron X-ray diffraction data (Diamond, I11) and powder neutron diffraction data (ISIS, GEM), using the computer program Topas [108].

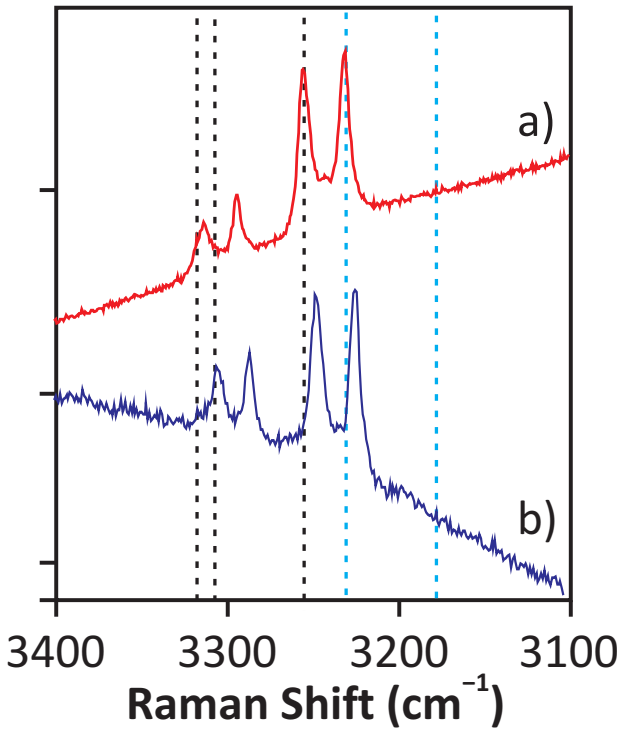

Figure 3.40: Raman spectra of (a) $Li_7(NH_2)_6Br$, (b) $Li_6Mg_{0.5}(NH_2)_6Br$. Peak positions highlighted by black ($LiNH_2$) and blue (Li_2NH) dotted lines.

The observed peak positions from the X-ray diffraction pattern of $Li_7(NH_2)_6Br$ were run through the indexing routine of the computer program Topas. This gave the most likely assignment of a rhombohedral unit cell with hexagonal symmetry; space group $R\bar{3}$ (number 148) with a = 9.84 Å and c = 8.98 Å. These lattice values were refined in Topas through a Pawley fit; this fit is shown in figure 3.41. The Pawley fit allowed for more accurate lattice parameters to obtained, these were a = 9.84893(9) Å and c = 8.9845(3) Å, giving a unit cell volume of 754.75(1) Å^3. For this Pawley fit statistical values of R_{wp} = 14.944, R_{wp} = 4.006 and χ^2 = 13.913 were obtained. This Pawley fit was also refined against the neutron diffraction data, this is shown in figure 3.42.

This unit cell is seen to be similar to that of the hexagonal $Li_4(NH_2)_3Cl$ discussed previously (chapter 3.3.3), however this unit cell is seen to around 2.7% larger, consistent with the larger Br^- ion. The structural model of hexagonal

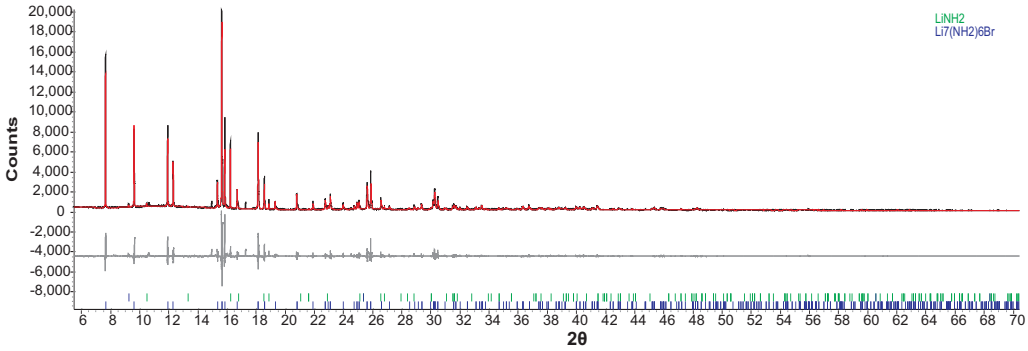

Figure 3.41: Powder synchrotron X-ray diffraction pattern showing a Pawley fit to the hexagonal $Li_7(NH_2)_6Br$; observed (black), calculated Pawley fit (red), difference (grey) plots and peak positions for $Li_7(NH_2)_6Br$ (blue) are shown.

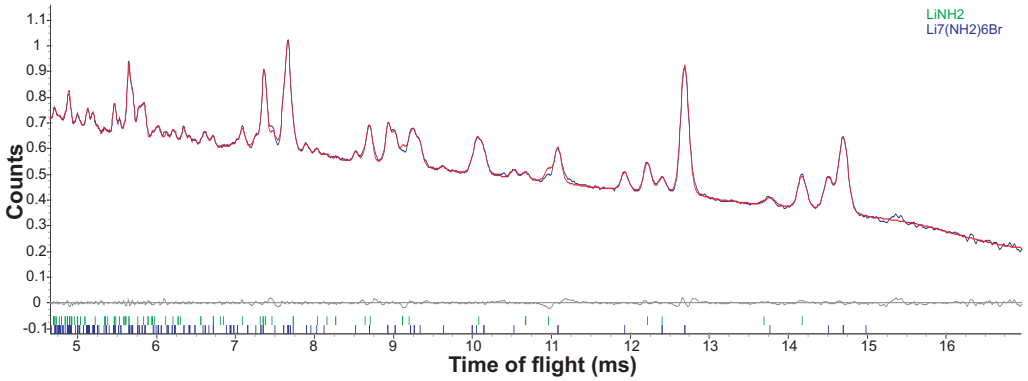

Figure 3.42: Powder neutron diffraction pattern showing a Pawley fit to the hexagonal $Li_7(NH_2)_6Br$; observed (blue), calculated Pawley fit (red), different (grey) plots and peak positions for $Li_7(NH_2)_6Br$ (blue) are shown.

$Li_4(NH_2)_3Cl$ was therefore used as a starting point for producing a model for the Rietveld refinement of $Li_7(NH_2)_6Br$.

This structure contains larger formula units than $Li_4(NH_2)_3Cl$, with six $LiNH_2$ formula units ($\approx$ 32.60 Å^3) and a $LiBr$ formula unit ($\approx$ 40.25 Å^3). From this we can approximate that one formula unit of $Li_7(NH_2)_6Br$ will have a volume of 235.85 Å^3, given the total unit cell volume of 754.75 Å^3 we get a multiplicity of $Z = 3.2$. This is compared to a value of $Z \approx 6$ for hexagonal $Li_4(NH_2)_3Cl$, however the site multiplicities for space group $R\bar{3}$ (table 3.4) allow for a value of 3. The atoms were tested on the postions given in table 3.5 with bromine

sitting on the Cl1 site and nitrogen fully occuppied on the N site. The atoms were first individually allowed to refine freely and it was seen that all atoms sat on sites near to the amide-chloride positions. Following this all the atoms were refined together with dampening factors to maintain them close to these positons, while the occupancies were also refined. The occupancies refined towards one for bromine, nitrogen and hydrogen, and to around 0.5 for lithium; giving the correct stoichiometries for a value of $Z = 3$. At this point the model was tested on the neutron diffraction data, allowing the atomic positions and occupancies to refine.

After a good structural model had been obtained, a full Rietveld refinement was performed in Topas on both the X-ray and neutron diffraction data. A zero point error, pseudo-Voigt peak shape (6 parameters) and Chebyshev background function (16 parameters) were refined along with the lattice parameters, atomic positions and thermal parameters. The resultant crystal structure (fig. 3.43) and Rietveld refinement to the X-ray (fig. 3.44) and neutron (fig. 3.45) diffraction data are shown below. The resultant crystallographic data is shown in table 3.8.

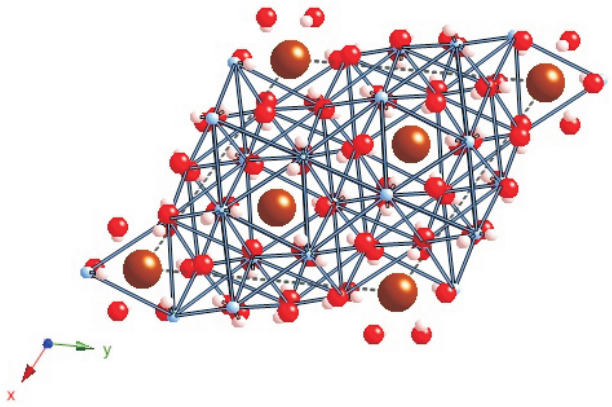

Figure 3.43: Crystal structure of $Li_7(NH_2)_6Br$ showing the chlorine (green), nitrogen (blue), lithium (red) and hydrogen (white) atoms. The unit cell is shown as a black dotted line.

The geometry around indivdual atoms is seen to be similar to that of hexagonal $Li_4(NH_2)_3Cl$, with octahedrally coordinated bromine (figure 3.46b) and tetrahedrally coordinated lithiums (figure 3.46a). The bromine atoms are coordinated

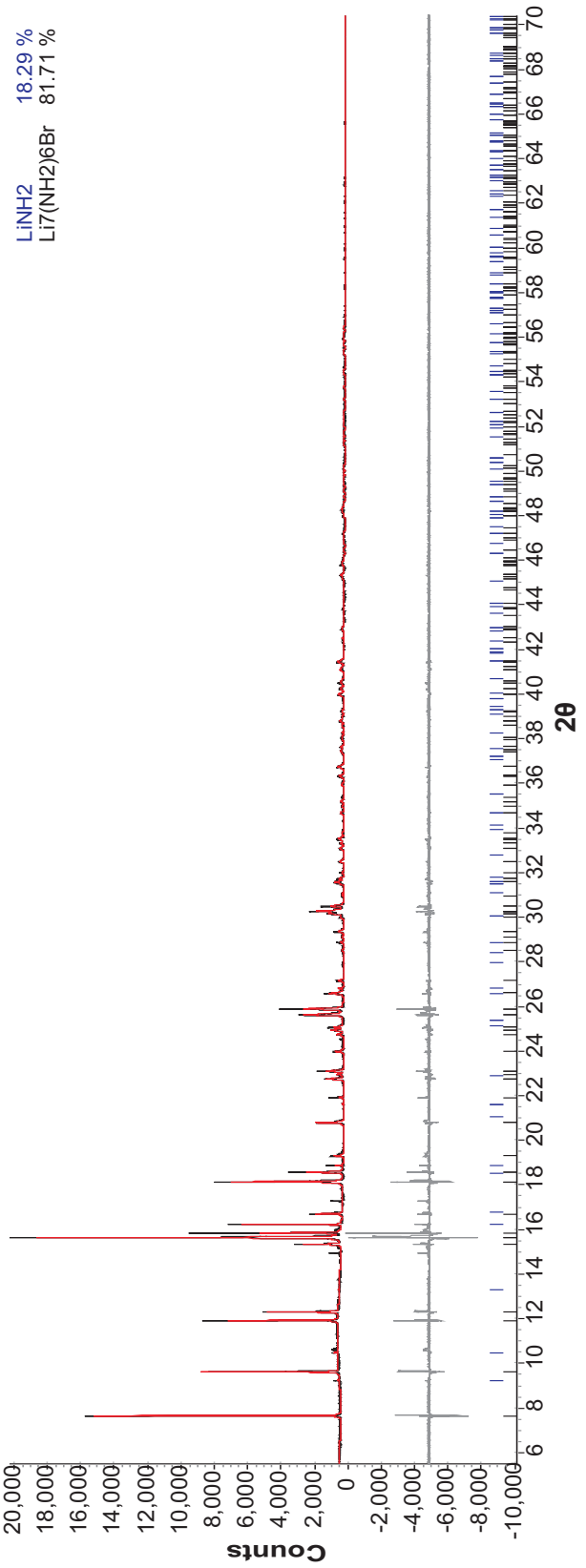

Figure 3.44: Powder synchrotron X-ray diffraction pattern showing the final Rietveld refinement to the $Li_7(NH_2)_6Br$ phase. Observed (black), calculated Rietveld fit (red), difference (grey) plots, and peak positions for $Li_7(NH_2)_6Br$ (black) are shown.

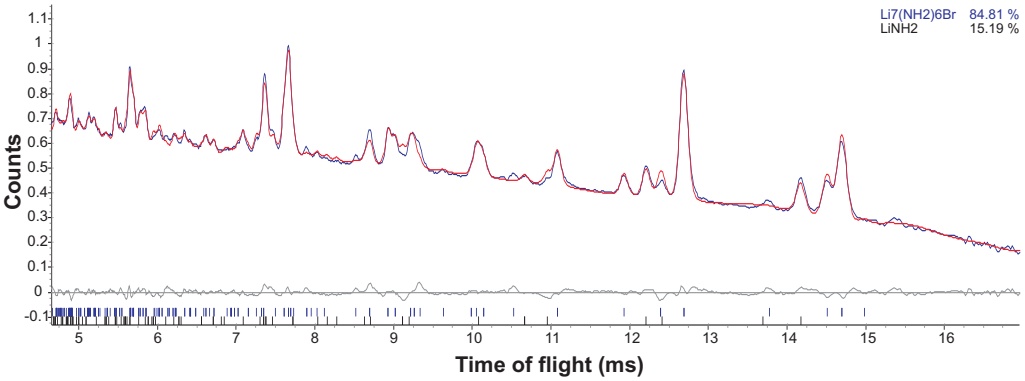

Figure 3.45: Powder neutron diffraction pattern showing the final Rietveld refinement to the $Li_7(NH_2)_6Br$ phase. Observed (blue), calculated Rietveld fit (red), difference (grey) plots, and peak positions for $Li_7(NH_2)_6Br$ are shown (blue).

Table 3.8: Refined crystallographic data for$Li_7(NH_2)_3Br$

Atom	Site	x	y	z	Occupancy	B_{iso}
Br	3a	0	0	0	1	1.48(6)
N	18f	0.1976(6)	0.2349(2)	0.6522(6)	1	1.6(1)
H1	18f	0.223(6)	0.303(4)	0.677(6)	1	5.1(5)
H2	18f	0.138(6)	0.175(4)	0.683(6)	1	5.1(5)
Li1	18f	0.178(2)	0.197(3)	0.420(3)	1/2	4.3(3)
Li2	18f	0.124(2)	0.412(3)	0.767(2)	7/12	4.3(3)

Space group $R\bar{3}$ (no. 148), $a = 9.84893(9)$ Å, $c = 8.9845(3)$ Å
X-ray data: $R_{wp} = 14.944$, $R_{exp} = 4.006$, $\chi^2 = 13.913$
Neutron data: $R_{wp} = 1.260$, $R_{exp} = 0.483$, $\chi^2 = 6.802$

to six lithium (Li2) atoms with a bond length of 2.487(6) Å; the octahedron is, however, very distorted with Li-Br-Li angles varying between 72° and 108°. The lithium (Li1) atoms are coordinated to four nitrogens. This tetrahedron is also distorted with Li-N bond lengths between 2.02 Å and 2.50 Å and N-Li-N bond angles of between 102° and 123°.

3.5.4 Crystal Structure Investigation - $Li_6Mg_{0.5}(NH_2)_6Br$

The crystal structure of $Li_6Mg_{0.5}(NH_2)_6Br$ was refined against using laboratory X-ray diffraction data using the computer program Topas. The observed peak positions from the X-ray diffraction pattern of $Li_6Mg_{0.5}(NH_2)_6Br$ were run through the indexing routine of Topas. This gave the most likely assignment to the same

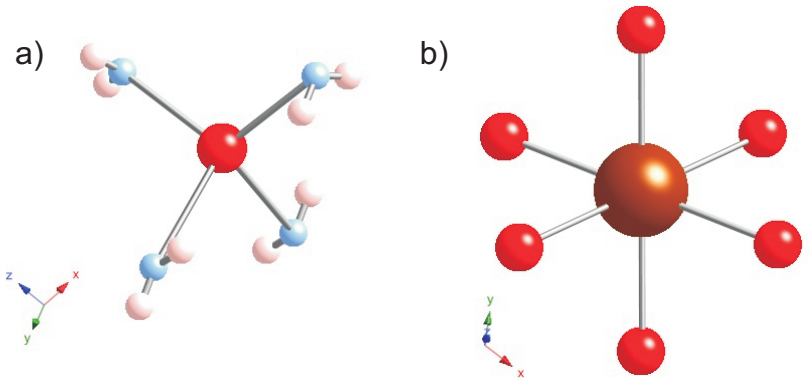

Figure 3.46: Geometry around a) Li1 site and b) Br site within cubic $Li_7(NH_2)_6Br$ showing the bromine (brown), nitrogen (blue), lithium (red) and hydrogen (white) atoms.

hexagonal space group as the purely lithium equivalent, $R\bar{3}$ (number 148) with lattice parameters of $a = 9.80$ Å and $c = 8.95$ Å. These values were then refined through a Pawley fit in Topas give more accurate lattice parameters of $a = 9.8111(6)$ Å and $c = 8.9571(6)$ Å to be obtained, giving a cell volume of 746.68(4) $Å^3$. This fit was shown in figure 3.39 and gave statistical values of $R_{wp} = 12.184$, $R_{exp} = 5.642$ and $\chi^2 = 4.666$.

Due to the similarity in the diffraction pattern and determined unit cell with the pure lithium amide-bromide, this structure was used as the starting point for this refinement (table 3.8). Firstly the heavier scattering atoms of bromine and nitrogen were refined and it was clear that they were sitting in the same sites as the pure lithium equivalent. Secondly three lithium atoms were replaced by half as many magnesium atoms. This was tested on both lithium sites in turn, this gave equally good results on each site, the occupancies were fixed so as to have the correct stoichiometry. It was presumed from these results that the magnesium atoms have a random arrangement across the lithium sites.

Finally a full Rietveld refinement was performed in Topas, this was done with the magnesium atoms sitting on the Li2 site, refining the zero point error, a pseudo-Voigt peak shape (6 parameters) and a Chebyshev background function (16 parameters); atomic positions were also refined. This Rietveld plot of the

X-ray data is shown in figure 3.47, this fit gave statistical values of $R_{wp} = 13.798$ %, $R_{exp} = 5.642$ % and $\chi^2 = 5.983$.

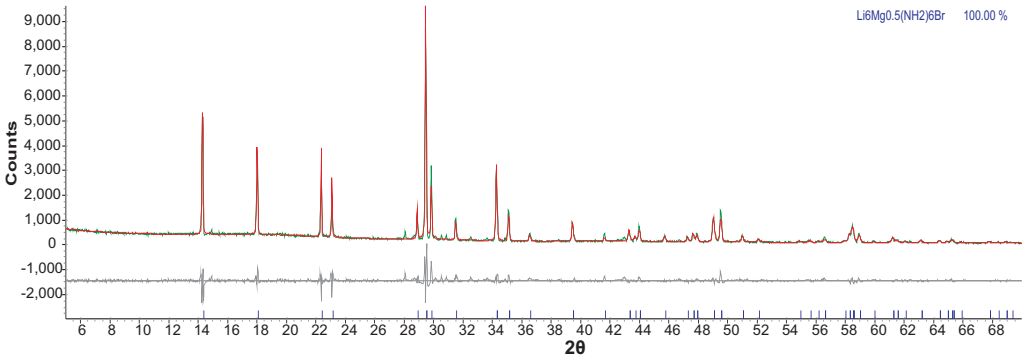

Figure 3.47: Powder X-ray diffraction pattern showing the final Rietveld refinement to the $Li_6Mg_{0.5}(NH_2)_6Br$ phase. Observed (green), calculated Rietveld fit (red), difference (grey) plots, and peak positions for $Li_6Mg_{0.5}(NH_2)_6Br$ (black) are shown.

3.5.5 Investigations into a solid solution

As with the amide-chlorides (chapter 3.3.6), due to the relatively heavy nature of the bromide ions in this system, it was decided to investigate the lower limits of the new structure with regards to the bromide ion content. Reactions of the stoichiometry $(3 + x)LiNH_2 + (1 - x)LiBr$ were performed with values of $x = 0$ - 0.5, these mixtures were heated at 250 °C for twelve hours.

The change in cell volume for the hexagonal phases formed is shown in figure 3.48 for the range of x values. This shows that there was a steady decrease is cell volume of values of $x = 0$ to 0.4. This change gives a total decrease in cell volume of around 1.24%. There was a similar trend seen in the change in the a and c lattice parameters (fig. 3.49) showing an overall contraction in the unit cell. This change in stoichiometry from $Li_7(NH_2)_6Br$ to $Li_7(NH_2)_{6.4}Br_{0.6}$ would equate to a decrease in weight of 11.37 % per formula unit and, when reacted with LiH, an increase of over 0.7 wt % H_2 released from the samples.

By analysis of the X-ray diffraction patterns of the products from these re-

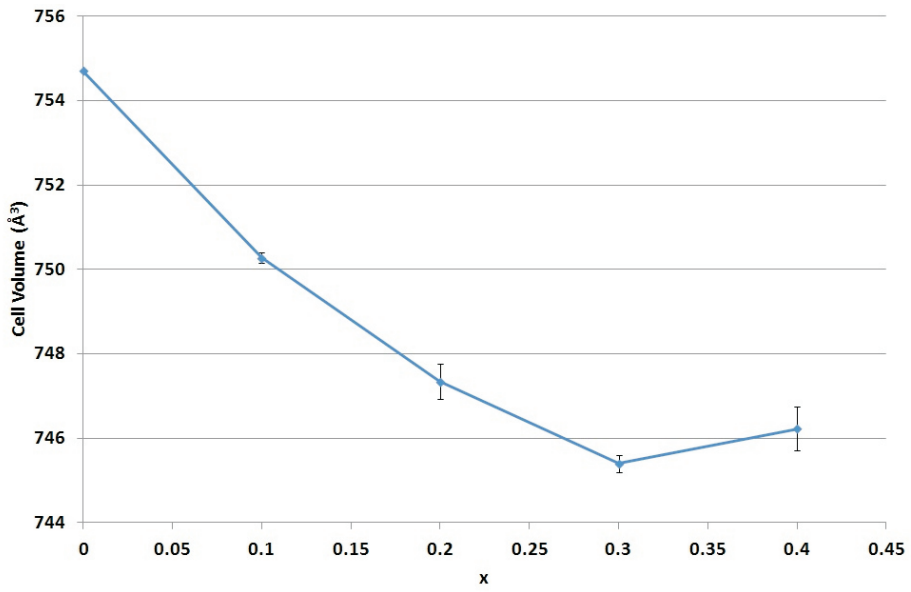

Figure 3.48: Change in cell volume for $Li_7(NH_2)_6Br$ from reactions of $(6+x)LiNH_2$ + $(1-x)LiBr$.

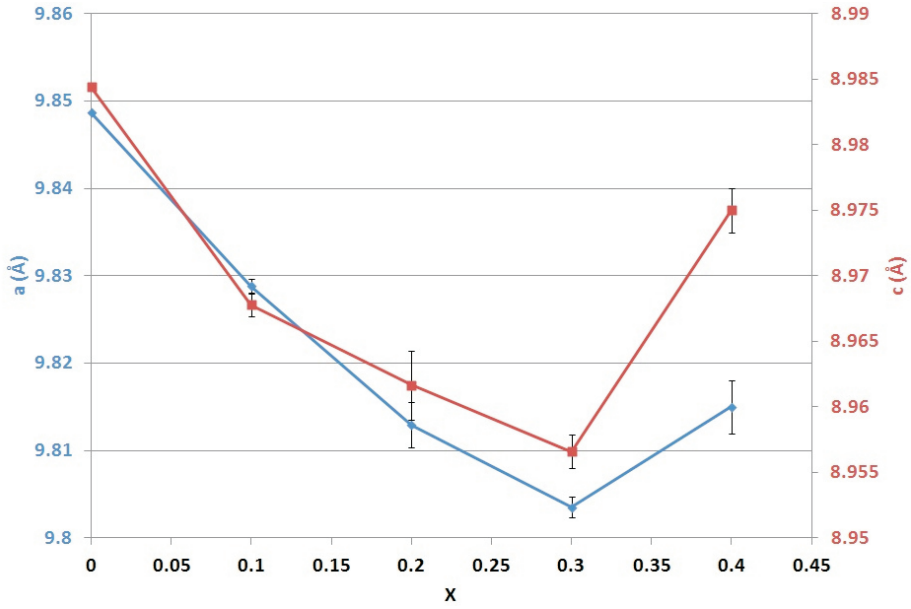

Figure 3.49: Change in the lattice parameters for $Li_7(NH_2)_6Br$ from reactions of $(6+x)LiNH_2$ + $(1-x)LiBr$; change in the a (blue) and c (red).

actions, it can be seen that there were levels of $LiNH_2$ alongside the amide-bromide phase at all values of x (fig. 3.50). This suggests that while the material $Li_7(NH_2)_6Br$ can accommodate a degree of non-stoichiometry, the exact extent of this non-stoichiometry may not be as high as first thought and may be difficult to determine due to remaining starting material present.

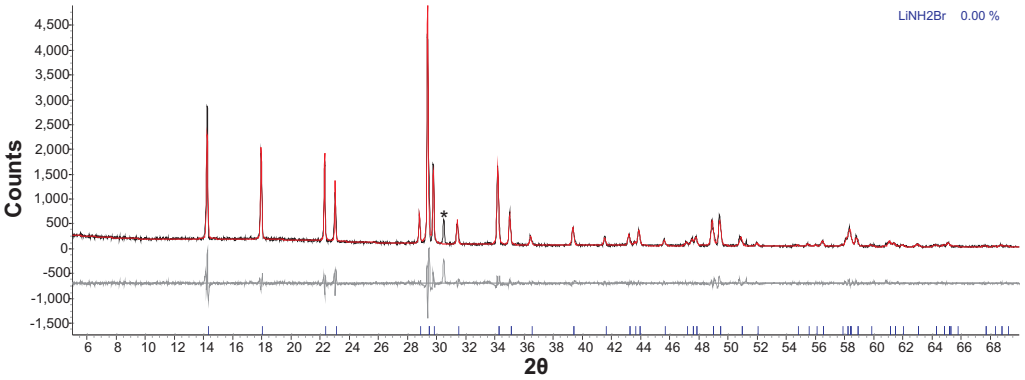

Figure 3.50: Powder X-ray diffraction pattern of products from reaction of $6.1LiNH_2 + 0.9LiBr$ at 250 °C for 12 hours, showing observed (black), calculated Pawley fit (red) and difference (grey) plots. Peak positions for $Li_7(NH_2)_6Br$ are shown (blue) and the main peak for $LiNH_2$ is highlighted (*).

3.6 Imide-bromides: $xLi_2NH + yLiBr$ or $(y/2)MgBr_2$

3.6.1 Synthesis

In this section, Li_2NH was used to prepare both pure lithium and mixed lithium-magnesium imide-bromides through reaction with lithium and magnesium bromide separately at 400 °C. Reaction stoichiometries were selected to match the nitrogen to halide ratio of the amide-halides prepared in section 3.5.1. As we shall see, equivalent products were obtained from the decomposition of the amide-bromides with LiH. While the decomposition of these phases will be discussed in the next chapter (4.3.2) the products will be discussed here for comparison with those formed directly from Li_2NH.

Reaction of Li_2NH with LiBr, similarly to that of LiCl (chapter 3.4.1), did

not result in the formation of a pure phase. There seemed to be the formation of a face centred cubic solid solution range, with lattice parameter a = 5.14 - 5.22 Å and most likely space group of $Fm\bar{3}m$; however, unlike the chloride case, the upper limit of the lattice parameter did not match that of the pure halide (5.44 Å).

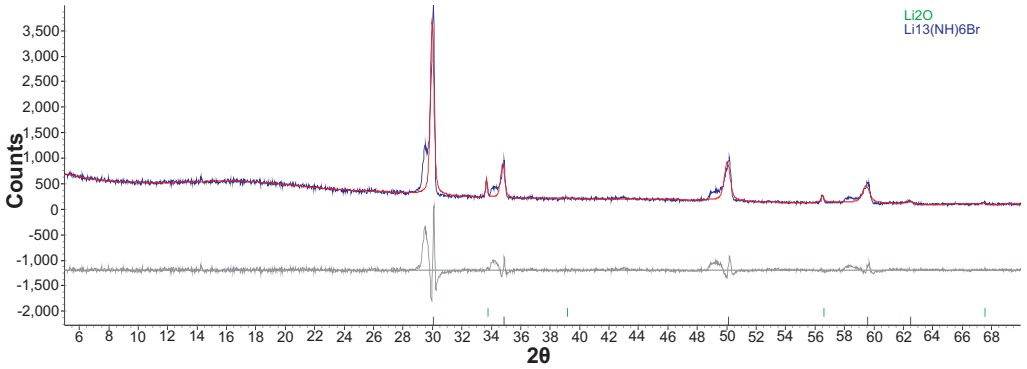

Figure 3.51: Powder X-ray diffraction pattern of $Li_{13}(NH)_6Br$ made by reaction of $6Li_2NH$ + LiBr at 400 °C for twelve hours, showing observed (blue), calculated Pawley fit (red) and difference (grey) plots. Peak positions for $Li_{13}(NH)_6Br$ are shown (blue).

In the case of the mixed lithium magnesium imide-chlorides, reaction of Li_2NH with $MgBr_2$ at 400 °C (fig. 3.52) gave two distinct face centred cubic Li_2NH-like phases with space group $Fm\bar{3}m$ and lattice parameters a = 5.0578(8) å and 5.0739(8) Å. The separation between these two distinct phases can be seen more clearly in figure 3.53, highlighted by the black and green check marks. Alongside these two new phases is a larger cubic phase with space group $Fd\bar{3}m$ and lattice parameter a = 10.6573(9) Å.

The products formed from the decomposition of $Li_7(NH_2)_6Br$ with LiH heated to 400 °C match closely those formed directly from Li_2NH, fitting to the same $Fm\bar{3}m$ unit cell. As is the case with the imide-chlorides (chapter 3.4.1), the product formed *via* the reaction of the amide-bromide with LiH appeared more distinct than that formed form Li_2NH, with sharper, more symmetrical peaks. From this a more accurate lattice parameter of a = 5.398(3) Å could be obtained.

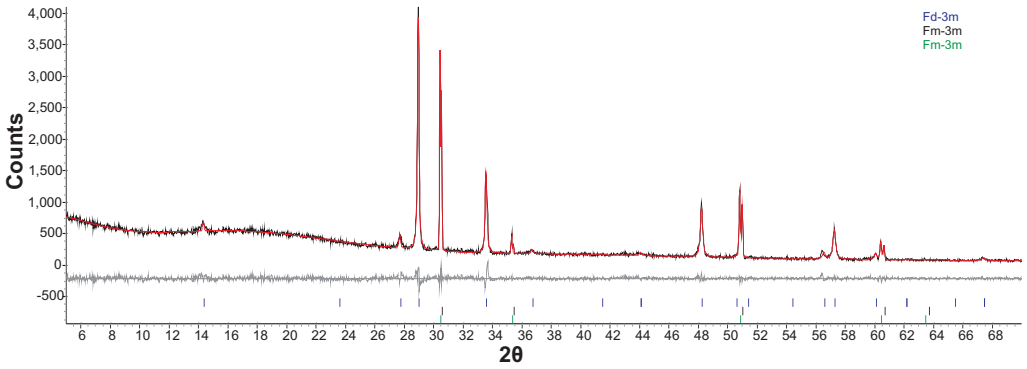

Figure 3.52: Powder X-ray diffraction pattern of $Li_{12}Mg_{0.5}(NH)_6Br$ made by reaction of $6Li_2NH + 1/2MgBr_2$ at 400 °C for twelve hours, showing observed (black), calculated Pawley fit (red) and difference (grey) plots. Peak positions for the $Fd\bar{3}m$ cell are also shown (blue) and for the $Fm\bar{3}m$ cell (black).

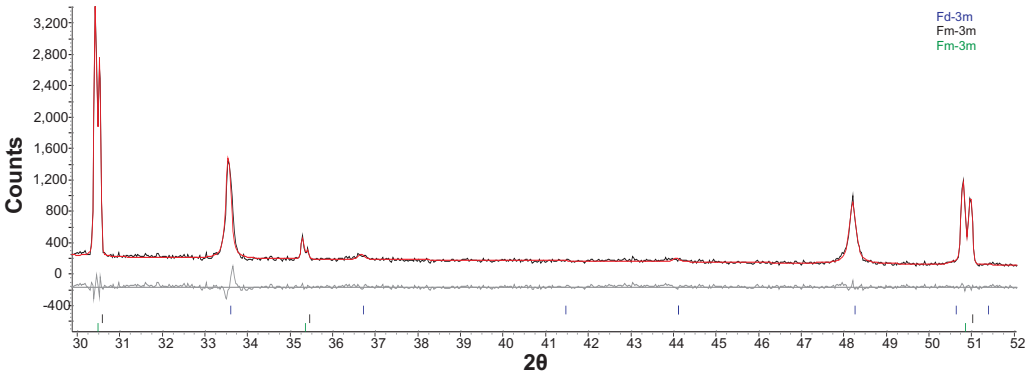

Figure 3.53: Powder X-ray diffraction pattern of $Li_{12}Mg_{0.5}(NH)_6Br$ made by reaction of $6Li_2NH + 1/2MgBr_2$ at 400 °C for twelve hours, showing observed (black), calculated Pawley fit (red) and difference (grey) plots. Peak positions for the $Fd\bar{3}m$ cell are also shown (blue) and for the $Fm\bar{3}m$ cell (black).

There was however, a significant amount of Li_2NH formed from this reaction, which was not seen in the products formed directly from Li_2NH (fig. 3.51). This may suggest a different stoichiometry in the imide-bromide phase compared to the amide-bromide, which could have an effect on the products from rehydrogenation attempts of the imide-bromide discussed later (chapter 4.4).

The products formed *via* the reaction of $Li_6Mg_{0.5}(NH_2)_6Br$ with LiH heated to 400 °C are shown in figure 3.55. They match closely to those seen from the reaction of Li_2NH and $MgBr_2$, forming a cubic phase with space group $Fd\bar{3}m$ and

lattice parameter $a = 10.7668(3)$ Å. However, where as the products made from direct reaction of Li_2NH with $MgBr_2$ showed two distinct, smaller cubic phases of space group $Fm\bar{3}m$ and lattice parameter of $a = 5.0578(1)$ å and 5.0739(1) Å, here only one phase was seen to form with lattice parameter $a = 5.0621(1)$ Å.

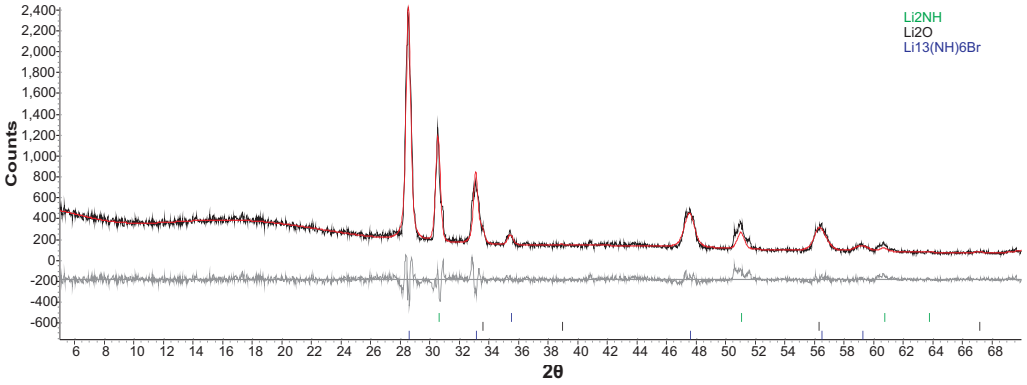

Figure 3.54: Powder X-ray diffraction pattern of the products of the reaction of $Li_7(NH_2)_6Br + 6LiH$ at 400 °C, showing observed (black), calculated Pawley fit (red) and difference (grey) plots. Peak positions for $Li_{13}(NH)_6Br$ are shown in blue.

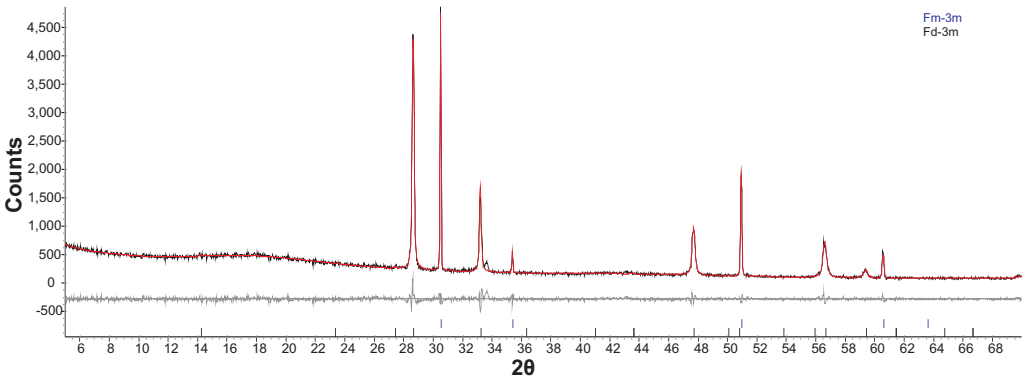

Figure 3.55: Powder X-ray diffraction pattern of the products of the reaction of $Li_6Mg_{0.5}(NH_2)_6Br + 6LiH$ at 400 °C, showing observed (black), calculated Pawley fit (red) and difference (grey) plots. Peak positions for the $Fm\bar{3}m$ unit cell are shown in blue while those of the $Fd\bar{3}m$ are shown in black.

3.6.2 Investigations into a solid solution

It was seen earlier that the amide-bromide phase, $Li_7(NH_2)_6Br$, can accommodate a range of non-stoichiometry, increasing the amount of NH_2^- ions present and reducing the amount of Br^- ions, although the materials of the form $Li_7(NH_2)_{6+x}Br_{1-x}$ formed alongside $LiNH_2$ so the exact amount of non-stoichiometry was unknown. In this section the materials synthesised previously (chapter 3.5.5) were heated with LiH and the products analysed.

It was seen in the previous section (chapter 3.6.1) that a distinct imide-bromide phase was formed but alongside significant amounts of Li_2NH (fig. 3.54). It is seen that reactions of the type $Li_7(NH_2)_{6+x}Br_{1-x} + (6+x)LiH$ form an imide-bromide phase and Li_2NH, however, the amount of Li_2NH was significantly increased from the $x = 0$ reaction. The imide-bromide phase was also significantly less crystalline than the Li_2NH.

The figures below show the products for the reactions for values of $x = 0.2$ and 0.3 (fig. 3.56 and 3.57, respectively). The lattice parameters for the imide-bromide products in these reactions are $a = 5.325(1)$ Å and $a = 5.316(1)$ Å; this is compared to the value of $a = 5.398(1)$ Å for $x = 1$. While the poor crystallinity of these samples makes accurate lattice parameters difficult to obtain, the values given here show a decrease in the unit cell size. This suggests that there is an increase in the amount of NH_2^- present in the material as it is smaller than the Br^- ion.

3.7 Amide-iodides: $xLiNH_2$ + $yLiI$ or $(y/2)MgI_2$

3.7.1 Synthesis

Lithium amide and lithium iodide were ground together at molar ratios between 1:1 and 4:1 and heated at temperatures between 100 and 400 °C. No reaction was seen below 100 °C but at temperatures higher than this a new phase was seen to

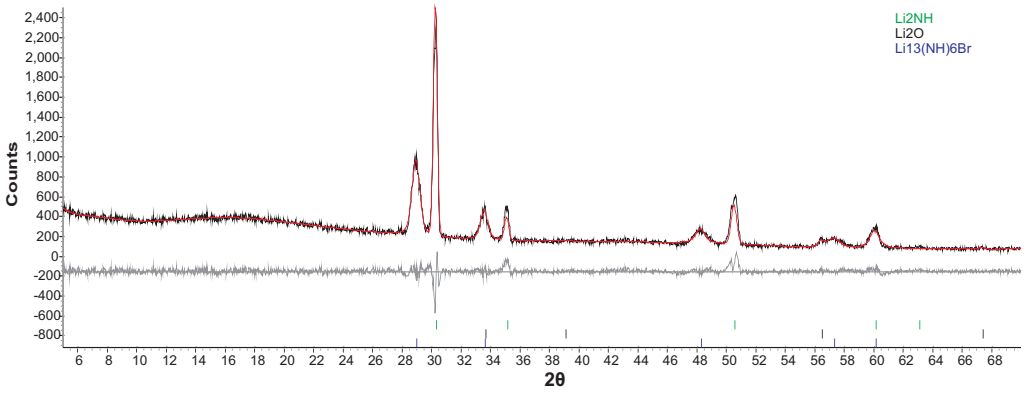

Figure 3.56: Powder X-ray diffraction pattern of the products of the reaction of $Li_7(NH_2)_{6.2}Br_{0.8}$ + 6.2LiH at 400 °C, showing observed (black), calculated Pawley fit (red) and difference (grey) plots. Peak positions for $Li_{13}(NH)_6Br$ are shown in blue.

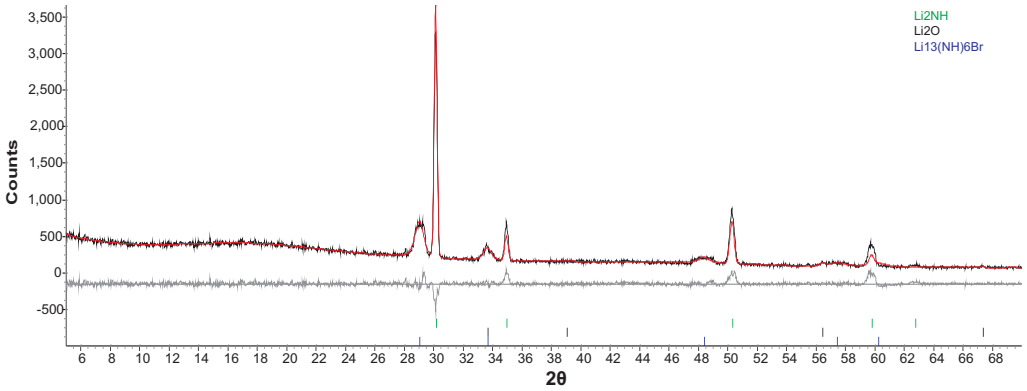

Figure 3.57: Powder X-ray diffraction pattern of the products of the reaction of $Li_7(NH_2)_{6.3}Br_{0.7}$ + 6.3LiH at 400 °C, showing observed (black), calculated Pawley fit (red) and difference (grey) plots. Peak positions for $Li_{13}(NH)_6Br$ are shown in blue.

be formed.

The synthesis of a lithium amide-iodide, $Li_3(NH_2)_2I$, by mechanical milling and subsequent heat treatment has been reported [84]. Reactions of $2LiNH_2$ + LiI, heated at 2 °C min^{-1} to 150 °C for twelve hours gave rise to a hexagonal phase which matched the reported structure of $Li_3(NH_2)_2I$ [84]. This phase is hexagonal with space group of $P6_3mc$ with lattice parameters a = 7.0903(9) Å and c = 11.492(3) Å; the diffraction pattern for this phase is shown below (fig. 3.58).

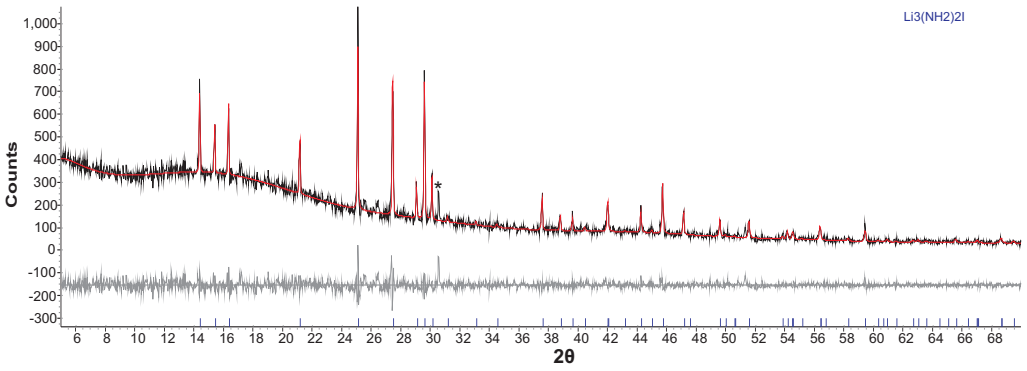

Figure 3.58: Powder X-ray diffraction pattern of $Li_3(NH_2)_2I$ made by reaction of $2LiNH_2$ + LiI at 150 °C for twelve hours, showing observed (black), calculated Pawley fit (red) and difference (grey) plots. Peak positions for $Li_3(NH_2)_2I$ are shown (blue) and the main $LiNH_2$ peak is highlighted(*).

In the case of reaction between lithium amide and magnesium iodide, molar ratios were again chosen so as to maintain the NH_2^- to I^- ratios similar to the equivalent purely lithium reaction. The reaction of $2LiNH_2$ + $1/2MgI_2$, heated at 2 °C min^{-1} 200 °C for 12 hours formed a similar unit cell to that of the purely lithium equivalent. This phase has the space group $P6_3mc$ with lattice parameters a = 7.0650(6) Å and c = 11.521(3); a Pawley fit to the data based on this unit cell is shown in figure 3.59.

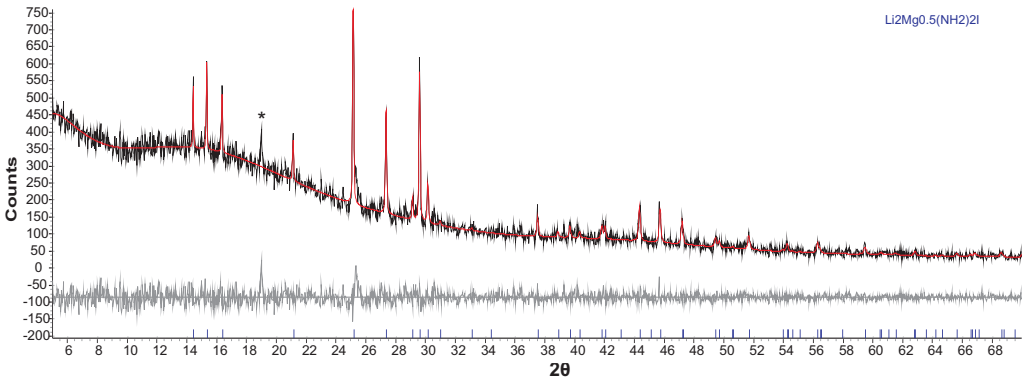

Figure 3.59: Powder X-ray diffraction pattern of hexagonal $Li_2Mg_{0.5}(NH_2)_2I$ made by reaction of $2LiNH_2$ + MgI_2 at 200 °C for twelve hours, showing observed (black), calculated Pawley fit (red) and difference (grey) plots. Peak positions for $Li_3(NH_2)_2I$ are shown (blue) and an impurity peak is highlighted (*).

3.7.2 Raman Spectroscopy

As with the previous sections, Raman spectroscopy was performed on these samples to check that the new phases contained purely NH_2^- groups and not NH^{2-} imide groups as discussed earlier (chapter 3.3.2).

The Raman spectra of the two new phases formed in this section are below (fig. 3.60), along with the peak positions of $LiNH_2$ and Li_2NH from figure 3.6. The peaks for both of these amide-iodide phases clearly shows that the phases contain NH_2^-, although the spectrum for $Li_3(NH_2)_2I$ (fig. 3.60a) does show a small broad peak which could be indicative of an NH^{2-} stretch.

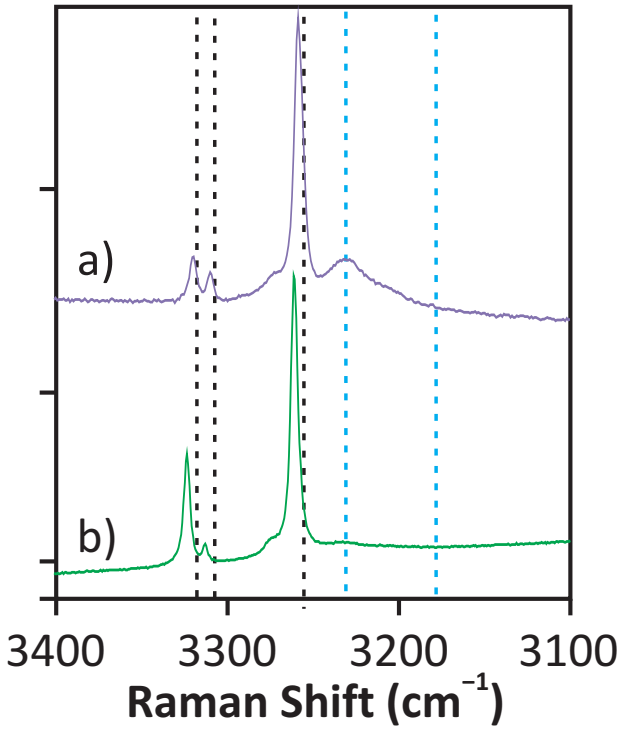

Figure 3.60: Raman spectra of (a) $Li_3(NH_2)_2I$, (b) $Li_2Mg_{0.5}(NH_2)_2I$. Peak positions highlighted by black ($LiNH_2$) and blue (Li_2NH) dotted lines.

3.7.3 Crystal Structure Investigation - $Li_3(NH_2)_2I$

The crystal structure of the amide-iodide, $Li_3(NH_2)_2I$, is published in the literature as a hexagonal unit cell, space group $P6_3mc$ and lattice parameters a =

7.09109 Å and $c = 11.50958$ Å [84]. This structure was used as the starting point for the refinement of this data.

The observed peak positions for this data were run through the indexing routine of the computer program Topas [108] and this confirmed the most likely assignment as a hexagonal unit cell with space group $P6_3mc$ (number 186), giving lattice parameters of $a = 7.08$ Å and $c = 11.45$ Å. A Pawley fit was carried out using these lattice parameters and gave the refined values of $a = 7.0903(9)$ Å and $c = 11.492(3)$ Å. This gives a unit cell volume of 500.4(1) Å^3, roughly 0.16 % smaller than the published cell volume. This Pawley fit to the data is shown in figure 3.58 and gave statistical values of $R_{wp} = 8.934$, $R_{exp} = 7.942$ and $\chi^2 = 1.265$.

The published crystal structure has a value of $Z = 4$ [84], this can be confirmed by analysis of the formula unit cell volumes of the starting materials. A single $LiNH_2$ forumla unit has a volume of 32.60 Å^3, while LiI is 54.70 Å^3, assuming these stayed approximately the same, this gives a volume of one formula unit of $Li_3(NH_2)_2I$ of 119.90 Å^3. For a unit cell volume of 500.4 Å^3 this gives a value of $Z = 4.16$ and a crystallographic density of 1.43 g cm^{-3}.

Using the published atomic positions shown in table 3.9 a pseudo-Rietveld refinement was run to data, refining the lattice parameters, background and peak shape functions but with fixed atomic positions and occupancies. Figure 3.61 and shows a good fit to the data with a statistical values of $R_{wp} = 10.564$ % and $\chi^2 = 1.626$.

These atomic positions were first tested in different sites of the same multiplicity; once it had been confirmed that they were in the correct sites they were allowed to refine. They were at first allowed to refine freely; in the case of the iodine, nitrogen and lithium atoms, they refined quickly to positions very close to the literature values. The hydrogen atoms were added in as a NH_2^- rigid body which was allowed to rotate.

The atomic positions for this refinement changed slightly from the literature

Table 3.9: Literature crystallographic data for $Li_3(NH_2)_2I$ [84]

Atom	Site	x	y	z	Occupancy
I1	2b	1/3	2/3	0.9264	1
I2	2b	1/3	2/3	0.5505	1
N1	2a	0	0	0.5140	1
N2	6c	0.1775	0.8225	0.2571	1
H1	6c	0.0737	0.1474	0.4789	2/3
H2	6c	0.1705	0.3410	0.1773	1
H3	6c	0.1056	0.2112	0.2526	1
Li1	6c	0.8929	0.1071	0.3792	1
Li2	6c	0.8662	0.1338	0.1733	1

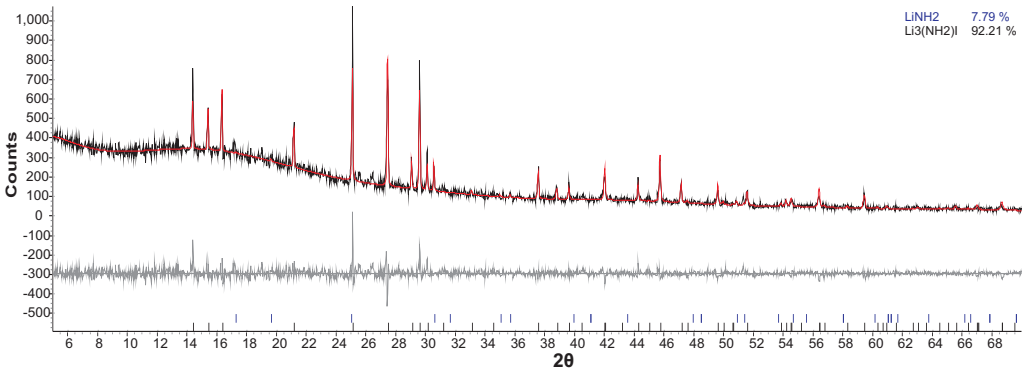

Figure 3.61: Powder X-ray diffraction pattern of $Li_3(NH_2)_2I$ made by reaction of $2LiNH_2$ + LiI at 150 °C for twelve hours, showing observed (black), calculated Rietveld fit from the published structure [84](red) and difference (grey) plots. Peak positions for $Li_3(NH_2)_2I$ are shown (black).

values and statistical values of $R_{wp} = 9.767$ % and $\chi^2 = 1.545$ were obtained (fig. 3.62). However, the error values (3 ESDs) obtained from this data were too high to say that the structural model produced from this work is significantly different from the published structure.

3.7.4 Crystal Structure Investigation - $Li_2Mg_{0.5}(NH_2)_2I$

In the case of the mixed lithium-magnesium amide-iodide, $Li_2Mg_{0.5}(NH_2)_2I$, a similar unit cell was seen to that of the purely lithium system. The observed peak positions from the X-ray diffraction pattern of $Li_2Mg_{0.5}(NH_2)_2I$ were run through the computer program Topas. This confirmed the most likely assignment

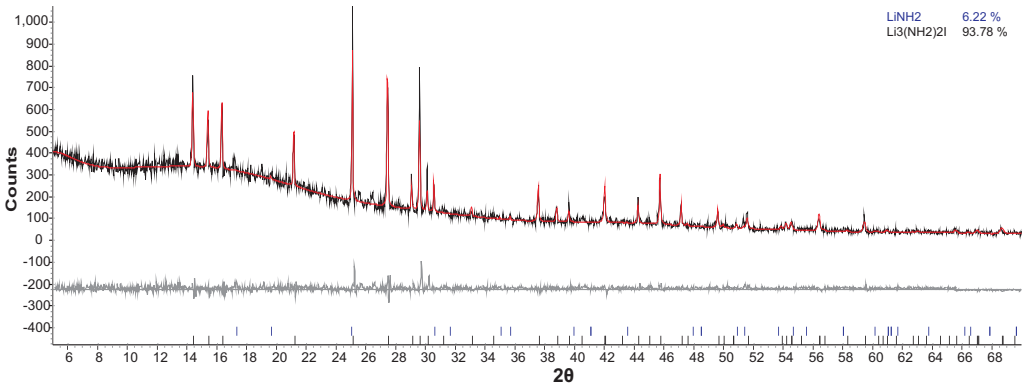

Figure 3.62: Powder X-ray diffraction pattern of $Li_3(NH_2)_2I$ made by reaction of $2LiNH_2$ + LiI at 150 °C for twelve hours, showing observed (black), calculated Rietveld fit from the refined structure (red) and difference (grey) plots. Peak positions for $Li_3(NH_2)_2I$ are shown (black).

of a hexagonal unit cell, space group $P6_3mc$ (number 186) with lattice parameters $a = 7.06$ Å and $c = 11.51$ Å. These lattice parameters were then refined in Topas *via* a Pawley fit; more accurate lattice parameters of $a = 7.0650(9)$ Å and $c = 11.521(1)$ Å were found, giving a cell volume of 497.4(1) Å^3, slightly smaller (around 1.4 %) larger than the purely lithium system. This Pawley fit gave a statistical values of $R_{wp} = 8.839$, $R_{exp} = 7.733$ and $\chi^2 = 1.306$.

The published structure for $Li_3(NH_2)_2I$ was used as the starting point for this refinement [84]. This structure (table 3.9) with no magnesium atoms added, gave a good fit to the data, with $R_{wp} = 10.338$ %. The magnesium atoms were then added into the structure, tested separately on the two lithium sites and then tested on both sites together. The statistics improved slightly for all three possibilities; the best were achieved by replacing half of the lithium ions from the Li1 site with half as many magnesium atoms, although it is possible that the magnesium atoms are disordered across the two lithium sites. The diffraction pattern for this best fit is shown in figure 3.63 and gave statistical values of $R_{wp} = 10.009$ and $\chi^2 = 1.633$. A structural representation of this material, based on the literature structure is shown in figure 3.64 [84].

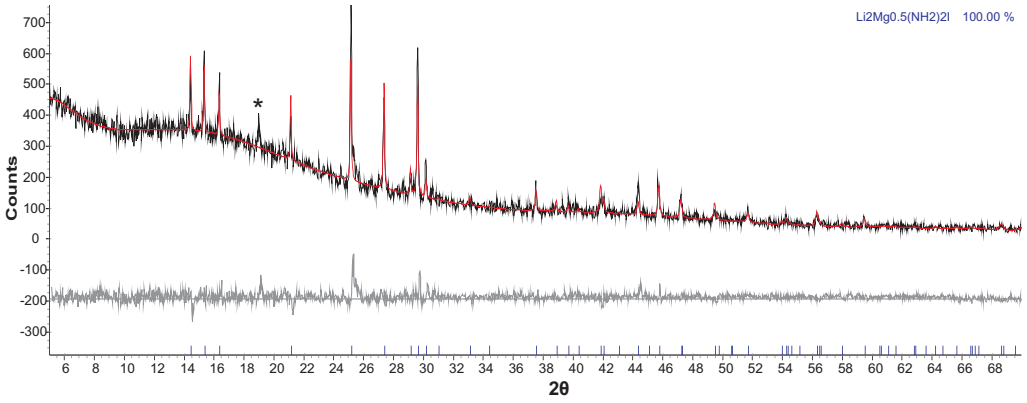

Figure 3.63: Powder X-ray diffraction pattern of $Li_2Mg_{0.5}(NH_2)_2I$ made by reaction of $2LiNH_2$ + $1/2MgI_2$ at 200 °C for twelve hours, showing observed (black), calculated Rietveld fit from the refined structure (red) and difference (grey) plots. Peak positions for $Li_2Mg_{0.5}(NH_2)_2I$ are shown (blue).

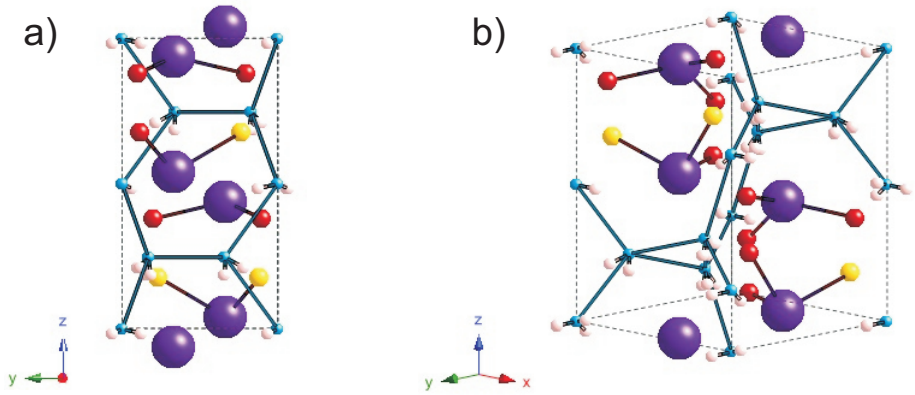

Figure 3.64: Crystal structure of $Li_2Mg_{0.5}(NH_2)_2I$, in a) the x direction and b) the (111) direction. Showing the iodine (purple), nitrogen (blue), lithium (red), magnesium (yellow) and hydrogen (white) atoms. The unit cell is shown as a black dotted line.

3.7.5 Investigations into a solid solution

As in previous sections with the chloride (chapter 3.3.6) and the bromide (chapter 3.5.5) systems, the amide-iodide material was investigated for any non-stoichiometry which could lower the amount of halide present, therefore maximising the gravimetric hydrogen storage capacity, while maintaining any improved hydrogen storage properties. Reactions of the stoichiometries $(2 + x)\mathrm{LiNH_2} + (1 - x)\mathrm{LiI}$ were performed with values of $x = 0$ - 0.5, these mixtures were heated at 150 °C for twelve hours to attempt to make phases of the form $\mathrm{Li_3(NH_2)_{2+x}I_{1-x}}$.

Figure 3.65 shows the cell volume of the amide-iodide product for values of x between 0 and 0.5. It can be seen that there is, within error (3 ESD's), no systematic variation in the cell volume of the amide-iodide formed from these reactions. The values associated with the graph may be found in appendix table A.4. Analysis of the diffraction patterns of the products from these reactions show both $\mathrm{Li_3(NH_2)_2I}$ and $\mathrm{LiNH_2}$ present, where the value of x is greater than zero; the diffraction pattern for the reaction where $x = 0.3$ is shown in figure 3.66.

3.8 Imide-iodides: $\mathbf{xLi_2NH + yLiI}$ or $\mathbf{(y/2)MgI_2}$

3.8.1 Synthesis

As in previous sections, $\mathrm{Li_2NH}$ was used to prepare both pure lithium and mixed lithium-magnesium imide-iodides through reaction with lithium and magnesium iodide at 400 °C. Reaction stoichiometries were selected to match the nitrogen to halide ratio of the amide-halides prepared in section 3.7.1. As we shall see, equivalent reactions were performed from the reaction of the amide-iodides with LiH, the products of which will be discussed here.

The reactions of $\mathrm{Li_2NH}$ with LiI and $\mathrm{MgI_2}$ at 400 °C formed new, distinct face centred cubic phases with space group $Fd\bar{3}m$ with lattice parameters $a =$

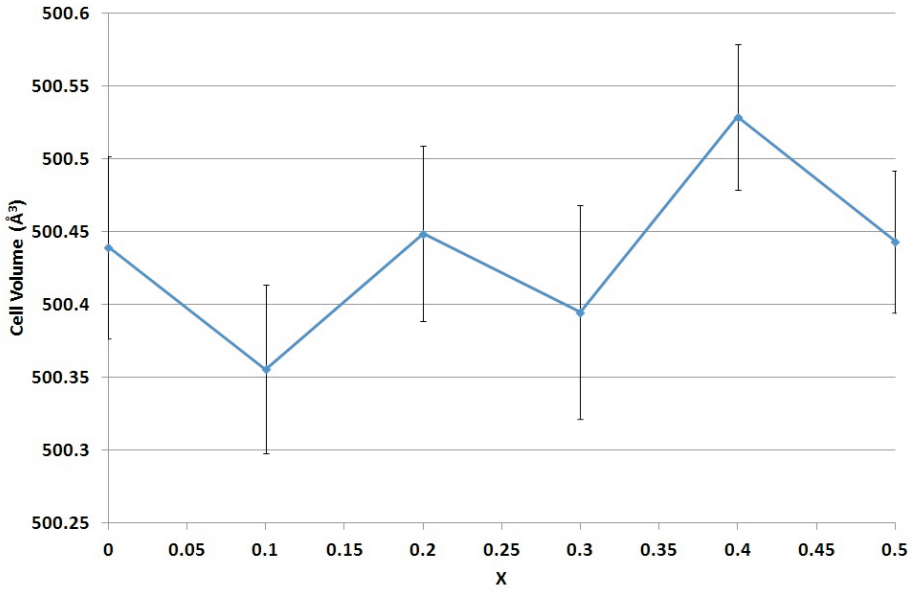

Figure 3.65: Graph showing the change in cell volume for $Li_3(NH_2)_2I$ from reactions of $(2+x)LiNH_2$ + $(1-x)$LiI.

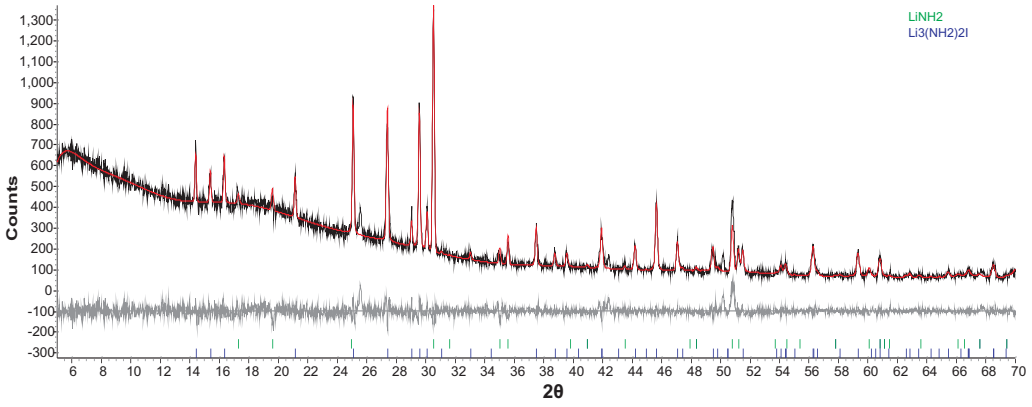

Figure 3.66: Powder X-ray diffraction pattern of the products from reaction of $2.3LiNH_2$ with 0.7LiI heated at 150 °C for 12 hours, showing observed (black), calculated Pawley fit (red) and difference (grey) plots. Peak positions for $Li_3(NH_2)_2I$ (blue) and $LiNH_2$ (green) are shown.

10.193(3) Å and 10.198(5) Å, respectively, alongside some remaining Li_2NH. The diffraction patterns for these products are shown figures 3.67 and 3.68.

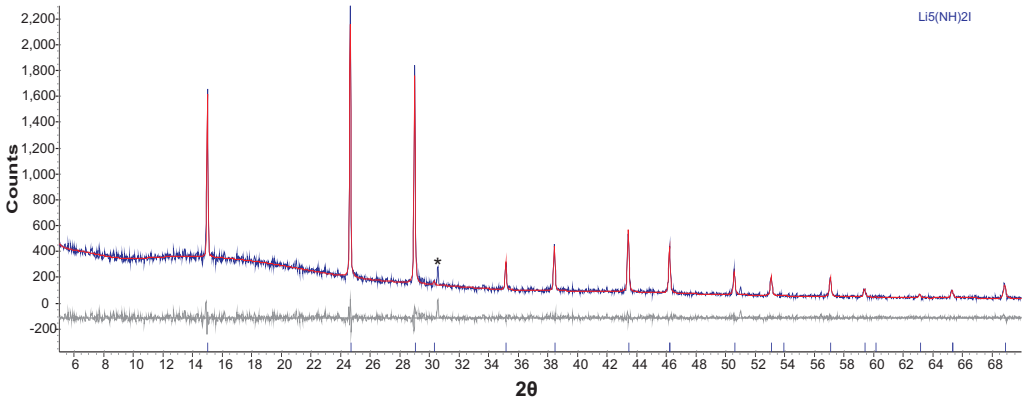

Figure 3.67: Powder X-ray diffraction pattern of $Li_5(NH)_2I$ made by reaction of $2Li_2NH$ + LiI at 400 °C for twelve hours, showing observed (blue), calculated Pawley fit (red) and difference (grey) plots. Peak positions for $Li_5(NH)_2I$ are shown (blue) and the main Li_2NH peak is highlighted (*).

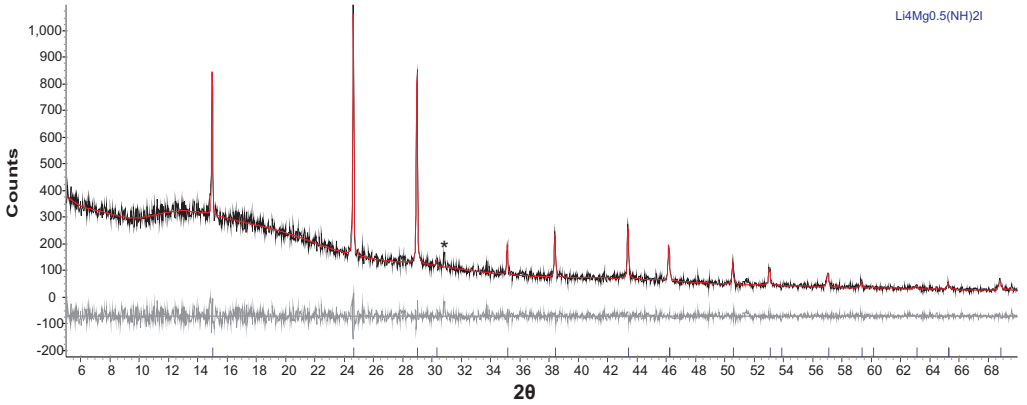

Figure 3.68: Powder X-ray diffraction pattern of $Li_4Mg_{0.5}(NH)_2I$ made by reaction of $2Li_2NH$ + $1/2MgI_2$ at 400 °C for twelve hours, showing observed (black), calculated Pawley fit (red) and difference (grey) plots. Peak positions for $Li_4Mg_{0.5}(NH)_2I$ are shown (blue) and the main Li_2NH peak is highlighted (*).

The products formed from the decomposition of $Li_3(NH_2)_2I$ and $Li_2Mg_{0.5}(NH_2)_2I$ with LiH, heated to 400 °C showed a good resemblance to those products formed directly from Li_2NH and a good fit to the same $Fd\bar{3}m$ unit cell. The products from these reactions had lattice parameters of $a = 10.194(6)$ Å and $a = 10.199(4)$

Å, respectively (fig. 3.69).

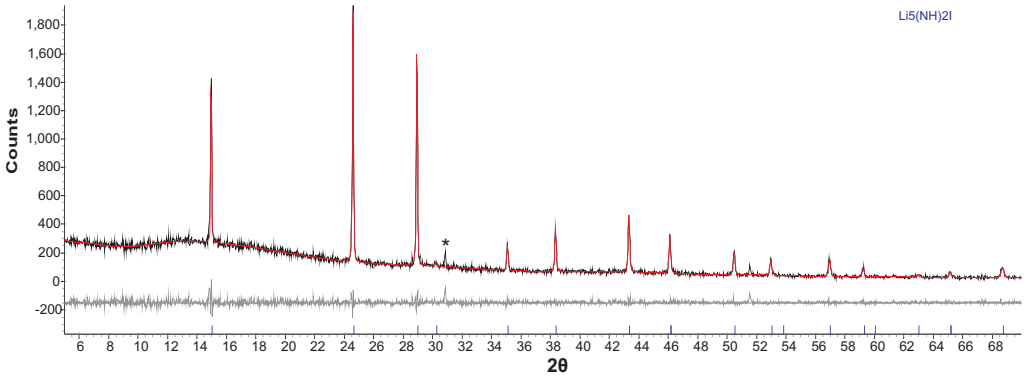

Figure 3.69: Powder X-ray diffraction pattern of $Li_5(NH)_2I$ made by reaction of $Li_3(NH_2)_2I$ + 2LiH at 400 °C, showing observed (black), calculated Pawley fit (red) and difference (grey) plots. Peak positions for $Li_5(NH)_2I$ are shown (blue) and the main Li_2NH peak is highlighted (*).

3.8.2 Crystal Structure Investigation - $Li_5(NH)_2I$

The crystal structure of $Li_5(NH)_2I$ was investigated with powder synchrotron X-ray diffraction data (Diamond, I11) neutron data (ISIS, I11). Unfortunately, this sample had significant impurity peaks and for this reason the basic structural model was obtained from laboratory X-ray data of a pure sample before the lattice parameters and atomic positions were refined using the synchrotron data.

The observed peak positions from the laboratory X-ray diffraction pattern of $Li_5(NH)_2I$ were run through the indexing routine of the computer program Topas[108]. This gave the most likely assignment as a cubic unit cell with space group $Fd\bar{3}m$ (number 227) with lattice parameter a = 10.19 Å. A Pawley fit against this data gave a more accurate lattice parameter of a = 10.193(3) Å, giving a cell volume of 1058.99(9) Å^3 with a statistical value of R_{wp} = 8.223 %. This unit cell was also refined against the neutron diffraction data .

The unit cell volume of Li_2NH is 130.65 Å^3 [102], with a value of Z = 4, this gives one formula unit of Li_2NH a volume of 32.66 Å^3. In the case if LiI, the cell volume is 218.79 Å^3 [111], giving one formula unit a volume of 54.70 Å^3.

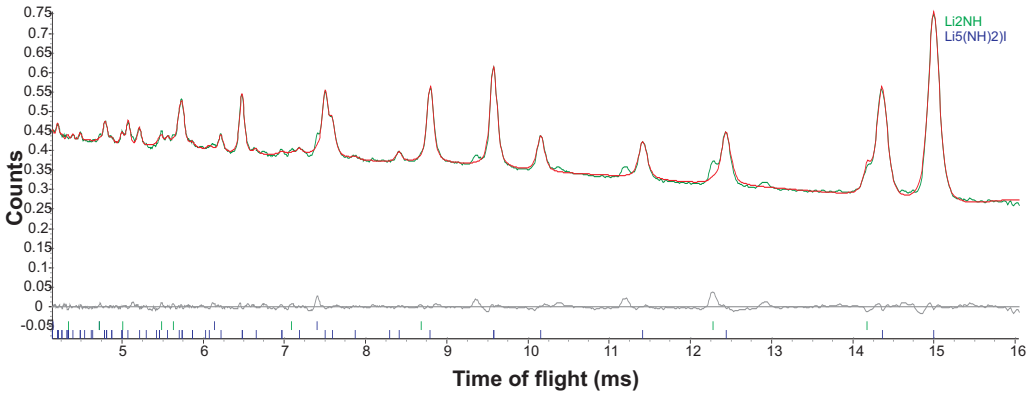

Figure 3.70: Powder neutron diffraction pattern showing a Pawley fit to the hexagonal $Li_5(NH)_2I$. Showing observed (green), calculated Pawley fit (red) and different (grey) plots; peak positions for $Li_5(NH)_2I$ are shown (blue).

Assuming that the formula unit volumes are approximately equal to those of the starting materials, then one formula unit of the imide-iodide, $Li_5(NH)_2I$, would have a volume of 120.02 Å^3. Given that the unit cell has a cell volume of 1058.99 Å^3 obtained from the Pawley fit, this gives a value of $Z = 8.82$. The allowed multiplicities for the space group $Fd\bar{3}m$ can be seen in table 3.10; these show that a value of $Z = 8$ is sensible and this value gives a realistic crystallographic density of 1.45 cm g^{-1}.

Table 3.10: Special positions available for the space group $Fd\bar{3}m$ (No. 277).

Multiplicity	Wyckoff letter	Site symmetry	Coordinates
192	i	1	(x,y,z)
96	h	2	$(\frac{1}{8}$,y,y+$\frac{1}{4})$
96	g	m	(x,x,z)
48	f	2mm	(x,0,0)
32	e	3m	(x,x,x)
16	d	-3m	$(\frac{5}{8},\frac{5}{8},\frac{5}{8})$
16	c	-3m	$(\frac{1}{8},\frac{1}{8},\frac{1}{8})$
8	b	-43m	$(\frac{1}{2},\frac{1}{2},\frac{1}{2})$
8	a	-43m	(0,0,0)

The first atom to be added to the model was iodine. As eight iodine ions will be required to be in the unit cell these were first tested in the 8a and 8b sites, with full occupancy. It was clear that the iodine ions sit on the 8a site and

when they were allowed to refine the atomic coordinates refined quickly towards zero. The nitrogen atoms were then introduced to the model; sixteen nitrogen ions are required for the unit cell for $Z = 8$. The nitrogen atoms were allowed to refine freely and the atomic coordinates refined to between values of 0.5 and 0.7. To maintain the appropriate multiplicity the nitrogen atoms were fixed on the 16d site with coordinates of 0.625 (5/8); this gave a good fit to the data both visually and statistically. To maintain the correct multiplicity for the unit cell forty lithium atoms are required. These atoms were allowed to refine freely and all the coordinates refined towards a value of approximately 0.4. Following this the lithium atoms were fixed to a 32e (x,x,x) position with full occupancy and the x parameter was allowed to refine; this refined to a stable position with $x = 0.39$. To maintain the correct stoichiometry for the unit cell a second lithium site was added. Refinements with lithiums on the 8b (1/2,1/2,1/2) site, fully occupied, gave an improvement to the visual and statistical fit. The final atoms to be added to the model were the hydrogen atoms. Due to the poor X-ray scattering of hydrogen atoms these were introduced as NH^{2-} rigid bodies, maintaining an N-H bond length of 1.0 Å. These rigid bodies were placed on the nitrogen positions and allowed to rotate freely. This model was then used with the synchrotron X-ray and neutron diffraction data to refine the lithium and hydrogen positions to more accurate values.

Once this good structural model had been formed a full Rietveld refinement was performed in Topas by refining a zero point error, a pseudo-Voigt peak shape (6 parameters) and a Chebyshev background function (16 parameters). The final Rietveld plot against the synchrotron data and laboratory data are shown in figures 3.71 and 3.72 respectively; the Rietveld plot against the neutron data is shown in figure 3.73. The resultant crystal structure is shown figure 3.74 and the refined crystallographic data are shown in table 3.11.

The geometries around the lithium (Li2) and iodine sites within the crystal structure of $Li_5(NH)_2I$ are shown in figure 3.75. It can be seen that the lithium

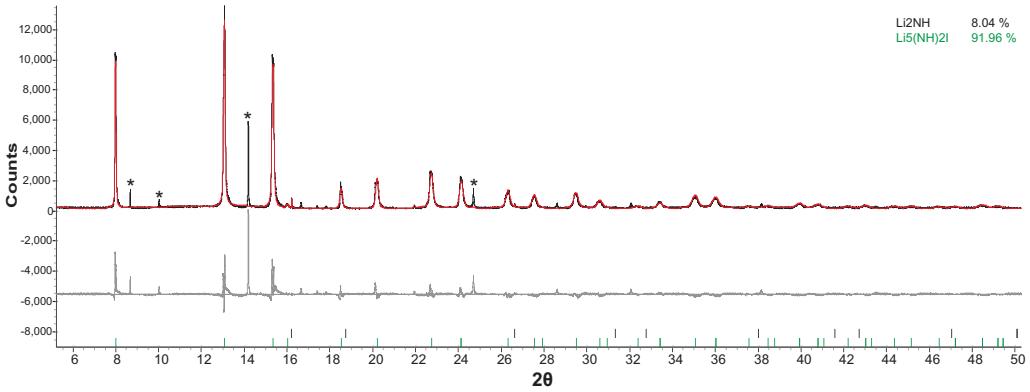

Figure 3.71: Rietveld refinement against powder synchrotron X-ray diffraction pattern data of the $Li_5(NH)_2I$ phase, showing observed (black), calculated Rietveld fit (red) and difference (grey) plots. Peak positions for $Li_5(NH)_2I$ are shown (green) and impurity peaks are highlighted (*).

Table 3.11: Refined crystallographic data for $Li_5(NH)_2I$

Atom	Site	x	y	z	Occupancy
I	8a	0	0	0	1
N	16d	0.625	0.625	0.625	1
Li1	32e	0.383(1)	x	x	1
Li2	8b	0.5	0.5	0.5	1
H	32e	0.57(2)	x	x	$\frac{1}{2}$

Space group $Fd\bar{3}m$ (no. 277), $a = 10.193(3)$ Å
X-ray data = $R_{wp} = 8.900$ %, $R_{exp} = 7.533$ %, $\chi^2 = 1.397$
Neutron data = $R_{wp} = 2.286$ %, $R_{exp} = 1.017$ %, $\chi^2 = 5.054$

atoms (Li2) sit in a tetrahedron with four nitrogen atoms (fig. 3.75a). This tetrahedron has four equal bond lengths of 2.31(2) Å and bond angles of 109.4(3)°. The N-H bond length has been refined to 1.05(9) Å. The iodine atoms are seen to also have a tetrahedral coordination with four lithium atoms (Li1). Here there are four equal bond lengths of 2.35(3) Å and bond angles of 109.4(3)°.

3.8.3 Crystal Structure Investigation - $Li_4Mg_{0.5}(NH)_2I$

The mixed lithium-magnesium imide-iodide, $Li_4Mg_{0.5}(NH)_2I$, formed a similar unit cell to that of the pure lithium equivalent. The observed peak positions from the X-ray diffraction pattern for $Li_4Mg_{0.5}(NH)_2I$ were run through the indexing routine of Topas, this confirmed the same space group of $Fd\bar{3}m$ with lattice

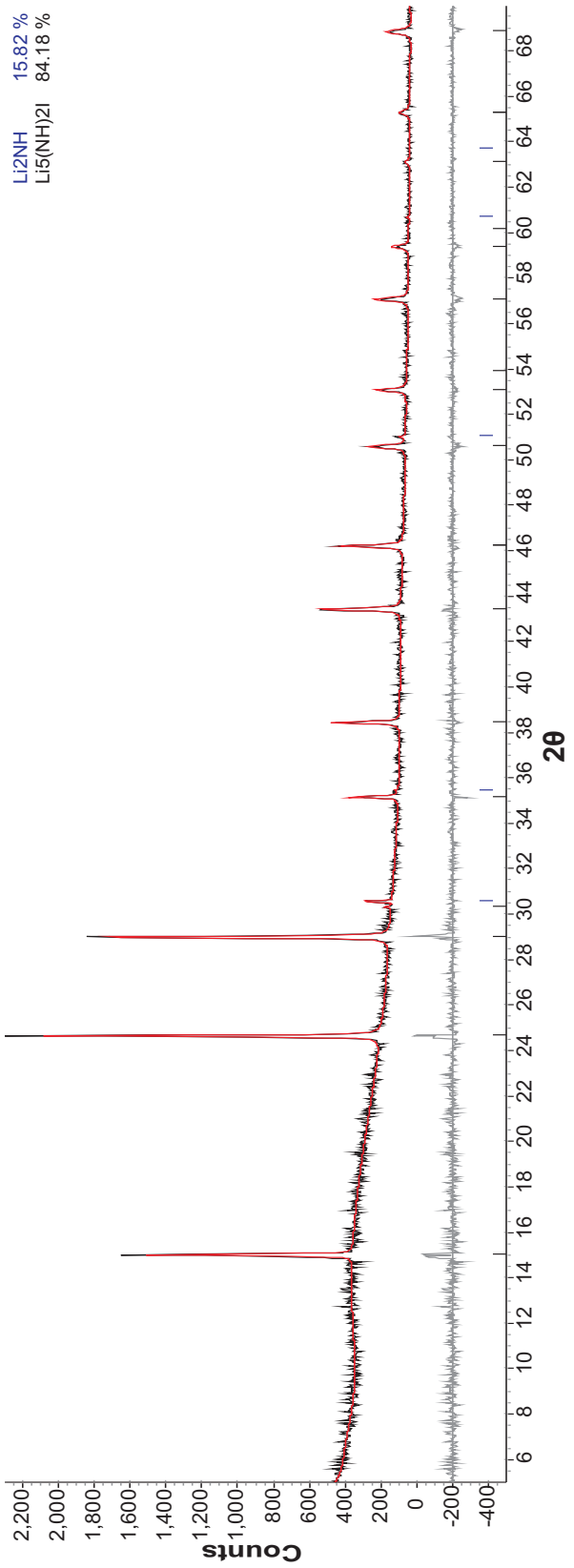

Figure 3.72: Powder X-ray diffraction pattern showing the final Rietveld refinement to $Li_5(NH)_2I$ phase; observed (black), calculated Rietveld fit (red) and difference (grey) plots and peak positions for $Li_5(NH)_2I$ (black) are shown.

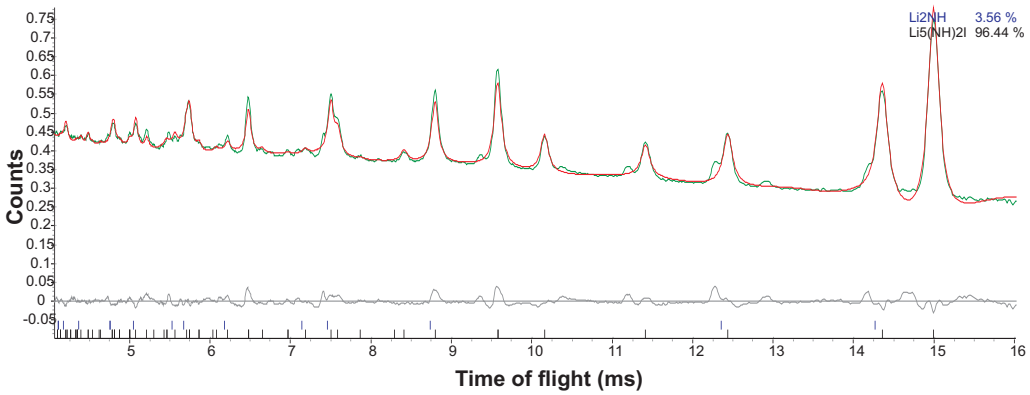

Figure 3.73: Powder neutron diffraction pattern showing the final Rietveld refinement to the cubic $Li_5(NH)_2I$ phase. Showing observed (green), calculated Pawley fit (red) and different (grey) plots; peak positions for $Li_5(NH)_2I$ are shown (purple).

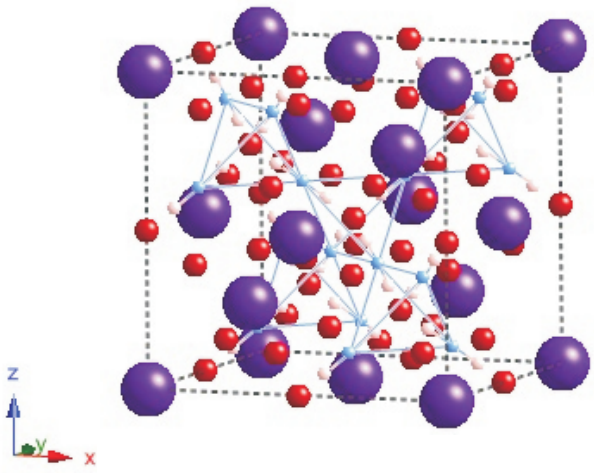

Figure 3.74: Crystal structure of cubic $Li_5(NH)_2I$ showing the iodine (purple), nitrogen (blue), lithium (red) and hydrogen (white) atoms. The unit cell is shown as a black dotted line.

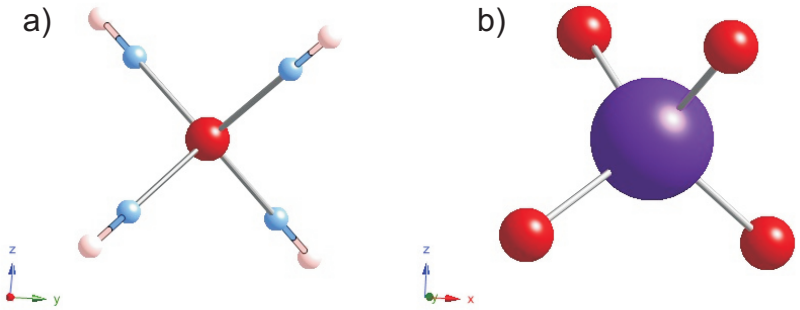

Figure 3.75: Diagram of the geometry around a) Li2 site and b) I site within cubic $Li_5(NH)_2I$ showing the iodine (purple), nitrogen (blue), lithium (red) and hydrogen (white) atoms.

parameter $a = 10.19$ Å. A Pawley refinement was carried out and gave a more accurate lattice parameter of $a = 10.198(5)$ Å with a cell volume of 1060.63 Å^3. This fit gave a statistical value of $R_{wp} = 8.995$ %.

The crystal structure determined for $Li_5(NH)_2I$ was used as the model for a refinement against these data and it gave a good visual and statistical fit. To achieve the correct atoms and stoichiometry for this cell, the occupancy of the lithium atoms was reduced by one fifth (8 atoms) and half as many magnesium atoms were placed on the same site. A full Rietveld refinement was carried out on this structure and the resultant fit to the data is shown in figure 3.76 and gave statistical values of $R_{wp} = 9.337$ %, $R_{exp} = 8.465$ and $\chi^2 = 1.228$.

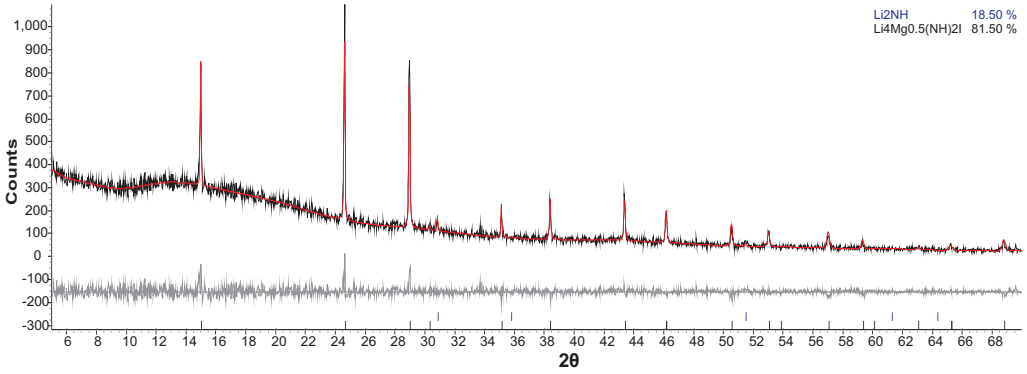

Figure 3.76: Rietveld refinement against powder X-ray diffraction data of the $Li_4Mg_{0.5}(NH)_2I$ phase, showing observed (black), calculated Rietveld fit (red) and difference (grey) plots. Peak positions for $Li_4Mg_{0.5}(NH)_2I$ are shown (black).

3.9 Conclusions

In this work the formation of lithium and mixed lithium/magnesium amide-halides was investigated. Amide-halides of the form $Li_{(1+n)}(NH_2)_nX$ and $Li_nMg_{0.5}(NH_2)_nX$ were synthesised from reaction of $LiNH_2$ and LiX or MgX_2; the compounds formed are summarised in table 3.12. Imide-halides of the form $Li_{(1+2n)}(NH)_nX$ and $Li_{2n}Mg_{0.5}(NH)_nX$ were synthesised both from Li_2NH with LiX or MgX_2 and from reaction of the equiavalent amide-halide with LiH; the imide-halides formed are summarised in table 3.13. Raman spectroscopy was used to probe the bonding in the NH_2^- and NH^{2-} anions within these structures. X-ray and neutron diffraction were used to investigate the crystal structures using the Reitveld refinement method and the computer program Topas. Work was also undertaken to investigate the lower solid solution limits of the amide- and imide-halides formed in this work to maximise the hydrogen storage content of the materials.

While this chapter has looked at the synthesis and characterisation of these materials, the following chapter will discuss the hydrogen storage properties of the same materials. Therefore further discussion of these materials will be found in chapter 4.7.

Molecular formula	Reaction conditions	Space group	a (Å)	c (Å)
$Li_4(NH_2)_3Cl$	400 °C	$R\bar{3}$	9.74487(9)	8.9365(3)
$Li_4(NH_2)_3Cl$	400°C, 1 hour	$I2_13$	10.4452(3)	-
$Li_3Mg_{0.5}(NH_2)_3Cl$	350°C	$I2_13$	10.4561(8)	-
$Li_7(NH_2)_6Br$	250°C	$R\bar{3}$	9.84893(9)	8.9845(3)
$Li_6Mg_{0.5}(NH_2)_6Br$	250°C	$R\bar{3}$	9.8111(6)	8.9556(6)
$Li_3(NH_2)_2I$	150°C	$P6_3mc$	7.0903(9)	11.492(3)
$Li_2Mg_{0.5}(NH_2)_2I$	200°C	$P6_3mc$	7.0650(6)	11.521(3)

Table 3.12: Summary of the amide-halide phases formed in this work. Reactions are for 12 hours unless stated otherwise.

Molecular formula	Reaction conditions	Space group	a (Å)	c (Å)
$Li_7(NH)_3Cl$	400°C	$Fm\bar{3}m$	5.157(3)	-
$Li_6Mg_{0.5}(NH)_3Cl$	400°C	$Pn\bar{3}$	5.137(3)	-
$Li_{13}(NH)_6Br$	400°C	$Fm\bar{3}m$	5.398(3)	-
$Li_{13}Mg_{0.5}(NH)_6Br$	400°C	$Fm\bar{3}m$	5.0578(8)	-
$Li_{13}Mg_{0.5}(NH)_6Br$	400°C	$Fd\bar{3}m$	10.6573(9)	-
$Li_5(NH)_2I$	400°C	$Fd\bar{3}m$	10.193(3)	-
$Li_4Mg_{0.5}(NH)_2I$	400°C	$Fd\bar{3}m$	10.198(5)	-

Table 3.13: Summary of the imide-halide phases formed in this work. Reaction times are 12 hours.

Chapter 4

Hydrogen Storage Properties of Amide- and Imide-Halides

4.1 Introduction

The thermal decomposition of lithium amide is known to release ammonia, but in reaction with LiH, hydrogen is released, forming first Li_2NH, then finally Li_3N. A reduction in the temperature of hydrogen release is seen when using magnesium amide, where ammonia is released, reacting quickly with LiH to form a mixed lithium-magnesium amide [104, 105].

As mentioned in the previous chapter (3.1), lithium ion mobility has been highlighted as a key factor in the structural transformation between $LiNH_2$ and Li_2NH *via* a solid solution of the form $Li_{(1+x)}NH_{(2-x)}$ [52]. A patent from 1983 showed that a series of lithium imide-halides could be synthesised with significant ionic mobility at room temperature, although lower than pure Li_2NH [112]. More recently the new phase, $Li_3(NH_2)_2I$, was synthesised and shown to have an ionic mobility three orders of magnitude greater than $LiNH_2$ [84].

In this section I report the hydrogen releasing properties of the amide-halide materials synthesised in chapter 3 through TPD-MS, before investigating the hydrogenation properties of the corresponding imide-halides through reaction under

a high pressure of hydrogen and also using an IGA. Finally the ionic mobility of these materials is investigated through ac impedance spectroscopy before an overall conclusion and discussion of these materials with respect to use for hydrogen storage.

4.2 Experimental

Samples were prepared by the methods discussed in chapter 3. TPD-MS (chapter 2.7) was performed on the mixtures of the prepared samples with LiH or MgH_2 (Sigma-Aldrich, $> 95\%$). These samples were prepared at various stoichiometries in an argon filled glove box (<10 ppm O_2, <1 ppm H_2O) and heated in quartz tubes within the TPD apparatus (chapter 2.7) at 2 °C min^{-1} to 400 °C.

Rehydrogenation was performed on imide-halide samples prepared as discussed in chapter 3. The samples were sealed within the reactor vessel (chapter 2.2) within an argon filled glove box, before being pressurised to 100 bar H_2 and heated to temperatures of 200 °C and 300 °C.

IGA measurements were performed using a Hiden Analytical IGA; following inert loading (chapter 2.9), measurements were run under 18.5 bar H_2 at 250 °C.

Ionic conductivities were evaluated by the ac complex impedance method (chapter 2.10) using a Hewlett Packard 4192A LF impedance analyser. Measurements were performed on pressed pellets (13 mm diameter, 1 mm thickness) within a sealed home built container; the surfaces of the pellets were coated with gallium-indium alloy to ensure good electrical contact.

4.3 Temperature Programmed Desorption

4.3.1 Amide-chlorides

In this section the hydrogen desorption properties of the pure lithium and mixed lithium-magnesium amide-halides were tested when mixed with LiH or MgH_2. All

of the samples were heated at 2 °C min^{-1} to 400 °C. The reaction stiochiometries were chosen so as to maintain a (NH_2^-) to (H^-) ratio of 1:1.

These results should be considered in comparison to the pure $LiNH_2$ system. The results of the decomposition of $LiNH_2$ with LiH and MgH_2 are shown in figure 4.1. The reaction of $LiNH_2$ + LiH (fig. 4.1a) showed a gradual increase in hydrogen release from just above 200 °C. The rate of hydrogen release is seen to increase more rapidly from 370 °C; this is just below the melting point of $LiNH_2$. Above the melting point, it has been observed that the rate of ammonia release from pure $LiNH_2$ increases [113]. This is thought to be why the main hydrogen release in figure 4.1 occurs with the release of a small amount of ammonia, making up roughly 2 mol % of the total gas released from this system.

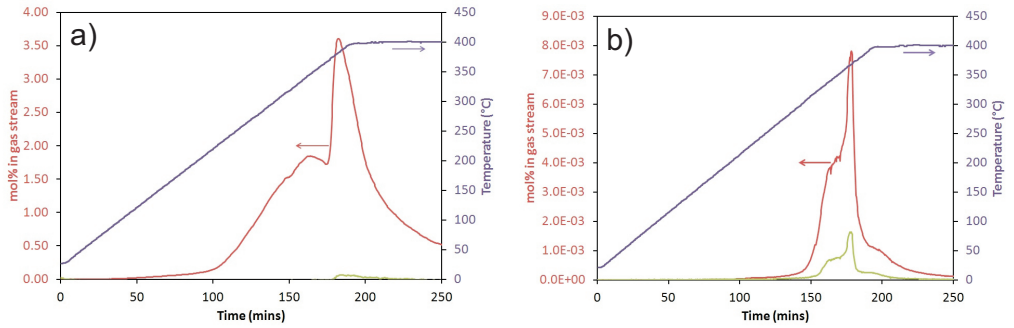

Figure 4.1: TPD-MS traces of the decomposition of $LiNH_2$ with (a) LiH or (b) MgH_2, heated at 2 °C min^{-1} to 400 °C, showing traces for hydrogen (red), ammonia (green) and temperature (purple).

The reaction of $2LiNH_2$ + MgH_2 (fig. 4.1b) released hydrogen as well as ammonia from around 300 °C. The rate of release increased rapidly at 350 °C, peaking at 370 °C. The ammonia released in this reaction accounts for around 15 mol % of the total gas released.

The reactions of $Li_4(NH_2)_3Cl$ + 3LiH and $Li_3Mg_{0.5}(NH_2)_3Cl$ + 3LiH (figures 4.2 and 4.3 respectively) showed an onset temperature of hydrogen release at roughly the same point as the pure $LiNH_2$ + LiH system, at around 210 °C. However, the rate of hydrogen release at lower temperatures was increased, with

the peak of hydrogen release occuring at 340 °C for the pure lithium system, and at 300 °C for the mixed lithium-magnesium phase. This is compared to a peak at around 380 °C for $LiNH_2$ + LiH.

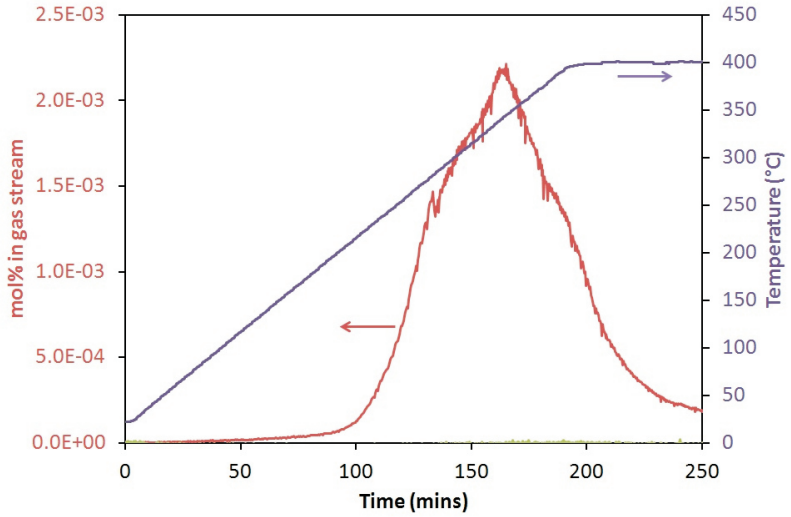

Figure 4.2: TPD-MS trace of the reaction of $Li_4(NH_2)_3Cl$ + 3LiH, heated at 2 °C min^{-1} to 400 °C, showing traces for hydrogen (red), ammonia (green) and temperature (purple).

As previously mentioned the main hydrogen release from the decomposition of $LiNH_2$ + LiH is accompanied by around 2 mol % of ammonia. The reaction of both of the two new phases, $Li_4(NH_2)_3Cl$ + LiH and $Li_3Mg_{0.5}(NH_2)_3Cl$, with LiH showed no release of ammonia. The detection limit of the mass spectrometer used is approximately 5 ppm in the argon carrier gas stream. A typical hydrogen release in this work was in the region of 10,000 ppm. This indicates that the presence of halide in the system has aided the suppression of ammonia release. It is worth mentioning that in the geometry of the TPD apparatus used in this work (fig. 2.5) the argon carrier gas flows above the sample. In previous work it has been seen that this geometry can suppress a small amount of ammonia release, compared to a geometry where the carrier gas flows directly around the sample.

As discussed previously, the solid products from these reactions matched those

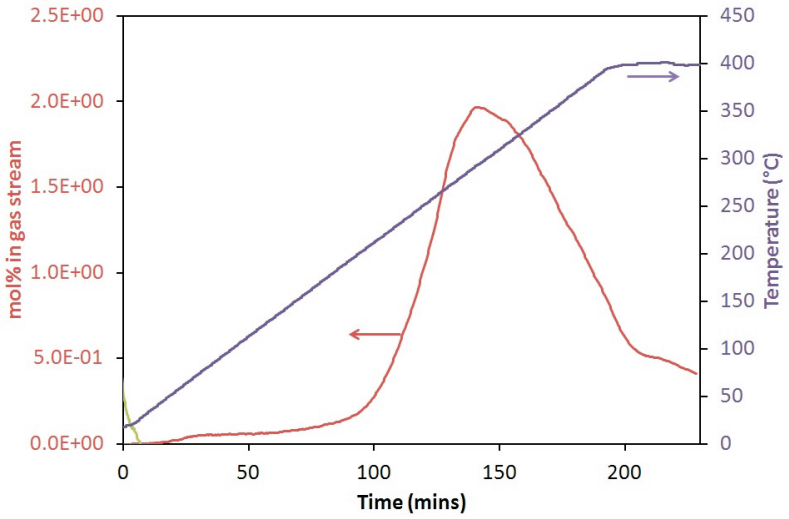

Figure 4.3: TPD-MS trace of the decomposition of $Li_3Mg_{0.5}(NH_2)_3Cl$ + 3LiH, heated at 2 °C min^{-1} to 400 °C, showing traces for hydrogen (red), ammonia (green) and temperature (purple).

formed directly from Li_2NH and $LiCl/MgCl_2$ (chapter 3.4.1). This lead to the assignment of the products as imide-chlorides, giving the reaction schemes shown below for both the pure lithium (eq. 4.1) and mixed lithium-magnesium phases (eq. 4.2). These reactions give theoretical hydrogen weight loss of around 4.44 and 4.27 wt %, respectively.

$$Li_4(NH_2)_3Cl + 3LiH \rightarrow Li_7(NH)_3Cl + 3H_2 \uparrow \tag{4.1}$$

$$Li_3Mg_{0.5}(NH_2)_3Cl + 3LiH \rightarrow Li_6Mg_{0.5}(NH)_3Cl + 3H_2 \uparrow \tag{4.2}$$

The reactions of $2Li_4(NH_2)_3Cl + 3MgH_2$ and $2Li_3Mg_{0.5}(NH_2)_3Cl$ with $3MgH_2$ (fig. 4.4 and 4.5) showed a significant decrease in the onset temperature of hydrogen release to around 275 °C, with the peaks of hydrogen release occurring at 325 °C and 310 °C respectively. This is in comparison to an onset temperature of 300 °C with a peak at 360 °C for $2LiNH_2$ + MgH_2.

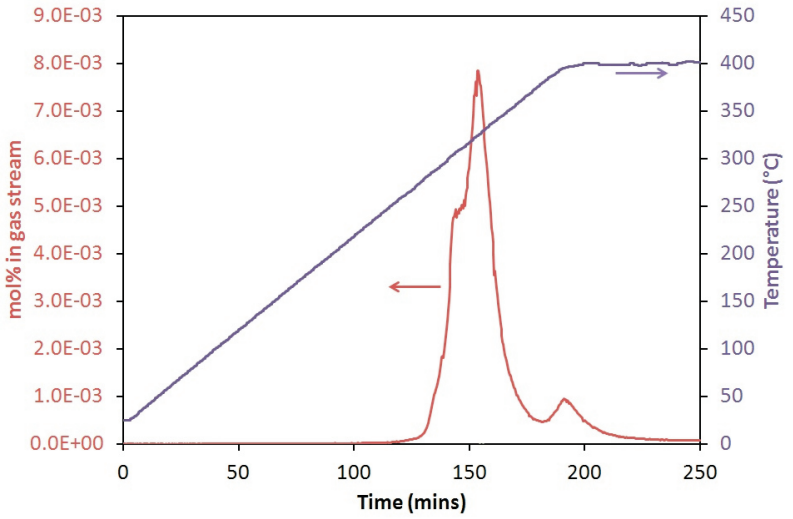

Figure 4.4: TPD-MS trace of the reaction of $2Li_4(NH_2)_3Cl + 3MgH_2$, heated at 2 °C min^{-1} to 400 °C, showing traces for hydrogen (red), ammonia (green) and temperature (purple).

In both the reactions of $2Li_4(NH_2)_3Cl$ and $2Li_3Mg_{0.5}(NH_2)_3Cl$ with $3MgH_2$, the amount of ammonia released alongside the hydrogen was reduced from 15 mol % to less than 1 mol %. As mentioned at an earlier point (chapter 3.4.1) the powder diffraction patterns of the solid products from these reactions did not match those of any previously synthesised imide-chlorides. While there are unidentified phases formed, there is seen to be LiCl present as a majority phase in the diffraction patterns (figure A.1). This suggests a metathesis type reaction, rather than the formation of an imide-chloride phase.

As discussed in the previous chapter (3.3.6), the new amide-chloride of the form $Li_4(NH_2)_3Cl$ can accommodate a range of stoichiometry. It can be seen to form a pure phase down to the halide-deficient stiochiometry of $Li_4(NH_2)_{3.5}Cl_{0.7}$; however, this is not useful unless the improved hydrogen release properties are maintained, relative to $LiNH_2$ + LiH (fig. 4.2).

The TPD traces shown in figure 4.6 show that the onset and peak of hydrogen release remained constant down to an x value of 0.3 (blue) compared to x = 0 (red) in the system $Li_4(NH_2)_{3+x}Cl_{1-x}$ + (3+x)LiH. The traces have been normalised

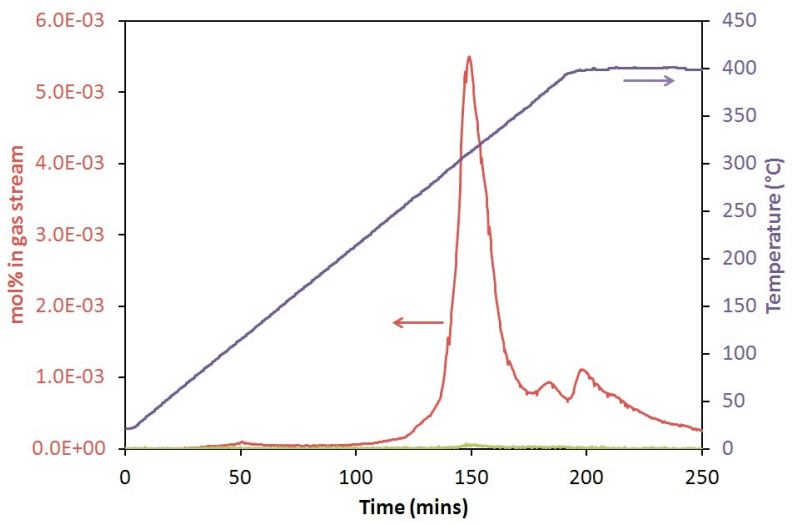

Figure 4.5: TPD-MS trace of the reaction of $2Li_3Mg_{0.5}(NH_2)_3Cl + 3MgH_2$, heated at 2 °C min^{-1} to 400 °C, showing traces for hydrogen (red), ammonia (green) and temperature (purple).

in this graph so that they may be more easily compared.

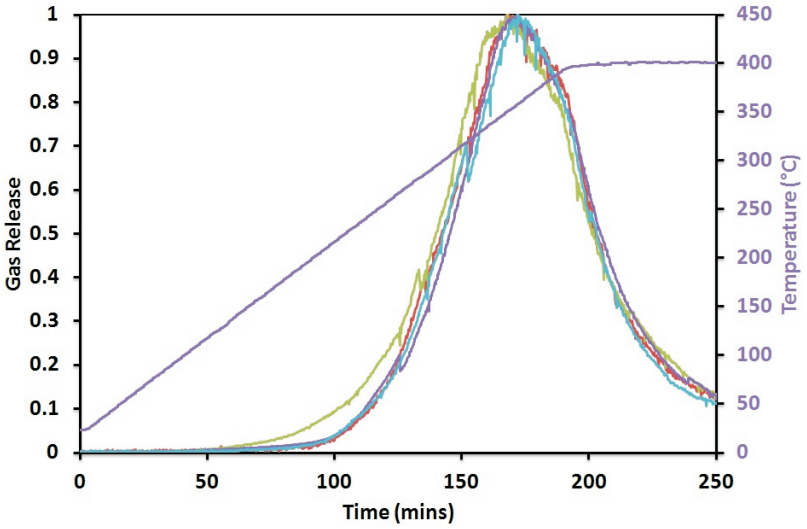

Figure 4.6: TPD-MS traces of the decomposition of $Li_4(NH_2)_{3+x}Cl_{1-x}$ + (3+x)LiH for values $x = 0$ (red), 0.1 (purple), 0.2 (green) and 0.3 (blue).

4.3.2 Amide-bromides

As in the previous section, the hydrogen desorption properties of the pure lithium and mixed lithium-magnesium amide-bromides were tested when mixed with LiH or MgH_2; the samples were heated at 2 °C min^{-1} to 400 °C. Reaction stiochiometries maintained a (NH_2^-) to (H^-) ratio of 1:1. Figure 4.1 shows the desorption from $LiNH_2$ and LiH or MgH_2 for comparison.

The desorption traces for reactions of $Li_7(NH_2)_6Br + 6LiH$ and $Li_6Mg_{0.5}(NH_2)_6Br + 6LiH$ are shown in figures 4.7 and 4.8, respectively. These reactions show an onset temperature for hydrogen release of below 200 °C with a peak of hydrogen release at around 330 °C for the pure lithium system and 290 °C for the lithium-magnesium system. This compares well to the pure $LiNH_2$ which has a peak of hydrogen release at 380 °C (fig. 4.1a) and to the chloride system discussed in the previous section with peaks of hydrogen release at 340 °C and 300 °C (figures 4.2 and 4.3).

As was the case with the chloride systems discussed previously, these bromide systems show no release of ammonia above the detection limit of the mass spectrometer (roughly 5 ppm in the argon carrier gas stream). This is compared to an ammonia release of around 2 mol % in the pure $LiNH_2$ system.

Similarly to the imide-chlorides discussed previously, the products from the reaction of these amide-bromides with LiH closely resembled those formed directly from Li_2NH and $LiBr/MgBr_2$. This gives the reaction schemes below (equations 4.3 and 4.4) with theoretical hydrogen weight loss of 4.45 wt % and 4.36 wt %, respectively.

$$Li_7(NH_2)_6Br + 6LiH \rightarrow Li_{13}(NH)_6Br + 6H_2 \uparrow \tag{4.3}$$

$$Li_6Mg_{0.5}(NH_2)_6Br + 6LiH \rightarrow Li_{12}Mg_{0.5}(NH)_6Br + 6H_2 \uparrow \tag{4.4}$$

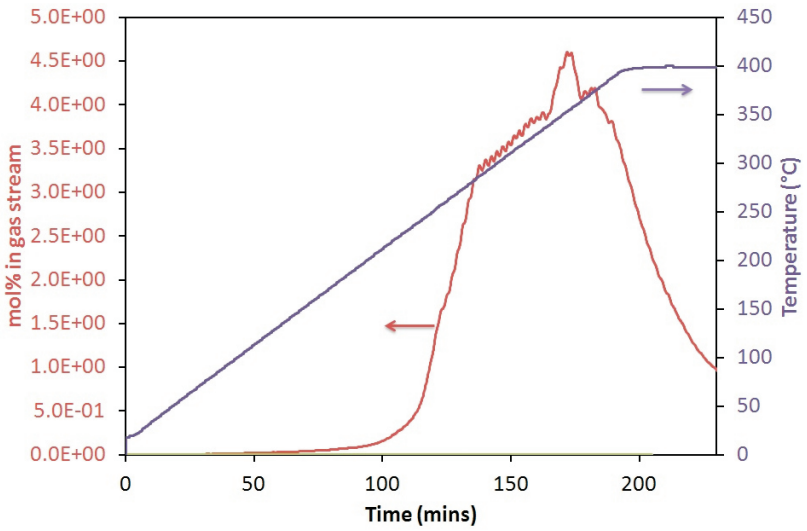

Figure 4.7: TPD-MS trace of the reaction of $Li_7(NH_2)_6Br$ + 6LiH, heated at 2 °C min^{-1} to 400 °C, showing traces for hydrogen (red), ammonia (green) and temperature (purple).

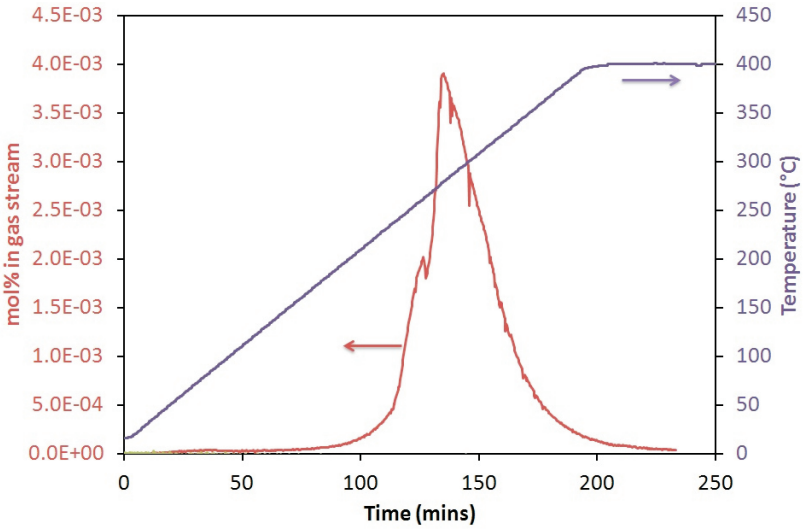

Figure 4.8: TPD-MS trace of the reaction of $Li_6Mg_{0.5}(NH_2)_6Br$ + 6LiH, heated at 2 °C min^{-1} to 400 °C, showing traces for hydrogen (red), ammonia (green) and temperature (purple).

The reactions of $Li_7(NH_2)_6Br$ and $Li_6Mg_{0.5}(NH_2)_6Br$ with $3MgH_2$ showed a sharp peak in the hydrogen desorption trace (figures 4.9 and 4.10) at 260 °C and 270 °C, respectively. This again compares well to the pure $LiNH_2$ system with a peak of hydrogen release at 360 °C (fig. 4.1b) and to the chloride systems with onset temperatures of 325 °C and 310 °C. Again there was no ammonia release seen within the limits of the mass spectrometer. As with the equivalent chloride reactions, unidentified phases are seen in the products from these reactions, alongside LiBr (figure A.2); again suggesting that no imide-bromide phase is formed.

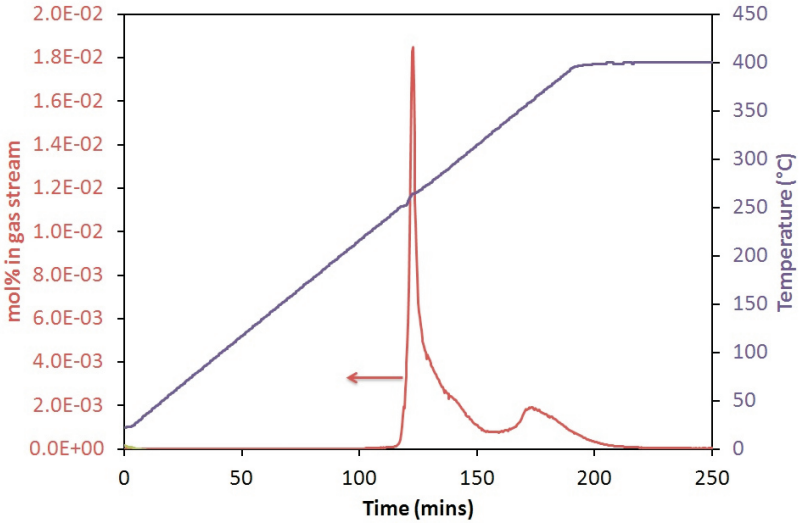

Figure 4.9: TPD-MS trace of the reaction of $Li_6Mg_{0.5}(NH_2)_6Br + 3MgH_2$, heated at 2 °C min^{-1} to 400 °C, showing traces for hydrogen (red), ammonia (green) and temperature (purple).

4.3.3 Amide-iodides

As in the previous two sections, the hydrogen desorption properties of the pure lithium and mixed lithium/magnesium amide-iodides were tested when mixed with LiH or MgH_2; the samples were heated at 2 °C min^{-1} to 400 °C. Reaction stoichiometries maintained a (NH_2^-) to (H^-) ratio of 1:1. For comparision, figure 4.1 shows the desorption from $LiNH_2$ and LiH or MgH_2.

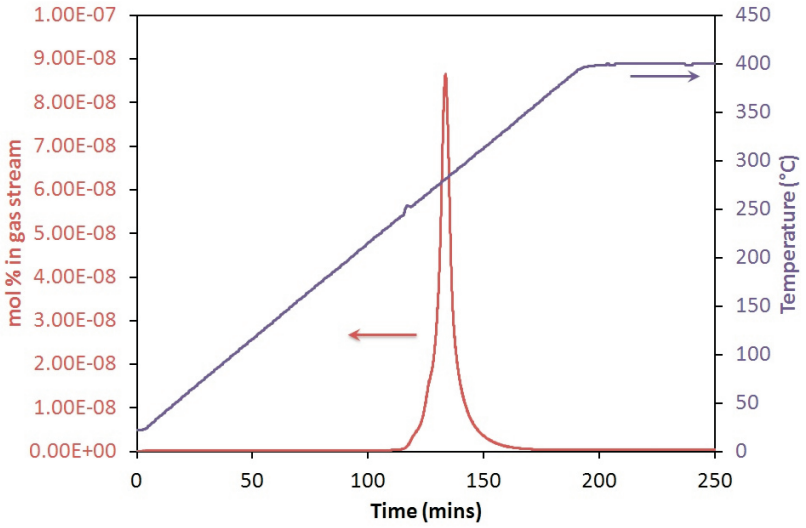

Figure 4.10: TPD-MS trace of the reaction of $Li_6Mg_{0.5}(NH_2)_6Br$ + $3MgH_2$, heated at 2 °C min^{-1} to 400 °C, showing traces for hydrogen (red), ammonia (green) and temperature (purple).

The temperature programmed desorption traces for reactions of $Li_3(NH_2)_3I$ + 2LiH and $Li_2Mg_{0.5}(NH_2)_2I$ + 2LiH are shown in figures 4.7 and 4.8 respectively and were more complex than those of the equivalent chloride and bromide phases. These reactions both show an onset temperature for hydrogen release of well below 150 °C, while the pure lithium system has a small peak around 200 °C before a much larger peak at 320 °C. The mixed lithium-magnesium system shows two large and distinct hydrogen peaks, one at 230 °C and one at 390 °C.

The onset temperatures for hydrogen release in these amide-iodide systems are the lowest seen in this work, beginning significantly at around 120 °C. However, it should be noted that the second peak in the lithium-magnesium system and a shoulder on the high temperature side of the main peak for the pure lithium system, match closely to the hydrogen release seen from the pure $LiNH_2$ + LiH reaction. This could suggest that the material decomposes to give some $LiNH_2$ which then gives off hydrogen itself, however, the diffraction pattern of the products (fig. 3.69) shows only the formation of the imide-iodide, $Li_5(NH)_2I$, confirming the nitrogen and iodide do not segregate into different phases. This

leads to equations 4.5 and 4.6, giving theoretical hydrogen release of 2.06 wt % and 2.01 wt %, respectively.

$$Li_3(NH_2)_2I + 2LiH \rightarrow Li_5(NH)_2I + 2H_2 \uparrow \tag{4.5}$$

$$Li_2Mg_{0.5}(NH_2)_2I + 2LiH \rightarrow Li_4Mg_{0.5}(NH)_2I + 2H_2 \uparrow \tag{4.6}$$

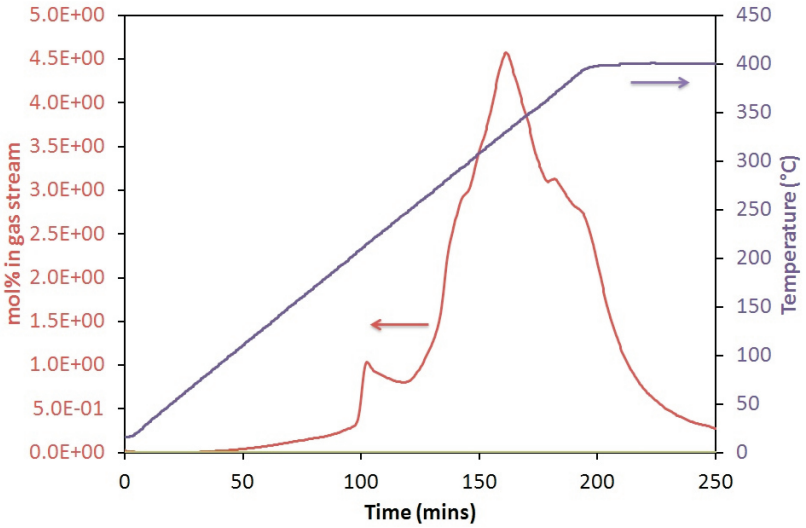

Figure 4.11: TPD-MS trace of the reaction of $Li_3(NH_2)_2I$ + 2LiH, heated at 2 °C min^{-1} to 400 °C, showing traces for hydrogen (red), ammonia (green) and temperature (purple).

The reactions of $Li_3(NH_2)_2I$ and $Li_2Mg_{0.5}(NH_2)_2I$ with MgH_2 (figures 4.13 and 4.14) showed hydrogen release beginning at 200 °C and 150 °C, respectively. The hydrogen release from the lithium only system showed a complicated trace with three peaks at 235 °C, 300 °C and 350 °C while the mixed lithium-magnesium system showed one main, sharp, hydrogen release at 250 °C. Further work is required to understand this multi-step decomposition process and the products formed; which are seen not to match the previously synthesised imide-iodide phase.

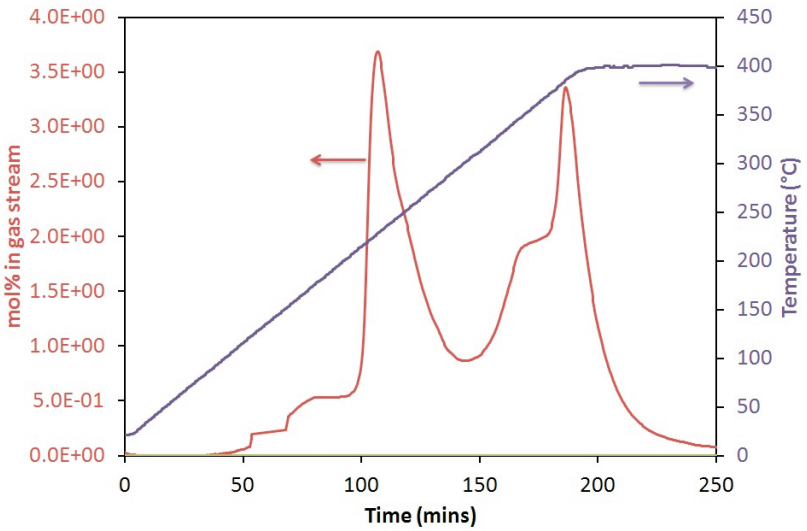

Figure 4.12: TPD-MS trace of the reaction of $Li_2Mg_{0.5}(NH_2)_2I$ + 2LiH, heated at 2 °C min^{-1} to 400 °C, showing traces for hydrogen (red), ammonia (green) and temperature (purple).

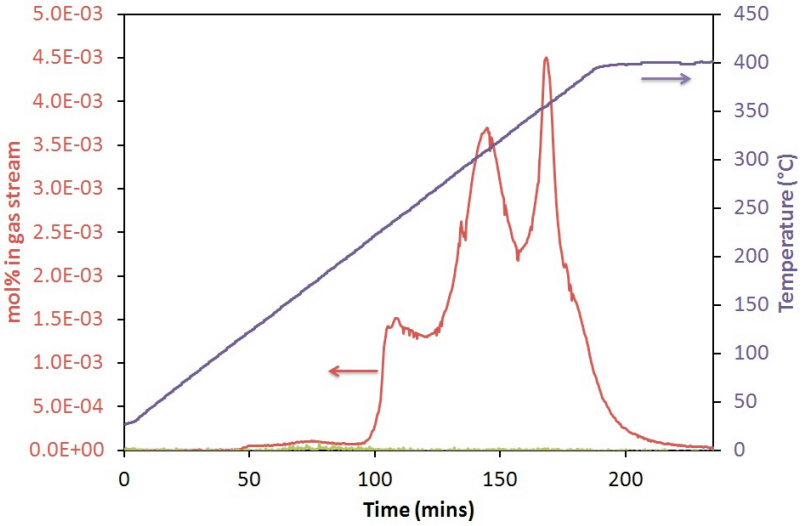

Figure 4.13: TPD-MS trace of the reaction of $Li_3(NH_2)_2I$ + MgH_2, heated at 2 °C min^{-1} to 400 °C, showing traces for hydrogen (red), ammonia (green) and temperature (purple).

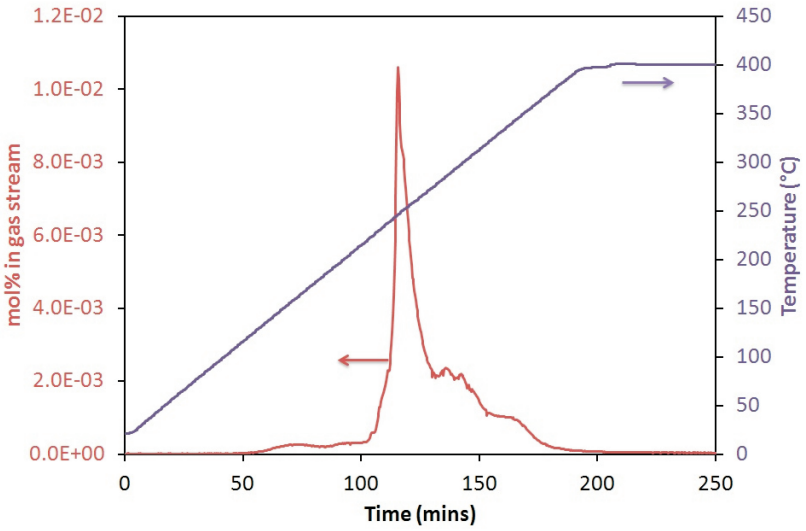

Figure 4.14: TPD-MS trace of the reaction of $Li_2Mg_{0.5}(NH_2)_2I$ + MgH_2, heated at 2 °C min^{-1} to 400 °C, showing traces for hydrogen (red), ammonia (green) and temperature (purple).

4.4 Rehydrogenation

4.4.1 High-pressure H_2 Reactor

In this section the rehydriding properties of pure lithium and mixed lithium/magnesium imide-halides were tested under 100 bar H_2 along with an Li_2NH control. All samples were heated at temperatures of 200 and 300 °C for between 1 and 24 hours.

To begin with samples were heated at 300 °C for 24 hours. Under these conditions all of the imide-halides as well as the Li_2NH control were seen to fully rehydride. In the case of the chlorides it is seen that the pure lithium imide-halide of the form $Li_7(NH)_3Cl$ rehydrided to hexagonal ($R\bar{3}$) phase of $Li_4(NH_2)_3Cl$ alongside LiH (fig. 4.15). The body centred cubic ($I2_13$) phase was not seen to be formed. For the mixed lithium-magnesium imide-halide a rhombohedral phase was formed of $Li_3Mg_{0.5}(NH_2)_3Cl$, nearly identical in unit cell parameters to that of the pure lithium system (fig. 4.16). When synthesising the corresponding amide-chlorides from $LiNH_2$, only the body centred cubic phase was seen to be

formed.

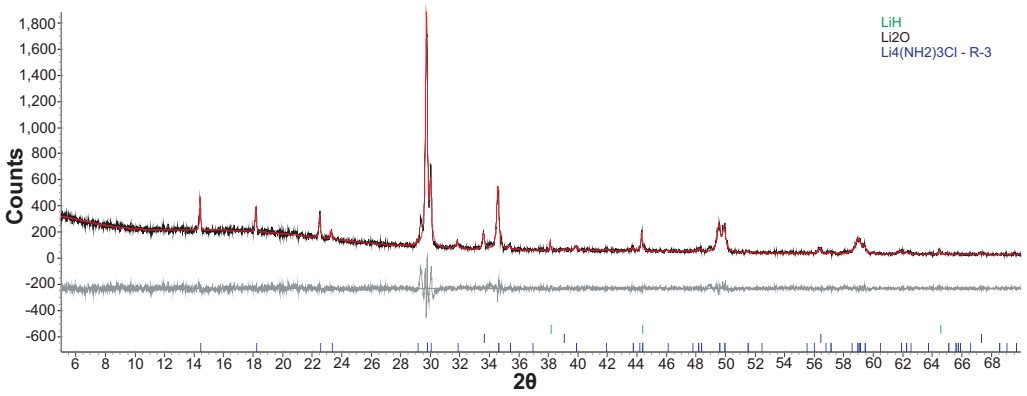

Figure 4.15: Powder X-ray diffraction pattern of products from hydrogenation of $Li_7(NH)_3Cl$ under 100 bar H_2, at 300 °C for 24 hours, showing observed (black), calculated Pawley fit (red) and difference (grey) plots. Peak positions for hexagonal $Li_4(NH_2)_3Cl$ are shown in purple.

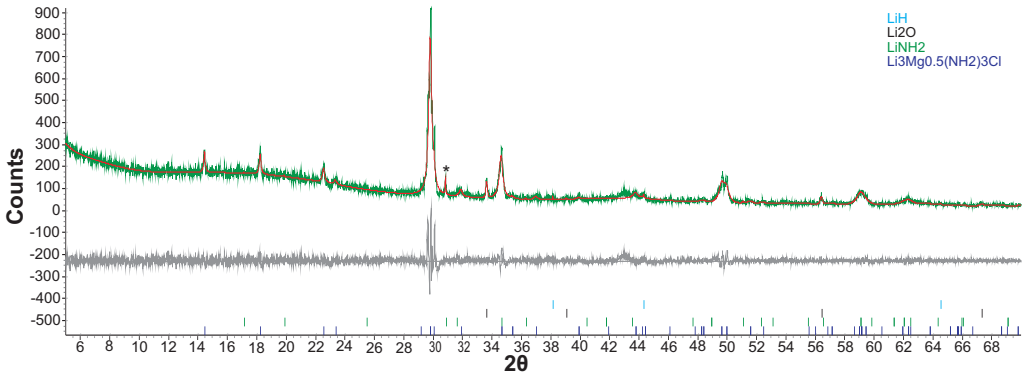

Figure 4.16: Powder X-ray diffraction pattern of products from hydrogenation of $Li_6Mg_{0.5}(NH)_3Cl$ under 100 bar H_2, at 300 °C for 24 hours, showing observed (green), calculated Pawley fit (red) and difference (grey) plots. Peak positions for hexagonal $Li_3Mg_{0.5}(NH_2)_3Cl$ are shown in purple and for $LiNH_2$ impurity marked *.

Raman spectroscopy was performed on the products from these hydrogenation reactions to check whether products contained amide NH_2^- groups, imide NH^{2-} groups or a mixture of the two. The Raman spectra of these groups have been discussed previously in chapter 3.3.2. The Raman spectra of the hydrogenated imide-chloride phases are shown in figure 4.17 and clearly show that the products are of amide form. These results, coupled with the X-ray diffraction patterns

confirm that the products from these hydrogenation reactions reform the amide-chlorides of the form $Li_4(NH_2)_3Cl$ and $Li_3Mg_{0.5}(NH_2)_3Cl$. The results from this section and the desorption results (chapter 4.3.1) give the following reversible reactions:

$$Li_4(NH_2)_3Cl + 3LiH \leftrightarrows Li_7(NH)_3Cl + 3H_2 \uparrow \tag{4.7}$$

$$Li_3Mg_{0.5}(NH_2)_3Cl + 3LiH \leftrightarrows Li_6Mg_{0.5}(NH)_3Cl + 3H_2 \uparrow \tag{4.8}$$

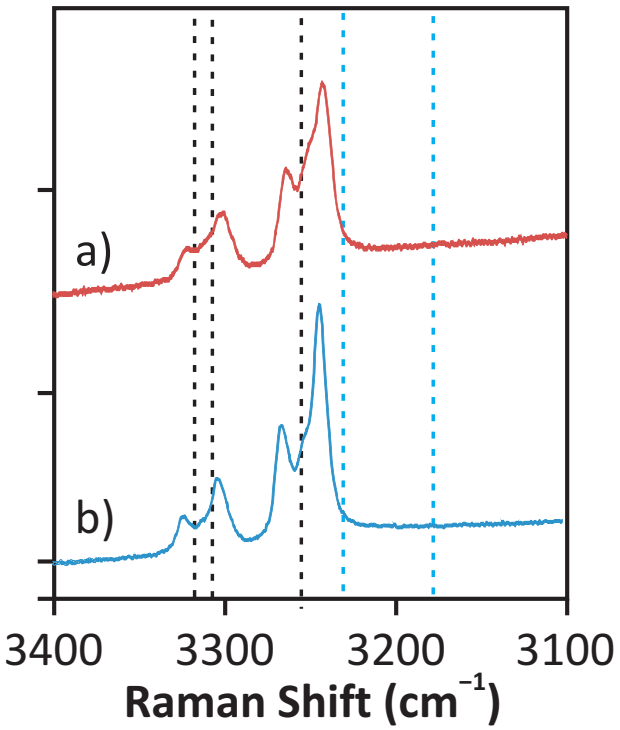

Figure 4.17: Raman spectra of products from the hydrogenation of (a) $Li_7(NH)_3Cl$ and (b) $Li_6Mg_{0.5}(NH)_3Cl$ under 100 bar H_2 at 300 °C for 24 hours. Peak positions highlighted by black ($LiNH_2$) and blue (Li_2NH) dotted lines.

The samples were then heated at 200 °C for 24 hours, the diffraction pattern from these reactions showed a mixture of the amide- and imide-chloride materials. The diffraction pattern of the pure lithium phase is shown in figure 4.18 and these

results are confirmed from the Raman spectroscopy for these products shown in figure 4.19, clearly showing both the NH_2^- peaks and the broader NH^{2-} peaks at lower wavenumber.

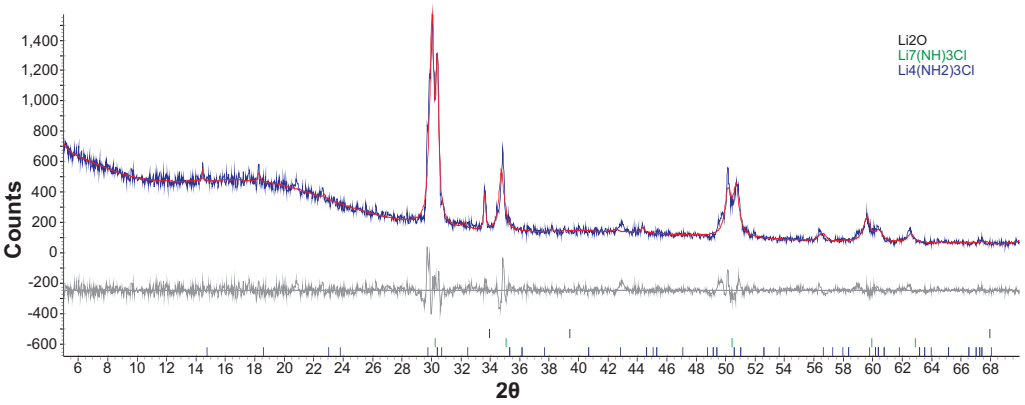

Figure 4.18: Powder X-ray diffraction pattern of products from hydrogenation of $Li_7(NH)_3Cl$ under 100 bar H_2, at 200 °C for 24 hours, showing observed (black), calculated Pawley fit (red) and difference (grey) plots. Peak positions for hexagonal $Li_4(NH_2)_3Cl$ are shown in blue and for $Li_7(NH)_3Cl$ in green.

The imide-bromide materials of the form $Li_{13}(NH)_6Br$ and $Li_{12}Mg_{0.5}(NH)_6Br$ were also heated under 100 bar H_2 at 300 °C for 24 hours. The X-ray powder diffraction patterns from these reactions showed the formation of the amide-bromide formed previously (chapter 3.5.1) along with some unidentified peaks (fig. 4.20).

By analysis of the Raman spectra of the pure lithium system (fig. 4.21a) we can see that the products from the reaction from $Li_{13}(NH)_6Br$ are of amide form. The spectrum shows that there are two symmetric and two asymmetric stretches for the NH_2^-. This suggests that there are two different NH_2^- environments in the structure and matches very well with the $Li_7(NH_2)_6Br$ (fig. 3.40a) formed in the previous chapter. The Raman spectrum of the mixed lithium/magnesium system (fig. 4.21b) clearly shows that the material is at least predominantly NH_2^-, although the peaks were not as sharp as in the pure lithium case and there was another peak seen at around 3280 cm^{-1}. This peak was not seen in the amide-bromide, $Li_6Mg_{0.5}(NH_2)_6Br$, formed previously (fig. 3.40b) and while the

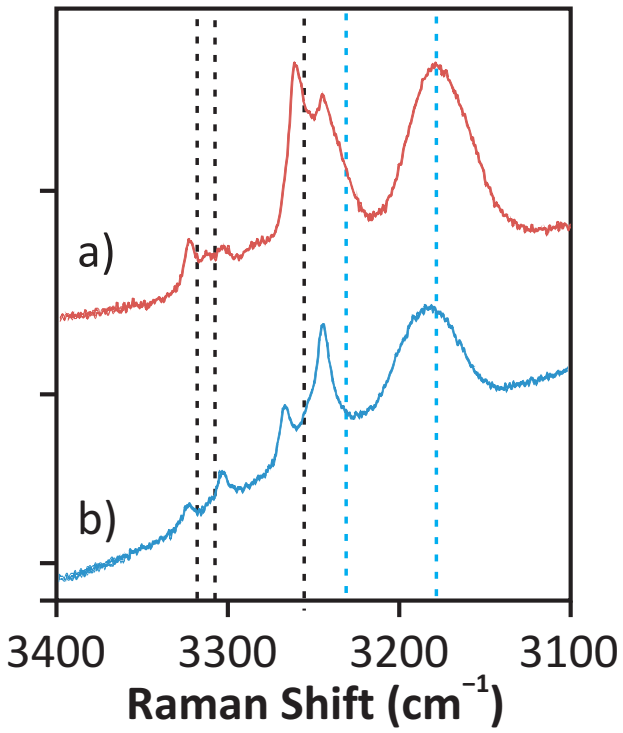

Figure 4.19: Raman spectra of products from the hydrogenation of (a) $Li_7(NH)_3Cl$ and (b) $Li_6Mg_{0.5}(NH)_3Cl$ under 100 bar H_2 at 200 °C for 24 hours. Peak positions highlighted by black ($LiNH_2$) and blue (Li_2NH) dotted lines.

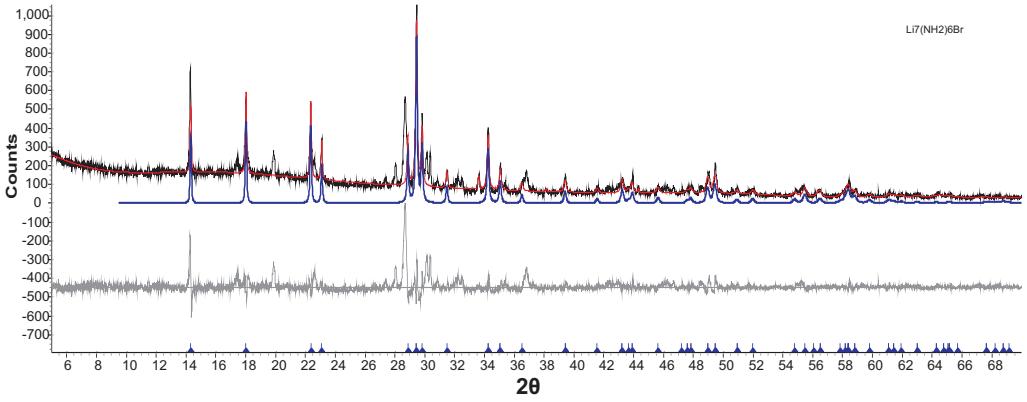

Figure 4.20: Powder X-ray diffraction pattern of products from hydrogenation of $Li_{13}(NH)_6Br$ under 100 bar H_2, at 300 °C for 24 hours, showing observed (black), calculated Pawley fit (red) and difference (grey) plots. Peak positions for $Li_7(NH_2)_6Br$ are highlighted in blue.

shape of the peak suggests it may be due to an NH^{2-} stretch, it is at significantly higher wavenumber than would be expected.

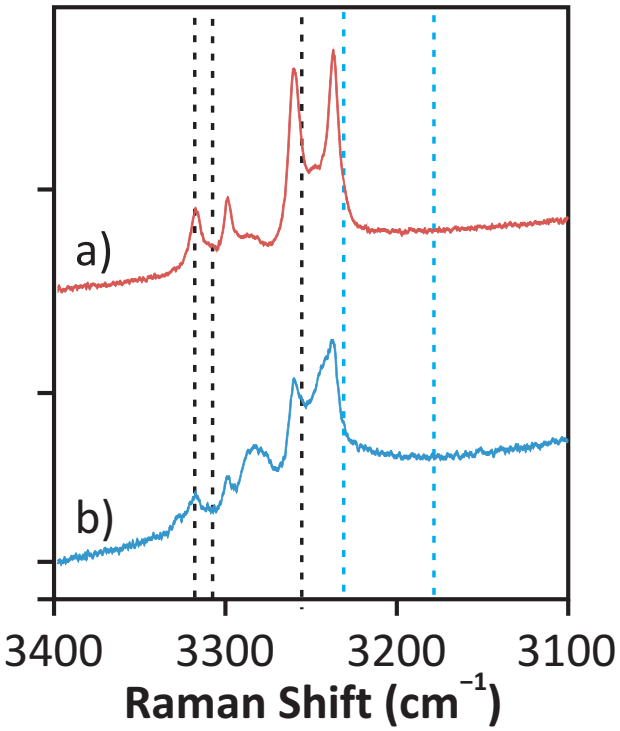

Figure 4.21: Raman spectra of products from the hydrogenation of (a) $Li_{13}(NH)_6Br$ and (b) $Li_{12}Mg_{0.5}(NH)_6Br$ under 100 bar H_2 at 300 °C for 24 hours. Peak positions highlighted by black ($LiNH_2$) and blue (Li_2NH) dotted lines.

The samples were then heated at 200 °C for 24 hours. The powder X-ray diffraction patterns for these reactions showed a mixture of the amide-bromide, the imide-bromide and some unidentified peaks. While the number of phases present, in particular the peaks between 28 and 30 °2θ, made an accurate structural fit to the data difficult, the main peaks for the phase $Li_6Mg_{0.5}(NH_2)_6Br$ have been highlighted (fig. 4.22) and showed that significant hydrogenation had occurred. The Raman spectroscopy performed on these samples (fig. 4.23) confirms that there were both amide, NH_2^- and imide, NH^{2-} groups present in the samples.

As with the chloride and bromide materials, the imide-iodide materials of the form $Li_5(NH)_2I$ and $Li_4Mg_{0.5}(NH)_2I$ were also heated under 100 bar H_2 at

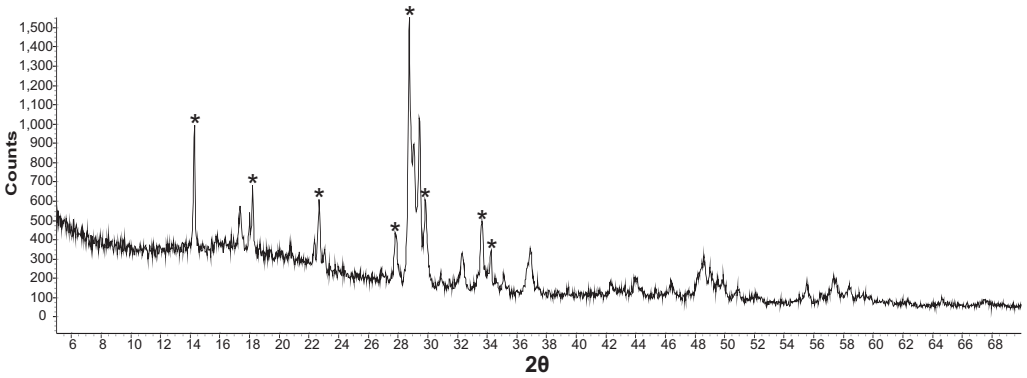

Figure 4.22: Powder X-ray diffraction pattern of products from hydrogenation of $Li_{12}Mg_{0.5}(NH)_6Br$ under 100 bar H_2, at 200 °C for 24 hours. Peak positions for $Li_6Mg_{0.5}(NH_2)_6Br$ are highlighted (*).

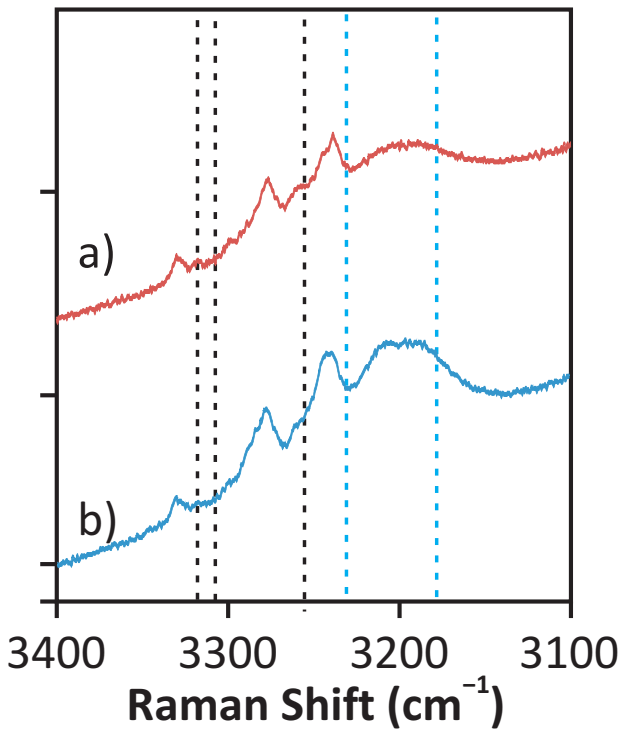

Figure 4.23: Raman spectra of products from the hydrogenation of (a) $Li_{13}(NH)_6Br$ and (b) $Li_{12}Mg_{0.5}(NH)_6Br$ under 100 bar H_2 at 200 °C for 24 hours. Peak positions highlighted by black ($LiNH_2$) and blue (Li_2NH) dotted lines.

200 °C and 300 °C for 24 hours. The powder X-ray diffraction patterns from these reactions show clearly the formation of the amide-iodide formed previously (chapter 3.7.1); shown in figure 4.24 is the mixed lithium-magnesium system heated at 300 °C and in figure 4.25 is the pure lithium system heated at 200 °C. Analysis of the Raman spectra of these samples shows that after heating at 300 °C (fig. 4.26) there was significant transformation of imide groups to amide, NH_2^- groups, while after heating at 200 °C (fig. 4.27) there was only partial hydrogenation.

The combination of the diffraction pattern, which appears to show a good structural match to the amide-iodide of the form $Li_3(NH_2)_2I$ formed previously (chapter 3.7.1), and the Raman spectra, which show only partial hydrogenation of the imide-iodide, suggests that the amide-iodide hexagonal structure can accommodate a mixture of amide and imide groups while maintaining the same structure.

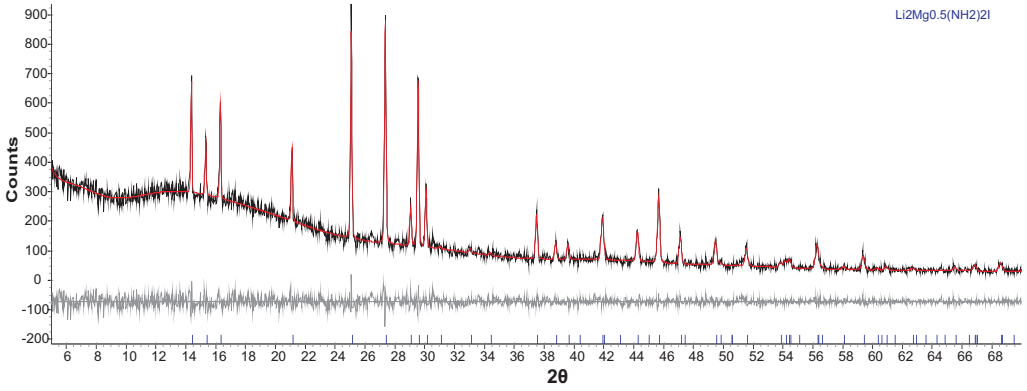

Figure 4.24: Powder X-ray diffraction pattern of products from hydrogenation of $Li_4Mg_{0.5}(NH)_2I$ under 100 bar H_2, at 300 °C for 24 hours, showing observed (black), calculated Pawley fit (red) and difference (grey) plots. Peak positions for $Li_2Mg_{0.5}(NH_2)_2I$ are highlighted in blue.

As the imide-iodides showed significant hydrogenation at 200 °C, new samples were again heated at 200 °C for just one hour. The powder diffraction patterns from these experiments show mostly the imide-iodide phases remaining, however, peaks can clearly be seen which match very closely to the amide-iodides formed

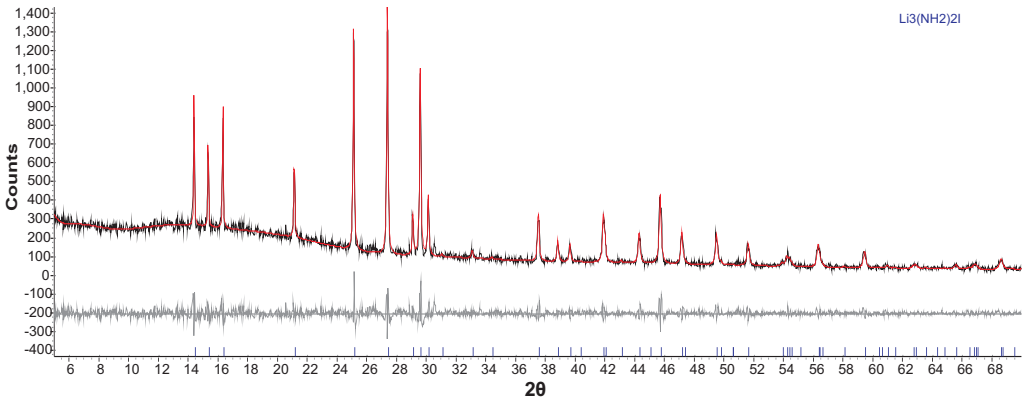

Figure 4.25: Powder X-ray diffraction pattern of products from hydrogenation of $Li_5(NH)_2I$ under 100 bar H_2, at 200 °C for 24 hours, showing observed (black), calculated Pawley fit (red) and difference (grey) plots. Peak positions for $Li_3(NH_2)_2I$ are highlighted in blue.

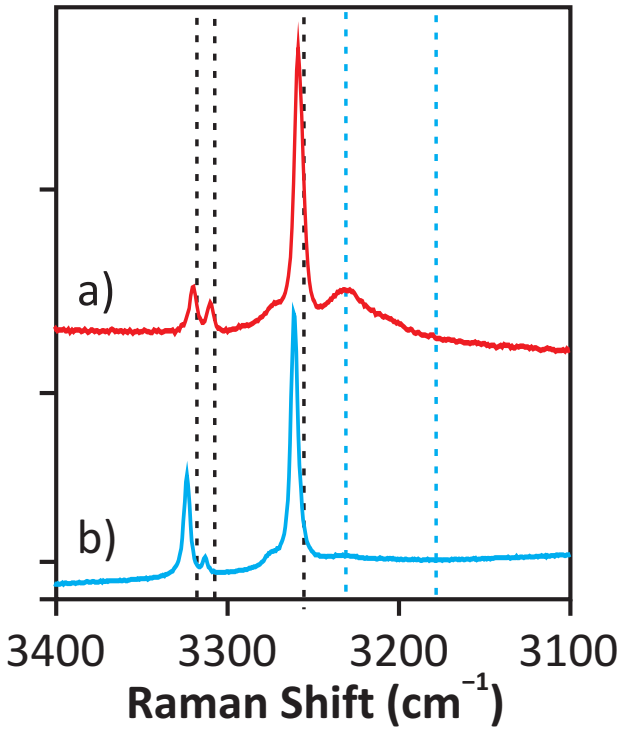

Figure 4.26: Raman spectra of products from the hydrogenation of (a) $Li_5(NH)_2I$ and (b) $Li_4Mg_{0.5}(NH)_2I$ under 100 bar H_2 at 300 °C for 24 hours. Peak positions highlighted by black ($LiNH_2$) and blue (Li_2NH) dotted lines.

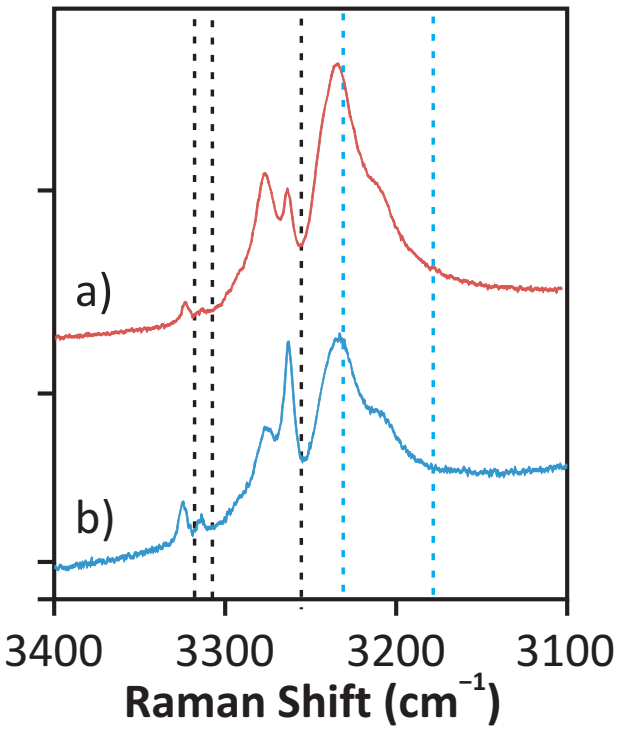

Figure 4.27: Raman spectra of products from the hydrogenation of (a) $Li_5(NH)_2I$ and (b) $Li_4Mg_{0.5}(NH)_2I$ under 100 bar H_2 at 200 °C for 24 hours. Peak positions highlighted by black ($LiNH_2$) and blue (Li_2NH) dotted lines.

previously (3.7.1). These peaks have been highlighted (*) in figure 4.28. The results of the Raman spectroscopy performed on these samples seem to show only imide, NH^{2-} peaks (fig. 4.29), however the resolution of these spectra is relatively low, so it is possible small NH_2^- peaks would not be visible.

4.4.2 Intelligent Gravimetric Analysis

As was seen in the previous section, the imide-halide materials are able to hydride up to amide-halide form, in the case of the imide-iodide, this was seen to begin to happen after only one hour. To try and ascertain further information on the kinetics of this hydrogen uptake, samples of the pure lithium imide-halides were investigated using an Intelligent Gravimetric Analyser (IGA). Samples of $Li_7(NH)_3Cl$, $Li_{13}(NH)_6Br$ and $Li_5(NH)_2I$ were inertly loaded into an IGA and placed under an atmosphere of hydrogen at 18.5 bar. The samples were then

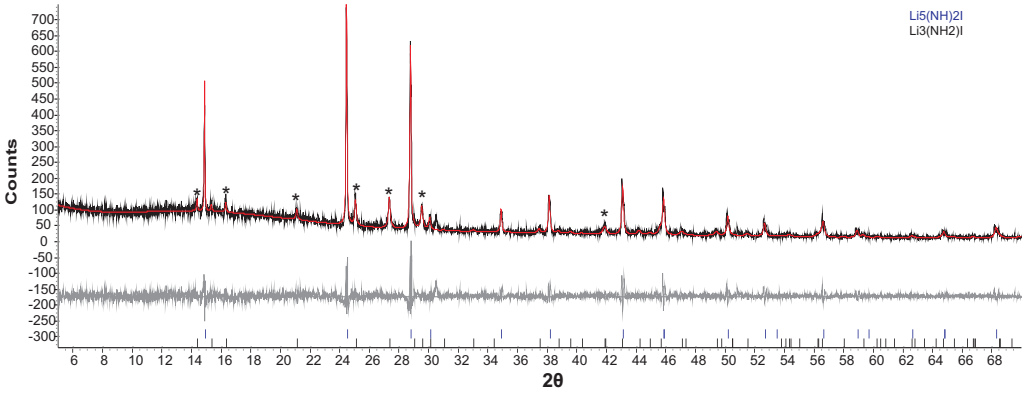

Figure 4.28: Powder X-ray diffraction pattern of products from hydrogenation of $Li_5(NH)_2I$ under 100 bar H_2, at 200 °C for 1 hour, showing observed (black), calculated Pawley fit (red) and difference (grey) plots. Peak positions for $Li_3(NH_2)_2I$ (*) and $Li_5(NH)_2I$ (blue) are highlighted.

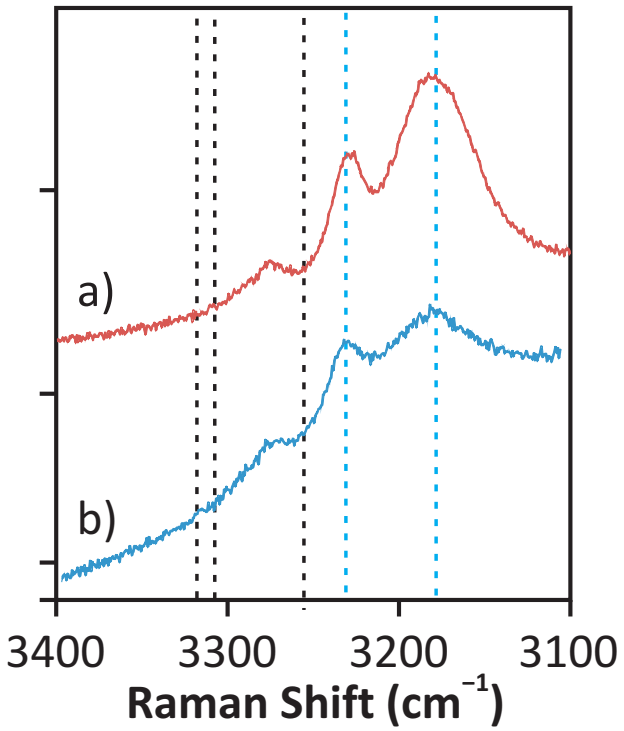

Figure 4.29: Raman spectra of products from the hydrogenation of (a) $Li_5(NH)_2I$ and (b) $Li_4Mg_{0.5}(NH)_2I$ under 100 bar H_2 at 200 °C for 1 hour. Peak positions highlighted by black ($LiNH_2$) and blue (Li_2NH) dotted lines.

heated at 2 °C min^{-1} to 250 °C and the change in mass was monitored for 90 hours.

As it was seen in section 4.4.1 to rehydride the quickest, the sample of $Li_5(NH_2)_2I$ was run first. In the previous section this was seen to begin to hydride within 1 hour, however, the conditions within the IGA are less stringent (18.5 bar H_2 compared to 100 bar H_2). The IGA trace for this sample can be seen in figure 4.30; this showed an overall weight gain of 2.6 % over the 90 hour period. While the trace took the full 90 hours to level off, it slowed down significantly over this time; 2.5 wt % was seen after 55 hours and 2 wt % was seen after 24 hours.

This overall gain of 2.6 wt % is higher than the theoretical value for the reaction seen in equation 4.9 of 2.11 wt %. This could be due to a small amount of oxidation of the sample during the inert loading process for the IGA. The sample was unloaded inertly and the diffraction pattern of the products is shown in figure 4.31; this shows that the product is amide-iodide of the form $Li_3(NH_2)_2I$, as expected from a full hydrogenation.

$$Li_5(NH)_2I + 2H_2 \rightarrow Li_3(NH_2)_2I + 2LiH \tag{4.9}$$

The sample of $Li_{13}(NH_2)_6Br$ was run in the IGA apparatus under the same conditions as the imide-iodide and the trace can be seen in figure 4.32. The trace showed an overall increase of around 0.8 wt % over the 90 hours. This change in mass does not appear to be complete after 90 hours and was not close to the theoretical value of 4.66 wt % for equation 4.10.

$$Li_{13}(NH)_6Br + 6H_2 \rightarrow Li_7(NH_2)_6Br + 6LiH \tag{4.10}$$

The sample was inertly unloaded and the diffraction pattern of the products is shown in figure 4.33. Along with the partial hydrogenation from the IGA data

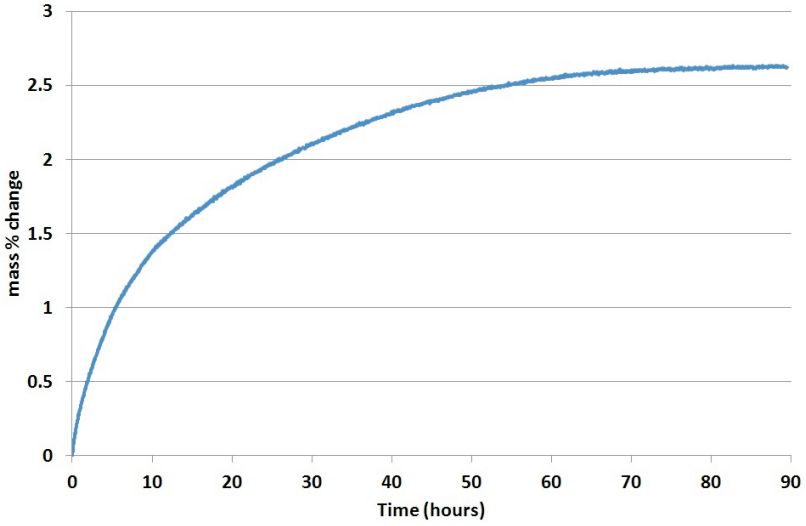

Figure 4.30: IGA trace of $Li_5(NH)_2I$ heated at 250 °C, under 18.5 bar H_2 for 90 hours.

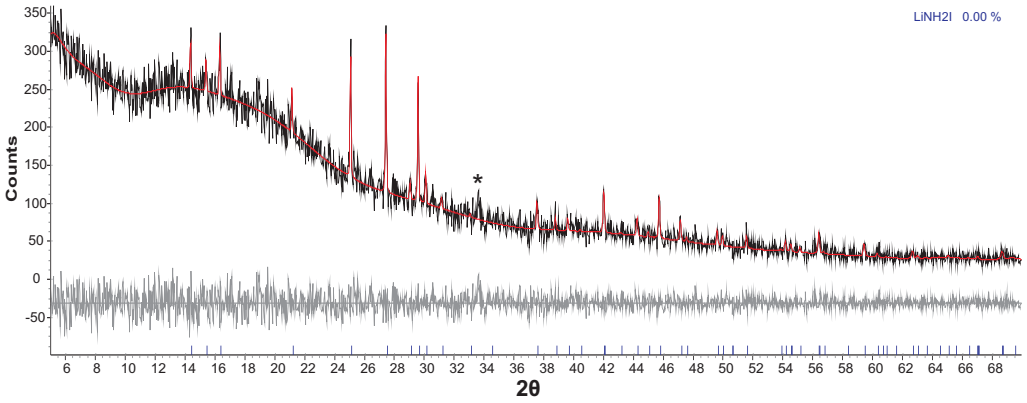

Figure 4.31: Powder X-ray diffraction pattern of products from hydrogenation of $Li_5(NH)_2I$ under 18.5 bar H_2, at 250 °C for 90 hour, showing observed (black), calculated Pawley fit (red) and difference (grey) plots. Peak positions for $Li_3(NH_2)_2I$ are shown in blue and a Li_2O peak is highlighted (*).

(fig. 4.32), the diffraction pattern shows partial formation of the $Li_7(NH_2)_6Br$ phase (peaks marked *). While the quality of the IGA trace is poor, in combination with the diffraction pattern of the product, it can be seen that some hydrogenation is occurring under these conditions.

The sample of $Li_7(NH)_3Cl$ was also inertly loaded and run in the IGA apparatus, however, under these conditions, no change in mass was observed.

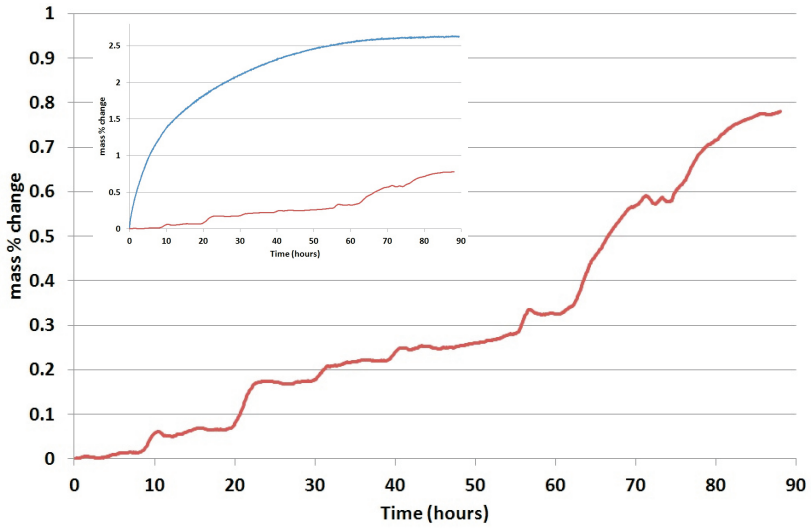

Figure 4.32: IGA trace of $Li_{13}(NH)_6Br$ heated at 250 °C, under 18.5 bar H_2 for 90 hours. Inset of IGA traces of $Li_5(NH)_2I$ and $Li_{13}(NH)_6I$ on the same scale.

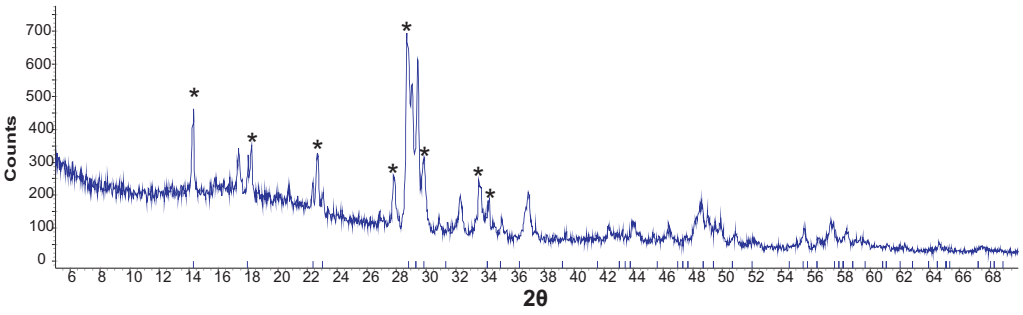

Figure 4.33: Powder X-ray diffraction pattern of products from hydrogenation of $Li_{13}(NH)_6Br$ under 18.5 bar H_2, at 250 °C for 90 hours. Peak positions for $Li_7(NH_2)_6Br$ are highlighted (*).

4.5 Ionic Mobility

In order to assess the the ionic mobility of these amide- and imide-halides, ionic conductivities were measured from room temperature up to 80 °C. The experimental setup (chapter 2.10) has a lower detection limit of $\approx 10^{-6}$ S cm^{-1}.

The results from this work should be taken as a comparison to similar systems, the results of which are shown in figure 4.34. This graph shows the results for Li_2NH [103], $LiNH_2$ and the amide-iodide formed in other work [84], and the mixtures of Li_2NH + LiCl/LiI discussed in the introduction to this chapter [112]. It can be seen that Li_2NH has a relatively high ionic conductivity ($\approx 10^{-2}$ S cm^{-1} at 100 °C) while $LiNH_2$ has a significantly lower ionic conductivity ($\approx 10^{-6}$ S cm^{-1} at 100 °C). It can be seen also from these results that the amide-iodide had an ionic conductivity around 1000 times higher than pure Li_2NH ($\approx 10^{-3}$ S cm^{-1} at 100 °C) [84], while mixtures of Li_2NH and lithium halides showed lower ionic conductivities ($\approx 10^{-3}$ - 10^{-5} S cm^{-1} at 100 °C) than pure Li_2NH [112].

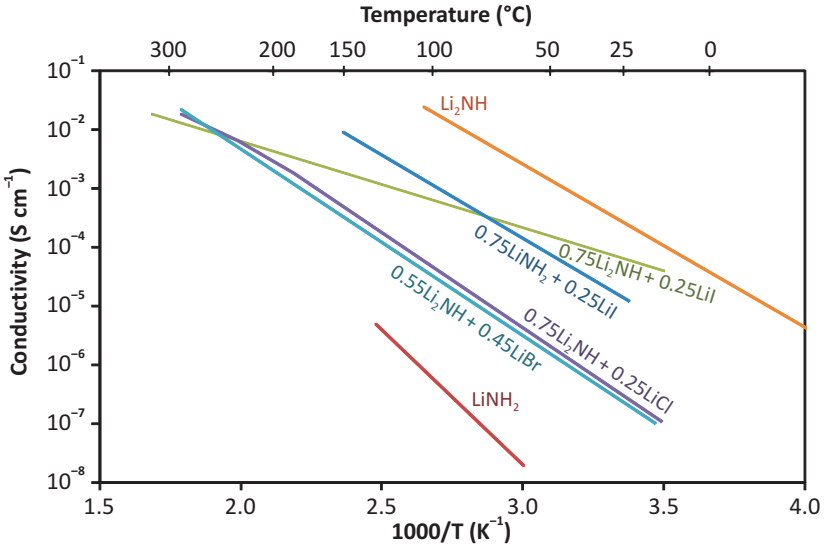

Figure 4.34: Temperature dependence of the ionic conductivity for reported species related to the lithium amide/imide hydrogen storage system [84, 103, 112].

The results from this work are shown in figure 4.35, superimposed upon the results from the literature; the corresponding figures for these results may be

found in table A.5. The highest ionic mobility seen in this work was 1.2 x 10^{-4} S cm^{-1} at 80 °C for $Li_3(NH_2)_2I$, while the lowest is seen for $Li_4(NH_2)_3Cl$ which only showed conductivity at 80 °C. These results agree with literature values, showing that the addition of halides increases the ionic conductivity of $LiNH_2$, but lowers the conductivity of Li_2NH. There can also be seen a clear trend in the ionic mobilities in which iodides > bromides > chlorides.

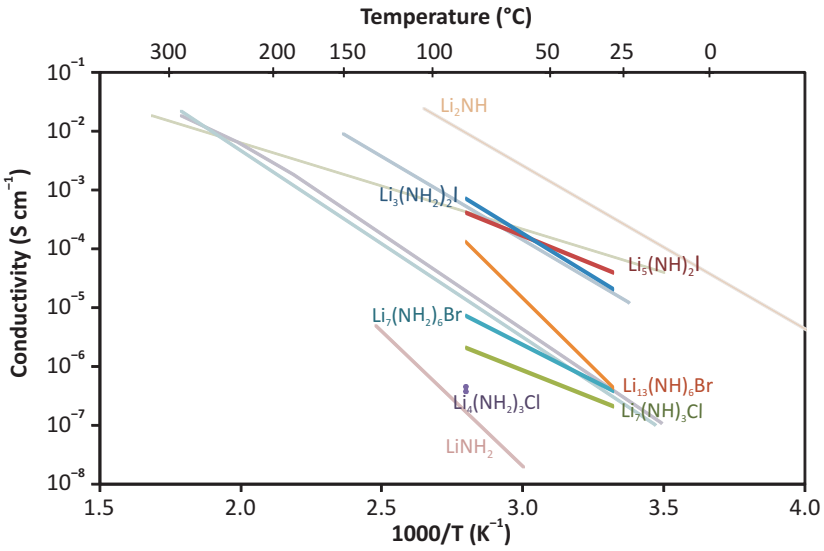

Figure 4.35: Temperature dependance of the ionic conductivity for lithium amide/imide halides synthesised in this work.

4.6 Conclusions

In this work the hydrogen storage properties of the synthesised amide- and imide-halides were investigated. The hydrogen release from the amide-halide materials with LiH and MgH_2 was investigated through TPD-MS. These results showed that all of the amide-halides released hydrogen at a lower temperature than $LiNH_2$ and LiH with a reduction in the amount of NH_3 released alongside H_2. The onset temperature of hydrogen release showed a trend of chlorides > bromides > iodides. The hydrogen uptake properties of the imide-halide materials were investigated in a high pressure H_2 reactor and an IGA. These results showed the

rates of hydrogenation to follow the trend iodides > bromides > chlorides. Finally the ionic mobility of these materials was tested. Here it was shown that the ionic mobility follows the trends of the hydrogen uptake/release properties of these materials with the iodides having the highest mobility, the lowest temperature of hydrogen release and the most favourable conditions for hydrogen uptake.

4.7 Discussions and further work

The work discussed in these first two results chapters was undertaken to investigate how the incorporation of halide anions within the lithium amide and imide structures affects the hydrogen storage properties of this system. It is therefore noteworthy that all of the amide-halide materials released hydrogen at lower temperatures than lithium amide; while the imide-halide materials hydrogenated more quickly than lithium imide. It should also be noted that this work has shown a potential link between the speed of hydrogen release/uptake and the ionic mobility of a material.

It is also seen that with reaction of LiH or MgH_2 there was a significant decrease in the amount of NH_3 compared to $LiNH_2$. It has been seen previously that magnesium halides can form stable ammoniate complexes which could trap any released NH_3 [114, 115]. However, it is seen in this work that the lithium only containing systems performed better in this respect; this suggests a different explanation. A possibility is that phases exhibit improved ion diffusion, favouring a topotactic mechanism [52], rather than one mediated by NH_3. This would in fact be the reverse of Li_2NH hydrogenation which is assumed does not involve NH_3.

It cannot of course be ignored that any improvements in the hydrogen release/uptake properties through the addition of a halide anion are gained at the cost of the gravimetric storage capacity. Figure 4.36 shows the gravimetric penalty for the introduction of halide ions in the amide system with both LiH

and MgH_2. The arrows show the stoichiometric compositions studied in this work. In this work the lower solid solution limits of the different materials were investigated. It can be seen from figure 4.36 that relatively small changes in the stoichiometry of these materials can have a significant effect on the gravimetric capacity of the system.

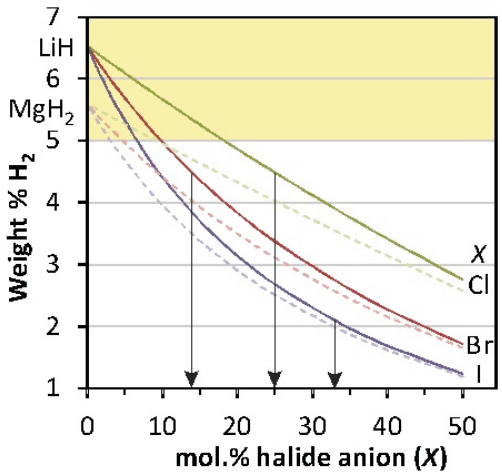

Figure 4.36: Gravimetric penalty for introducing halide anions into the lithium amide system upon reaction with LiH (full line) and MgH_2 (dashed line). Arrows indicate the compositions investigated in this study.

This work has shown the potential for amide- and imide-halides as good hydrogen storage materials, however, further work could be done to fully understand the mechanism for hydrogen release and uptake. Several of the TPD-MS traces show multiple hydrogen release peaks, suggesting a multistep desorption process. Deconvolution of these TPD-MS traces through an *ex-situ* X-ray diffraction study could provide important information on the steps in these decomposition pathways. Along with this an in depth IGA study could be undertaken to attempt to understand the hydrogenation process. While this work has shown a link between the hydrogen uptake and release properties of a material and its ionic mobility, a further, indepth conductivity study would be required to confirm and understand this link. Finally, while not in the remit of this study, work could be carried out into the optimisation of these materials for hydrogen storage. Im-

provements could be made in the kinetics of both hydrogen release and uptake through nanostructuring of these materials or through the use of catalysts.

Chapter 5

Reactions of $LiBH_4$ with $LiNH_2$, Li_2NH and Li_3N

5.1 Introduction

In the Li-N-H system Li_2NH acts as an intermediate between $LiNH_2$ and Li_3N as shown in equation 3.1. This makes the system more readily reversible as it is possible to cycle between $LiNH_2$ and Li_2NH without going to Li_3N which has less favourable thermodynamics for desorption and slow hydrogenation kinetics.

Reaction of $LiBH_4$ with $LiNH_2$ is known to form pure phases at ratios of 1:1 and 1:3; the products from these reactions are $Li_2BH_4NH_2$[72] and $Li_4BH_4(NH_2)_3$[73], respectively. In the Li-B-N-H system, unlike the Li-N-H system, there are no known hydrogen deficient intermediates and the decomposition product of Li_3BN_2 (equation 5.1) is currently known to have limited reversibility[74]. Li_3BN_2 is known to form three polymorphs, the $P2_1/c$[116] and $P4_22_12$[117] polymorphs, which can be formed from Li_3N and BN, and the $I4_1/amd$[118] polymorph formed from milled $LiBH_4$ and $LiNH_2$.

$$LiBH_4 + 3LiNH_2 \leftrightharpoons Li_4BH_4(NH_2)_3 \leftrightharpoons Li_3BN_2 + LiNH_2 + 4H_2 \uparrow \qquad (5.1)$$

In this section I have investigated reactions of $LiBH_4$ with $LiNH_2$ at varying stoichiometries and temperatures, and studied the decomposition properties and products. The reactions of $LiBH_4$ with Li_2NH and Li_3N were also be investigated to look at these previously unstudied parts of the system in the hope of finding new intermediates of interest.

5.2 Experimental

Samples of ground mixtures of lithium borohydride (Sigma-Aldrich, 95% purity) and either lithium amide (Sigma-Aldrich, 95% purity), lithium imide (made from lithium amide and lithium hydride) or lithium nitride (Sigma-Aldrich, 95% purity) were prepared in an argon filled glove box (<10 ppm O_2, <1 ppm H_2O). The samples were prepared in various stoichiometries and heated in quartz tubes under flowing argon at temperatures up to 600 °C for up to 12 hours.

Powder X-ray diffraction data were collected using a Bruker D8 instrument in transmission geometry with a wavelength of 1.54059 Å (chapter 2.4.1). Raman spectroscopy, scanning electron microscopy (SEM) and temperature programmed desorption coupled to a mass spectrometer (TPD-MS) were also performed on the samples (chapter 2).

5.3 $xLiBH_4 + yLiNH_2$

5.3.1 Powder X-ray Diffraction

The powder diffraction data were analysed using the computer programme Topas[108]. A zero point error and an 18 point Chebyshev background were refined for each diffraction pattern. For each of the known phases present, lattice parameters, along with a pseudo-Voigt peak shape were refined. Where available, atomic positions and thermal parameters were taken from reported structures and a full Rietveld refinement was performed on the structures. The estimated weight per-

centage and standard error for each compound present were reported by Topas and were converted into mole percent values.

The known phase $Li_4BH_4(NH_2)_3$[73] forms pure from a reaction of $LiBH_4$ and $3LiNH_2$ heated at 190 °C for 12 hours under flowing argon. The sample was reground and annealed at the same temperature to improve crystallinity (fig: 5.1).

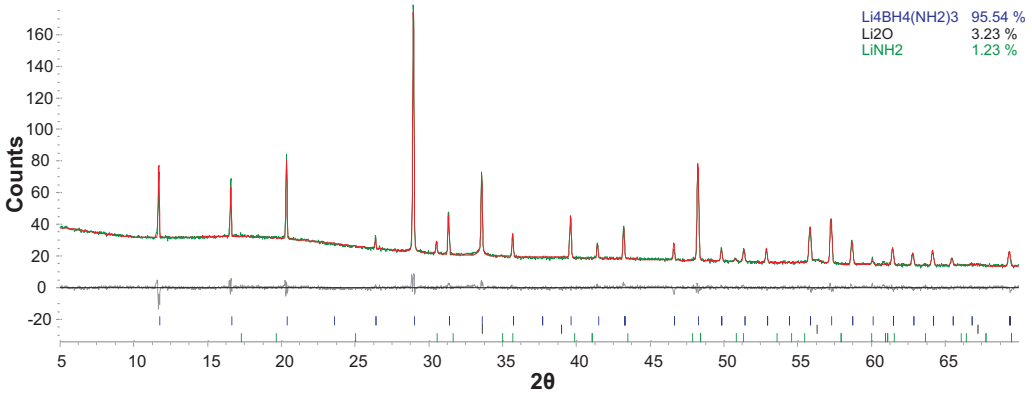

Figure 5.1: Powder X-ray diffraction pattern of $Li_4BH_4(NH_2)_3$ showing observed (green), calculated (red) and difference (grey) plots. Peak positions for $Li_4BH_4(NH_2)_3$ are shown (blue).

The decomposition of $Li_4BH_4(NH_2)_3$ gives a mixture of the $I4_1/amd$ and $P2_1/c$ polymorphs of Li_3BN_2 [73]; to investigate possible reversibility in the system the synthesis of phase pure samples of all three polymorphs of Li_3BN_2 was attempted. $LiBH_4$ and $LiNH_2$ were heated together in a 1:2 ratio at various temperatures from 200 to 600 °C; all reactions had a 2 °C min^{-1} ramp rate and were held at temperature for 12 hours. The resultant X-ray diffraction patterns were analysed and the products formed at each temperature can be seen in figure 5.2.

At high temperatures (>550 °C) it can be seen that the $P4_22_12$ polymorph of Li_3BN_2 formed pure. This can be confirmed by looking at the individual XRD pattern from reaction at 600 °C (fig. 5.3).

In the temperature range of 225-525 °C we see the formation of both the

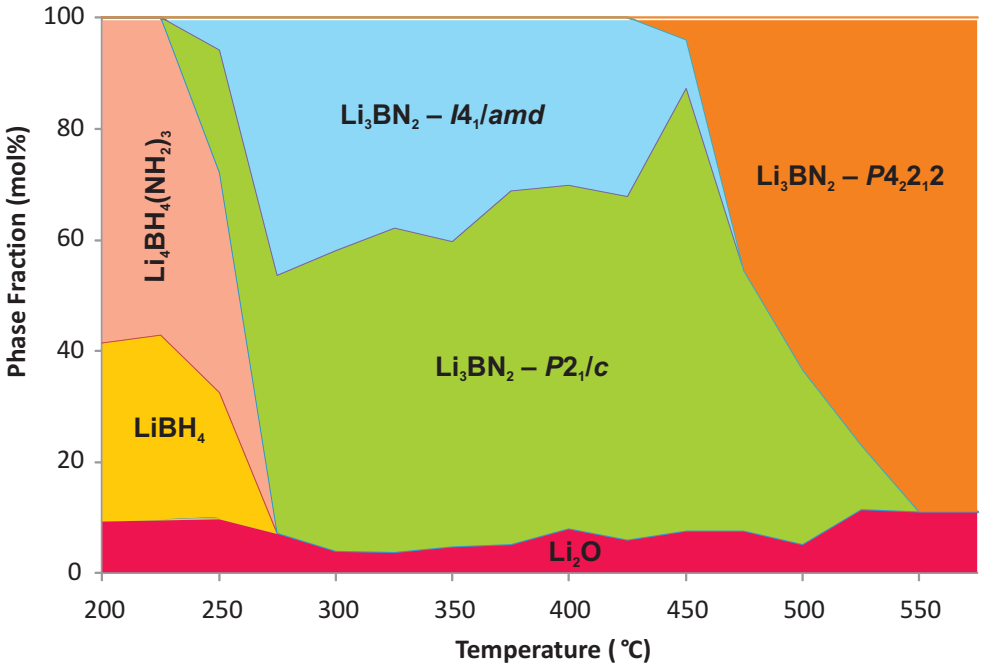

Figure 5.2: Phase map of the products from reaction of $LiBH_4$ + $2LiNH_2$ at different temperatures. All reactions had a 2 °C min^{-1} ramp rate and were held at temperature for 12 hours.

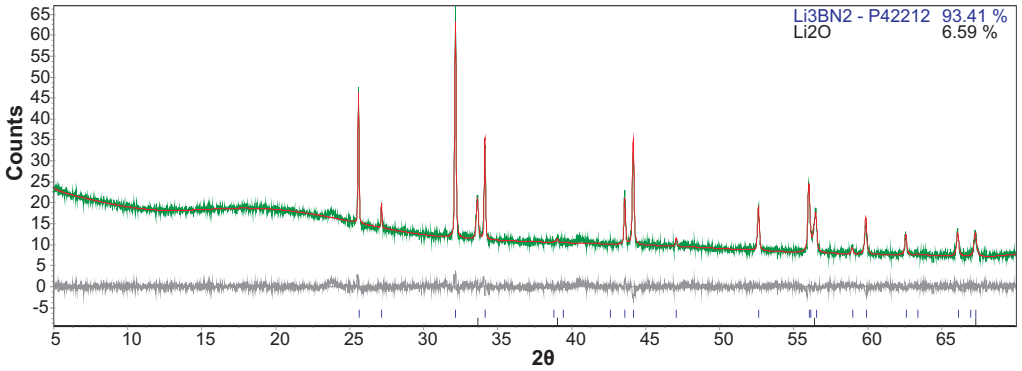

Figure 5.3: Powder X-ray diffraction pattern of Li_3BN_2 ($P4_22_12$) made at 600 °C showing observed (green), calculated (red) and difference (grey) plots. Peak positions for Li_3BN_2($P4_22_12$) are shown (blue).

$I4_1/amd$ and $P2_1/c$ polymorphs (fig. 5.2). It can be seen, however, that the $P2_1/c$ polymorph began to form at slightly lower temperatures compared to the $I4_1/amd$ polymorph. Reactions were therefore performed at a constant temperature while varying the ramp rate to investigate whether this had an effect on the ratio of polymorphs of Li_3BN_2 (fig. 5.4).

The figure shows that at slow ramp rates of 1-2 °C min^{-1} the $P2_1/c$ polymorph, or a mix with the $I4_1/amd$ polymorph is favoured. Conversely a fast ramp rate of 3-5 °C min^{-1} mostly favours formation of the $I4_1/amd$ polymorph, with a ramp rate of 10 °C min^{-1} forming a pure product. The diffraction pattern of the products of this reaction at 350 °C with a ramp rate of 10 °C min^{-1} is shown in figure 5.5.

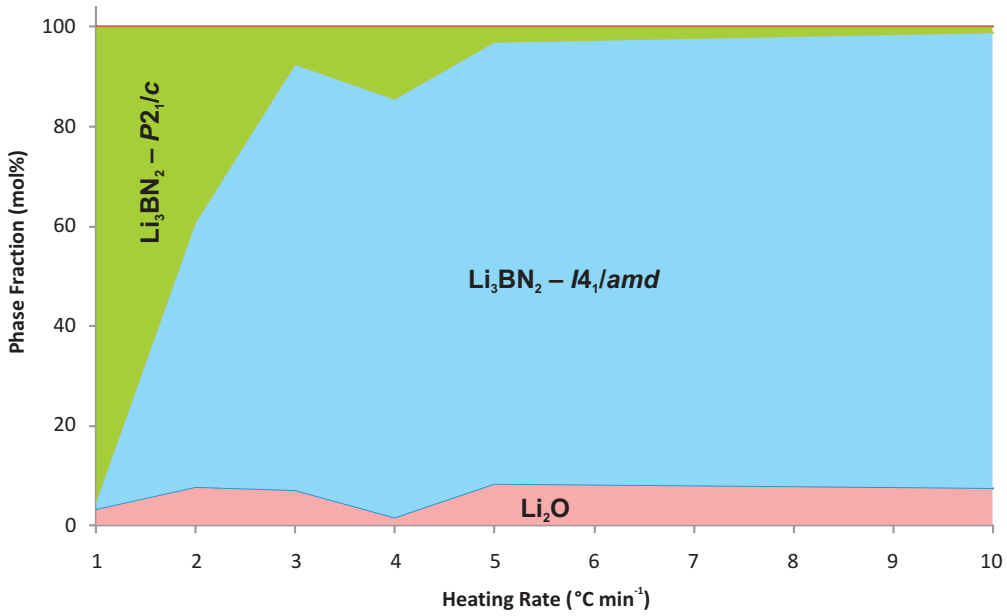

Figure 5.4: Phase map of the products from reaction of $LiBH_4$ + $2LiNH_2$ with varying ramp rate. All reactions were heated to 350 °C and held for 12 hours.

A similar experiment was carried out at 450 °C where it appeared that the $P2_1/c$ polymorph may form most pure (fig. 5.6). This shows that at this temperature a slow ramp rate of 1 °C min^{-1} favoured the formation of the $P2_1/c$ polymorph of Li_3BN_2, whereas faster heating rates of 2 °C min^{-1} or greater

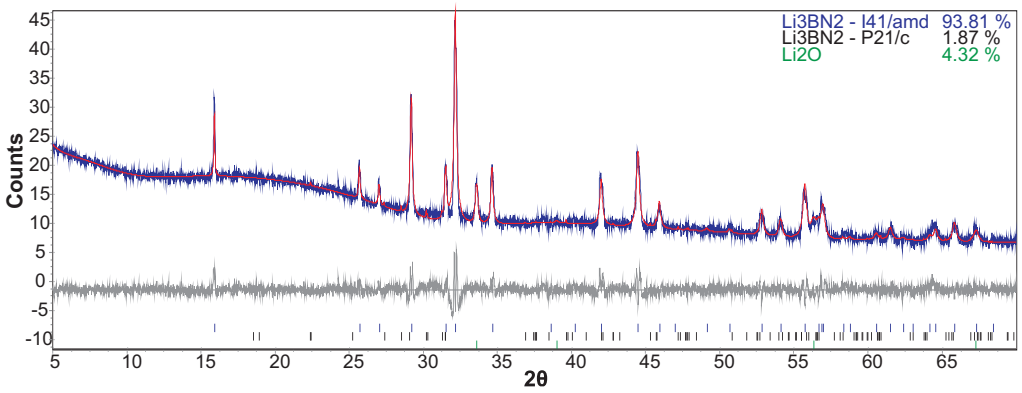

Figure 5.5: Powder X-ray diffraction pattern of Li_3BN_2 ($I4_1/amd$) made at 350 °C with ramp rate of 10 °C min^{-1} showing observed (blue), calculated (red) and difference (grey) plots. Peak positions for Li_3BN_2($I4_1/amd$) are shown (blue).

formed a mixture of the $P2_1/c$ and the $I4_1/amd$ polymorphs.

The $P2_1/c$ polymorph can be seen to form at its most pure (>95 mol%) from reaction of $LiBH_4$ + $2LiNH_2$ at 450 °C with a ramp rate of 1 °C min^{-1} (fig. 5.7).

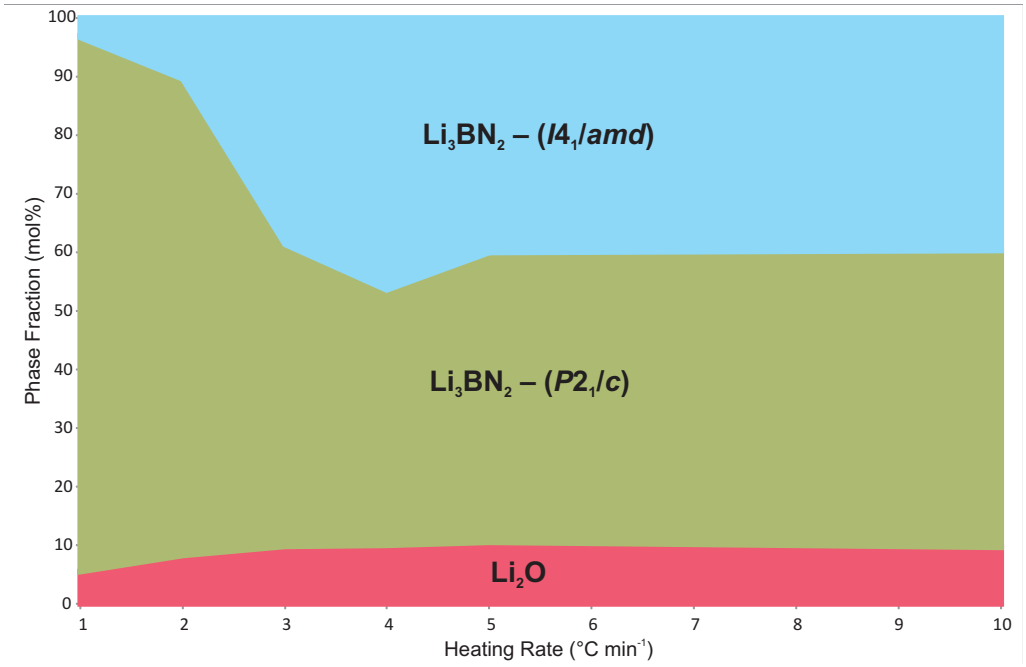

Figure 5.6: Phase map of the products from reaction of $LiBH_4$ + $2LiNH_2$ with varying ramp rate. All reactions were heated to 450 °C and held for 12 hours.

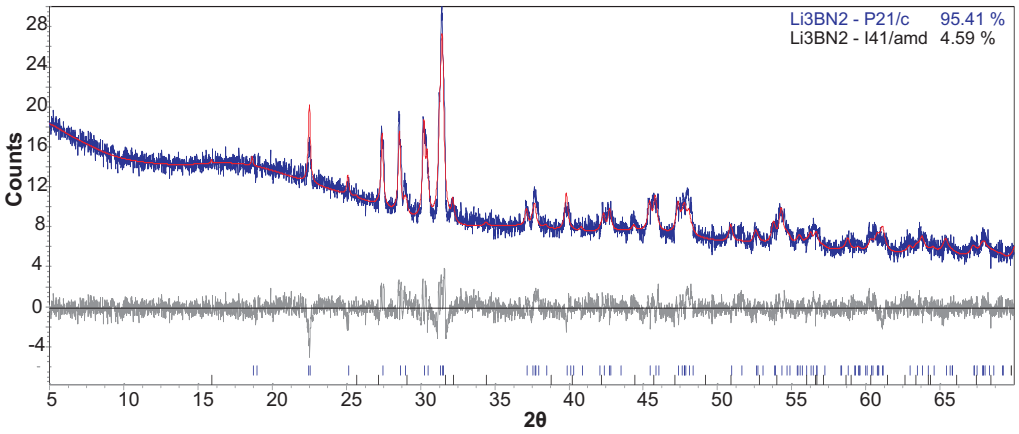

Figure 5.7: Powder X-ray diffraction pattern of Li_3BN_2 ($P2_1/c$) made at 450 °C with ramp rate of 1 °C min^{-1} showing observed (blue), calculated (red) and difference (grey) plots. Peak positions for $Li_3BN_2(P2_1/c)$ are shown (blue).

5.3.2 Temperature Programmed Desorption

In this section the hydrogen desorption properties of mixtures of $LiBH_4$ and $LiNH_2$ were tested. The molar ratios of the reactants were varied, as was the heating rate, however, all samples were heated to 400 °C.

The gas release from the reaction of $LiBH_4 + 2LiNH_2$ is shown in figure 5.8. It can be seen that the onset of hydrogen release is at around 240 °C, peaking at 330 °C; this is also accompanied by a small amount of ammonia release. It was noted that the hydrogen release from this reaction occurred at a slightly lower temperature than that of the reaction at a 1:3 molar ratio, made to form $Li_4BH_4(NH_2)_3$. It can be seen that there is a slight shoulder on the low temperature side of the hydrogen release peak in the TPD-MS trace (fig. 5.8), which suggests a two-step hydrogen release process.

Due to this fact desorption reactions were carried out with different molar ratios of the type $xLiBH_4 + yLiNH_2$ to investigate the effect on the desorption temperature. The results are shown below in figure 5.9. It can be seen that the more borohydride-rich compositions released hydrogen at a lower temperature compared to the more amide-rich systems. The total shift seen in these

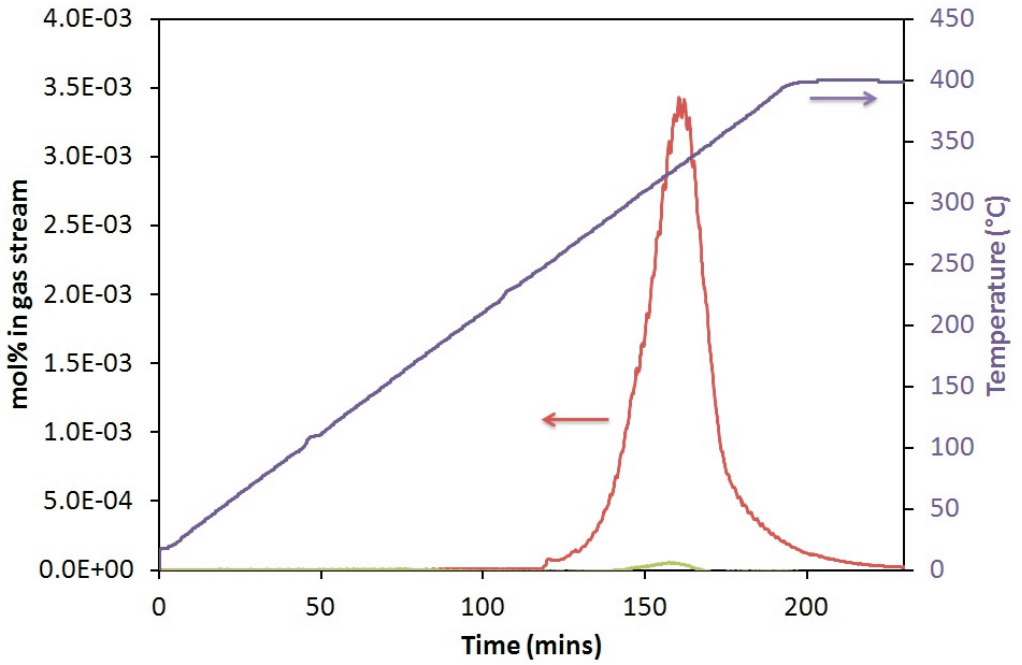

Figure 5.8: TPD-MS traces of the decomposition of $LiBH_4 + 2LiNH_2$, heated at 2 °C min^{-1} to 400 °C. Traces for hydrogen (red), ammonia (green) and temperature (purple) are shown.

experiments was around 40 °C.

5.3.3 B=N bond strength

This section reports the results of Raman spectroscopy performed on the three polymorphs of Li_3BN_2, the differences in vibrational frequency of the polymorphs will correspond to the differences in the B=N bond length (and therefore bond strength), which will be required to be broken for a rehydrogenation reaction to occur. These results will be compared to those from Topas in this work (section 5.3.1), where full Rietveld refinements were performed on the pure polymorphs and the B=N bond lengths taken from the resultant structures. They will also be compared to values taken from the literature [118, 119].

The BN_2^{3-} group is linear with the point group $C_{\infty v}$ and is isoelectronic with CO_2. While the infinite nature of the groups makes the group theory difficult, it can easily be seen that only the symmetric stretch (figure 5.10) causes a change in

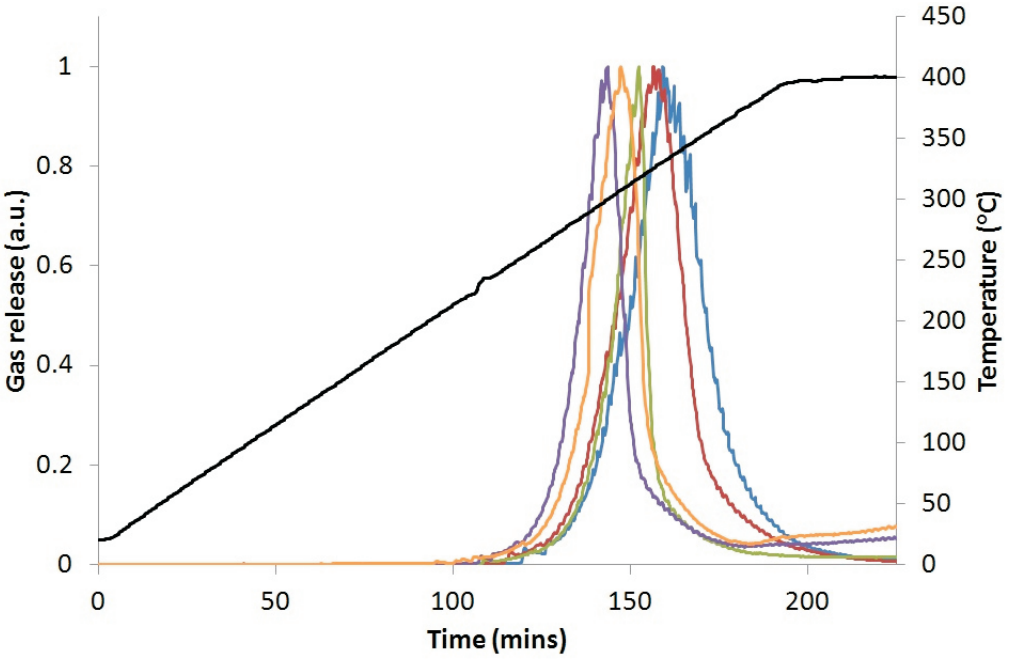

Figure 5.9: TPD-MS traces of the decomposition of $xLiBH_4 + yLiNH_2$, heated at 2 °C min^{-1} to 400 °C. Showing traces for x:y = 3:1 (purple), 2:1 (orange), 1:1 (green), 1:2 (red), 1:3 (blue) and temperature (black).

the polarisability of the molecule and therefore there should only be one Raman active band.

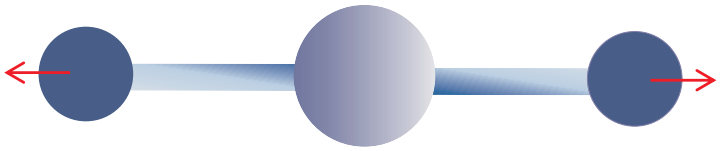

Figure 5.10: Representation of the BN_2 symmetric stretch.

The Raman spectra taken for the three polymorphs of Li_3BN_2 are given below in figure 5.11, and show the single expected band for the $BN_2{}^{3-}$ symmetric stretch. The wavenumbers of these peaks are $I4_1/amd$ = 1050.5 cm^{-1}, $P2_1/c$ = 1067.0 cm^{-1} and $P4_22_12$ = 1054.5 cm^{-1}. These results correspond to relative B-N bond lengths of $I4_1/amd > P4_22_12 > P2_1/c$.

It can be seen from reference to table 5.1 that the relative bond lengths from my Raman data match the bond lengths obtained from the refined structures in

Topas, which in turn closely match experimental values from the literature[113, 119]. The values calculated in the literature keep the $P2_1/c$ polymorph as having the shortest B=N bond but give the $I4_1/amd$ and $P4_22_12$ polymorphs the same bond length.

The results show that the $I4_1/amd$ polymorph of Li_3BN_2 has the longest B=N bond length while the $P2_1/c$ polymorph has the shortest. This therefore suggests that the $I4_1/amd$ polymorph, with the longest and therefore weakest B=N bond should most easily hydride, via the breaking of the B=N bond and the formation of BH_4^- and NH_2^- units.

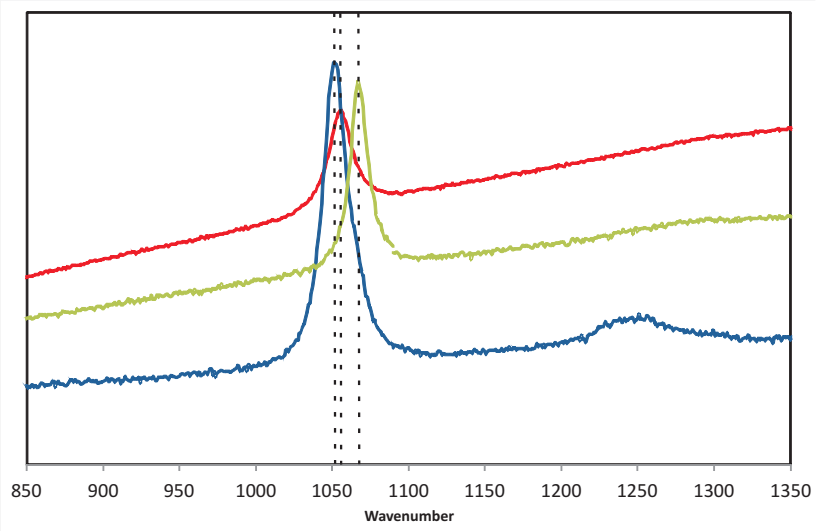

Figure 5.11: Raman spectra of Li_3BN_2 showing $I4_1/amd$ (blue), $P4_22_12$ (red) and $P2_1/c$ (green).

Table 5.1: B=N bond lengths from refinements done in this work using Topas, as refined in the literature and as calculated in the literature.

Polymorph	Topas	Lit. expt[113, 119]	Lit. calc[113]
$I4_1/amd$	1.379	1.382	1.346
$P2_1/c$	1.334	1.336	1.341
$P4_22_12$	1.336	1.338	1.346

5.3.4 SEM

Scanning electron microscopy was performed on the three polymorphs of Li_3BN_2 as made previously in this work (chapter 5.3.1). This was done as an attempt to investigate possible differences in particle size and morphology between the polymorphs, which could lead to differences in the kinetics of hydrogen uptake.

The $I4_1/amd$ polymorph was seen to form irregular shaped particles (fig. 5.12) between 2 and 5 μm in size. Some of the particles can be seen to have strong triangular edges, suggesting that they may favour an octahedral crystal habit.

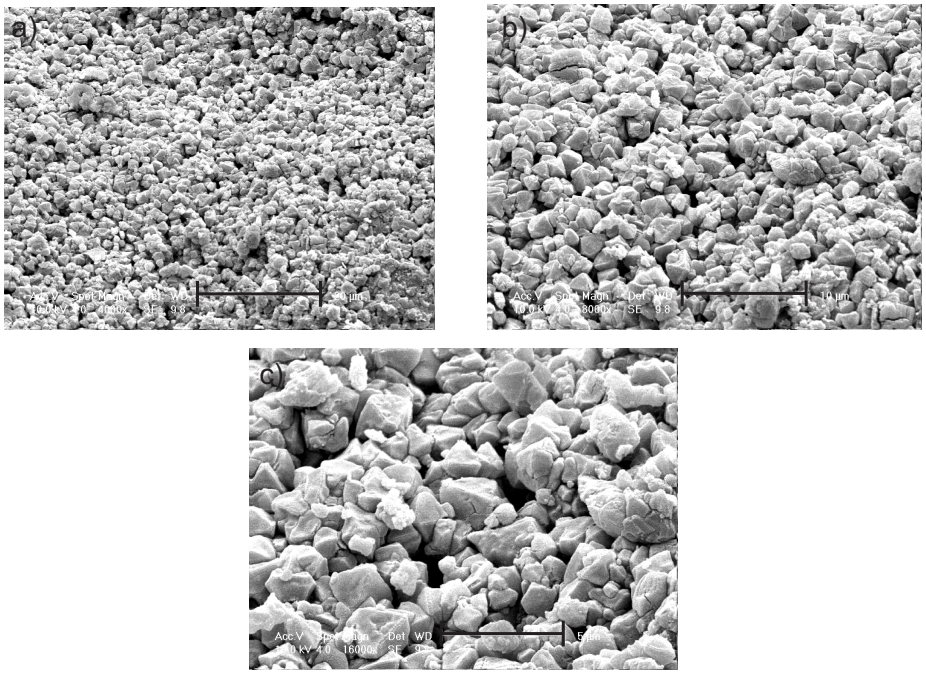

Figure 5.12: Scanning electron microscopy images of Li_3BN_2 ($I4_1/amd$), the scale of the images is at a) 20 μm b) 10 μm and c) 5 μm.

The $P2_1/c$ polymorph of Li_3BN_2 formed variously shaped particles, including rod-like particles measuring between 5 and 8 μm (fig. 5.13).

The $P4_22_12$ polymorph of Li_3BN_2 formed clumps or globules of particles with no defined edges, although there did seem to be a few smaller particles as well (fig. 5.14). As this is the high temperature form of Li_3BN_2, formed at 600 °C,

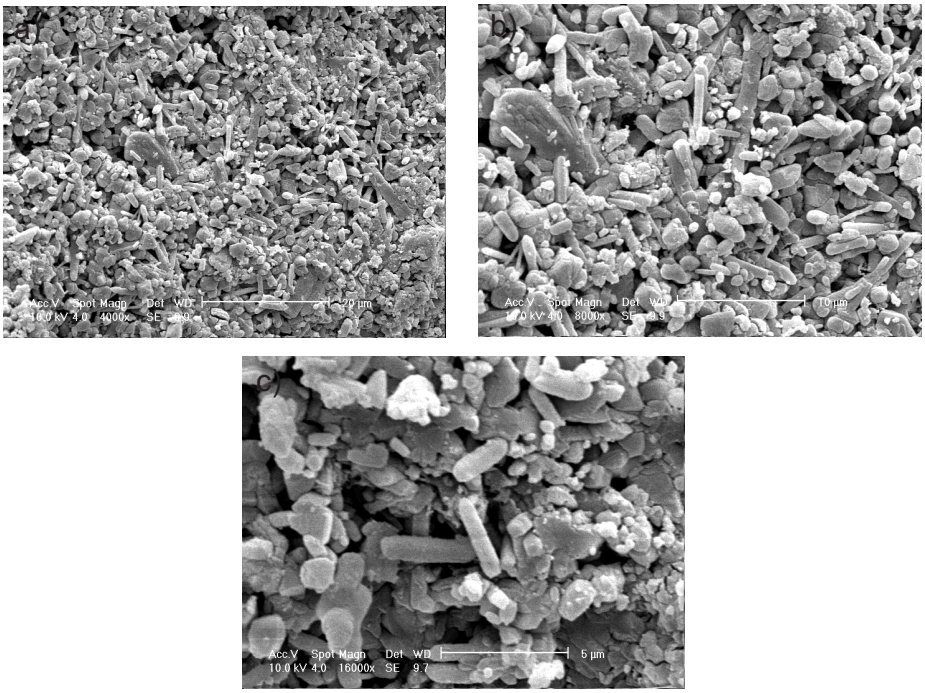

Figure 5.13: Scanning electron microscopy images of Li_3BN_2 ($P2_1/c$), the scale of the images is at a) 20 μm b) 10 μm and c) 5 μm.

these rounded shapes are consistent with high temperature sintering.

These data would suggest that if particle size is the predetermining factor in the kinetics of hydrogenation of different polymorphs of Li_3BN_2 then there would be significant differences between the polymorphs. The $P4_22_12$ polymorph would be expected to have the slowest kinetics as it doesn't form distinct particles. The formation of clumps of particles into essentially much larger particles would greatly slow the diffusion of hydrogen into the material. Both the $I4_1/amd$ and $P2_1/c$ polymorphs form more distinct particles, the $P2_1/c$ particles were slightly larger than those of the $I4_1/amd$ polymorph and have a more varied size and shape. For this reason it would be expected that the $I4_1/amd$ polymorph of Li_3BN_2 may have the fastest kinetics of hydrogen uptake. It should be noted that it is unclear from these images as to whether it is the crystallite size which is being seen, or whether they are showing ground, polycrystalline aggregates. Further analysis of these materials would be required to ascertain whether or not

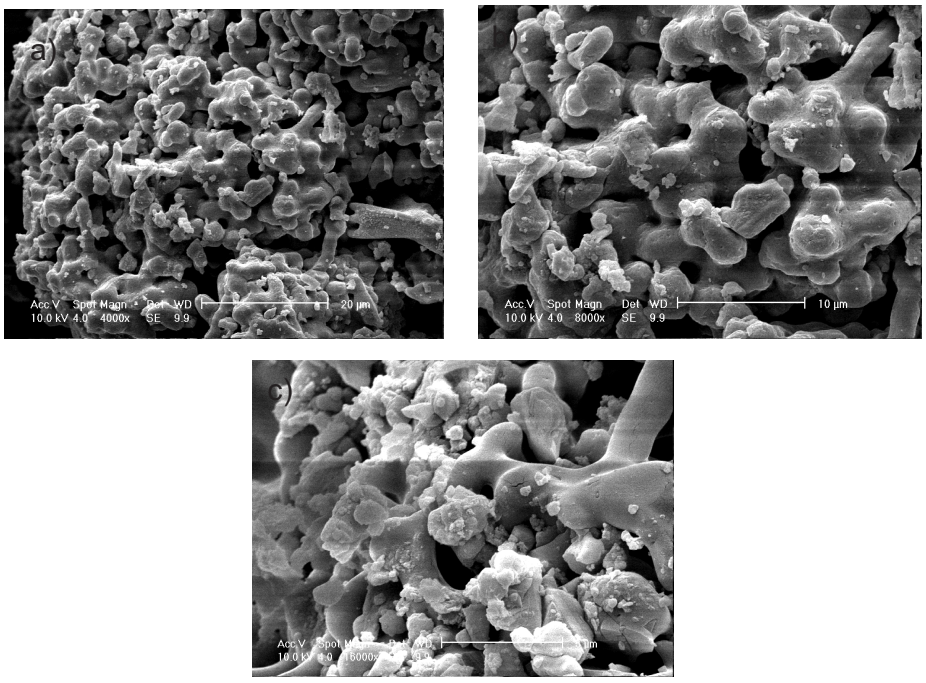

Figure 5.14: Scanning electron microscopy images of Li_3BN_2 ($P4_22_12$), the scale of the images is at a) 20 μm b) 10 μm and c) 5 μm.

the crystallite size is smaller than seen in this work, which could have a significant effect on the hydrogenation properties.

If this data is taken in parallel with the data on the B=N bond strengths (chapter 5.3.3) then we would perhaps expect the $I4_1/amd$ polymorph of Li_3BN_2 to rehydride most easily as it had the longest B=N bond and the smallest particle size. The $P2_1/c$ and $P4_22_12$ polymorphs of Li_3BN_2 may be expected to rehydride at similar rates as, while the $P4_22_12$ polymorph has a slightly longer B=N bond, it has the largest particle size, slowing the kinetics of hydrogenation.

5.3.5 Hydrogenation

In this section the rehydriding properties of the three polymorphs of Li_3BN_2 were tested under 100 bar H_2; all of the samples were heated to temperatures from 150 °C to 350 °C for between 24 and 140 hours. The mass was taken before and after the reaction to judge any weight gain as well as comparison of the diffraction

patterns.

For use in mobile fuel cell applications it can be calculated that the desorption reaction must be endothermic with $\Delta H \approx 20$ - 50 kJ/(mol H_2) if the system is going give off and take up hydrogen under reasonable conditions. For the reaction shown below (equation 5.2) the calculated enthalpy of formation of Li_3BN_2 is ΔH = 11.1 kJ/(mol H_2)[120]. While this is obviously outside of the desired range, the thermodynamics suggest that hydrogenation should be possible, however high pressures may be required. The kinetics of the materials could still be an issue with regards to the hydrogenation process; increasing the temperature will improve the kinetics, however this will have a thermodynamic effect, meaning even higher pressures would be required.

$$LiBH_4 + 2LiNH_2 \rightarrow Li_3BN_2 + 3H_2 \uparrow \tag{5.2}$$

The samples were first heated to 150 °C for 24 hours, the diffraction patterns from these hydrogenation attempts showed no change from the starting products so another reaction was tried heating the samples to 200 °C for 48 hours. Figure 5.15 shows the X-ray diffraction patterns of the products from the heating at 200 °C for 48 hours. This shows that there was only the starting polymorph of Li_3BN_2 present in each pattern, telling us that there is no hydrogen uptake under these conditions. This is confirmed as there was no change in the mass of these samples following the experiment.

The samples were then heated to 300 °C and 350 °C, the results again showed no change from the starting polymorphs of Li_3BN_2. Making the assumption that these materials were not going to rehydride under practical laboratory conditions of temperature and pressure it was decided to test whether any small amount of hydrogen uptake would be seen over longer periods of time. Figure 5.16 shows the diffraction patterns of the products from heating each polymorph of Li_3BN_2 at 300 °C for 140 hours under 100 bar H_2. Again this shows no change in the

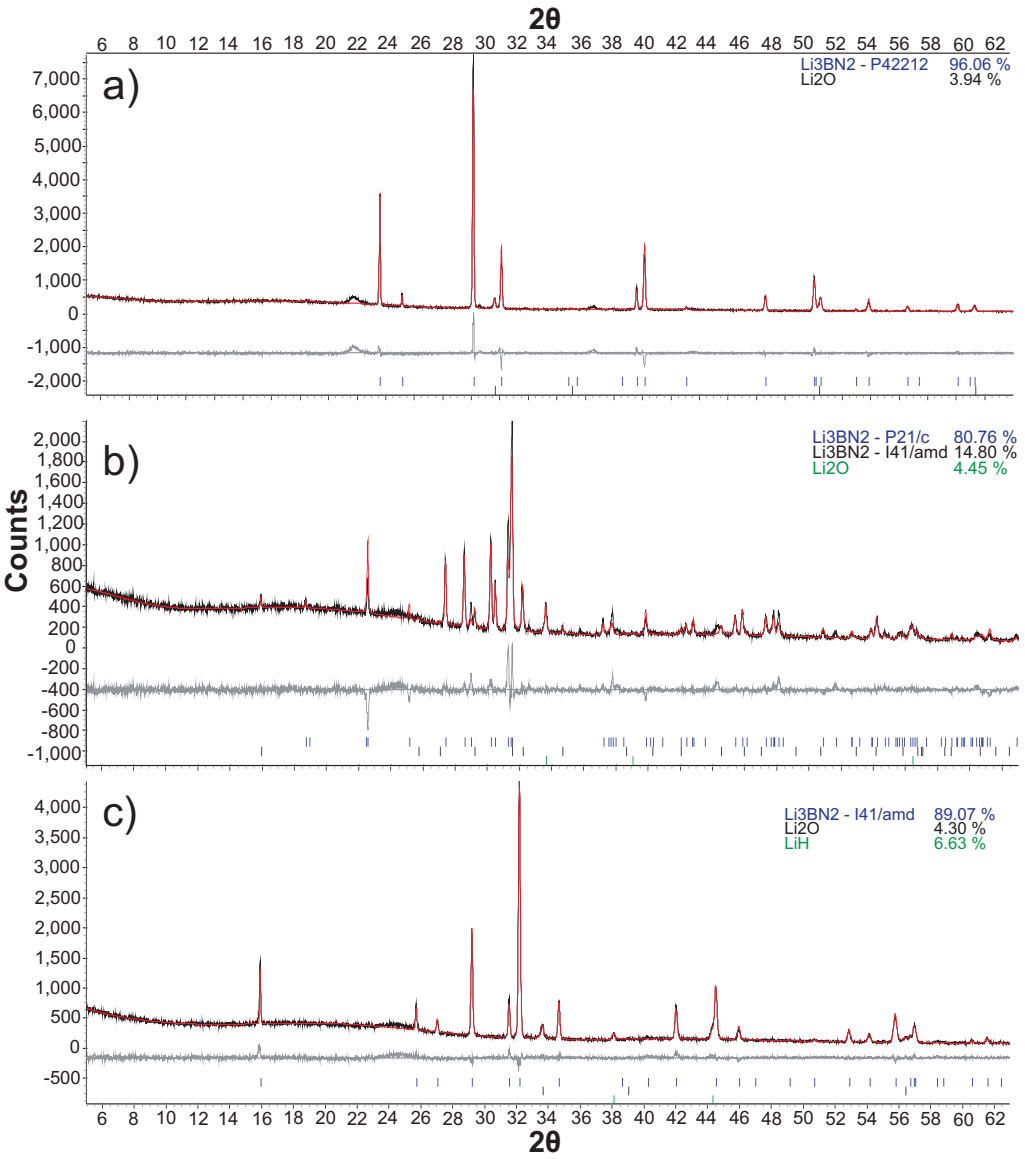

Figure 5.15: Powder X-ray diffraction patterns of a) $P4_22_12$, b) $P2_1/c$ and c) $I4_1/amd$ Li_3BN_2, heated under 100 bar H_2 at 200 °C for 48 hours. Observed (black), calculated (red) and difference (grey) plots, and peak positions for each polymorph of Li_3BN_2 are shown (blue).

materials under these conditions.

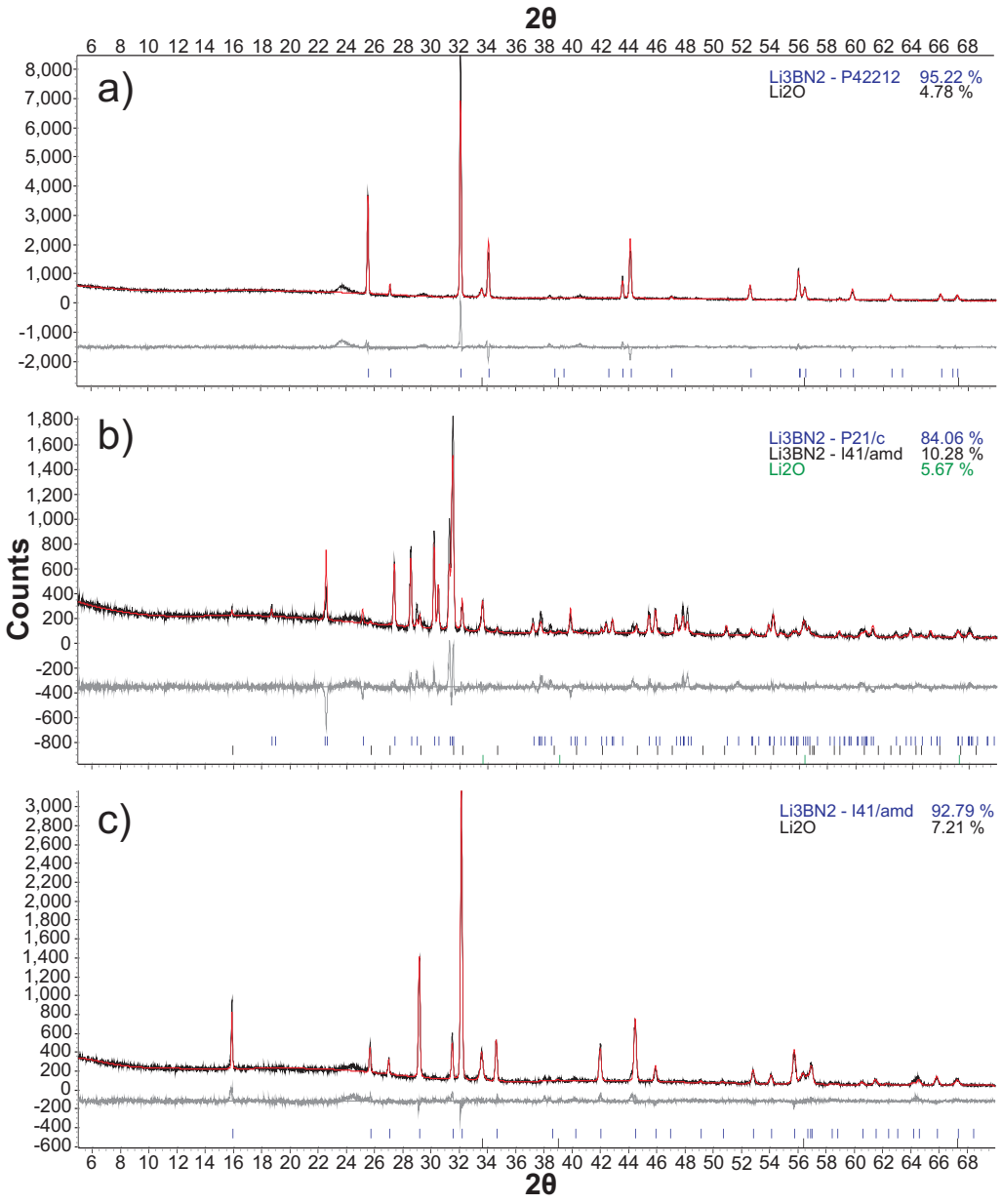

Figure 5.16: Powder X-ray diffraction patterns of a) $P4_22_12$, b) $P2_1/c$ and c) $I4_1/amd$ Li_3BN_2, heated under 100 bar H_2 at 300 °C for 140 hours. Observed (black), calculated (red) and difference (grey) plots, and peak positions for each polymorph of Li_3BN_2 are shown (blue).

It has been shown in the literature that by incorporation of the Li_3BN_2 material into a porous carbon aero-gel, thereby decreasing the particle size, some

level of hydrogen uptake can be seen[74]. In this work around 3.5 wt % H_2 uptake was seen in 12 hours at 300 °C under 50 bar H_2. Because of this it was decided to decrease the particle size of these materials through ball-milling of the samples for five hours. Figure 5.17a shows the $I4_1/amd$ polymorph of Li_3BN_2 after ball-milling; it can been seen that there was an increase in the width of the peaks, consistent with a decrease in grain size. This ball-milled sample was then heated under 100 bar H_2 at 300 °C for 140 hours; it can be seen that there was still no evidence for hydrogen uptake (fig. 5.17b). Similar results have been seen for the $P2_1/c$ and $P4_22_12$ polymorphs of Li_3BN_2; the diffraction patterns of the ball-milled samples, heated under 100 bar H_2 at 300 °C for 140 hours may be seen in figures A.3 and A.4, respectively.

5.4 xLiBH$_4$ + yLi$_2$NH

5.4.1 Powder X-ray Diffraction

The powder diffraction data for this section was analysed with the same technique and strategy as in section 5.3.1. Reactions in this section were carried out at various stoichiometries, both $LiBH_4$ and Li_2NH rich, at temperatures between 100 and 250 °C.

Upon heating at temperatures of up to 100 °C for up to 24 hours, no reaction was observed, the diffraction patterns from the reactions showing purely the starting materials. From temperatures of 125 °C unidentified peaks were seen in the diffraction pattern (fig. 5.18); these have been identified as corresponding to two separate phases, which are highlighted separately in figures 5.18a and 5.18b.

The observed peak positions from the X-ray diffraction of the two new imide-borohydride phases were run through the indexing routine of the computer program Topas. This gave the most likely assignment of one of the new phases as an orthorhombic unit cell, space group $Pnma$ with lattice parameters $a = 10.14$ Å, $b = 11.48$ Å $c = 7.03$ Å. The lattice parameters were then refined using a

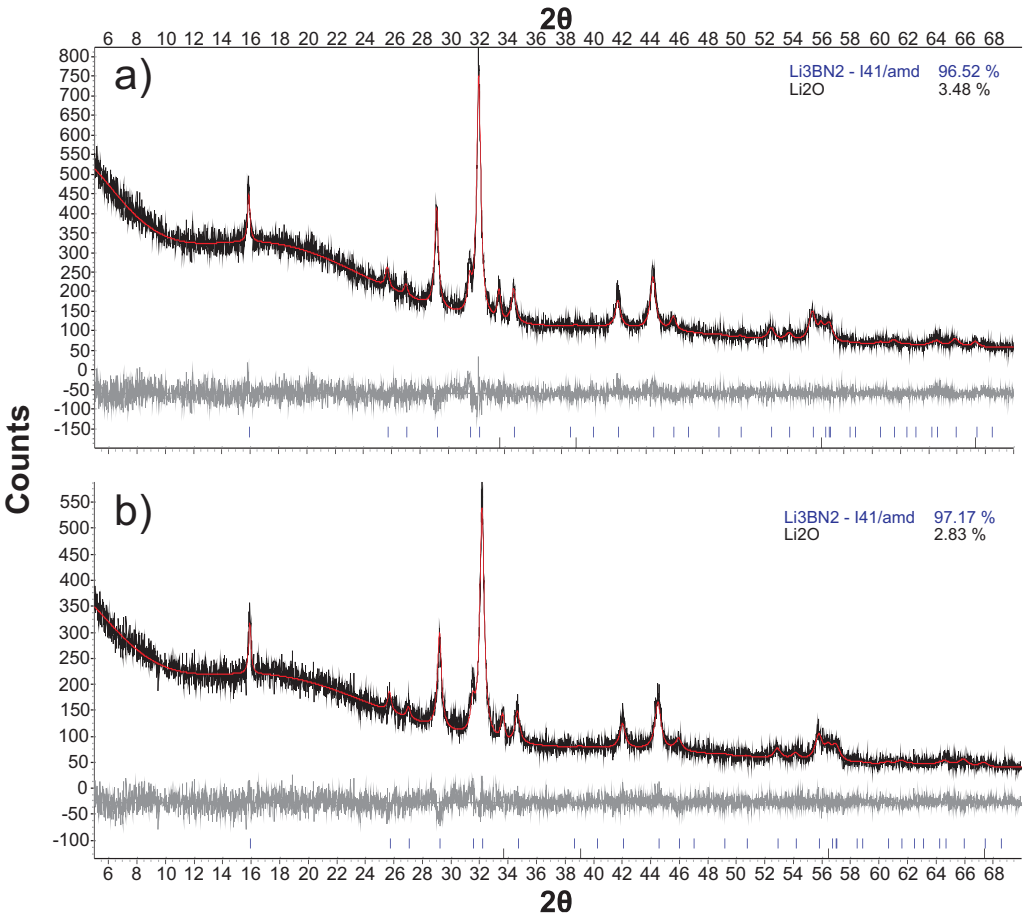

Figure 5.17: Powder X-ray diffraction patterns of ball milled Li_3BN_2 ($I4_1/amd$) a) before and b) after heating under 100 bar H_2 at 300 °C for 140 hours. Observed (black), calculated (red) and difference (grey) plots, and peak positions for Li_3BN_2 ($I4_1/amd$) are shown (blue).

Pawley fit in Topas; this fit is shown in figure 5.18a. The Pawley fit allowed for more accurate lattice parameters of a = 10.1459(9) Å, b = 11.483(1) Å and c = 7.0302(4) Å to be obtained, with a unit cell volume of 819.1(1) Å^3. The other new phase gave the most likely assignment as a cubic unit cell, space group $P2_3$ with lattice parameter a = 5.60 Å. This parameter was then also refined in Topas using a Pawley fit, giving a more accurate value of a = 5.609(2) Å with a cell volume of 176.51(1) Å^3; this fit is shown in figure 5.18b. As neither phase could be isolated and formed pure it is not possible to build an accurate structural model as the stoichiometry of each phase is unknown. However, is it noted

that the new orthorhombic imide-borohydride phase has the same space group as $LiBH_4$ (*Pnma*) with a unit cell volume of just under four times that of the $LiBH_4$ volume (819.1 Å^3 and 217.87 Å^3 respectively). It is therefore suggested that this may have a similar structure with smaller NH^{2-} substituting in place of some of the BH_4^- units. The new cubic phase has a significantly larger unit cell than that of Li_2NH (roughly 40% larger) but appears to have a similar structure with substitution of BH_4^- units in place of NH^{2-}.

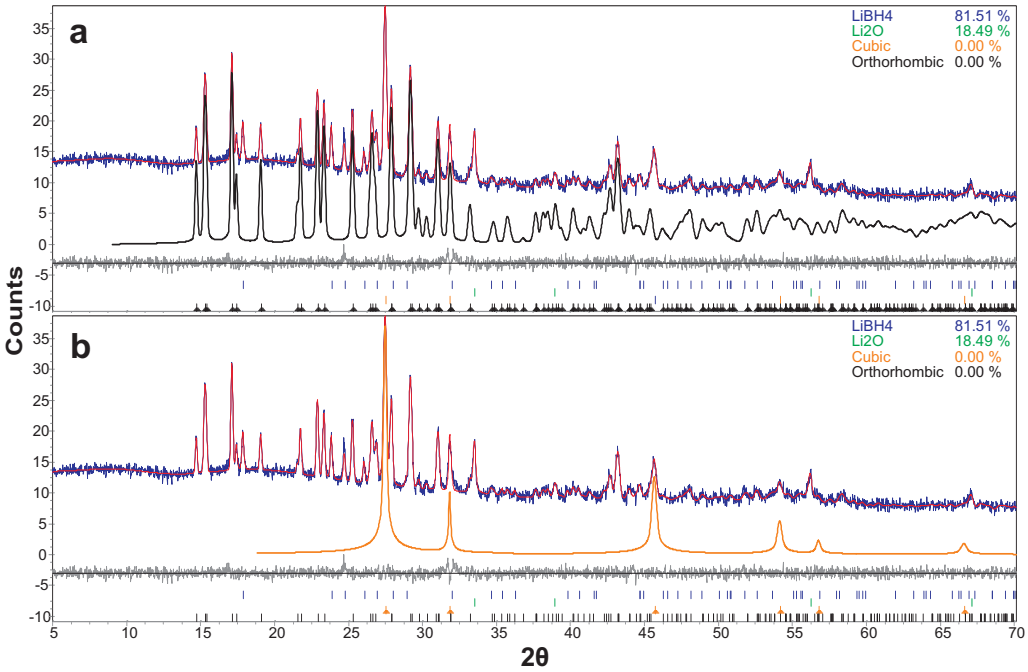

Figure 5.18: Powder X-ray diffraction pattern of the products from the reaction of $LiBH_4 + Li_2NH$ at 125 °C for 12 hours, showing observed (blue), calculated (red) and difference (grey) plots. Pattern (a) has the orthorhombic phase highlighted, pattern (b) the cubic phase.

Reactions at higher temperatures of 200 °C showed the only new phase present was the cubic phase (fig. 5.19). It was not possible to isolate the orthorhombic phase, with the cubic phase also being present. Attempts were made at making the new cubic phase pure by going to a Li_2NH rich stoichiometry, however, no phase could be isolated with no starting material remaining.

Reaction at temperatures between 215 and 230 °C (fig. 5.20) showed the

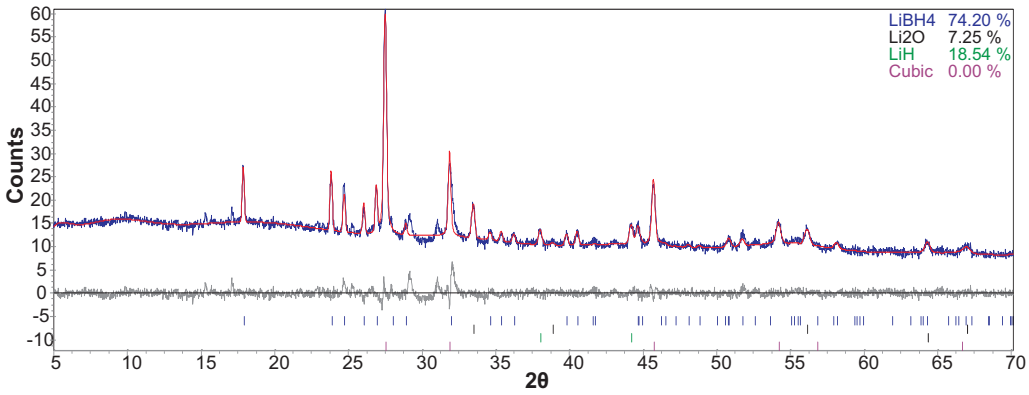

Figure 5.19: Powder X-ray diffraction pattern of the products from the reaction of $LiBH_4$ + Li_2NH at 200 °C for 12 hours, showing observed (blue), calculated (red) and difference (grey) plots. Peak positions for new cubic phase are shown in purple.

formation of the mixed lithium borohydride-amide phase, $Li_4BH_4(NH_2)_3$ [73]. This suggests that some Li_2NH was reduced to $LiNH_2$ by the $LiBH_4$ (a previously unreported phenomenon) before then reacting with the $LiBH_4$. Alternatively, Li_2NH may have been hydrogenated by H_2 released upon the formation of Li_3BN_2.

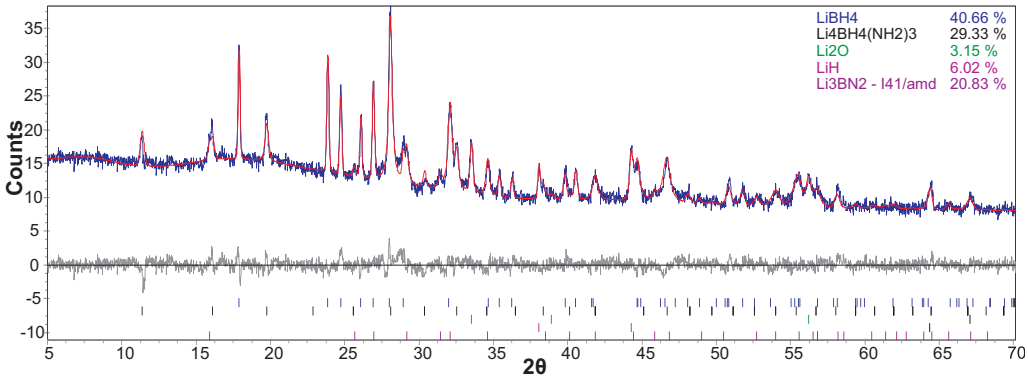

Figure 5.20: Powder X-ray diffraction pattern of the products from the reaction of 3$LiBH_4$ + 2Li_2NH at 215 °C for 12 hours, showing observed (blue), calculated (red) and difference (grey) plots. Peak positions for $Li_4BH_4(NH_2)_3$ are shown in black.

At temperatures of greater than 230 °C the $Li_4BH_4(NH_2)_3$ was seen to decompose to give the $I4_1/amd$ polymorph of Li_3BN_2 with remaining $LiBH_4$ (fig. 5.21).

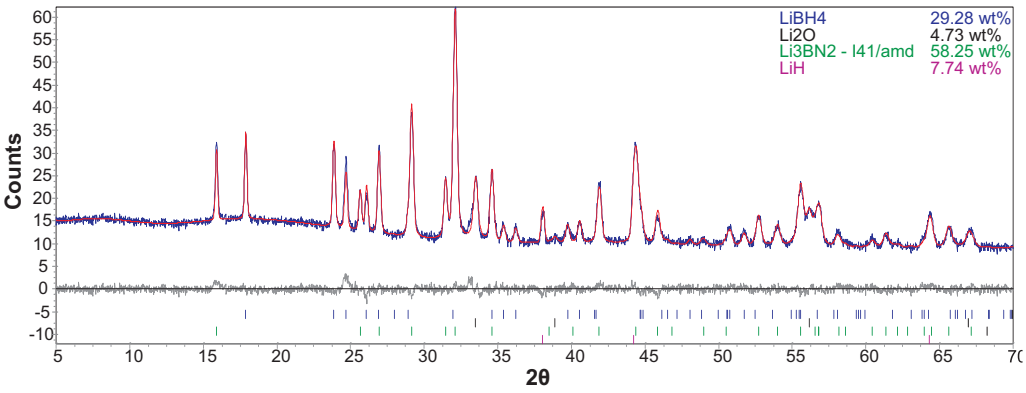

Figure 5.21: Powder X-ray diffraction pattern from reaction of $3LiBH_4 + 2Li_2NH$ at 250 °C for 12 hours, showing observed (blue), calculated (red) and difference (grey) plots. Peak positions for $Li_3BN_2(I4_1/amd)$ are shown in green.

5.4.2 Temperature Programmed Desorption

Thermal desorption data from a mixture of $LiBH_4 + Li_2NH$ heated at a ramp rate of 2 °C min^{-1} to a temperature of 350 °C are shown in figure 5.22. The endothermic event at 110 °C is consistent with the phase change of $LiBH_4$ from the low temperature orthorhombic phase to the high temperature hexagonal phase [121].

Figure 5.22 shows that H_2 release began at 250 °C peaking at 305 °C and showed no detectable release of NH_3. This H_2 release is at a slightly lower temperature than the equivalent $LiNH_2$ reaction, which also occurs with a small release of NH_3 (fig. 5.8). This may be expected as it is presumed that ammonia release comes from the decomposition of $LiNH_2$.

Thermal decomposition from either a $LiBH_4$ or Li_2NH rich mixture shows a similar H_2 release peak (fig. 5.23) but shifted to a lower temperature (300 °C) for a $LiBH_4$ rich mixture and to a higher temperature (320 °C) for a Li_2NH rich mixture. This is consistent with results seen in the $LiBH_4 + LiNH_2$ system (fig. 5.9).

In all three stoichiometries the peak shape is a smooth single peak with no shoulders (figures 5.22 and 5.23). This is different to the $LiBH_4 + LiNH_2$ case

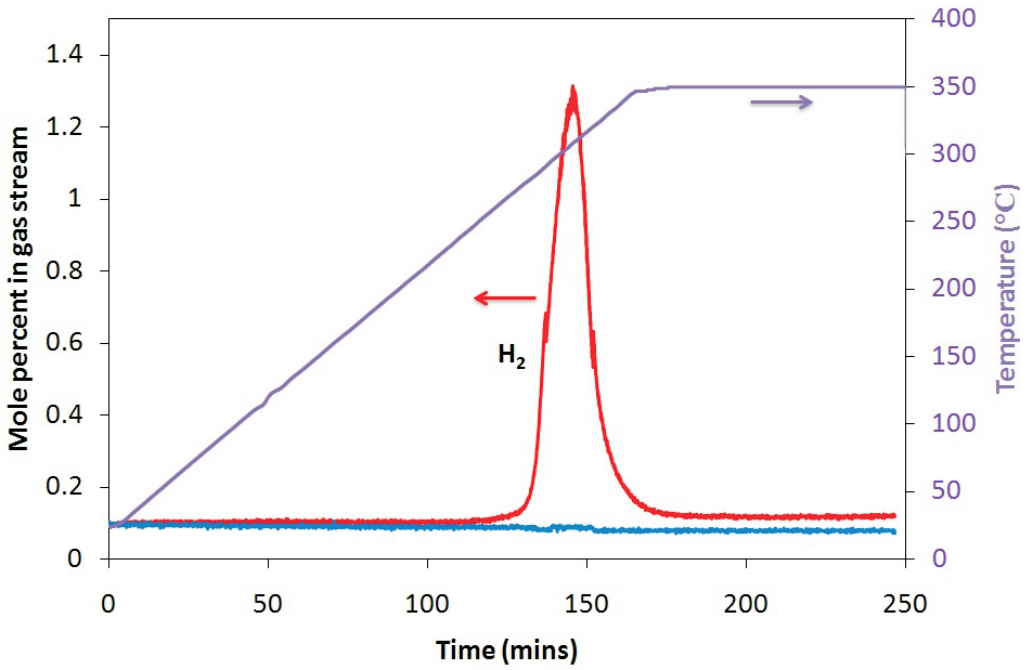

Figure 5.22: TPD-MS trace of $LiBH_4 + Li_2NH$, heated to 350 °C at a ramp rate of 2 °C min^{-1}. H_2 release is shown in red and NH_3 release in blue.

where a shoulder is seen on the low temperature side of the H_2 release peak (fig. 5.8). This shoulder is assigned to there being a two-step decomposition pathway; this suggests that in the case of $LiBH_4 + Li_2NH$ that, despite forming the same $Li_4BH_4(NH_2)_3$ intermediate, there is only one decomposition pathway. If a second decomposition pathway was present then it is likely that the other product would be boron nitride. Only Li_3BN_2 was seen as a product, further suggesting that there is a single decomposition pathway.

5.4.3 Hydrogenation

In this section the two new imide-borohydride phases were heated in 100 bar H_2 to investigate hydrogen uptake by the NH^{2-} groups and to see if any possible new phases are formed.

The sample made from reaction of $LiBH_4 + Li_2NH$ at 150 °C, containing both the new orthorhombic and cubic phases (fig. 5.18), was heated under 100 bar

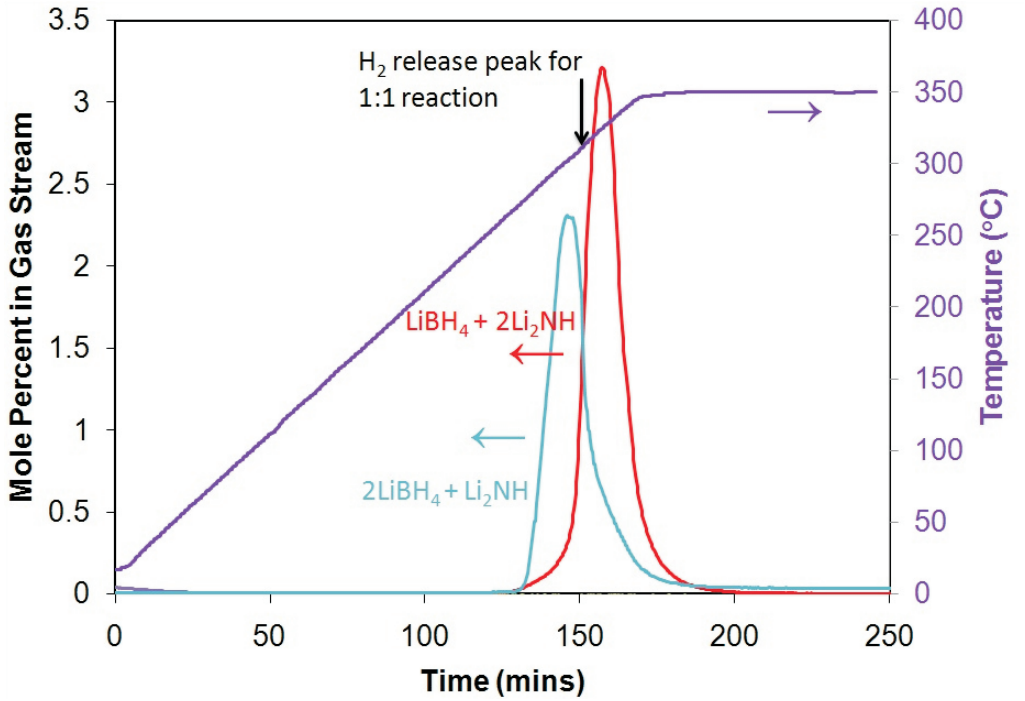

Figure 5.23: TPD-MS trace of xLiBH$_4$ + yLi$_2$NH, heated to 350 °C at a ramp rate of 2 °C min^{-1}. H_2 release from LiBH$_4$ + 2Li$_2$NH is shown in red and H_2 release from 2LiBH$_4$ + Li$_2$NH is shown in light blue. The peak position for LiBH$_4$ + Li$_2$NH is also shown.

H_2 at 100 °C for 48 hours. The XRD pattern for the products of this reaction is shown in figure 5.24, and shows LiBH$_4$ and a small amount of Li$_2$O as in the starting materials (fig. 5.18); however, the main product was the lithium amide-borohydride, Li$_4$BH$_4$(NH$_2$)$_3$, along with some LiH. This is consistent with the suggestion that a lithium imide-borohydride was being formed in the previous section (5.3.1) and here the NH^{2-} groups are being hydrided to $NH_2{}^-$.

The products from the reaction of LiBH$_4$ + Li$_2$NH at 200 °C (fig. 5.19), which formed only the new cubic imide-borohydride phase was also heated under 100 bar H_2 at 100 °C for 48 hours; the diffraction pattern from this experiment is shown in figure 5.25. As with the previous case we see the products as Li$_4$BH$_4$(NH$_2$)$_3$ and LiH, with LiBH$_4$ and Li$_2$O from the original materials.

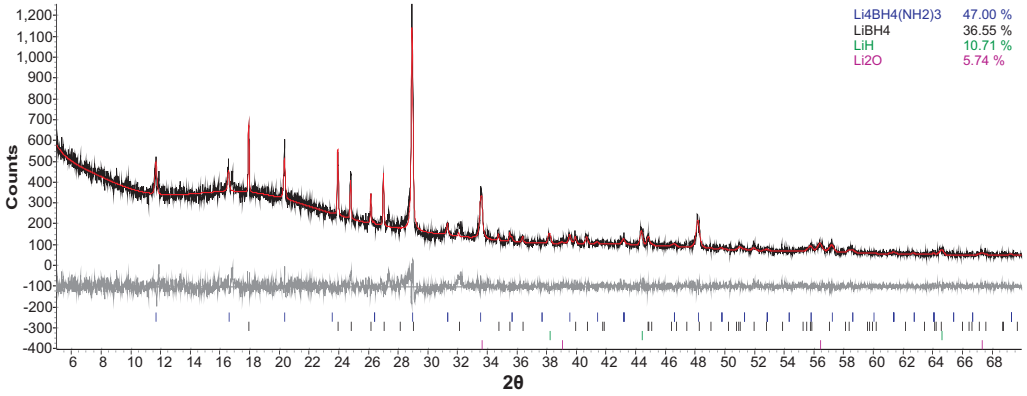

Figure 5.24: Powder X-ray diffraction pattern of the products of the hydrogenation of pre-heated $LiBH_4$ + Li_2NH at 100 °C under 100 bar H_2 for 48 hours, showing observed (black), calculated (red) and difference (grey) plots. Peak positions for $Li_4BH_4(NH_2)_3$ are shown in blue.

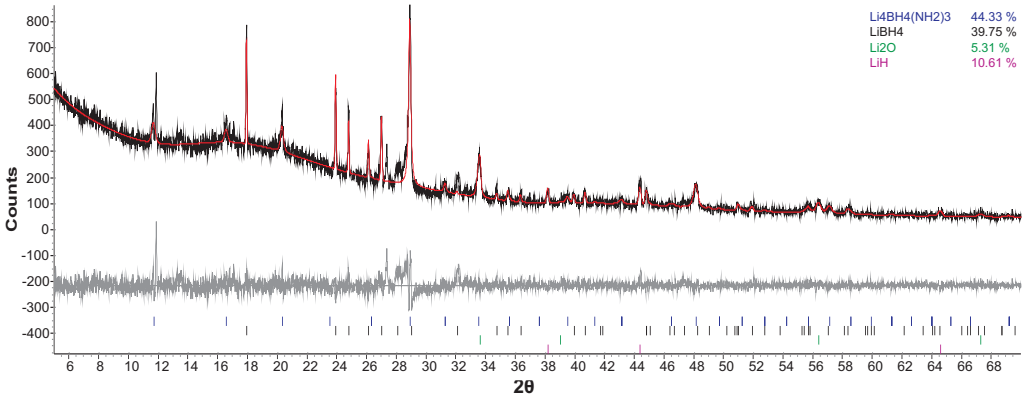

Figure 5.25: Powder X-ray diffraction pattern of the products from the hydrogenation of pre-heated $LiBH_4$ + Li_2NH at 100 °C under 100 bar H_2 for 48 hours, showing observed (black), calculated (red) and difference (grey) plots. Peak positions for $Li_4BH_4(NH_2)_3$ are shown in blue.

5.5 $xLiBH_4 + yLi_3N$

5.5.1 Powder Diffraction Study

The powder diffraction data was analysed with the same technique and strategy as in the previous two sections. Reactions in this section were carried out at various stoichiometries, both $LiBH_4$ and Li_3N rich, at temperatures between 150 and 250 °C.

Upon heating to temperatures up to 150 °C no reaction was observed, with only the starting materials being present in the diffraction pattern. At temperatures of 200 °C the formation of Li_3BN_2 ($I4_1/amd$) was seen. The reaction, however, was slow as even after 12 hours, followed by re-grinding the sample and annealing at the same temperature for a further 12 hours, significant amounts of starting material still remained.

Due to the formation of Li_3BN_2 as the reaction product the stoichiometry $LiBH_4 + 2Li_3N$ was tried to attempt to make a pure product (fig. 5.26). Significant amounts of starting materials remained even after annealing several times.

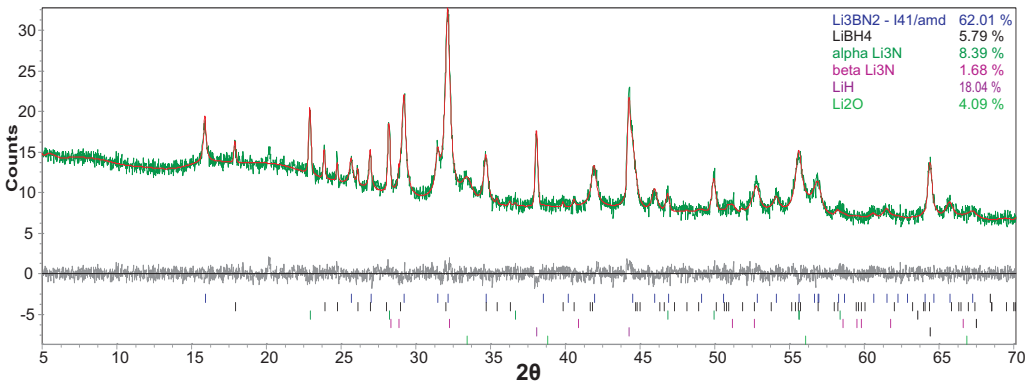

Figure 5.26: Powder X-ray diffraction pattern of the products from the reaction of $LiBH_4 + Li_3N$ at 200 °C for 12 hours, after the sample was re-ground and annealed at the same temperature, showing observed (green), calculated (red) and difference (grey) plots. Peak positions for $Li_3BN_2(I4_1/amd)$ are shown in blue.

Reaction at the higher temperature of 250 °C showed a complete reaction with the formation of the $P2_1/c$ polymorph of Li_3BN_2 with LiH (fig. 5.27). This

reaction is presumed to occur without the release of H_2 via the following reaction:

$$LiBH_4 + 2Li_3N \rightarrow Li_3BN_2 + 4LiH \tag{5.3}$$

Further investigation showed that this reaction occurred very rapidly at around 235 °C; this is investigated further in the following two sections (5.5.2 and 5.5.3).

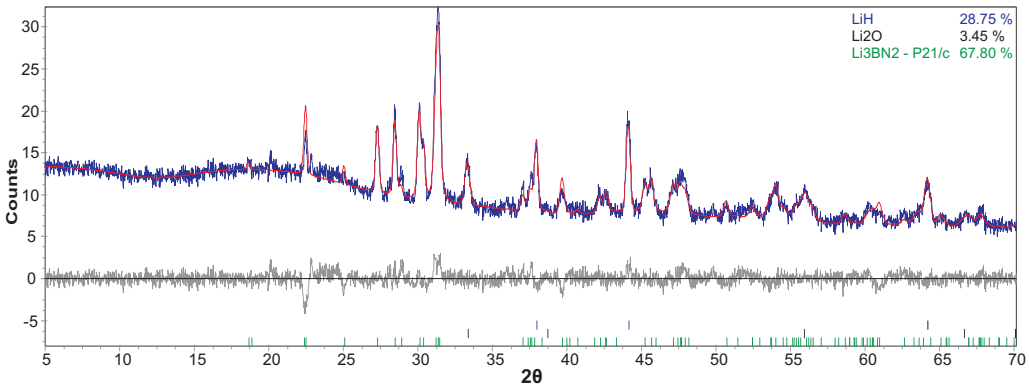

Figure 5.27: Powder X-ray diffraction pattern of the products from the reaction of $LiBH_4 + 2Li_3N$ at 250 °C for 12 hours, showing observed (blue), calculated (red) and difference (grey) plots. Peak positions for $Li_3BN_2(P2_1/c)$ are shown in green.

The reaction at the stoichiometry $LiBH_4 + Li_3N$ also showed a rapid reaction occurring at around 235 °C. In this case the reaction products were LiH and amorphous BN *via* reaction 5.4, with the formation of a small amount of Li_3BN_2 $(P2_1/c)$ (fig. 5.28).

$$LiBH_4 + Li_3N \rightarrow BN + 4LiH \tag{5.4}$$

Reaction products from reactions at higher temperatures (>250 °C) and from reactions that were not held at temperature showed no difference from those discussed above (fig. 5.29), again suggesting that the reaction occurs very rapidly at around 235 °C.

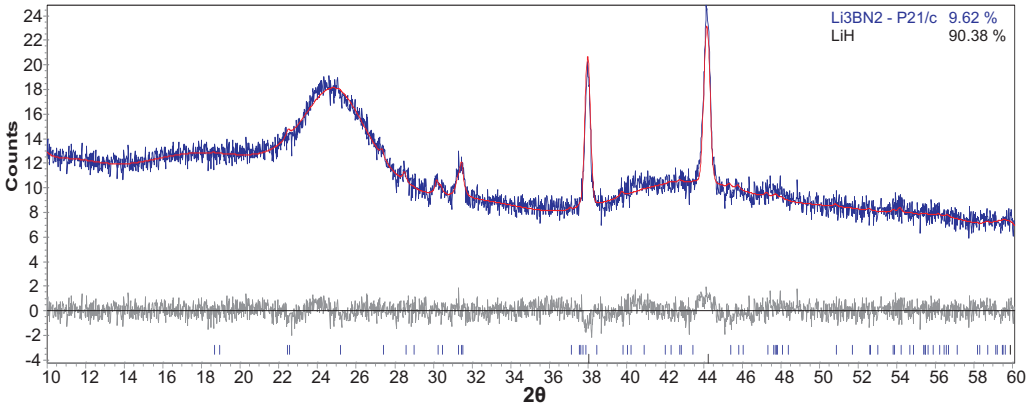

Figure 5.28: Powder X-ray diffraction pattern from reaction of $LiBH_4$ + Li_3N at 250 °C for 12 hours, showing observed (blue), calculated (red) and difference (grey) plots.

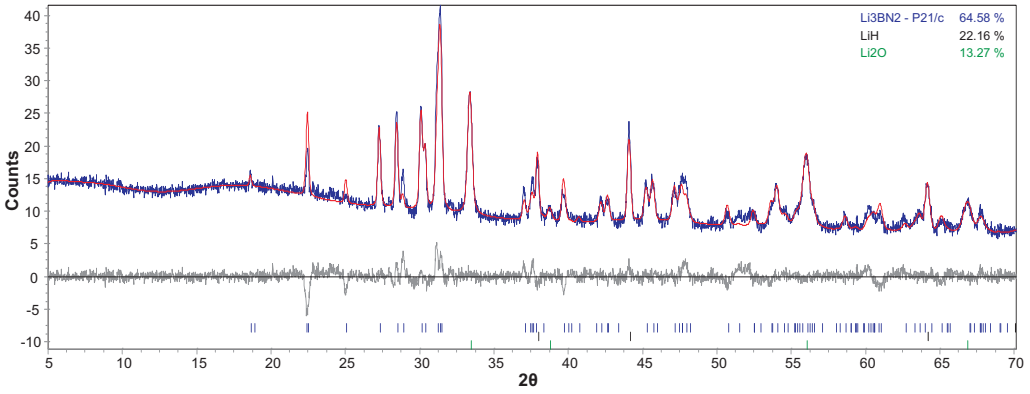

Figure 5.29: Powder X-ray diffraction pattern from reaction of $LiBH_4$ + $2Li_3N$ at 250 °C, cooled immediately, showing observed (blue), calculated (red) and difference (grey) plots. Peak positions for $Li_3BN_2(P2_1/c)$ are shown in purple.

5.5.2 Temperature Programmed Desorption

The thermal decomposition of $LiBH_4$ + $2Li_3N$ heated at a ramp rate of 2 °C min^{-1} to a temperature of 350 °C is shown in figure 5.30. This shows a sharp release of H_2, but despite the relatively large height of the peak, the overall area, and therefore the amount of H_2 released was small. While the proposed reaction scheme (equation 5.3) shows the release of no H_2, the small amount seen to be released here is most likely due to the decomposition of some remaining $LiBH_4$ caused by local heating during the reaction.

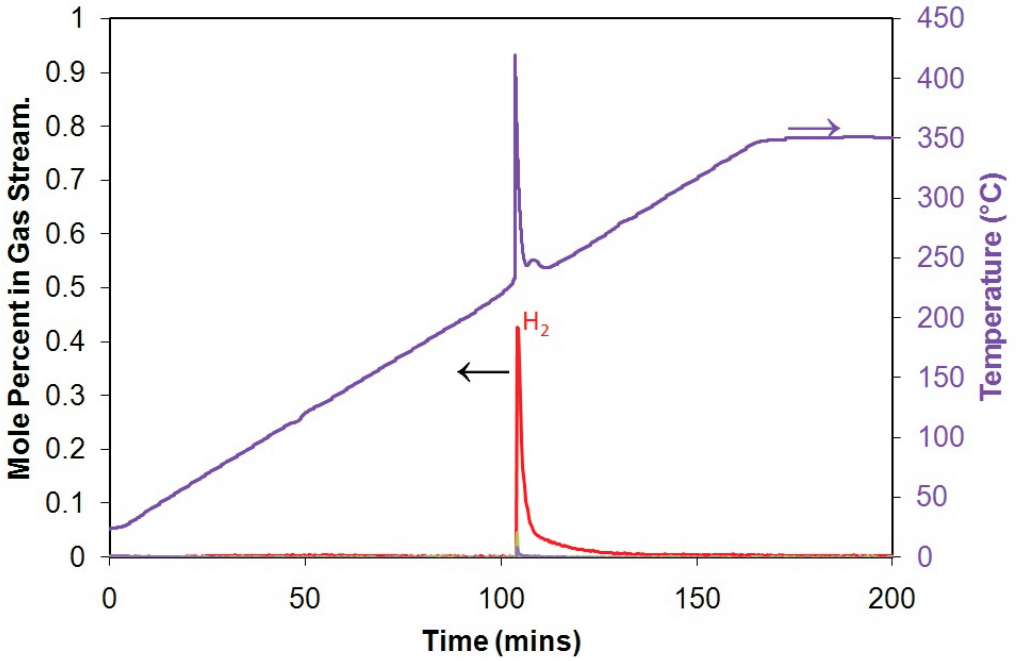

Figure 5.30: TPD-MS trace of $LiBH_4 + 2Li_3N$, heated to 350 °C at a ramp rate of 2 °C min^{-1}. H_2 release is shown in red and NH_3 release in blue.

The TPD-MS trace also shows a large exothermic event in the temperature trace at 230 °C, this shows the temperature leap up around 200 °C to 425 °C. This exothermic event explains why the reaction seemed to occur immediately, and why heating to higher temperatures, or for a longer time, had no affect on the reaction products.

The reaction of $LiBH_4 + Li_3N$ (equation 5.4) shows the same exothermic event coupled with a small H_2 release (fig. 5.31). The fast reaction, however, occurred at the slightly lower temperature of 225 °C. This is consistent with the $n$$LiBH_4$ + (*1-n*)$LiNH_2$ system where the more borohydride-rich the system (n>0.5) is, the lower the temperature of H_2 release.

The products from these TPD-MS experiments were confirmed by powder diffraction as the same as from the original reactions (section 5.5.1), confirming the previously stated reactions (equations 5.3 and 5.4).

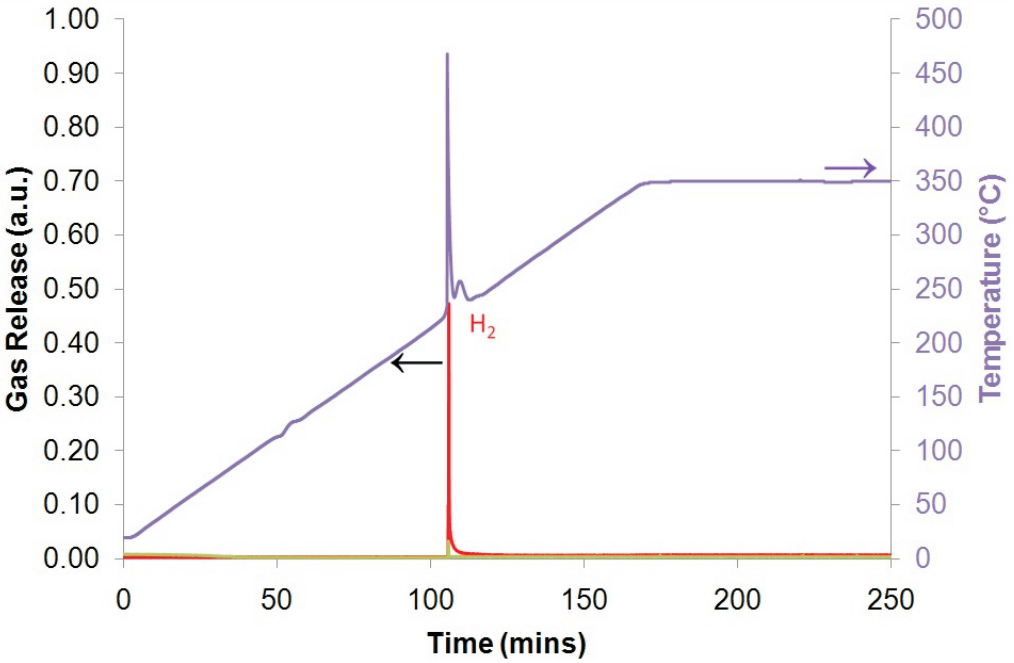

Figure 5.31: TPD-MS trace of $LiBH_4$ + Li_3N, heated to 350 °C at a ramp rate of 2 °C min^{-1}. H_2 release is shown in red and NH_3 release in blue.

5.5.3 Investigation of Exothermic Conversion

The large exothermic event seen in the TPD-MS traces from reactions of $LiBH_4$ and Li_3N (fig. 5.30 and 5.31) led us to investigate this reaction further. The reaction of $LiBH_4$ + $2Li_3N$ (eq. 5.3) is calculated to be highly exothermic with $\Delta H = -355.4$ kJ mol^{-1} so the event seen in the TPD-MS is to be expected [120].

The reaction of $LiBH_4$ + $2Li_3N$ was carried out in a different way to provide greater control over temperature and permit visual inspection. In this experiment the reactants were mixed and ground before being placed into a quartz crucible and sealed within a three-necked round bottomed flask inside an argon filled glove box. This was then removed from the glove box, allowed to have argon flowing through the flask and placed in a heating mantle. Figure 5.32a shows the reactants before heating was started; figure 5.32b shows the reactants at 235 °C. It can be seen that the reactants glow red hot; this glow was present for roughly two seconds. This shows both how exothermic the reaction is and how fast the

reaction occurs. Rough estimates of the temperature of this mixture from black body radiation suggest it could be as high as 800 °C.

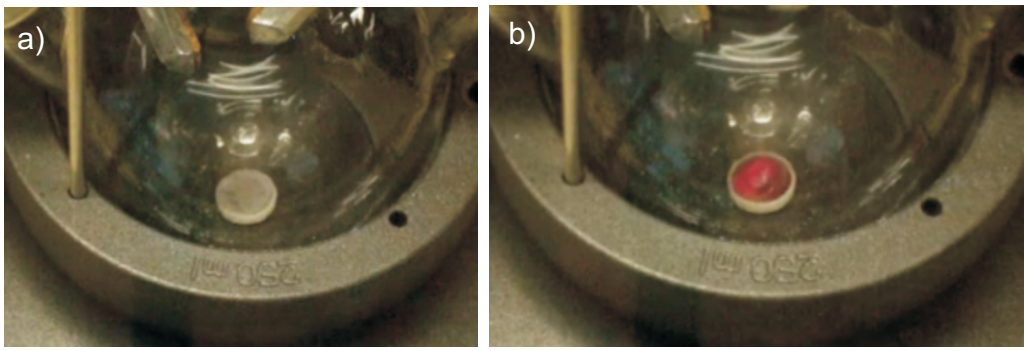

Figure 5.32: Screen shots from a video of the reaction of $LiBH_4 + 2Li_3N$ a) before and b) during the reaction.

The difference in morphology of the $P2_1/c$ polymorph of Li_3BN_2 formed from this reaction and from $LiBH_4 + 2LiNH_2$ was investigated using SEM (fig. 5.33). It can be seen that the material formed from $LiBH_4 + 2Li_3N$ (fig. 5.33a and 5.33b) does not form distinct particles as seen for the $P2_1/c$ polymorph of Li_3BN_2 formed from $LiBH_4$ and $LiNH_2$ (fig. 5.33c).

5.6 Conclusions and further work

In this work the formation of the three polymorphs of Li_3BN_2 was investigated as the decomposition product of $LiBH_4 + 2LiNH_2$ and a complex relationship was found between the polymorphs. The $P2_1/c$ polymorph formed from the reaction $LiBH_4 + 2LiNH_2$ at temperatures as low as 230 °C, although the rate of reaction was very slow and the phase could not be produced pure, with slightly higher temperatures increasing the reaction rate but also favouring the formation of the $I4_1/amd$ polymorph. The I41/amd polymorph was favoured at temperatures around 350 °C, whereas temperatures of 450 °C again favoured the production of the $P2_1/c$ polymorph. At temperatures greater than 500 °C the $P4_22_12$ polymorph was favoured. These three polymorphs were investigated for the best

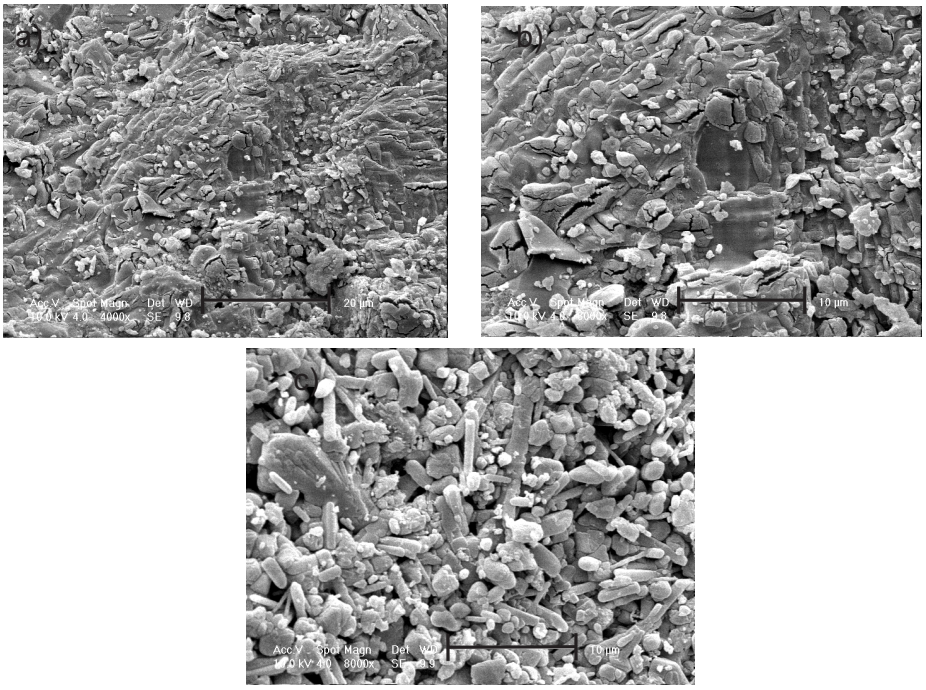

Figure 5.33: Scanning electron microscopy images of Li_3BN_2 ($P2_1/c$), made from (a and b) $LiBH_4$ + $2Li_3N$ and (c) $LiBH_4$ + $2LiNH_2$; the scale of the images is at a) 20 μm b) 10 μm and c) 10 μm.

candidate for hydrogenation, however, no hydrogenation was seen in this work. Further work could be done into the possibility of hydrogenation in these materials through further nanostructuring and the use of additives.

The other areas of this system were studied with a view to isolating potential intermediates in this system, with reactions between $LiBH_4$ and Li_2NH or Li_3N. Two new imide-borohydride phases were found to form at temperatures around 150 °C from the reaction of Li_2NH + $LiBH_4$. However they could not be isolated as pure phases. These phases then decompose with limited NH_3 release to give the $I4_1/amd$ polymorph of Li_3BN_2 along with LiH. Further work could be done into this system, attempting to isolate a new pure imide-borohydride phase and to see whether this could act as an intermediate with an amide-borohydride. The system $LiBH_4$ + $2Li_3N$ was also investigated, while no significant hydrogen release was seen, it was found to be highly exothermic reaction. A summary of

the reaction products formed in this work is shown in figure 5.34.

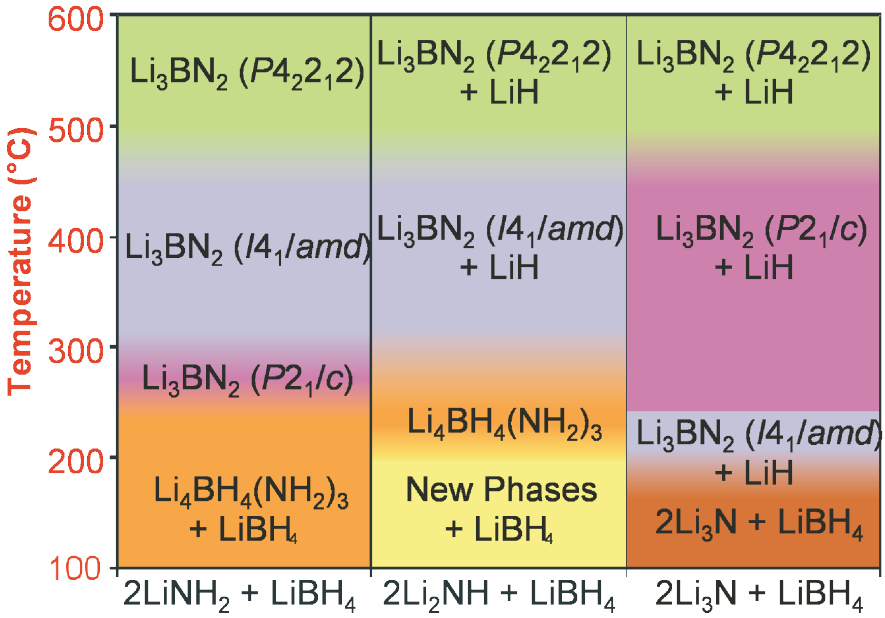

Figure 5.34: Summary of the reaction products of the Li-B-N-H system at various temperatures.

Bibliography

[1] A. Zuttel, *Naturwissenschaften*, 2004, **91**, 157–172. [cited at p. 1, 2, 11, 12, 13, 14, 197]

[2] G. Marban and T.Valdes-Solis, *Int. J. Hydrogen Energ.*, 2007, **32**, 1625–1637. [cited at p. 1]

[3] S. Pacala and R. Socolow, *Science*, 2004, **305**, 968–972. [cited at p. 1]

[4] L. Schlapbach and A. Zuttel, *Nature*, 2001, **414**, 353–358. [cited at p. 2, 10]

[5] P. P. Edwards, V. L. Kuznetsov, and W. I. F. David, *Phil. Trans. R. Soc.*, 2007, **365**, 1043–1056. [cited at p. 2, 11, 14]

[6] M. Balat, *Int. J. Hydrogen Energ.*, 2008, **33**, 4013–4029. [cited at p. 2]

[7] J. D. Holladay, J. Hu, D. L. King, and Y. Wang, *Catalysis Today*, 2009, **138**, 244–260. [cited at p. 3, 4]

[8] R. S. Cherry, *Int. J. Hydrogen. Energ.*, 2004, **29**, 125–129. [cited at p. 3]

[9] J. Turner, G. Sverdrup, M. K. Mann, P. C. Maness, B. Kroposki, M. Ghirardi, R. J. Evans, and D. Blake, *Int. J. Hydrogen. Energ.*, 2008, **32**, 379–407. [cited at p. 4]

[10] W. Kreuter and H. Hofmann, *Int. J. Hydrogen. Energ.*, 2008, **23**(8), 661–666. [cited at p. 4]

[11] S. Z. Baykara, *Int. J. Hydrogen. Energ.*, 2004, **29**, 1451–1458. [cited at p. 4]

[12] H. L. . Chum and R. P. Overend, *Fuel Processing Technology*, 2001, **71**, 187–195. [cited at p. 4]

[13] A. J. Guwy, R. M. Dinsdale, J. R. Kim, J. Massanet-Nicolau, and G. Premiet, *Bioresource Technology*, 2011, **102**(18), 8534–8542. [cited at p. 5]

[14] U. Bossel, *Well-to-wheel studies, heating values and the energy conversation principle, European Fuel Cell Forum Technical Report*, 2003. [cited at p. 6]

[15] L. M. Das, *Int. J. Hydrogen. Energ.*, 1990, **15**, 425–443. [cited at p. 6]

[16] C. Sopena, P. M. Dieguez, D. Sainz, J. C. Urroz, E. Guelbenzu, and L. M. Gandia, *Int. J. Hyrog. Energ.*, 2010, **35**, 1420–1429. [cited at p. 6]

[17] S. Verhelst and T. Wallner, *Progress in Energy and Combustion Science*, 2009, **35**, 490–527. [cited at p. 6]

[18] A. E. Lutz, R. S. Larson, and J. O. Keller, *Int. J. Hydrogen Energ.*, 2010, **27**, 1103–1111. [cited at p. 6]

[19] D. Sainz, P. M. Dieguez, C. Sopena, J. C. Urroz, and L. M. Gandia, *Int. J. Hyrog. Energ.*, 2012, **37**, 1781–1789. [cited at p. 7]

[20] P. P. Edwards, V. L. Kuznetsov, W. I. F. David, and N. P. Brandon, *Energy Policy*, 2008, **36**, 4356–4362. [cited at p. 7]

[21] Y. Wang, K. S. Chen, J. Mishler, S. C. Cho, and X. C. Adroher, *Applied Energy*, 2011, **88**, 981–1007. [cited at p. 7, 8]

[22] S. Zhang, X.-Z. Yuan, J. C. Hin, H. Wang, K. A. Friedrich, and M. Schulze, *Journal of Power Sources*, 2009, **194**, 588–600. [cited at p. 7]

[23] *U.S. Department of Energy - Energy Efficiency and Renewable Energy - Types of Fuel Cells*, 2012. [cited at p. 8, 197]

[24] R. Hammerschlag and P. Mazza, *Energ. Policy*, 2005, **33**(16), 2039–2043. [cited at p. 9]

[25] E. Kriegler, *Energy Economics*, 2011, **33**, 594–596. [cited at p. 9]

[26] S. Dunn, *Int. J. Hydrog. Energ.*, 2002, **27**, 235–264. [cited at p. 9]

[27] S. M. Aceves, G. D. Berry, J. Martinez-Frias, and F. Espinosa-Loza, *Int. J. Hydrog. Energ.*, 2006, **31**, 2274–2283. [cited at p. 11]

[28] H. W. Langmi, A. Walton, M. M. Al-Mamouria, S. R. Johnson, D. Book, J. D. Speight, P. P. Edwards, I. Gameson, P. A. Anderson, and I. R. Harris, *J. Alloys Compd.*, 2003, **356**, 710–715. [cited at p. 12]

[29] J. G. Vitillo, G. Ricchiardi, G. Spoto, and A. Zecchina, *Phys. Chem. Rev. Phys.*, 2005, **7**(23), 3948–3954. [cited at p. 12]

[30] J. L. C. Rowsell and O. M. Yaghi, *Angew. Chem. Int. ed.*, 2005, **44**, 4670–4679. [cited at p. 12]

[31] M. Latroche, S. Surble, C. Serre, C. Mellot-Draznieks, P. L. Llewellyn, J. H. Lee, J. S. Chang, S. H. Jhung, and G. Ferey, *Angew. Chem. Int. ed.*, 2006, **45**, 8227–8231. [cited at p. 12]

[32] H. Reardon, J. M. Hanlon, R. W. Hughes, A. Godula-Jopek, T. K. Mandal, and D. H. Gregory, *Energy Environ. Sci.*, 2012, **5**, 5951–5979. [cited at p. 12]

[33] H. M. El-Kaderi, J. R. Hunt, J. L. Mendoza-Cortes, A. P. Cote, R. E. Taylor, M. O'Keeffe, and O. M. Yaghi, *Science*, 2007, **316**, 268–272. [cited at p. 13]

[34] N. B. McKeown, B. Gahnem, K. J. Msayib, P. M. Budd, C. F. Tattershall, K. Mahmood, S. Tan, D. Book, H. W. Langmi, and A. Walton, *Angew. Chem. Int. Ed.*, 2006, **45**, 1804–1807. [cited at p. 13]

[35] P. M. Budd, A. Butler, J. Selbie, K. Mahmood, N. B. McKeown, B. Gahnem, K. J. Msayib, D. Book, and A. Walton, *Phys. Chem. Chem. Phys*, 2007, **9**, 1802–1808. [cited at p. 13]

[36] K. L. Lim, H. Kazemian, Z. Yaakob, and W. R. W. Daud, *Chem. Eng. Technol.*, 2010, **33**(2), 213–226. [cited at p. 14]

[37] B. Bogdanovic, K. Bohmhammel, B. Christ, A. Reiser, K. Schlichte, R. Vehlen, and U. Wolf, *J. Alloys. Compd.*, 1999, **282**, 84–92. [cited at p. 15]

[38] S. R. Johnson, P. A. Anderson, P. P. Edwards, I. Gameson, J. W. Prendergast, M. Al-Mamouri, D. Book, I. R. Harris, J. D. Speight, and A. Walton, *Chem. Commun.*, 2005, **22**, 2823–2825. [cited at p. 15]

[39] S. Orimio, Y. Nakamori, J. R. Eliseo, and C. M. Jensen, *Chem. Rev.*, 2007, **107**(10), 4111–4132. [cited at p. 15, 16]

[40] B. Bogdanovic, R. A. Brand, A. Marjanovic, and M. Schwickardi, *J. Alloys Compd.*, 2000, **302**, 36–58. [cited at p. 15]

[41] M. Fichtner, O. Fuhr, and O. Kircher, *J. Alloys Compd.*, 2003, **418**, 356–357. [cited at p. 15, 16]

[42] J. Block and A. P. Gray, *Inorg. Chem.*, 1965, **4**(3), 304. [cited at p. 16]

[43] E. C. Ashby and P. Kobetz, *Inorg. Chem.*, 1966, **5**, 1615. [cited at p. 16]

[44] B. Bogdanovic and M. Schwickardi, *J. Alloys. Compd.*, 1997, **253**, 1–9. [cited at p. 16, 22]

[45] S. S. Srinivasan, H. W. Brinks, B. C. Hauback, D. Sun, and C. M. Jensen, *J. Alloys. Compd.*, 2004, **377**, 283–289. [cited at p. 16]

[46] A. W. Titherley, *J. Chem. Soc.*, 1894, **65**, 504. [cited at p. 16]

[47] F. W. Bergstrom and W. C. Fernelius, *Chem. Rev.*, 1933, **12**, 43. [cited at p. 16, 17]

[48] Y. Nakamori, G. Kitahara, and S. Orimo, *J. Power Sources*, 2004, **138**, 309–312. [cited at p. 17, 18]

[49] P. Chen, Z. Xiong, J. Luo, J. Lin, and K. L. Tan, *Nature*, 2002, **420**, 302–304. [cited at p. 17, 51]

[50] Y. H. Hu and E. Ruckenstein, *J. Phys. Chem.*, 2003, **107**, 9737–9739. [cited at p. 17, 18]

[51] P. Chen, Z. Xiong, J. Luo, J. Lin, and K. L. Tan, *J. Phys. Chem.*, 2003, **107**, 10967–10970. [cited at p. 17]

[52] W. I. F. David, M. O. Jones, D. H. Gregory, C. M. Jewell, S. R. Johnson, A. Walton, and P. P. Edwards, *J. Am. Chem. Soc*, 2007, **129(6)**, 1594. [cited at p. 18, 51, 119, 148]

[53] J. J. Hu, G. T. Wu, Y. F. Lui, Z. T. Xiong, and P. Chen, *J. Phys. Chem. B*, 2006, **110**, 14688. [cited at p. 18]

[54] H. Y. Leng, T. Ichikawa, and S. Hino, *J. Phys. Chem. B*, 2004, **108**, 8763–8765. [cited at p. 18]

[55] C. Liang, Y. Liu, H. Fu, Y. Ding, M. Gao, and H. Pan, *J. Alloys Compd.*, 2011, **509**, 7844–7853. [cited at p. 18]

[56] W. Luo and E. Ronnerbro, *J. Alloys Compd.*, 2006, **404-406**, 392–395. [cited at p. 18]

[57] R. A. Varin, M. Jang, and M. Polanski, *J. Alloys Compd.*, 2010, **491**, 658. [cited at p. 19]

[58] T. Ichikawa, I. Shigehito, N. Hanada, and H. Fujii, *J. Alloys Compd.*, 2004, **365**, 271. [cited at p. 19]

[59] H. I. Schlesinger and H. C. Brown, *J. Am. Chem. Soc.*, 1940, **62**, 3429–3435. [cited at p. 19]

[60] H. I. Schlesinger, H. C. Brown, H. R. Hoekstra, and L. R. Rapp, *J. Am. Chem. Soc.*, 1953, **75**, 199–204. [cited at p. 19]

[61] A. Zuttel, P. Wenger, S. Rentsch, P. Sudan, P. Mauron, and C. Emmenegger, *J. Power Sources*, 2003, **118**, 1–7. [cited at p. 19, 20]

[62] N. Ohba, K. Miwa, M. Aoki, T. Noritake, and S. I. Towata, *Phys. Rev. B*, 2006, **74**, 075110. [cited at p. 19]

[63] S. I. Orimo, Y. Nakamori, N. Ohba, K. Miwa, M. Aoki, and S. I. Towata, *Appl. Phys. Lett.*, 2006, **89**, 021920. [cited at p. 19]

[64] S. J. Hwang, C. Robert, J. Bowman, J. W. Reiter, J. Rijssenbeek, G. I. Soloveichik, and J. C. Zhao, *J. Phys. Chem. C*, 2008, **112**, 3164–3169. [cited at p. 19]

[65] C. Li, P. Peng, D. W. Zhou, and L. Wan, *Int. J. Hydrog. Energ.*, 2011, **36**, 14512–14526. [cited at p. 20]

[66] J. J. Vajo, T. T. Salguero, A. F. Gross, S. L. Skeith, and G. L. Olson, *J. Alloys Compd.*, 2007, **446-447**, 409–414. [cited at p. 20]

[67] M. Au, A. Jurgensen, and C. Zeigler, *J. Alloys Compd.*, 2008, **462**, 303–309. [cited at p. 20, 22]

[68] Z. Z. Fang, P. Wang, T. E. Rufford, X. D. Kang, G. Q. Lu, and H. M. Cheng, *Acta. Mater.*, 2008, **56**, 6257–6263. [cited at p. 20]

[69] D. M. F. Santos and C. A. C. Sequeira, *Ren. Sus. Energ. Rev.*, 2011, **15**, 3980–4001. [cited at p. 21]

[70] G. Severa, E. Ronnebro, and C. M. Jensen, *Chem. Commun.*, 2010, **46**, 421–423. [cited at p. 21]

[71] Y. Filinchuk, B. Richter, T. R. Jensen, V. Dmitriev, D. Chernyshov, and H. Hagemann, *Angew. Chem. Int. Ed.*, 2011, **50**, 11162–11166. [cited at p. 21]

[72] P. A. Chater, W. I. F. David, and P. A. Anderson, *Chem. Commun.*, 2007, **45**, 4770–4772. [cited at p. 21, 151]

[73] P. A. Chater, W. I. F. David, S. R. Johnson, P. P. Edwards, and P. A. Anderson, *Chem. Commun.*, 2006, **23**, 2439–2441. [cited at p. 21, 69, 151, 153, 170]

[74] H. Wu, W. Zhou, and K. Wang, *Nanotech*, 2009, **20**, 204002. [cited at p. 21, 151, 167]

[75] P. A. Chater, P. A. Anderson, J. W. Prendergast, A. Walton, V. S. J. Mann, D. Book, W. I. F. David, S. R. Johnson, and P. P. Edwards, *J. Alloys Compd.*, 2007, **446-447**, 350–354. [cited at p. 21, 43, 197]

[76] R. Mohtadi, P. Sivasubramanian, S. J. Hwang, A. Stowe, J. Gray, T. Matsungaga, and R. Zidan, *Int. J. Hydrogen. Energ.*, 2012, **37**, 2388–2396. [cited at p. 22]

[77] I. P. Jain, P. Jain, and A. Jain, *J. Alloys. Compd.*, 2010, **503**, 303–339. [cited at p. 22]

[78] C. Price, J. Gray, R. L. Jr, and D. L. Anton, *Int. J. Hydrogen. Energ.*, 2012, **37**, 2742–2749. [cited at p. 22]

[79] I. E. Malka, T. Czujko, and J. Bystrzycki, *Int. J. Hydrogen. Energ.*, 2010, **35**, 1706–1712. [cited at p. 22]

[80] L. H. Rude, E. Groppo, L. M. Arnbjerg, D. B. Ravnsbaek, R. A. Malmkjaer, Y. Filinchuk, M. Baricco, F. Besenbacher, and T. R. Jensen, *J. Alloys Compd.*, 2011, **509**, 8299–8305. [cited at p. 22, 23]

[81] M. Matsuo and S. I. Orimo, *Adv. Energy Mater.*, 2011, **1**, 161–172. [cited at p. 23]

[82] J. Y. Lee, Y. S. Lee, J. Y. Suh, J. H. Shim, and Y. W. Cho, *J. Alloys Compd.*, 2010, **506**, 721–727. [cited at p. 23]

[83] H. Barlage and H. Jacobs, *Z. Anorg. Allg. Chem*, 1994, **620**, 479. [cited at p. 23, 85]

[84] M. Matsuo, T. Sato, Y. Miura, H. Oguchi, Y. Zhou, H. Maekawa, H. Takamara, and S. Orimo, *Chem. Mater.*, 2010, **22**, 2702. [cited at p. 23, 52, 100, 103, 104, 105, 119, 146, 205, 211, 217]

[85] W. Grochala and P. P. Edwards, *Chem. Rev.*, 2004, **104**, 1283–1315. [cited at p. 23]

[86] *Targets for Onboard Hydrogen Storage Systems for Light-Duty Vehicles, US Department of Energy Office of Energy Efficiency and Renewable Energy and The FreedomCAR and Fuel Partnership*, 2009. [cited at p. 25, 217]

[87] G. Burns and A. M. Glazer, *Space Groups for Solid State Scientists*, 1978. [cited at p. 31]

[88] A. R. West, *Basic Solid State Chemistry*, 1999. [cited at p. 31, 33]

[89] L. E. Smart and E. A. Moore, *Solid State Chemistry: An Introduction*, 2005. [cited at p. 31]

[90] C. Hammond, *The Basics of Crystallography and Diffraction*, 2001. [cited at p. 33]

[91] G. E. Bacon, *Neutron Diffraction*, 1962. [cited at p. 38]

[92] W. Marshall and R. D. Lowde, *Rep. Prog. Phys*, 1968, **31**, 705. [cited at p. 38]

[93] H. M. Rietveld, *J. App. Cryst.*, 1969, **2**, 65–71. [cited at p. 38]

[94] R. A. Young, *The Rietveld Method*, 1993. [cited at p. 38]

[95] C. Daas, *Fundamental of Contemporary Mass Spectrometry*, 2007. [cited at p. 40]

[96] M. Linscheid, *Ullman's Encyclopedia of Industrial Chemistry: Mass Spectrometry*, 2001. [cited at p. 40]

[97] E. B. Wilson, J. C. Decius, and P. C. Cross, *Molecular Vibrations: The Theory of Infrared and Raman Vibrational Spectra*, 1980. [cited at p. 45]

[98] H. A. Szymanski, *Raman Spectroscopy: Theory and Practice*, 1970. [cited at p. 45]

[99] G. D. Damilatos, *Advan. Elec. Phys*, 1988, **71**, 109. [cited at p. 50]

[100] G. D. Damilatos and G. C. Lewis, *US Patent 4823006*, 1989. [cited at p. 50]

[101] M. Nagib and H. Jacobs, *Atomkernenerg*, 1973, **21**, 275. [cited at p. 52, 59, 197]

[102] K. Ohoyama, Y. Nakamori, S. I. Orimo, and K. Yamada, *J. Phys. Soc. Jpn.*, 2005, **74**, 483. [cited at p. 52, 110, 197]

[103] B. A. Boukamp and R. A. Huggins, *Phys. Lett. A.*, 1979, **22**, 464. [cited at p. 52, 146, 211]

[104] W. F. Luo, *J. Alloys Compd.*, 2004, **381**, 284. [cited at p. 52, 119]

[105] H. Y. Leng, T. Ichikawa, S. Hino, N. Hanada, and S. I. amd H . Fujii, *J. Phys. Chem. B*, 2004, **108**, 8763. [cited at p. 52, 119]

[106] J. P. Bohger, R. R. Ebmann, and H. Jacobs, *J. Mole. Struct.*, 1995, **348**, 325–328. [cited at p. 57]

[107] Y. Kojima and Y. Kawai, *J. Alloy. Compd.*, 2005, **395**, 236–239. [cited at p. 57]

[108] A. A. Coelho, *Bruker AGS, Karlsruhe, Germany, 3rd Edn*, 2004. [cited at p. 59, 68, 74, 86, 103, 110, 152]

[109] H. K. Roobottom, H. D. Jenkins, J. Passmore, and L. Glasser, *J. Chem. Ed.*, 1999, **76**, 1570–1573. [cited at p. 76]

[110] *CRC Handbook of Chemistry and Physics, ed. D. R. Lide, Taylor and Francis, Boca Raton, FL, 87th ed.*, 2007. [cited at p. 76]

[111] E. Posnjak and R. W. G. Wyckoff, *J. Washington Acad. Sciences*, 1922, **12**, 248–251. [cited at p. 110]

[112] A. Gotoh, H. Obayoshi, R. Nagai, S. Mochizuki, and T. Kodu, *US Patent*, 4,411,971, p. 1983. [cited at p. 119, 146, 211]

[113] F. E. Pinkerton, *J. Alloys. Compd.*, 2005, **400**, 76. [cited at p. 121, 160]

[114] C. H. Christensen, R. Z. Sorensen, T. Johannessen, U. J. Quaade, K. Honkala, T. D. Elmoe, R. Kohler, and J. K. Norskov, *J. Mater. Chem.*, 2005, **15**, 4106. [cited at p. 148]

[115] A. Leineweber, M. W. Friedriszik, and H. Jacobs, *J. Solid State Chem.*, 1999, **47**, 229. [cited at p. 148]

[116] H. Yamane, S. Kikkawa, H. Horiuchi, and M. Koizumi, *J. Solid State Chem.*, 1986, **65**, 6–12. [cited at p. 151]

[117] H. Yamane, S. Kikkawa, and M. Koizumi, *J. Solid State Chem.*, 1987, **1**, 1–11. [cited at p. 151]

[118] F. E. Pinkerton and J. F. Herbst, *J. Appl. Phys. Chem.*, 2006, **99**, 113523. [cited at p. 151, 158]

[119] P. Villars, *Pearsons Handbook: desk edition (ASM internation material)*, 1997, p. 771. [cited at p. 158, 160]

[120] D. J. Seigel and C. Wolverton, *Phys. Rev. B*, 2007, **75**, 014101. [cited at p. 164, 179]

[121] J. P. Soulie, G. Renaudin, R. Cerny, and K. Yvon, *J. Alloys Compd.*, 2002, **346**, 200–205. [cited at p. 171]

Appendix A

Appendix

x	Cell volume (Å^3)	a (Å^3)	c (Å^3)
0	734.5(2)	9.742(1)	8.937(1)
0.1	731.8(2)	9.729(1)	8.927(1)
0.2	728.7(3)	9.717(2)	8.911(1)
0.3	723.3(5)	9.699(3)	8.881(3)
0.4	733.8(7)	9.736(4)	8.929(4)
0.5	734.5(7)	9.739(3)	8.939(4)

Table A.1: Lattice parameter values for materials of the $R\bar{3}$ form of $Li_4(NH_2)_{3+x}Cl_{1-x}$.

x	Cell volume (Å^3)	a (Å^3)
0	137.2(2)	5.158(1)
0.1	136.9(4)	5.152(1)
0.2	135.8(4)	5.139(2)
0.3	134.7(4)	5.126(2)
0.4	135.7(4)	5.144(2)

Table A.2: Lattice parameter values for materials of the form $Li_7(NH)_{3+x}Cl_{1-x}$.

x	Cell volume (Å^3)	a (Å^3)	c (Å^3)
0	754.70(2)	9.8487(1)	8.9844(1)
0.1	750.3(1)	9.8288(8)	8.9678(9)
0.2	747.3(4)	9.813(4)	8.962(2)
0.3	745.4(2)	9.804(1)	8.957(1)
0.4	746.2(5)	9.815(3)	8.975(4)

Table A.3: Lattice parameter values for materials of the $R\bar{3}$ form of $Li_7(NH_2)_{6+x}Br_{1-x}$.

x	Cell volume (Å^3)	a (Å^3)	c (Å^3)
0	500.43(18)	7.0903(9)	11.494(3)
0.1	500.36(17)	7.0897(9)	11.496(2)
0.2	500.45(18)	7.0901(9)	11.495(3)
0.3	500.39(22)	7.0909(9)	11.492(3)
0.4	500.53(15)	7.0906(6)	11.496(2)
0.5	500.44(14)	7.0901(9)	11.494(3)

Table A.4: Lattice parameter values for materials of the $P63_{mc}$ form of $Li_3(NH_2)_2I$ made via reaction of $(2+x)LiNH_2 + (1-x)LiI$.

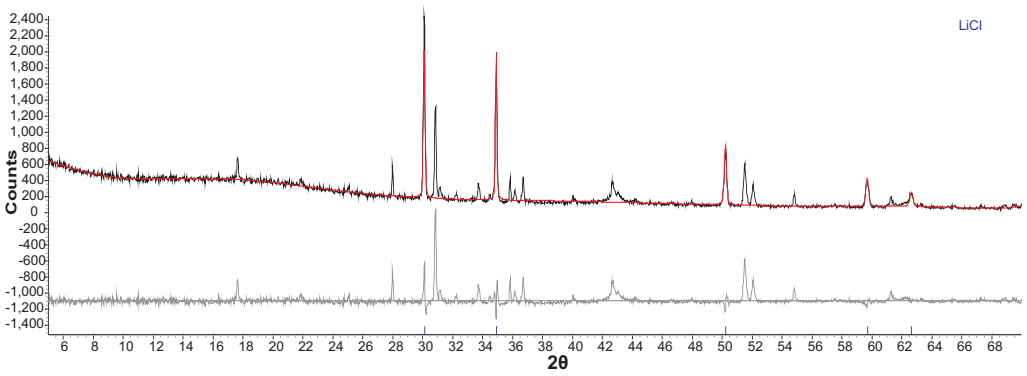

Figure A.1: Powder X-ray diffraction pattern of the products from reaction of $2Li_4(NH_2)_3Cl + 3MgH_2$, heated at 2 °C min^{-1} to 400 °C. Observed (black), calculated (red) and difference (grey) plots, and peak positions for LiCl (blue) are shown.

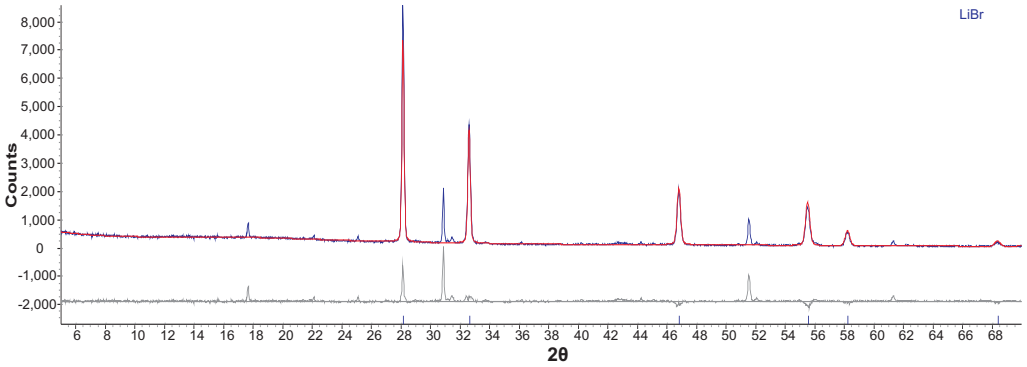

Figure A.2: Powder X-ray diffraction pattern of the products from reaction of $Li_7(NH_2)_6Br$ + $3MgH_2$, heated at 2 °C min^{-1} to 400 °C. Observed (black), calculated (red) and difference (grey) plots, and peak positions for LiBr (blue) are shown.

		Conductivity (S cm^{-1})					
T (K)	1000/T	Imide-I	Amide-I	Imide-Br	Amide-Br	Imide-Cl	Amide-Cl
300	3.356	$3.90x10^{-5}$	$2.02x10^{-5}$	$4.02x10^{-7}$	$3.50x10^{-7}$	$1.89x10^{-7}$	-
313	3.195	$1.76x10^{-4}$	$3.70x10^{-5}$	$1.70x10^{-5}$	$5.08x10^{-7}$	$5.05x10^{-7}$	-
323	3.096	$2.19x10^{-4}$	$6.17x10^{-5}$	$5.17x10^{-5}$	$9.15x10^{-7}$	$5.98x10^{-7}$	-
333	3.003	$3.09x10^{-4}$	$8.86x10^{-5}$	$7.36x10^{-5}$	$2.19x10^{-6}$	$9.15x10^{-7}$	-
343	2.915	$3.54x10^{-4}$	$2.65x10^{-4}$	$1.15x10^{-4}$	$5.17x10^{-6}$	$1.63x10^{-6}$	-
353	2.883	$4.20x10^{-4}$	$7.29x10^{-4}$	$1.30x10^{-4}$	$7.02x10^{-6}$	$1.92x10^{-6}$	$3.79x10^{-7}$

Table A.5: Temperature dependence of ionic mobility of lithium amide- and imide-halides. Phases are denoted as Amide-X and Imide-X, where X = Cl, Br or I.

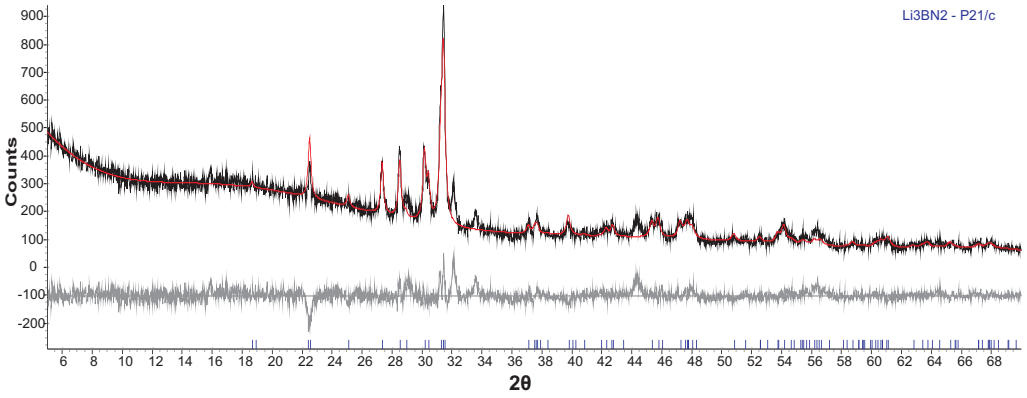

Figure A.3: Powder X-ray diffraction pattern of ball milled Li_3BN_2 ($P2_1/c$) after heating under 100 bar H_2 at 300 °C for 140 hours. Observed (black), calculated (red) and difference (grey) plots, and peak positions for Li_3BN_2 ($P2_1/c$) are shown (blue).

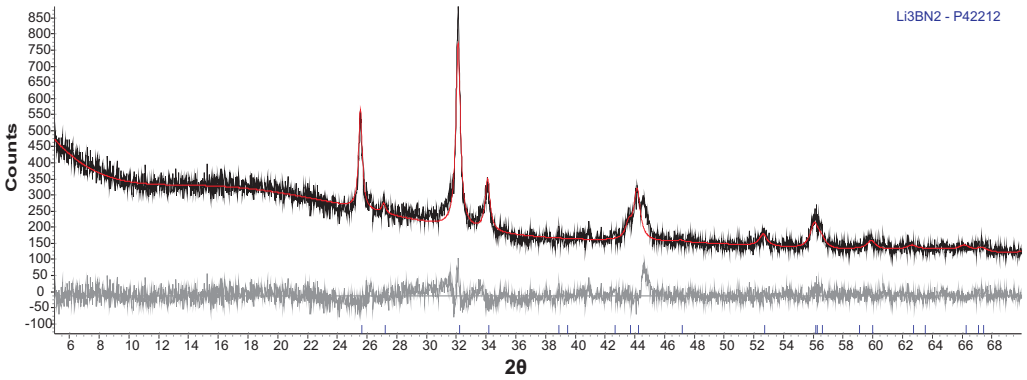

Figure A.4: Powder X-ray diffraction pattern of ball milled Li_3BN_2 ($P4_22_12$) after heating under 100 bar H_2 at 300 °C for 140 hours. Observed (black), calculated (red) and difference (grey) plots, and peak positions for Li_3BN_2 ($P4_22_12$) are shown (blue).

List of Figures

List of Tables